

D I S S E R T A T I O N

The Role of Carbon in Creating Insulating Behavior in GaN-on-Si Buffers: A Physical Model

ausgeführt zum Zwecke der Erlangung des akademischen Grades
eines Doktors der technischen Wissenschaften
unter der Leitung von

Ao. Univ. Prof. Dipl.-Ing. Dr. Dionyz Pogany
Institut für Festkörperelektronik

eingereicht an der Technischen Universität Wien
Fakultät für Elektrotechnik und Informationstechnik

von

Christian Koller

Marksgasse 5/10
A-9500 Villach, Österreich

geboren am 11. Jänner 1989 in Zwettl.

Wien, am 16. Dezember 2018

Abstract

The extensive market growth in emerging fields such as electric/hybrid vehicles and renewable energies increases the demand for electrical power conversion systems with higher efficiencies. As silicon (Si) approaches its physical limits, wide band gap semiconductors such as gallium nitride (GaN) with significantly higher critical electric fields are increasingly considered as feasible alternatives. For cost-competitiveness GaN is grown on Si substrates (i.e. GaN-on-Si), which requires highly insulating GaN buffers to isolate electrically active GaN layers from conductive Si. Although it is empirically well-known that insulating behavior can be achieved by carbon-doping, the actual role of carbon is not understood yet.

The main obstacle in previous investigations was the focus on characterization of entire multilayer GaN-on-Si buffers, used for electronic devices. Their multilayer nature impedes extraction of the electrical behavior of a single layer and consequently the identification of the role of carbon in making GaN insulating. In order to overcome this apparent deficiency, we develop novel test structures, in which a single carbon doped GaN (GaN:C) layer is embedded between a metal and a highly n-doped GaN layer that acts as back electrode. This allows characterization of single GaN:C layers and derivation of a fundamental physical model. By substituting the single GaN:C layer with simple multilayers, the interaction of GaN:C with other layers is studied.

Characterization employs primarily capacitance-voltage (*CV*) and current-voltage (*IV*) measurements as well as fast (μs) transient capacitance measurements (*Ct*) after various bias steps. We introduce a straightforward analysis technique that enables direct extraction of potential and charge distributions from *CV* curves. *Ct* measurements even allow time-dependent tracking of charge transport through GaN:C and charge capture and emission in carbon defects. A cryogenic probe station allows to investigate the temperature dependence of these processes in a wide range between 20 and 560 K. Furthermore, electrical characterization equipment is extended by optical setups for illumination with monochromatic light and transient electroluminescence analysis.

Main results include evidence that the Fermi level is pinned in GaN:C approximately 0.7 eV above the valence band maximum, energetically close to the carbon acceptor level. We found that carbon atoms predominantly form acceptors and to a smaller extent also donors, whereby we demonstrate the crucial role of donors for achieving insulating behavior. Leakage current as well as capture and emission processes are solely determined by the charge transport through GaN:C. While for small carbon concentrations this transport occurs via the valence band (i.e. p-type), this behavior changes significantly when exceeding a critical concentration of $(1-10)\times 10^{18}\text{ cm}^{-3}$. In this case, charges propagate within the band gap in so-called "defect bands", which are formed by carbon acceptors, likely located at threading dislocations. In contrast to our analysis technique, classical extraction of defect parameters from Arrhenius-plot fails due to the non-Arrhenius temperature dependence of the transport process. Although carbon introduces conductive channels

in GaN, experiments reveal enhanced insulating behavior of multilayers including GaN:C layers. The key therefore is the ability of GaN:C to accumulate charges in carbon acceptors that prevent conduction via valence and conduction bands.

The developed physical GaN:C model will support future optimization of insulating buffers in GaN-on-Si devices such as HEMTs (high-electron-mobility transistors). It will help to understand the electrical behavior of existing buffers and allow for development the prediction of the behavior of new buffers before manufacture.

Kurzfassung

Das starke Wachstum in zukunftsweisenden Märkten wie Elektro-/Hybridfahrzeugen sowie erneuerbare Energien steigert die Nachfrage nach elektrischen Energieumwandlungssystemen mit höheren Wirkungsgraden. Da Silizium (Si) zunehmend an seine physikalischen Grenzen stößt, werden Halbleiter mit breiter Bandlücke wie Galliumnitrid (GaN) durch seine weitaus höheren kritischen elektrischen Feldstärke zunehmend als Alternativen betrachtet. Aus Kostengründen wird GaN auf Si-Substraten gewachsen (GaN-on-Si). Um die elektrisch aktiven GaN-Schichten von leitendem Si zu isolieren, werden hochisolierende GaN-„Buffer“ benötigt. Obwohl empirisch bekannt ist, dass Kohlenstoff-Dotieren GaN isolierend macht, fehlen genaue Kenntnisse über die tatsächliche Rolle von Kohlenstoff.

Das Hauptproblem früherer Untersuchungen war der Fokus auf die Charakterisierung von ganzen GaN-on-Si-Buffern, wie sie für elektrische Anwendungen zum Einsatz kommen. Deren vielschichtige Struktur verhindert jedoch die Extraktion des elektrischen Verhaltens einer einzelnen Schicht und in weiterer Folge die Identifikation der Rolle von Kohlenstoff für das isolierende Verhalten von GaN. Um diese Unzulänglichkeit zu überwinden entwickeln wir neuartige Teststrukturen, in welchen eine einzelne kohlenstoffdotierte GaN-Schicht (GaN:C) eingebettet ist zwischen einem Metall und einer hoch n-dotierten GaN Schicht, die als untere Elektrode dient. Dies ermöglicht die Charakterisierung von einzelnen GaN:C-Schichten und die Herleitung eines fundamentalen physikalischen Modells. Austausch der einzelnen GaN:C-Schicht durch einfache mehrschichtige Strukturen ermöglicht zudem die Untersuchung der Interaktion von GaN:C mit anderen Schichten.

Zur Charakterisierung werden größtenteils Kapazitäts-Spannung- (CV) und Strom-Spannung- (IV) sowie schnelle transiente Kapazitäts-Messungen (Ct) nach verschiedenen Spannungsänderungen eingesetzt. Wir stellen eine einfache Analysetechnik vor, die eine direkte Extraktion von Potential- und Ladungsverteilungen auf Basis von CV -Kurven ermöglicht. Ct -Messungen erlauben sogar zeitabhängiges Mitverfolgen vom Ladungstransport durch GaN:C sowie von Ladungseinfang und -emission in Kohlenstoffdefekten. Ein kryogener Spitzenmessplatz ermöglicht die Untersuchung des Temperaturverhaltens dieser Prozesse in einem weiten Temperaturbereich zwischen 20 und 560 K. Weiters werden die elektrischen Messeinrichtungen durch optische erweitert, die die Bestrahlung mit monochromatischem Licht sowie transiente Elektrolumineszenzanalyse ermöglichen.

Die wichtigsten Ergebnisse beinhalten den Nachweis, dass das Fermi-Niveau in GaN:C ungefähr 0.7 eV über dem Valenzbandkante festgehalten wird, energetisch nahe des Kohlenstoff-Akzeptors. Wir stellen fest, dass Kohlenstoff großteils Akzeptoren und in gerinerem Maße auch Donatoren bildet. Dabei demonstrieren wir, dass diese Donatoren eine wesentliche Voraussetzung sind, um isolierendes Verhalten zu erzeugen. Sowohl Leckstrom als auch Ladungseinfangs- und Emissions-Prozesse in GaN:C werden vollständig durch den Ladungstransport in GaN:C bestimmt. Während für geringe Kohlenstoffkonzentrationen dieser Transport über das Valenzband stattfindet

(p-Leitung), ändert sich dieses Verhalten erheblich sobald die Konzentration einen Wert von $(1-10) \times 10^{18} \text{ cm}^{-3}$ übersteigt. In diesem Fall findet der Ladungstransport innerhalb der Bandlücke in sogenannten "Defektbändern" statt, welche von Kohlenstoff-Akzeptoren, vermutlich an Versetzungen, gebildet werden. Im Gegensatz zu unserer Analysemethode ist die klassische Ermittlung von Defektparametern aus Arrhenius-Plots nicht möglich, da die Temperaturabhängigkeit des Transportprozesses nicht dem Arrhenius-Gesetz folgt. Obwohl Kohlenstoff stromleitende Pfade in GaN einführt, zeigen Experimente bessere Isoliereigenschaften von mehrschichtigen Strukturen, die GaN:C-Schichten enthalten. Der Schlüssel dafür liegt in der Fähigkeit von GaN:C, Ladungen in Kohlenstoff-Akzeptoren anzusammeln, was Leitung über Valenz- und Leitungsband verhindert.

Das entwickelte physikalische GaN:C Modell wird zur zukünftigen Optimierung von isolierenden Buffern in GaN-on-Si-Bauteilen wie HEMTs ("high-electron-mobility transistors") beitragen. Es wird helfen, das elektrische Verhalten von existierenden Buffern zu verstehen sowie in der Entwicklung das Verhalten von neuen Buffern vor ihrer Produktion vorherzusagen.

Contents

1	Introduction	8
2	State of the art knowledge and characterization	11
2.1	GaN-based high-electron-mobility transistors (HEMTs)	11
2.2	Carbon-doped GaN (GaN:C): Literature review	13
2.2.1	Conduction through GaN:C buffers	16
2.2.2	Trapping dynamics in GaN:C buffers	21
3	Characterization of single GaN:C layers: Derivation of a physical model	28
3.1	Concept of "layer under test" (LUT) test structures	28
3.1.1	Fundamental idea of LUT structures	28
3.1.2	Experimental details of LUT structures	29
3.1.3	Proof of concept: electrical behavior of LUT structures	30
3.2	Electrostatics of LUT structures	31
3.2.1	Extraction of potential and charge distribution	31
3.2.2	Fermi level pinning at dominant acceptor	35
3.3	Transient behavior of LUT structures	40
3.3.1	Dynamic characterization technique	41
3.3.2	Temperature dependence of relaxation processes in GaN:C	46
3.3.3	Necessity of defect bands	47
3.3.4	Comparison of defect band model with literature results	56
3.3.5	Leakage current in GaN:C	59
3.4	Influence of carbon concentration ([C]) for GaN:C	64
3.4.1	Highly carbon-doped GaN:C ($[C] \geq 10^{19} \text{ cm}^{-3}$)	65
3.4.2	Moderately carbon-doped GaN:C ($[C] \leq 10^{18} \text{ cm}^{-3}$)	67
3.4.3	Synthesis of carbon doping effects in GaN:C layers	70
3.5	Transition from "plateau" to "Ohmic regime" ("current filamentation")	72
3.5.1	Ohmic regime	72
3.5.2	Electrostatic electrical characterization of current filamentation	72
3.5.3	Emission microscopy (EMMI): Current filamentation during transition	74
3.5.4	Luminescence spectroscopy	78
3.5.5	Time dependence of filamentation	82
3.5.6	Statistical distribution of filamentation voltage	83
3.5.7	Current filamentation model	87
3.6	LUT structures under illumination	91

3.6.1	Static behavior	91
3.6.2	Dynamic behavior	98
4	Extension of LUT concept to multilayer structures and AlGaN:C: Interaction of (Al)GaN:C with other layers	103
4.1	Simplification of GaN:C model and application to simple fictive multilayer structures	103
4.2	Electrical behavior of GaN:C/GaN:uid multilayers (sample S _{10,uid})	109
4.2.1	Static behavior of sample S _{10,uid}	109
4.2.2	Dynamic behavior of S _{10,uid}	113
4.3	Electrical behavior of AlGaN:C and GaN:C/AlGaN:C multilayers	121
4.3.1	Polarization in (Al)GaN	123
4.3.2	Polarization in AlGaN:C/GaN:Si bilayers	124
4.3.3	Electrical behavior of AlGaN:C	126
4.3.4	GaN:C/AlGaN:C vs. AlGaN:C/GaN:C interfaces	127
5	Conclusion	134
6	Outlook	137
A	Appendix A: Experimental details of optical setup	139
A.1	Light source	139
A.2	Monochromator	139
A.3	Light transmission	141
A.4	Light on sample surface	141
	Bibliography	142

Disclaimer

A few of the central findings of this thesis base on material which has been partly published during the work on the thesis in different forms of media like journal publications and conference proceedings, see bibliography at the end of the thesis. According to the consensus of several guidelines of Austrian funding agencies and Austrian universities regarding proper scientific work [Gam09], the ideas of these publications are re-used with explicit citation at several positions in this thesis. The thesis puts the individual topics of the publications together with unreported topics into a larger context.

Ich erkläre hiermit an Eides statt, dass ich die vorliegende Arbeit selbständig sowie ohne unzulässige Hilfe Dritter und ohne Benutzung anderer als der angegebenen Hilfsmittel angefertigt habe. Die aus anderen Quellen direkt oder indirekt übernommenen Daten und Konzepte sind unter Angabe der Quelle gekennzeichnet.

Wien, am 16. Dezember 2018

Acknowledgments

First of all, I want to sincerely thank my three supervisors: Prof. Dionyz Pogany of the Institute of Solid State Electronics at Vienna University of Technology for sharing his in-depth understanding of semiconductor physics and measurement techniques in general as well as his critical reflections that pushed me towards a more meticulous approach; Gregor Pobegen from KAI GmbH for his professional supervision, motivation and for helping me not getting lost in details; and finally Clemens Ostermaier from Infineon Technologies AG for his mentoring and sharing his creativity in generating new ideas for physical models, measurement methods and presentations. It was their exceptional guidance that enabled this thesis.

My gratitude further goes to my colleagues Gerald Rescher, Roberta Stradiotto, Fabian Rasinger, Bernhard Ruch, Judith Berens and Valeria Padovan at KAI GmbH who helped me out in the many situations when I struggled with the measurement equipment, the analysis software or when they were just there to lend me an ear. Fabian Rasinger additionally paved the way for electrical characterization in a wide temperature range utilizing a cryogenic probe station which turned out to be a critical feature. Magdalena Weger investigated the temperature dependence of leakage currents in AlGaIn samples which contributed to this work. I further thank the whole GaN team at Infineon Technologies AG including Oliver Häberlen, Thomas Detzel, Ingo Daumiller, Lauri Knuuttila and especially Martin Huber for manufacturing the investigated samples. Gebhard Hecke and Richard Neumann supported me with their technical know-how for emission microscopy measurements and Martin Holzbauer from the Vienna University of Technology deposited the semi-transparent contacts that enabled usage of this technique. Gerhard Prechtel and Sun Jinming from Infineon Technologies AG as well as Dario Pagnano from the University of Cambridge helped me with technology computer aided design (TCAD) simulations.

My exchange with Prof. Michael Uren from the University of Bristol, one of the most experienced people when it comes to carbon-doped GaN, was especially fruitful. It led to several critical discussions and provided insight on how simulation experts can interpret my models.

Moreover, I highly appreciate the personal support from my family and friends for reminding me that there is also space for a life besides a PhD and for motivating, supporting and joining in countless adventures over the last years - you are the best.

This work was jointly funded by the Austrian Research Promotion Agency (FFG, Project No. 854247) and the Carinthian Economic Promotion Fund (KWF, Contract No. KWF-1521/28101/40388).

1

Introduction

Motivation for GaN power devices

The world's hunger for electrical power has been increasing constantly over the past decades and is not expected to stop soon [Demli]. Between generation of electrical energy and its consumption, electrical power has to change its form several times, i.e. frequency and voltage levels have to be adjusted. For example the *dc* output of a photovoltaic solar panel has to be converted to *ac* before being fed into the electric grid. After transmission, many applications such as computers require conversion from *ac* back to *dc*. Additionally, e.g. in electric vehicles the voltage level of *dc* current has to be changed. A great part of these power conversions is performed by power semiconductors, extensively dominated by Si for the last four decades. Starting from the first power MOSFET (metal-oxide-semiconductor field-effect transistor) tremendous progress has been achieved, resulting in performance approaching the theoretical limit of Si. Although with sophisticated designs as in super-junction devices and IGBTs (insulated-gate bipolar transistors) the steady improvement still continues, however it is slowing down and requires higher and higher efforts [Lid+14; Ama+18].

Consequently, in more recent history exploration of new materials apart from Si with higher theoretical performance has started. One of the most promising materials is GaN, which outperforms Si at material level due to its wide band gap, large critical electric field and high electron mobility. GaN has already demonstrated its outstanding potential for photonic (e.g. LEDs) and high frequency communication applications. Owing to its superior material properties, there is also great potential for GaN in power conversion applications, enabling high switching speed, low specific resistivity and low saturation switching transistors. Already at this early stage of development, GaN devices can compete and in many cases outperform Si; and in contrast to Si, today's GaN devices are far from utilizing the full potential of the material, leaving plenty room for future development.

In concrete terms, GaN transistors are smaller, more energy-efficient and can operate at higher switching frequency, exploiting the MHz regime. Additionally, in converters the higher switching frequency reduces the size of passive elements and switching losses, leading to smaller, lighter and more energy-efficient devices. Considering that more than 10% of all generated power is lost in power conversion [Cor08], efficient GaN power converters can play an important role in future's society with its increasing demand for power combined with efforts to cut energy consumption for environmental reasons. For hybrid and electric vehicles not only the increased efficiency but also the smaller size and lower weight of power converters utilizing GaN enable larger ranges, which can push the technology and have significant impact on the environment.

Motivation for thesis

In order to stay cost-competitive to currently available Si technologies, GaN power devices predominantly employ a horizontal HEMT (high-electron-mobility transistor) design, grown on Si substrates [Lid+14]. It is critical for these GaN-on-Si devices to isolate active layers on the top from the conductive Si substrate on the bottom. Carbon doping is empirically well known to make GaN insulating, but also to cause dynamic device performance due to charge trapping in carbon defects. The ideal buffer should show following two features:

1. It blocks as much voltage as possible, ultimately limited by the critical electric field of GaN; and keeps the leakage current as low as possible. This can increase the energy efficiency and reduce buffer thicknesses, which can save a great part of manufacturing time and costs.
2. It shows no dynamic response due to charge trapping, which would delay or slow down the switching behavior of the device.

With currently mainly empiric knowledge it is unclear how these properties can be achieved, especially both simultaneously.

Scope of thesis

The ultimate goal is to find the critical parameters for achieving an as "ideal" buffer as possible. As carbon plays a key role for this goal, the objective of this thesis is to derive a physical model for carbon-doped GaN (GaN:C) that explains the role of carbon in making GaN insulating. The model should further describe conduction (i.e. leakage current) and charge trapping in carbon defects accurately. In order to achieve this, test structures are to be developed that allow for characterization of single GaN:C layers, in contrast to available structures that allow only investigation of complex multilayer buffer stacks. Characterization techniques are to be developed that enable extraction of all relevant carbon defect parameters and expose a physical model for GaN:C with its electric behavior concerning conduction and charge trapping. Various parameters such as GaN:C layer thickness, carbon concentration and Al-content are to be assessed. Finally, the interaction of GaN:C layers with other layers in more complex multilayer stacks is to be investigated.

Structure of thesis

Chapter 1 provides motivation and a short overview of the work. Chapter 2 gives an introduction to GaN-based HEMTs, the role of GaN:C and currently utilized characterization techniques with their shortcomings. Chapter 3 builds the core of this thesis and describes the concept, experimental

details as well as the electrostatic and transient behavior of used test structures, which reveal a novel charge transport mechanism in GaN:C. Charge transport is considered to take place in so-called defect bands within the GaN band gap instead of transport via valence or conduction bands. In Chapter 4 the gained physical GaN:C model is used to describe the interaction between various GaN and AlGaN based layers. Finally, Chapters 5 and 6 give a conclusion and outlook of the work.

2

State of the art knowledge and characterization

2.1 GaN-based high-electron-mobility transistors (HEMTs)

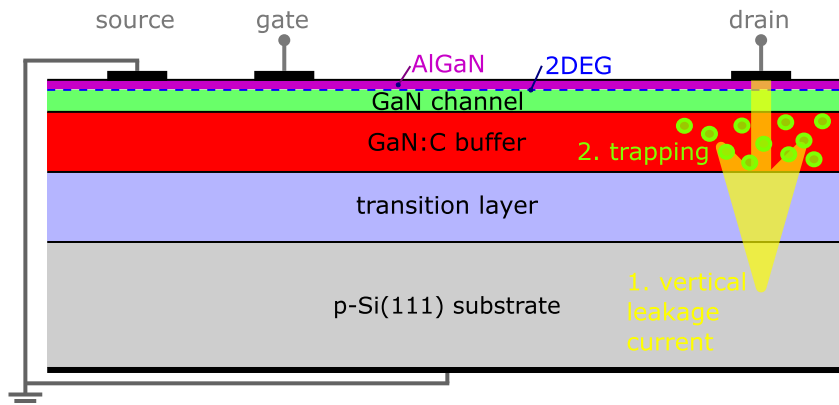


Fig. 2.1: Schematic of a HEMT indicating the GaN:C buffer's two main features of interest: 1. vertical leakage current and 2. trapping dynamics.

Fig. 2.1 depicts the most common form of GaN-based transistors for power electronics: the HEMTs. HEMTs are well known from GaAs-based devices for a long time; details on the principles can be found in standard semiconductor textbooks such as [SN06], only relevant parts will be summarized. Although GaN-based HEMTs can be produced on various substrates such as free-standing GaN, Al_2O_3 (sapphire) or SiC, due to its cost-efficiency Si(111) substrates are most promising for near-future power electronic applications [Che+17; Ama+18]. GaN is grown by metalorganic chemical vapor phase epitaxy (MOCVD) on top of p-doped Si(111) substrate wafers, but due to both thermal and lattice mismatch of Si(111) and GaN a transition layer is required [Fel+01]. Transition layers, often also referred to as strain relief layer or stress relief layer commonly

consist of many GaN and AlGaN layers with varying Al and carbon concentrations ($[Al]$, $[C]$) as well as different growth parameters. As AlGaN we define $Al_xGa_{1-x}N:C$ with $x = [Al]/([Ga] + [Al])$, $[Ga]$ being the Ga concentration. The transition layer helps to decrease mechanical stress as well as the amount of vertical threading dislocations significantly. Their role for leakage current and trapping dynamics is widely discussed [Rac+18b; Zha+15b; Ure+14c; Yac+16; Ure+17], however without a clear consensus yet, also due to their largely varying stack design throughout literature. E.g. threading dislocations are often speculated to increase vertical leakage current, which influences also the trapping dynamics. However, details on conduction mechanisms are rather speculative. Furthermore, there are debates whether screw, mixed or/and edge dislocations are conducting [Usa+18a].

On top of the transition layer a GaN:C buffer, an unintentionally doped GaN (GaN:uid) channel and an AlGaN barrier layer are grown. The different spontaneous polarization in GaN and AlGaN as well as the piezoelectric polarization in the AlGaN barrier give rise to a polarization charge at the GaN/AlGaN interface. This is compensated by a two-dimensional electron gas (2DEG) in GaN next to its interface to AlGaN. Source and drain are connected via the 2DEG, resulting in its high electron mobility of roughly $2000 \text{ cm}^2 \text{ V}^{-1} \text{ s}^{-1}$ [Feh+11] and thus small on-resistance $R_{ds,on}$. Applying negative bias at the gate pinches off the subjacent 2DEG, causing off-state condition. Consequently, an unbiased device is in on-state, commonly referred to as "normally-on" or "depletion mode" transistor. In order to make it "normally-off" ("enhancement mode"), various techniques are known, such as recessing part of [ON08; Pal+06; Sai+06; Ima+11; Chu+11; Cor+11] or the entire [Cho+14] AlGaN barrier below the gate, fluorine implanting the AlGaN barrier [Cai+05] or adding a p-doped AlGaN layer under the gate (gate-injection transistor - GIT) [Uem+07]. Although mentioned for the sake of completeness, this thesis is limited to the discussion of GaN:C buffers, for which all HEMT layers above the 2DEG, including AlGaN barrier, passivation, field plates and gate stacks are irrelevant.

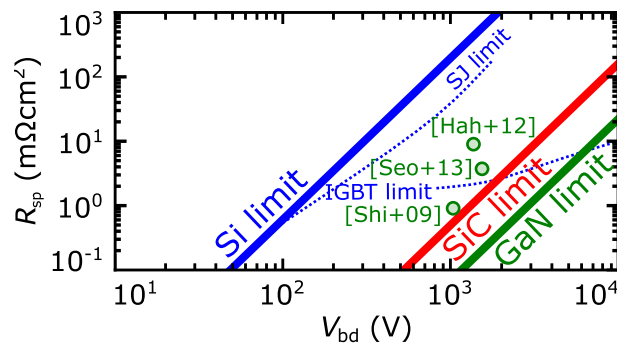


Fig. 2.2: Theoretical possible specific on-resistance (R_{sp}) vs. breakdown voltage (V_{bd}) for the three semiconductors relevant for power semiconductors: Si, SiC and GaN [Bal89]. Markers further show the performance of real GaN-based HEMT devices [Seo+13; Shi+09; Hah+12].

$R_{ds,on}$ in a HEMT is determined among other parameters by its gate-drain-distance (L_{gd}). A decrease in L_{gd} decreases $R_{ds,on}$, but as illustrated in Fig. 2.2 concomitantly decreases also its breakdown-voltage (V_{bd}). The figure further shows that due to the superior GaN material properties for a given V_{bd} lower $R_{ds,on}$ can be achieved compared to Si and SiC. However, this represents only the physical limit, real devices are still rather far from this theoretical limits as represented by the three example devices. For this thesis the most relevant aspect is that

although HEMTs being lateral devices, also a vertical electric field occurs within the stack. Fig. 2.1 shows that in packaged devices the Si substrate is commonly grounded together with the source. Consequently, the drain-source bias does not only drop laterally between drain and source but also vertically between drain and Si substrate. The resulting vertical electric field (\mathcal{E}) causes vertical leakage current and above a critical field vertical breakdown. These effects are of great importance during off-state, when the 2DEG is pinched off and the lateral resistivity is high. In order to avoid increased off-state leakage current and eventually breakdown via a vertical path, highly resistive HEMT stacks (buffer + transition layer) are required. Lateral resistivity and lateral V_{bd} can be increased by increasing L_{gd} , although to the cost of higher $R_{\text{ds,on}}$, see Fig. 2.2. Analogously, increasing the HEMT stack thickness would also result in increased vertical resistivity and V_{bd} , even without increasing $R_{\text{ds,on}}$. However, besides causing significantly higher costs, increased mechanical stresses due to thermal and lattice mismatch of Si and GaN limits the HEMT thickness to several micrometers, thicker layers eventually lead to crack formation [SSE09]. The vertical resistivity is mainly provided by carbon-doped GaN and AlGaN layers, especially the GaN:C buffer, to which this thesis is mainly dedicated to.

2.2 Carbon-doped GaN (GaN:C): Literature review

Carbon-doping is well known to make GaN resistive, also called semi-insulating. In order to understand the underlying principles we first discuss charge transport via conduction or valence band (CB/VB) by simple Ohmic conduction (I_{Ohm}):

$$I_{\text{Ohm}} = q\mathcal{E}(n\mu_n + p\mu_p), \quad (2.1)$$

$$n = N_{\text{CB}} f_{\text{FDD}}(E_{\text{bg}} - E_{\text{F}}), \quad (2.2)$$

$$p = N_{\text{VB}} f_{\text{FDD}}(E_{\text{F}}), \quad (2.3)$$

$$f_{\text{FDD}}(E_x) = \frac{1}{1 + \exp(\frac{E_x}{k_{\text{B}}T})}, \quad (2.4)$$

$$N_{\text{CB}} = 2 \left(\frac{m_e k_{\text{B}}T}{2\pi\hbar^2} \right)^{3/2}, \quad (2.5)$$

$$N_{\text{VB}} = 2 \left(\frac{m_h k_{\text{B}}T}{2\pi\hbar^2} \right)^{3/2}, \quad (2.6)$$

with q as elementary charge, \mathcal{E} as electric field, n as free electron density in CB, p as free hole density in VB, μ_n/μ_p as respective electron/hole mobility, f_{FDD} as Fermi-Dirac distribution, E_{bg} as band gap, N_{CB} as effective density of states (DOS) in CB, N_{VB} as DOS in VB and m_e/m_h as respective effective electron/hole mass. Within this thesis we define the energy of the valence band maximum (VBM) as zero point, all other energies are defined by their energy difference to this value. Further we use $m_e = 0.2 \times m_0$ [LRS01] and $m_h = 0.8 \times m_0$ [Pan75] with m_0 being the rest mass of an electron. Study of upper relations exhibits that the parameter determining I_{Ohm} by far most, is E_x which is the energy difference of E_{F} from conduction band minimum (CBM) or VBM.

In an ideal unbiased semiconductor E_{F} could be located approximately in the center of the band gap, resulting in small conductivity. However, epitaxial grown GaN-on-Si, even if not inten-

tionally doped, contains always background donors. These originate mainly from residual oxygen or silicon [Wat+03; Par+00; Wic+04], in smaller portions possibly also from nitrogen vacancies, anti-site or other point defects [WN04]. These shallow donors pin E_F close to CBM, resulting in high n and consequently large I_{Ohm} , i.e. n-type behavior. To avoid this n-type behavior the shallow background dopants can be compensated by adding additional impurities, which are deeper in the band gap and consequently pin E_F more distant from the band edges CBM and VBM. Relevant candidates for counter dopants are Fe and C. While Fe dopants form deep acceptors roughly 0.6-0.9 eV below CBM [Pol+03; UMK12], C atoms form acceptors 0.5-1.1 eV above VBM, derived electrically e.g. in [Wri02; Bis+13; Bis+14a; Ure+14a; Ver+14; Moe+16; Tan+13; Chi+16; Bis+14b; Ure+14b; Zho+12]. An increase of the distance of E_F of a band edge from 30 meV to 0.9 eV decreases n or p and consequently I_{Ohm} at room temperature by 15 orders of magnitude. While in general both, Fe and C, are capable of making GaN highly-resistive, Fe incorporation is reported to result in strong memory effects [Hei+02]. Consequently, for power semiconductor devices commonly only C doping is considered and hence investigated within this thesis.

Carbon in GaN from an atomistic point of view

In general, carbon atoms can either substitute a Ga (C_{Ga}) or an N atom (C_{N}) in the GaN crystal. For matter of simplicity, for the moment we neglect other defects such as possibly existing carbon interstitials or carbon complexes with oxygen or hydrogen [RM05; Res+14]. As C is a group IV (14) element with four valence electrons and Ga a group III (13) element with three valence electrons, C_{Ga} provides an additional electron to the system and therefore acts as donor. In contrast, as N is a group V (15) element, C_{N} acts as acceptor. Whether C substitutes Ga or N is determined mainly by the position of E_F during epitaxy and can be understood by discussion of formation energy plots as depicted in Fig. 2.3. It shows the case for Ga-rich conditions which are commonly established in GaN grown by MOCVD [Yac17]. The formation energy plot in Fig. 2.3 is calculated using density functional calculations based on a hybrid functional, giving e.g. a (0/-) transition level for C_{N} at 0.9 eV [LJW14]. GaN:uid is n-type, therefore E_F is close to CBM, i.e. $E_F \approx E_{\text{bg}} \approx 3.4$ eV [LRS01]. Consequently, the formation energy for C_{N} is smaller than for C_{Ga} (and C_{I}) so that carbon dopants will first be built in at the N-site. As the donors C_{N} shift E_F towards VBM, the likelihood for C_{N} formation decreases while the likelihood for C_{Ga} formation increases. This continues until both C_{N} and C_{Ga} show same likelihood and E_F saturates, in Fig. 2.3 at roughly 0.5 eV. In theory, the formation energy plot determines the concentrations of C_{N} and C_{Ga} and also E_F within the GaN:C layer, however their exact values are unknown for real GaN:C.

The consideration that introduction of deep defects pins E_F deep in the band gap may sound trivial but the determination of its actual position requires information on the exact concentration and energy of all acceptors and donors, which are in general not available. Common GaN:C considerations include carbon acceptors in the bottom half of the band gap and donors in the upper half. A major point, in which no consensus has been found in the community yet concerns the ratio of acceptor concentration (N_{acc}) to donor concentration (N_{don}). In many publications such as [Ure+17; LJW14] N_{acc} is considered to exceed N_{don} significantly, referred to as dominant acceptor model (DAM). In this case E_F pins near the acceptor energy E_{acc} and while practically all donors are unoccupied (positively charged), acceptors are partly occupied (negatively charged) and partly unoccupied (neutral). In contrast, in the auto-compensation model (ACM) N_{acc} and N_{don} are exactly identical so that acceptors as well as donors are almost completely ionized, i.e.

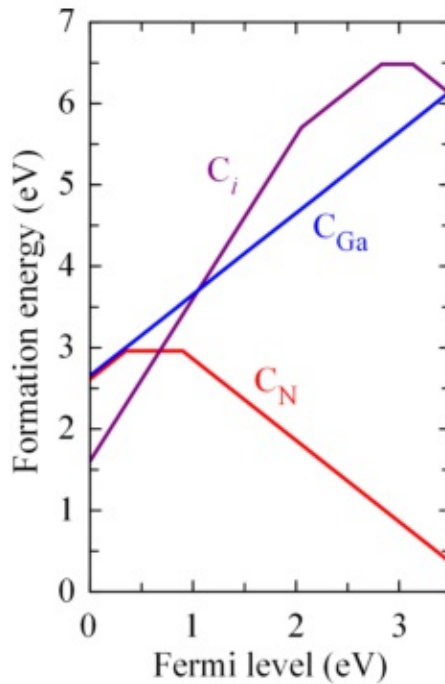


Fig. 2.3: Formation energy plot for carbon-doped GaN with C_N , C_{Ga} and carbon interstitials C_i . Figure from [LJW14].

donors are positively charged, acceptors negatively charged. In this way, E_F pins exactly between E_{acc} and the donor energy (E_{don}), which is also deep in the band gap and makes GaN:C therefore insulating, sometimes also called "semi-insulating". In the ACM the formation energy plot has to look slightly different in a way, as it is often considered for GaN grown in N-rich condition, e.g. in molecular beam epitaxy (MBE). Although considered in literature [Wri02; Arm+06; Ver+14] we will present in Section 3.2.2 besides more detailed discussion also electrical considerations that strongly suggest that DAM has to be favored over ACM, although from growth point of view both might be reasonable.

Electrical behavior of GaN:C

The above discussed models can explain how carbon-doping makes GaN insulating by pinning E_F closer to the center of the band gap. However, it does not explain the vertical leakage mechanism through a GaN:C buffer layer and especially not through a full HEMT structure. A yet unmentioned aspect is that carbon dopants do not just increase the resistivity of GaN but also act as trap centers. E.g. they can capture ("trap") electrons during off-state and increase $R_{ds,on}$ in the subsequent on-state, referred to as "dynamic $R_{ds,on}$ " and "current collapse" [MMZ18]. Schematically depicted in Fig. 2.1, trapping and vertical leakage current are the most critical features of GaN:C buffers and the aspects this thesis is dedicated to. Vertical breakdown might be a third major point of interest, which is to a certain degree related to vertical leakage current but it has many aspects that would need separate discussion, going beyond the scope of this thesis. In the following two subsections we discuss trapping and conduction in GaN:C as well as used characterization techniques on basis of previous studies. We further point out weaknesses of former analysis

that motivated us to develop our novel characterization technique, building the foundation of investigations in this thesis.

2.2.1 Conduction through GaN:C buffers

In order to investigate the nature of the vertical leakage, bias is applied in HEMT-like structures commonly solely between a top contact and the Si substrate on bottom. The steady-state leakage current (I_{SS}) is measured as function of bias (V) and temperature (T) and these dependencies compared to I_{SS} - V and I_{SS} - T dependencies of known conduction mechanisms. Alternatively, results are compared to technology computer aided design (TCAD) simulations. Due to the complexity of the HEMT stack it is not obvious which layers limit the leakage current and which electric fields are present in which layer. Therefore, more sophisticated studies identify also the effect and conduction mechanism of single layers, e.g. by varying growth parameters and analyzing the effect on electrical properties (e.g. [Yac+17; Yac+18]). In general, throughout previous publications three main conduction mechanisms are reported to play a role in vertical leakage currents. In the following section these mechanisms will be introduced and afterwards we will review representative previous studies and their conclusions regarding conduction mechanisms.

Conduction mechanisms in general

For discussion of the present conduction mechanism we first briefly introduce the conduction mechanisms that are commonly associated with vertical leakage in GaN:C.

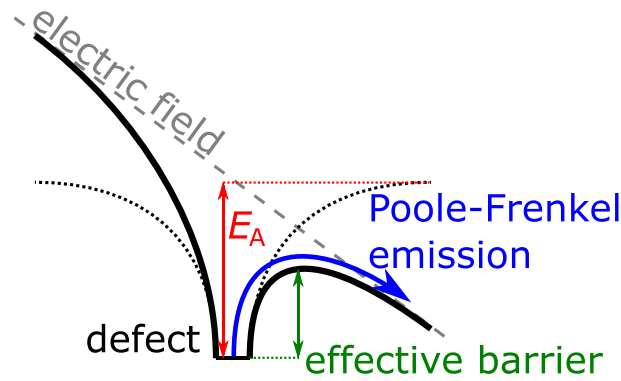


Fig. 2.4: Schematic Poole-Frenkel emission from a trap demonstrating how an applied electric field lowers the effective barrier.

Poole-Frenkel conduction: As demonstrated in Fig. 2.4, trapped electrons can be thermally excited from the trap level to CB, whereby the effective barrier is reduced by an applied \mathcal{E} . Consequently, Poole-Frenkel conduction shows strong \mathcal{E} and T dependence and dominates rather at high values of \mathcal{E} and T . The current density for Poole-Frenkel conduction can be described by

$$I_{PF} = q\mu N_{CB}\mathcal{E} \exp\left[\frac{-q(E_A - \sqrt{q\mathcal{E}/(\pi\epsilon)})}{k_B T}\right], \quad (2.7)$$

with E_A being the activation energy, i.e. the energy difference between trap and CBM; ϵ the permittivity which is the product of vacuum (ϵ_0) and relative permittivity ($\epsilon_r \approx 9.5$ [LRS01;

BI73]) and k_B being the Boltzmann constant. While above description refers to conduction in the conduction band, analogously conduction can occur in the valence band.

Space-charge-limited conduction: Space-charge-limited conduction (SCLC) was first proposed by Child already in 1911 as charge transport mechanism in vacuum diodes. In solids it can be observed when low Ohmic conductivities increase the electrical relaxation time (i.e. product of resistivity and permittivity) to values larger than the transit time of charges [Lam56; Wri61; Yac17]. Fig. 2.5 shows the typical I_{SS} - V characteristic for a semiconductor with large trap density [Lam56]. For small bias the dominant conduction mechanism is Ohmic conduction until at a certain bias all traps become filled, referred to as "trap-filled limit voltage V_{TFL} ". Above this bias the current approaches asymptotically space-charge-limited conduction described by Child's law, sometimes also referred to as Mott-Gurney law:

$$I_{SCLC} = \frac{9}{8} \varepsilon \mu \frac{V^2}{L^3}, \quad (2.8)$$

where L is the length of the space charge region.

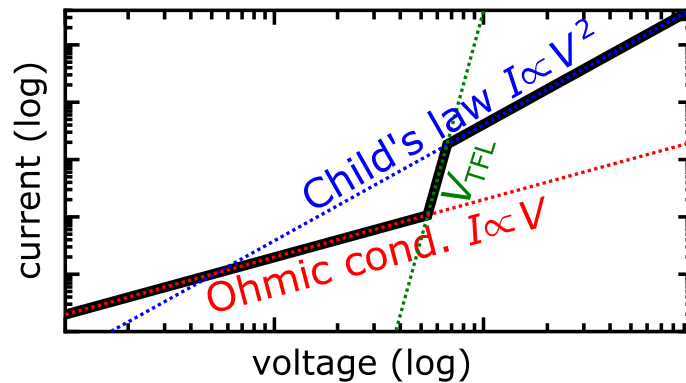


Fig. 2.5: Schematic I_{SS} - V characteristic for SCLC as proposed by Lampert [Lam56] for semiconductors with large trap densities. At $V = V_{TFL}$ conduction changes from being limited by Ohmic conduction to being determined by SCLC.

Hopping conduction: Hopping conduction is similar to Poole-Frenkel conduction in a sense that charges move from one trap site to another. The difference is that while in Poole-Frenkel conduction charges overcome the potential barrier between two trap sites thermally, in hopping conduction this process is assisted by quantum-mechanic tunneling, as depicted in Fig. 2.6. Hopping can be divided into nearest neighbor hopping (NNH), also referred to as fixed range hopping (FRH), and Mott variable range hopping (VRH). At high temperatures charges rather hop into the nearest trap (i.e. NNH), which can be described by [MD12; LI15]:

$$I_{NNH} = \sigma_0 \mathcal{E} \exp\left(-\frac{T_0}{T}\right), \quad (2.9)$$

where σ_0 is the electrical conductivity at temperature T_0 . At low T on the other hand charges rather hop into trap sites further away but with lower trap energy. Hopping can occur either in

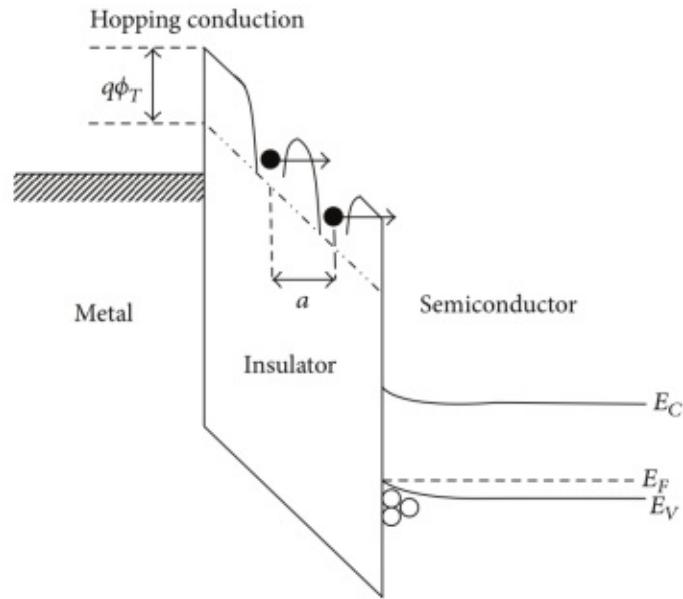


Fig. 2.6: Band diagram demonstrating hopping conduction in a metal-insulator-semiconductor (MIS) structure. Figure from [Chi14].

the bulk in all three dimensions ($I_{VRH,3D}$) or it can also be limited to one dimension ($I_{VRH,1D}$), e.g. if traps are located only in one-dimensional columns:

$$I_{VRH,3D} = \sigma_0 \mathcal{E} \exp\left(-\frac{T_0}{T}\right)^{1/4}, \quad (2.10)$$

$$I_{VRH,1D} = \sigma_0 \mathcal{E} \exp\left(-\frac{T_0}{T}\right)^{1/2}. \quad (2.11)$$

Although within this thesis we consider mainly the expressions above, in parallel in literature also the following expression for hopping conduction is found [Chi14; LI15]:

$$I_{\text{hopping}} = qan\nu_{\text{vib}} \exp\left(\frac{qa\mathcal{E} - E_A}{k_B T}\right), \quad (2.12)$$

where a is the mean hopping distance and ν_{vib} the thermal vibration frequency of trapped charges.

Characterization of conduction mechanisms in GaN

The main challenge for the characterization of the vertical leakage current is the complexity of GaN-on-Si stacks which can consist of up to 100 layers with different growth conditions (e.g. [C], [Al], pressure, ...), whereby they can be grouped in layers as depicted in Fig. 2.1. Uren et al. [Ure+17] present a simplified equivalent circuit, depicted in Fig. 2.7 which is mainly supposed to explain buffer trapping, but it also gives an idea of the parts that have to be considered for investigating vertical leakage current. E.g. the GaN:uid layer is rather blocking for positive bias on top and conducting for opposite polarity (i.e. diode-like, D_1). The series resistance R_{dis1} represents leakage current via extended defects such as threading dislocations. Analogous, in the GaN:C bulk leakage current can be determined by conduction in the bulk (R_{GaN}), but also in extended defects (R_{dis2}). The complexity of the stack makes it almost impossible to derive accurate potential distributions

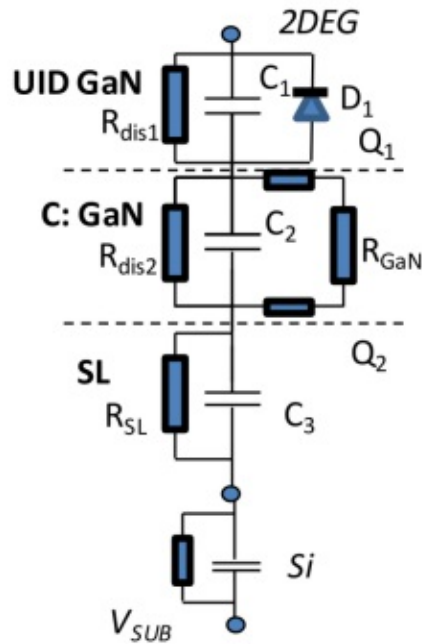


Fig. 2.7: one-dimensional equivalent circuit representing the HEMT stack according to Uren et al. [Ure+17]. Figure from [Ure+17].

and understand the influence of every layer. In the following we present representative examples how this issue has been treated in the past:

Most groups (e.g. [Zho+12; Moe+15a; Bis+14b]) do not consider the inhomogeneous stack at all and therefore treat it as a single GaN layer with a homogeneous electric field without explicitly mentioning. They analyze vertical I_{SS} - V characteristics as depicted in Fig. 2.8 from [Zho+12] and solely based on the V and T dependence some speculate that results can be explained best by SCLC [Zho+12; Moe+15a] while others suggest Poole-Frenkel or hopping conduction to explain results better [Bis+14b].

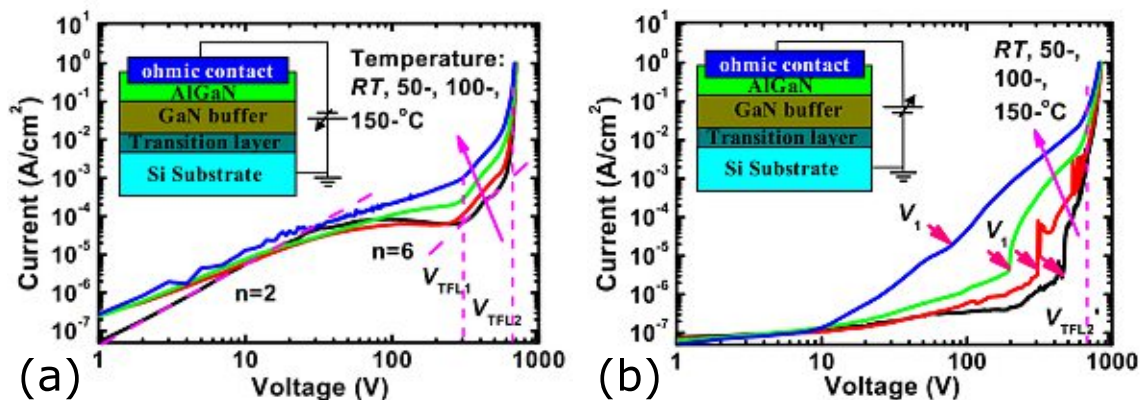


Fig. 2.8: Vertical leakage current vs. (a) reverse and (b) forward bias indicating SCLC according to Zhou et al. [Zho+12]. Figure from [Zho+12].

As introduced above, not every layer contributes equally to suppressing leakage current. In order to figure out the effect of a single layer and its electrical behavior, one can vary the growth

conditions of a single layer and determine the effect on the electrical behavior. E.g. Yacoub et al. [Yac17] varied the thickness of an AlN layer that is grown between Si substrate and transition layer between 0.47 and 1.47 μm . Fig. 2.9 demonstrates that the breakdown voltage, defined by Yacoub as the bias at which $I = 1 \text{ A cm}^{-2}$, shows no dependence on the AlN thickness for positive bias but very large dependence for negative bias. He concludes that for negative bias the AlN layer is the main current-blocking layer, in which most of the voltage drops. The AlN thickness variation delivers besides the V and T dependence a third parameter, the leakage current depends on. As depicted in Fig. 2.10(a) the dependence of the leakage current on the AlN thickness and V within a limited range suggests SCLC as dominant conduction mechanism. As the AlN thickness has no effect on the leakage current for positive bias on top, Yacoub et al. considers the buffer as homogeneous layer and from the V and T dependence shown in Fig. 2.10(b) they suggest Poole-Frenkel conduction to be most likely. From the T dependence they extracted an activation energy of 0.7 eV.

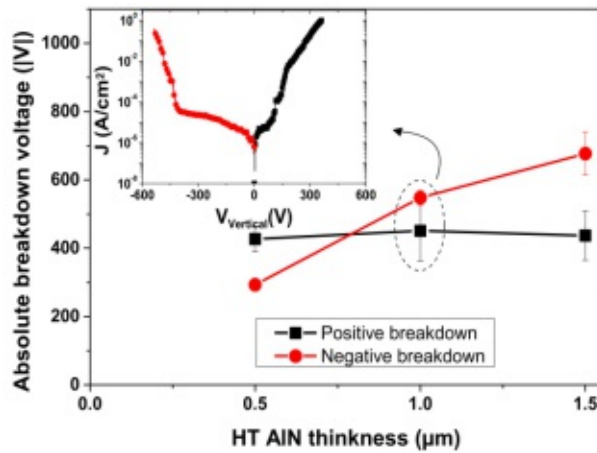


Fig. 2.9: Vertical breakdown voltages as function of the AlN thickness. Figure from [Yac17].

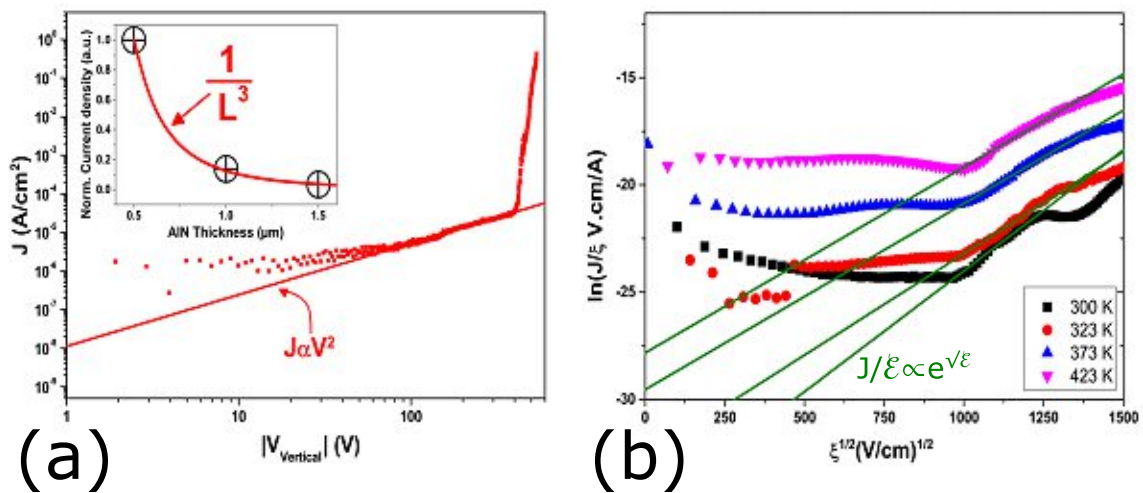


Fig. 2.10: (a) Leakage current for negative bias on top with variation of the AlN thickness in the inset indicating SCLC, see Eq. (2.8). (b) Leakage current for positive bias for various temperatures indicates Poole-Frenkel conduction, see Eq. (2.7). Figure from [Yac17].

A more sophisticated approach is followed by Uren et al. in [Ure+14a], in which they consider the HEMT stack as depicted in the equivalent circuit in Fig. 2.7. Additionally to the T -dependent steady-state (SS) I_{SS} - V characteristics, they perform pulsed and ramped substrate bias measurements with varying ramp rates on devices without gate. From these dynamic measurements a rough estimation of the trapped charges in every layer is derived, from which voltage drops and electric fields in every layer can be estimated for every value of applied bias. On this basis I_{SS} - V characteristics with voltage drops in single layers can be derived for varying temperatures as shown in Fig. 2.11. Uren et al. conclude that for low positive biases on top (i.e. 0.1 - 0.3 MV cm $^{-1}$). Poole-Frenkel conduction seems most likely and they further suggest conduction via threading dislocations. At higher biases the transition layer starts to conduct, explained best by Poole-Frenkel conduction, probably again via threading dislocations, however Schottky emission would fit the results similarly well.

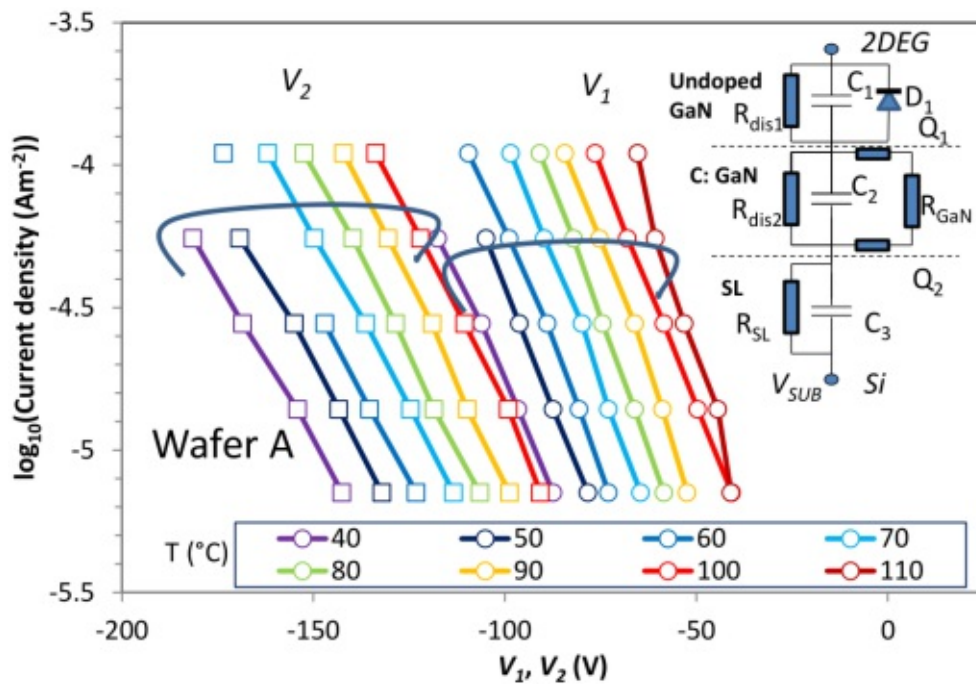


Fig. 2.11: Leakage current as function of estimated voltage drops in GaN:uid (V_1) and in GaN:C (V_2). Figure from [Ure+14a].

We conclude that conduction depends strongly on the exact epitaxial structure, from which the differences in leakage currents from various groups result. This leads to different interpretation of the conduction mechanisms. Due to the complexity of HEMT structures we consider that from available publications no reliable information on the intrinsic conduction mechanism in GaN:C can be extracted.

2.2.2 Trapping dynamics in GaN:C buffers

One of the most promising fields for GaN HEMTs are power transistors for power converters, in which HEMTs are switched several thousand times per second [Yac17; Hug+12; Lid+14]. In these applications the vertical electric field in the GaN:C buffer can cause a number of detrimental dynamic operation conditions such as e.g. a shift of the threshold voltage (ΔV_{th}) or a dynamic on-

resistance. While ΔV_{th} is related mainly to trapping in the gate stack region, dynamic on-resistance is a phenomenon directly resulting from trapping in the GaN:C buffer [Bis+14b; Ure+17; Bis+13; Bis+14a; Bis+15; Ure+14a; Ure+14b; Moe+16; Tan+13; Chi+16; Zho+12]. More precisely, besides the GaN:C buffer there are several other locations, where trapping might cause dynamic on-resistance, e.g. above the 2DEG at the AlGaN barrier surface. As explained later one can well distinguish between traps above and below the 2DEG and therefore identify the effect of the carbon-doped layers.

Dynamic on-resistance

Applying bias to a HEMT causes an electric field in the GaN:C buffer which leads to charges being trapped in the HEMT stack. If negative/positive charges are trapped in the stack, this leads to a decrease/increase of the 2DEG density, respectively. This can e.g. occur during operation, i.e. on-state, but the more severe case is that charges are trapped in the stack during off-state. When switching from off- to on-state trapped charges detrap, however depending on the trap location this might occur slowly. Especially due to the deep level of carbon acceptors, charge emission from traps commonly exceeds the time of a switching cycle, resulting in output current losses. In order to quantify and compare this degradation, the two terms "current collapse" (CC) and "dynamic $R_{ds,on}$ " have established, whereby the definitions are not strict and sometimes defined differently. Technically, both describe a dynamic on-resistance, but as demonstrated in Fig. 2.12, CC commonly refers to the decreased drain current in the saturation regime while dynamic $R_{ds,on}$ describes the increased on-resistance in the linear regime.

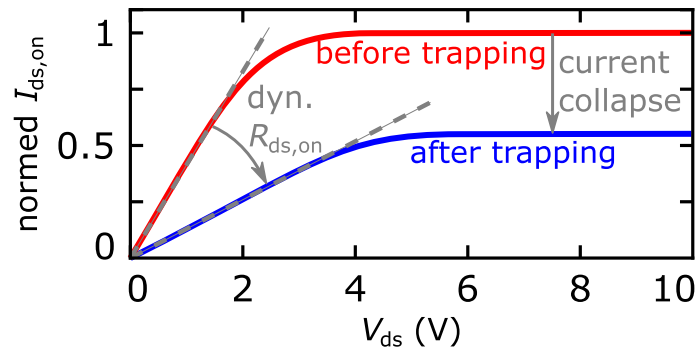


Fig. 2.12: Schematic figure of drain current in on-state vs. drain bias, before and after trapping, illustrating the terms current collapse and dynamic $R_{ds,on}$.

Characterization techniques

In order to investigate dynamic effects in GaN-on-Si HEMT buffers, detailed characterization of carbon defects is required. The main information of interest is the quantity and energetic position of carbon acceptors, which can be determined either by electrical or optical characterization. Electrical measurements are predominant in literature, whereby several different forms are known, from which the two most common ones are described in the following.

Substrate ramp

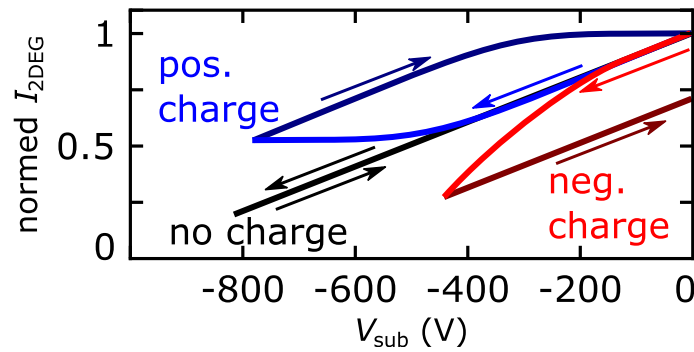


Fig. 2.13: Schematic substrate ramp measurement illustrating hysteresis curves for no trapping (black), positive charge trapping (blue) and negative charge trapping (red). Arrows indicate the sweep direction, i.e. increasing/decreasing bias.

The simplest method was first introduced for GaN-based HEMTs by Uren et al. [UrenPSSA01] and is performed by measuring the current between two top contacts connected via the 2DEG while applying a voltage ramp to the Si substrate at the bottom (V_{sub}). Fictive substrate ramp measurements in Fig. 2.13 demonstrate the different curve forms considering trapping of 1) no, 2) positive and 3) negative charges during the measurement:

1. An ideal insulating buffer without traps would behave like a capacitor, accumulating fictive positive charge at the top and negative charge at the bottom. More precisely the fictive positive charge at the top is a decrease in the negative 2DEG density and therefore leads to a decreasing 2DEG current ($I_{2\text{DEG}}$). Due to the absence of trapping $I_{2\text{DEG}}$ decreases linearly with $|V_{\text{sub}}|$ and up- and down-sweeps are identical.
2. In contrast, if during the ramp the net positive charge increases by hole capture or electron emission, higher $I_{2\text{DEG}}$ values are measured. The deviation from the ideal buffer without traps increases with decreasing ramp speed, leading also to decreasing hysteresis between up- and down-sweeps.
3. For increasing net negative charge (i.e. decreasing net positive charge) during the measurement results in lower $I_{2\text{DEG}}$ with same dependencies on ramp speed as above.

In the following we tentatively consider case 3) from above and that changes in the net charge occur by electron capture and emission. In this case during down-sweeps (i.e. increasing negative bias) electrons are captured and the dependence of $I_{2\text{DEG}}$ on the ramp rate gives information on capture processes. On the other hand during up-sweeps (i.e. decreasing negative bias) electrons are emitted, consequently giving information on emission processes.

In an adapted form of the substrate ramp experiment V_{sub} is not ramped continuously with measurements during applied V_{sub} . Instead, in this "on-the-fly" (OTF) called method, illustrated in Fig. 2.14, V_{sub} is ramped but between bias steps a short period with $V_{\text{sub}} = 0$ is added, in which the 2DEG current is measured. In this way the measured $I_{2\text{DEG}}$ can be directly related to trapped charges without comparison to a fictive ideal capacitive buffer. A further advantage is that vertical leakage current, which can complicate substrate ramp measurements significantly, can be neglected.

Substrate ramps are widely used as method to get an overview of the dynamic behavior of GaN:C buffers, e.g. in [Yac+18; Yac+17; Yac+16; Ure+15; Rac+18a; Ure+14a; Moe+15a;

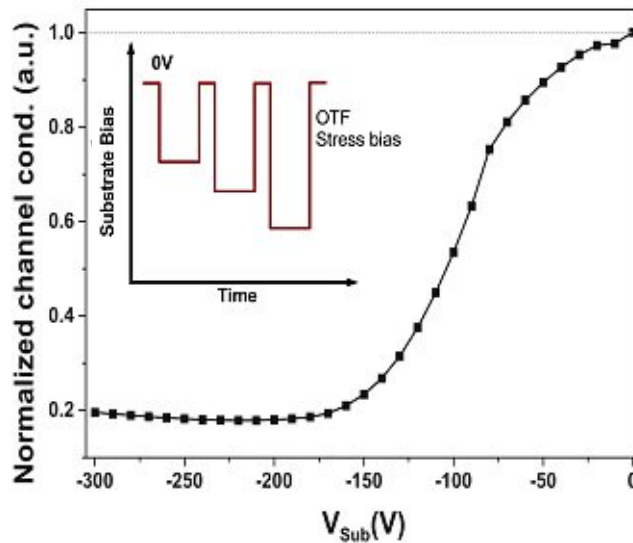


Fig. 2.14: "On-the-fly" (OTF) measurement on a GaN:C buffer indicating decreasing $I_{2\text{DEG}}$ with increasing negative V_{sub} , corresponding to negative charge capture. The inset demonstrates the measurement sequence. Figure from [Yac17].

Bis+14b; Ure+17; Men+17; Moe+15b; Moe+16; Yan+14]. However, in order to get deeper knowledge on the involved traps, information on the transient (i.e. time-dependent) behavior is required.

Current transient spectroscopy (CTS)

In order to gain quantitative information on the time dependence of trapping, which delivers also activation energies and hence a fingerprint of involved defects, substrate ramps are not suitable. Instead, a method in the following referred to as "current transient spectroscopy" (CTS) is by far the most common characterization technique for analyzing dynamic properties of HEMT buffers. E.g. Ref. [Bis+13] provides a database with data from more than 60 journal papers until 2013.

Fig. 2.15 illustrates the principle of CTS: First, in the stress condition (a,b) a vertical electric field is applied in the carbon-doped buffer. This can be done in (a) "off-state", where the HEMT is brought to off-state by applying negative bias at the gate and grounding source and substrate. The vertical electric field is introduced by positive bias at the drain contact. In order to generate a more uniform electric field over the entire device in (b) "backgating" condition all top contacts are grounded and negative bias is applied to the substrate contact. Alternatively, for "backgating" also devices without gate can be used. The electric field causes charges to be captured in defects in the buffer; in carbon-doped GaN buffers these are commonly negative charges. After stress condition the HEMT is switched to on-state, e.g. with conditions as shown in (c) with gate, source and substrate contacts grounded and 0.5 V at the drain contact, while $R_{\text{ds,on}}$ is measured. As the negative charges captured by carbon defects are deep in the band gap they are emitted rather slowly (Eq. (3.13)) so that immediately after switching to on-state there is still negative charge in the buffer. In comparison to the condition before stress, the potential in the buffer is raised, which decreases the amount of electrons in the 2DEG and therefore increases $R_{\text{ds,on}}$. Alternatively, one could argue referring to charge neutrality: Very simplified, the sum of charges in the buffer and in

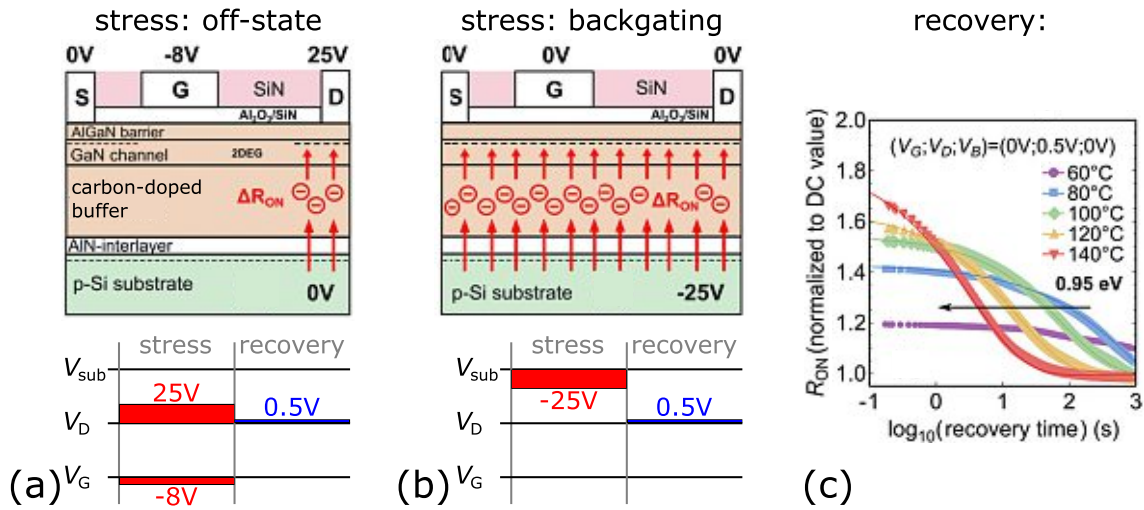


Fig. 2.15: Schematic HEMT structure and stress conditions for trapping negative charges in the buffer in (a) off-state and (b) backgating condition, figures from [Bis+14b]. (c) Recovery of $R_{ds,on}$ in on-state after the stress-condition due to detrapping from carbon defects, figure from [Bis+15].

the 2DEG has to remain roughly constant [Lag14]; thus negative charge in the buffer must reduce the electron density in the 2DEG. With ongoing time, negative charges are emitted from carbon defects to the 2DEG, decreasing $R_{ds,on}$ until it reaches again its SS value from before the stress, as shown in Fig. 2.15(c).

As carbon acceptors are considered to be located in the lower part of the band gap, negative charge emission is equivalent to hole capture. Detailed discussion of emission and capture processes is provided in Section 3.3.3, for the moment it is only important to know that for proper defect analysis characterization of both emission and capture processes is beneficial. Thus, often also the transient $R_{ds,on}$ during the stress condition is recorded, which can be done easily in the "backgating" version of CTS by applying additional to the large V_{sub} a small (commonly 0.1-0.5 V) source-drain bias.

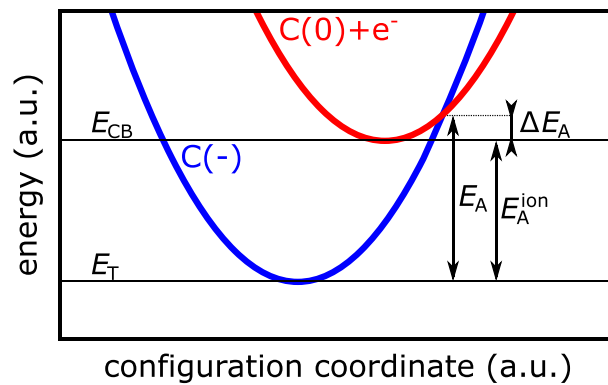


Fig. 2.16: Schematic configuration coordinate diagram for an occupied defect ($C(-)$) and an empty defect with an electron in the conduction band ($C(-)+e^-$), E_T represents the trap level. The energy barriers that have to be overcome for (phonon-assisted) electron capture and emission are ΔE_A and $E_A^{ion} + \Delta E_A$, respectively.

Although sometimes the extraction of capture and emission time constants itself is of interest, the main value of interest in CTS is the activation energy (E_A) of defects. As explained in

detail in Section 3.3.3 the (phonon-assisted) emission and capture time constant are given by $\tau_{\text{em}} \propto T^2 \exp\left(\frac{E_A}{k_B T}\right)$ and $\tau_{\text{cap}} \propto T^2 \exp\left(\frac{\Delta E_A}{k_B T}\right)$, respectively. Fig. 2.16 demonstrates that in general E_A is the sum of E_A^{ion} , determined by the energy difference between the minimas of E_T and E_{CB} (or the maximas of E_T and E_{VB}), and ΔE_A . Besides phonon-assisted transitions also optical transitions have to be considered in which electron capture is accompanied by photon emission and no energy barrier has to be overcome, see also Fig. 3.41. In CTS relaxation times τ are extracted for several temperatures and plotted in an Arrhenius-plot in Fig. 2.17. The slope of the linear fit gives E_A and consequently delivers a fingerprint of the relevant defect(s) in the buffer.

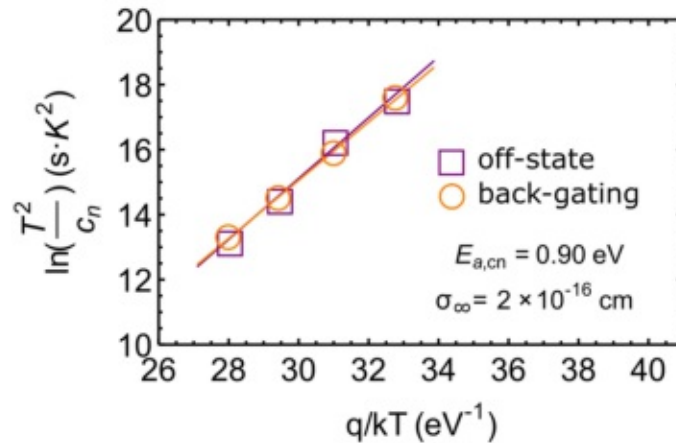


Fig. 2.17: Arrhenius plot with time constants derived in recovery after backgating and off-state stresses. c_n represents the trapping rate, which is equivalent to $1/\tau$. Figure from [Men+16].

Most CTS measurements in literature simply analyze emission transients. Considering compensation ratios (i.e. $N_{\text{don}}/N_{\text{acc}}$) in the range of 0.1-0.6 [Ure+17], time constants related to capture and emission show same temperature dependence: $\tau \propto T^2 \exp\left(\frac{E_A}{k_B T}\right)$ [Smi78]. For a compensation ratio in the range of 2 [Smi78] under certain circumstances it could even explain why both processes exhibit identical time constants, as observed e.g. in [Men+16]. However, more likely stress and recovery times are not determined by the capture/emission of holes but instead by the transport of charges between defect and 2DEG or Si substrate, as considered in [Ure+17]. Unfortunately, as emphasized in Section 2.2.1, the charge transport (i.e. conduction mechanism) is rather complex due to the complexity of the HEMT stack and not well understood yet.

There is a vast amount of studies in literature using CTS for defect characterization in carbon-doped buffers, delivering a very broad range of values for E_A between 0.5 and 1.1 eV [Bis+13; Bis+14b; Bis+14a; Bis+15; Ure+14a; Ure+14b; Moe+16; Tan+13; Chi+16; Zho+12]. However, there are several reasons why we mistrust conclusions based on this method: 1) The large range of found E_A , 2) the fact that in most cases transport mechanisms are completely neglected, 3) tiny amount of data points are used 4) within small temperature ranges. More detailed discussion of these points follows in Section 3.3.4.

Optical spectroscopy

A complementary method to the previous electrical measurements is optical spectroscopy. The principle is to change the occupation (i.e. charge) of defects either by 1) biasing the sample (see

emission spectroscopy in Section 3.5.4), 2) exposure to an electron beam (cathodoluminescence) or most common by 3) irradiation with a light beam (photoluminescence, see Section 3.5.4). Subsequently, in the recovery phase the defect in its excited state will relax again by emission of photons with a certain energy, whereby this energy depends on the energy level of the deep defect, see Fig. 3.41. For GaN:C commonly three major peaks are found in emission spectra, as indicated in Fig. 2.18:

1. One peak around 365 nm (i.e. 3.4 eV) is often referred to as near band edge emission (NBE) and originates from band-to-band recombination, i.e. electrons from CB and holes from VB recombine.
2. A peak at 430 nm (i.e. 2.9 eV), often referred to as "blue luminescence" rises due to recombination in carbon acceptors [AYW05].
3. Another peak, found at 560 nm (i.e. 2.2 eV) is dubbed as "yellow luminescence", whereby it is still unclear [Kne+16] whether it originates from carbon [Res+14] or gallium vacancies and oxygen [NW96].

Optical methods are powerful for deriving energy levels of deep defects and we also performed some simple measurements (see Section 3.5.4). However, within this thesis we focus on electrical measurements which deliver much more information on the behavior of GaN:C than a bare energy level.

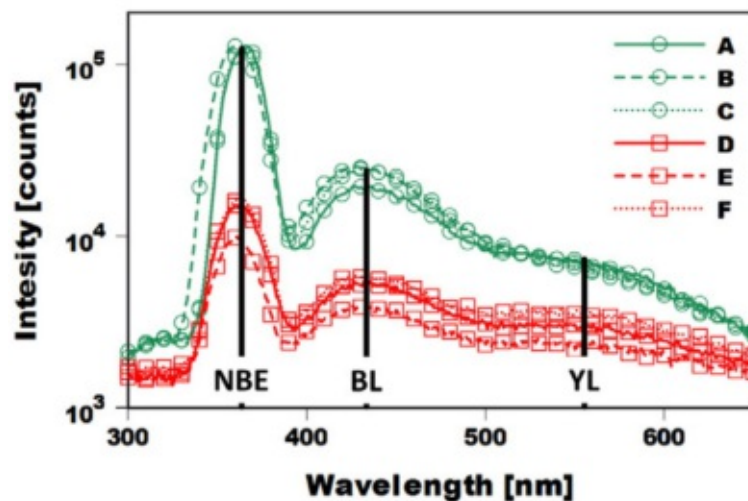


Fig. 2.18: Typical raw spectra of GaN:C, featuring peaks originating from near band edge emission (NBE), blue luminescence (BL) and yellow luminescence (YL). Indices 'A' to 'F' represent measurements from wafer center to wafer edge, respectively. Figure from [Kne+16].

3

Characterization of single GaN:C layers: Derivation of a physical model

This chapter builds the core of this thesis and is dedicated to detailed electrical (and optical) characterization of single GaN:C layers based on our developed "layer under test" (LUT) test structures.

In detail, in the first section we introduce the fundamental idea behind the LUT structures, show simple electrical characterization as proof of concept and to demonstrate their basic functionality as well as provide details on all different LUT structures investigated during the course of this thesis. Within this chapter we use the LUT concept in order to characterize single GaN:C layers. In the second and third sections we discuss their electrostatics (i.e. potential and charge distributions as well as leakage currents) and transient behavior (i.e. trapping), respectively, which requires the introduction of a novel physical model. The fourth section is dedicated to the influence of the carbon concentration, while in section five a breakdown-like transition at high electric fields is systematically analyzed. Sections six and seven focus on optical experiments, whereby the former focuses on optical spectroscopy while the latter discusses electrical measurements under illumination.

3.1 Concept of "layer under test" (LUT) test structures

3.1.1 Fundamental idea of LUT structures

As pointed out in the previous chapter, a great obstacle for gaining knowledge on the intrinsic electric behavior of GaN, especially GaN:C, is that it cannot be characterized in single layers. As GaN is commonly grown on different substrates (in our case Si), thick and complex transition layers are required in order to achieve high-quality GaN layers above. The evolving problem is

that the high-quality layers of interest cannot be investigated separately from the transition layer on bottom. The idea behind LUT structures is to introduce a highly n-doped GaN layer on top of the transition layer and to grow the layers of interest (i.e. "layer under test") on top. Finally, metal contacts are deposited on top, as demonstrated in Fig. 3.1. The conductive n-GaN layer distributes the current over a wide area so that the impedance of all layers below (i.e. the base structure) gets negligible. Besides acting as back electrode, the n-GaN layer also acts as sensor for the LUT above. For a rough estimation in the following we tentatively consider for the LUT a GaN:C layer which behaves similar to an insulator. In this case applying negative bias at the top depletes the n-GaN layer. Hence, capacitance-voltage analysis gives valuable information on the GaN:C layer, similar as in MOS capacitors. In summary, the core element of the LUT structures is the introduction of an n-GaN layer between the LUT and the transition layer, which acts as back electrode and as sensing layer.

3.1.2 Experimental details of LUT structures

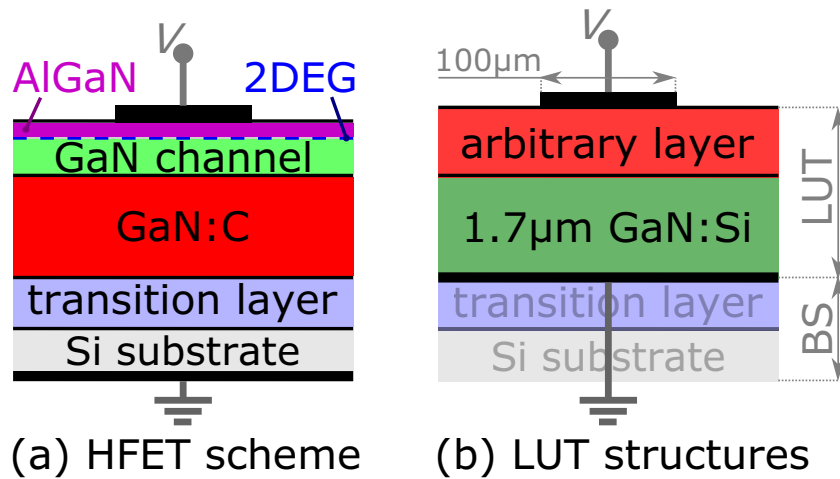


Fig. 3.1: Schematics of (a) a conventional HEMT stack and (b) an exemplary LUT structure consisting of the electrically inactive base structure and the LUT.

This paragraph is dedicated to the sample preparation and gives an overview of all used samples. Illustrated in Fig. 3.1, the basis of all samples are 6 inch n-doped Si(111) substrate wafers, on which III-N layers are grown by MOCVD in a commercially available multi-wafer reactor. The first layer is the transition layer, which consists of an AlN nucleation layer and several AlGaN layers with different [Al] and [C]. The Si substrate with the transition layer forms the base structure, which is analogous to the bottom layers of HEMT structures used in industry. The difference between HEMT stacks and structures used within this thesis, are the layers above the base structure. Instead of the GaN:C buffer, a 1.7 μm thick GaN:Si layer with an active donor concentration (N_{Si}) of $(8.2 \pm 1.0) \times 10^{16} \text{ cm}^{-3}$ (see Section 3.2.1) forms the n-GaN layer. Arbitrary layers on top of GaN:Si can be investigated without influence of the base structure, i.e. as "single layer" or "layer under test" (LUT). The top layer is not limited to single layers but can be extended to multilayer structures. Within this thesis various layers and multilayer structures with differences in [Al], [C] and their thicknesses are investigated, Tab. 3.1 shows all structures with their parameters. While the focus of this thesis lies on the characterization of single GaN:C layers, discussed in this chapter,

Section 4 is a first step towards understanding multilayer structures. [C] and [Al] are measured by secondary ion mass spectroscopy (SIMS) once per run, which consists of five wafers. Although building the back electrode, the GaN:Si layer itself also influences the electrical behavior of the top layers. Hence, as shown in Fig. 3.1, GaN:Si itself is part of the LUT.

For the top electrode different metals, thicknesses, shapes and sizes are used in order to match the needs of different characterizations. If not stated differently, square Ti contacts with an edge length of $100\ \mu\text{m}$ are deposited on top. For reason of comparison also Ni is used or in order to achieve semi-transparent contacts for light experiments, few nm thick Ti/Au films are used, see Section 3.6. For the thin Ti/Au films it has to be considered that needle movements due to e.g. thermal expansion during temperature-dependent measurements can detach part of the film, leading to measurement artifacts. Contact sizes range from diameters of $10\ \mu\text{m}$ up to $6\ \text{mm}$ with square and circular contacts, which has been proven to cause no significant edge effects.

Table 3.1: Stacks of all investigated samples (LUT structures) and designated names.

layer 2: d (nm) [C] ($10^{18}\ \text{cm}^{-3}$)						GaN:uid 200 -	GaN:C 200 10
layer 1: d (nm) [C] ($10^{18}\ \text{cm}^{-3}$)	GaN:C 200 1	GaN:C 200 10	GaN:C 300 10	GaN:C 200 70	AlGaN:C 100 >10	GaN:C 200 10	AlGaN:C 100 >10
1.7 μm GaN:Si, $N_{\text{Si}} \sim 8.2 \times 10^{16}\ \text{cm}^{-3}$							
transition layer							
Si substrate							
S_{Schottky}	S_{01}	S_{10}	S_{10b}	S_{70}	S_{Al}	$S_{10,\text{uid}}$	S_{SL}

3.1.3 Proof of concept: electrical behavior of LUT structures

This paragraph gives an overview over the electrical behavior of LUT structures on basis of sample S_{10b} , which uses as LUT a 300 nm thick GaN:C layer, see Fig. 3.2(a) and Tab. 3.1. The brevity of this section requires some oversimplification, which will be discussed in very detail in the subsequent sections. Fig. 3.2(a) shows a schematic of the test structure and (b-d) its electrical SS behavior, which is representative for all LUT structures. The electrical behavior can be divided into three bias regimes with very distinct features:

1. For $V \lesssim 1.5\ \text{V}$ in the "depletion regime" GaN:Si is with increasing negative bias increasingly depleted, resulting in the decreasing SS capacitance (C_{SS}) in Fig. 3.2(b).
2. For $1.5\ \text{V} \lesssim V \lesssim 15\ \text{V}$ in the "plateau regime" the depletion width in GaN:Si (w_{Si}) remains constant, resulting in the constant C_{SS} in Fig. 3.2(b).
3. For $V \gtrsim 15\ \text{V}$ after a sudden increase of I_{SS} by several orders of magnitude in the "Ohmic regime" I_{SS} converges towards a linear increase with V , observable in the saturation of the differential resistance (R_{diff}) with V in Fig. 3.2(d).

Remarkably, for $V \lesssim 15\ \text{V}$ I_{SS} and C_{SS} scale linearly with the contact area A , while for $V \gtrsim 15\ \text{V}$ I_{SS} is independent of A . We therefore consider the LUT structures as a series of the impedances of

the LUT (Z_{LUT}) and the base structure (Z_{BS}) as shown in Fig. 3.2(a). GaN:Si is highly conductive and connects Z_{LUT} and Z_{BS} . I_{SS} is therefore localized in LUT below the contact and scales with A , while I_{SS} spreads in GaN:Si over the entire wafer and permeates the base structure over the wafer area, independent of A . Obviously in the *Ohmic regime* Z_{BS} determines the electrical behavior, while for *depletion regime* and *plateau regime* Z_{BS} can be neglected, proving the LUT principle of single layer investigations.

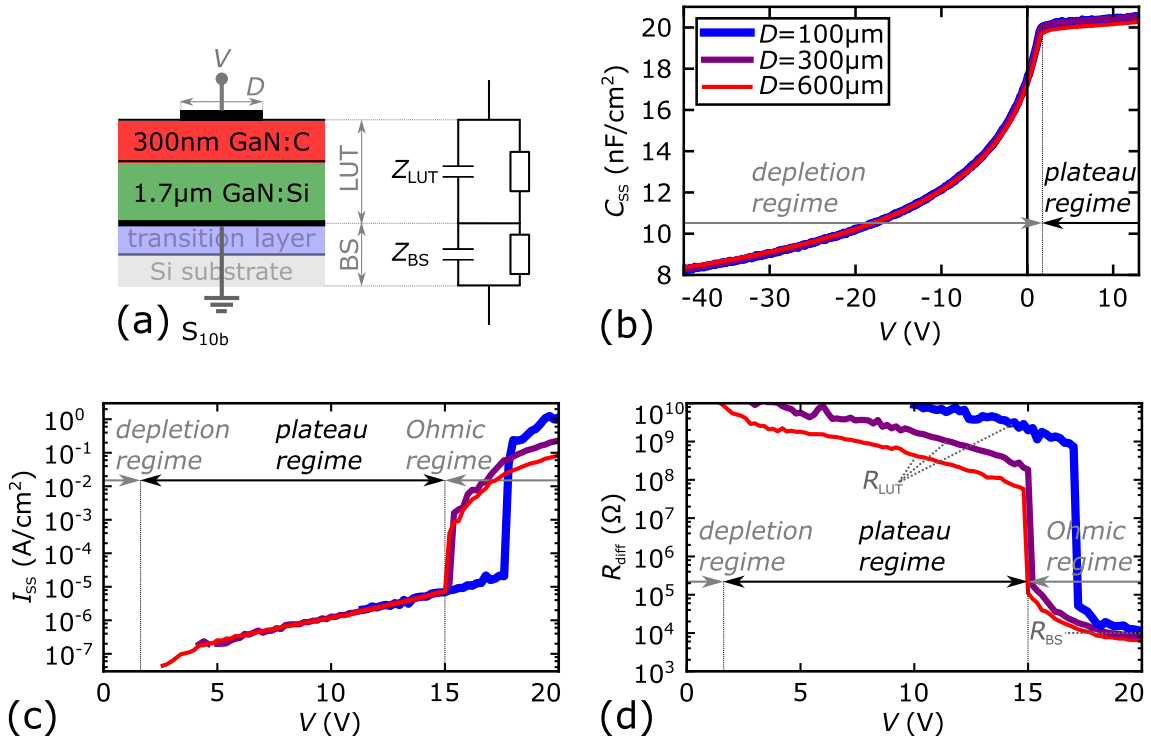


Fig. 3.2: (a) Schematic and simplified equivalent circuit of S_{10b} , (b) $C_{SS}-V$ and (c) $I_{SS}-V$ as well as from data in (c) extracted (d) differential resistance (R_{diff}) for circular contacts with various diameters D .

3.2 Electrostatics of LUT structures

3.2.1 Extraction of potential and charge distribution

A peculiarity of the LUT structures in contrast to complex multilayer HEMT structures is that they allow for the extraction of the potential distribution (i.e. band diagram) of the entire structure, based on simple $I_{SS}-V$ and $C_{SS}-V$ characteristics. If not explicitly stated different, ramp rates for voltage sweeps are chosen slow enough to establish SS in every point during a sweep. In a sweep, after every voltage step, values are only taken after a delay time exceeding the relaxation time constant in GaN:C. Hence, the actual rates depend on the used sample and temperature. If not stated explicitly, SS measurements are done at room temperature, where for S_{10} the relaxation time constant is roughly 300 ms and ramp rates of 30 mV s^{-1} are used. This ensures full trap relaxation at every data point. Capacitance measurements are performed with a small signal frequency of 10 kHz so that the inverse of angular frequency is smaller than the relaxation time constant or the

time constant originating from parallel conductivity. I.e. the trap occupancy follows the voltage ramp but not the small signal [Ure+14a; Kol+17b].

In this section we discuss considerations, assumptions and the procedure for this extraction on basis of the samples S_{Schottky} , S_{10} and S_{10b} . These are LUT structures without top GaN:C layer (i.e. Schottky diode) and with GaN:C layers on top with thicknesses of 200 and 300 nm, respectively. The groundwork of this section (3.2.1) with measurement data and assessment illustrated in Figs. (3.3-3.5) are published in our publication [Kol+17b].

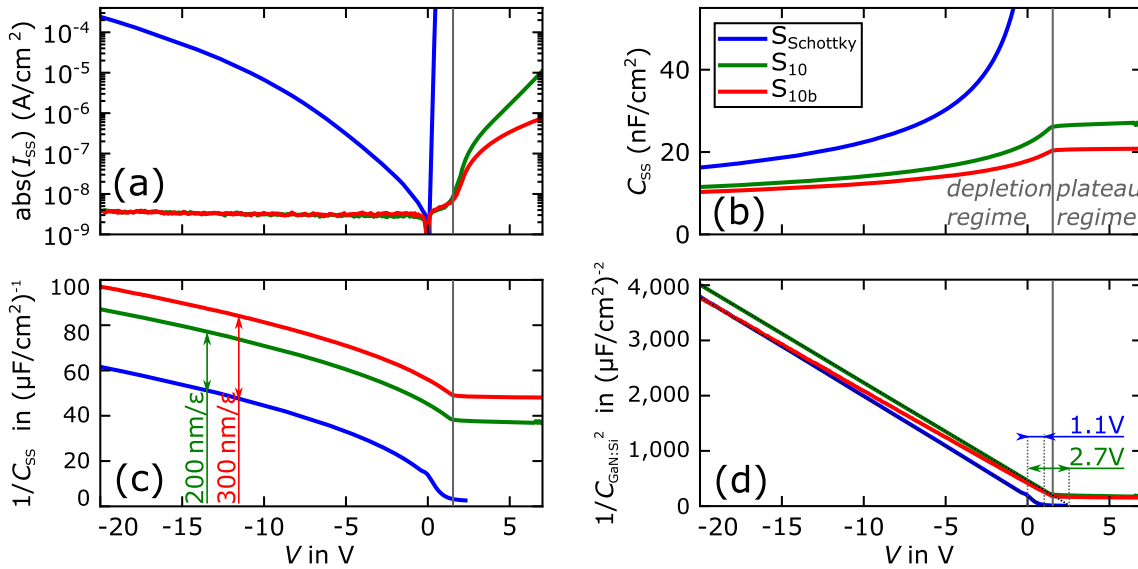


Fig. 3.3: (a) $I_{\text{SS}}-V$ and (b) $C_{\text{SS}}-V$ characteristics as well as extracted $1/C_{\text{SS}}-V$ and $1/C_{\text{Si}}^2 - V$ of S_{Schottky} , S_{10} and S_{10b} . Measurement data reused from [Kol+17b].

Fig. 3.3(a) shows negligible I_{SS} in S_{10} and S_{10b} for $V < 1.5$ V, followed by a strong rise for $V > 1.5$ V. S_{Schottky} on the other hand shows significant leakage current for reverse bias and a sharp I_{SS} increase in forward bias. $C_{\text{SS}}-V$ characteristics in Fig. 3.3(b) reveal in reverse bias depletion-like behavior for all three samples. The capacitance of a depleted GaN:Si layer (C_{Si}) can be calculated in general by:

$$C_{\text{Si}} = \sqrt{\frac{q\epsilon N_{\text{Si}}}{2V_{\text{Si}}}}, \quad (3.1)$$

$$w_{\text{Si}} = \epsilon/C_{\text{Si}}, \quad (3.2)$$

where N_{Si} is the Si doping concentration in GaN:Si and w_{Si} the depletion width in GaN:Si. As the electrically active layer in S_{Schottky} is a single GaN:Si layer, its capacitance (C_{SS}) should be identical to C_{Si} from Eq. (3.1). However, in S_{Schottky} an additional Schottky barrier of height V_{bi} has to be considered:

$$S_{\text{Schottky}} : V_{\text{Si}} = -V + V_{\text{bi}}. \quad (3.3)$$

From $1/C_{\text{Si}}^2 - V$ (Fig. 3.3(d)) $V_{\text{bi}} = 1.1$ V and $N_{\text{Si}} = 8.2 \times 10^{16} \text{ cm}^{-3}$ can be extracted from its root and slope, respectively. The value for N_{Si} is consistent with the growth data.

$C_{\text{SS}}-V$ curves of S_{10} and S_{10b} show similar depletion-like behavior for $V < 1.5$ V (*depletion regime*) and a slightly increasing plateau for $V > 1.5$ V (*plateau regime*). The low small-signal conductance values ($< 60 \mu\text{S cm}^{-2}$, not shown) within the *plateau regime* exclude that the plateau originates from an artifact arising from the increasing conductivity for $V > 1.5$ V. As under all

conditions C_{SS} is significantly lower than the capacitance of the depleted GaN:C layer ($C_{\text{GaN:C}} = \epsilon/d_{\text{LUT}}$ with GaN:C thickness d_{LUT}), we consider C_{SS} as two in series connected capacitances C_{Si} and $C_{\text{GaN:C}}$:

$$\frac{1}{C_{SS}} = \frac{1}{C_{\text{Si}}} + \frac{1}{C_{\text{GaN:C}}}. \quad (3.4)$$

In addition, for S_{10} and S_{10b} potential drops in GaN:C ($V_{\text{GaN:C}}$) and V_{bi} have to be considered:

$$S_{10}, S_{10b} : \quad V_{\text{Si}} = -V + V_{\text{bi}} - V_{\text{GaN:C}}, \quad (3.5)$$

whereby for LUT structures apart from S_{Schottky} the built-in potential (V_{bi}) has a slightly different meaning than in S_{Schottky} . As illustrated in Fig. 3.4(a) and explained in detail in Section 3.2.2, V_{bi} corresponds to the energy difference between E_{CB} and the pinned E_{F} in the GaN:C bulk. A possible potential drop resulting from a Schottky barrier at the GaN:C surface can be neglected. Due to $I_{\text{SS}} \approx 0$ (and $V_{\text{GaN:C}} = 0$, see next paragraph) within the *depletion regime*, electrostatic consideration is sufficient, a division of E_{F} in quasi- E_{F} is not required. Taking into account a GaN band gap at room temperature of 3.4 eV [LRS01], E_{F} pins at $E_{\text{CB}} - (2.7 \pm 0.2)$ eV, detailed discussion within the dominant acceptor model follows in Section 3.2.2.

Depletion regime ($V \lesssim 1.5$ V)

Fig. 3.3(c) proves that in the *depletion regime* $1/C_{SS}-V$ curves of S_{10} and S_{10b} are vertically shifted by d_{LUT}/ϵ from S_{Schottky} , confirming Eq. (3.4). This indicates that there is no significant amount of free charges in GaN:C, proving its semi-insulating behavior. Moreover, $1/C_{\text{Si}}^2 - V$ characteristics in Fig. 3.3(d) exhibit straight lines for S_{10} and S_{10b} , parallel shifted to S_{Schottky} data. This further proves the validity of Eq. (3.4), extracted values for N_{Si} vary only within less than 5% for all three samples. Independent of d_{LUT} , $V_{\text{bi}} = (2.7 \pm 0.2)$ V. The parallel shift of $1/C_{\text{Si}}^2 - V$ curves of S_{10} and S_{10b} compared to S_{Schottky} can only be achieved if $V_{\text{GaN:C}}$ is negligibly small, independent of V . A V -dependent $V_{\text{GaN:C}}$ would result in a non-linear $1/C_{\text{Si}}^2 - V$ curve that would also not be parallel for S_{10} , S_{10b} and S_{Schottky} . A V independent $V_{\text{GaN:C}} \neq 0$ on the other hand would result in a d_{LUT} dependence of V_{bi} , which is not observed and would also be not stable as long as $I_{\text{SS}} = 0$, obviously true for $V = 0$. The only possible solution is $V_{\text{GaN:C}} = 0$, i.e. flatband in GaN:C. This is attributed to the accumulation of negative charge in GaN:C near the GaN:Si/GaN:C interface with an "equivalent" sheet charge density σ_{C} . We use the term "equivalent" because as we show later, instead of a sheet charge, σ_{C} is a bulk charge in GaN:C next to its interface to GaN:Si. Due to the small width of this space charge region of few nm, causing a negligible potential drop well below 1 V [Kol+18a], we can consider σ_{C} for the sake of simplicity in first approximations as sheet charge. The experimentally observed condition $V_{\text{GaN:C}} = 0$ requires that $\sigma_{\text{C}} = N_{\text{Si}} \times q \times w_{\text{Si}}$, which is fulfilled for any bias condition in *depletion regime*.

Using only the extracted values from $1/C_{\text{Si}}^2 - V$ (i.e. $N_{\text{Si}} = 8.2 \times 10^{16} \text{ cm}^{-2}$ and $V_{\text{bi}} = 2.7$ V), potential (φ) distributions in GaN:Si as in Fig. 3.4 can be extracted directly from $C_{SS}-V$ curves using Eq. (3.1),(3.2) and (3.4):

$$\varphi(x < -w_{\text{Si}}) \approx 0, \quad (3.6)$$

$$\varphi(-w_{\text{Si}} < x < 0) = \frac{qN_{\text{Si}}(w_{\text{Si}} + x)^2}{2\epsilon}, \quad (3.7)$$

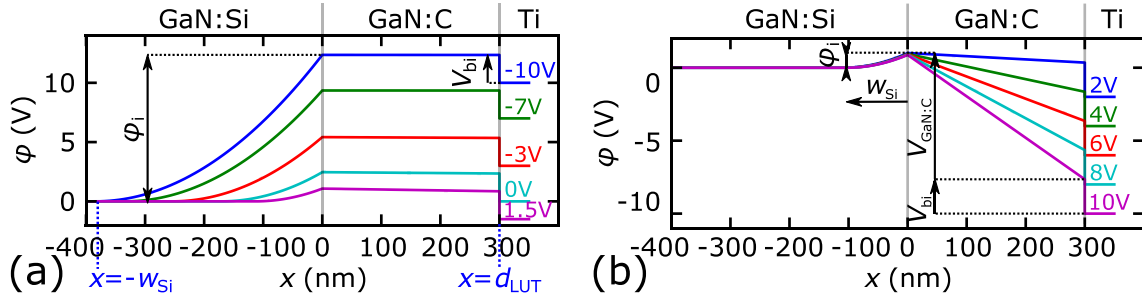


Fig. 3.4: Potential of conduction band minimum in S_{10b} for various V (colored values) in (a) *depletion regime* and (b) *plateau regime*. Interface potential φ_i , built-in voltage V_{bi} , depletion width in GaN:Si w_{Si} and potential drop in GaN:C $V_{GaN:C}$ are indicated for $V = \pm 10V$. Measurement data reused from [Kol+17b].

with x being the distance from the GaN:Si/GaN:C interface as indicated in Fig. 3.4. Neglecting the surface Schottky barrier, the potential in GaN:C at the surface ($\varphi(x = d_{LUT})$) is $-V + V_{bi}$. Within the *depletion regime* the GaN:Si/GaN:C interface potential ($\varphi(x = 0)$) is identical with $\varphi(x = d_{LUT})$ (Eq. (3.7)), demonstrating that $V_{GaN:C}$ must be 0. The only thermodynamically stable condition is a flatband in GaN:C, i.e. $\varphi(0 < x < d_{LUT}) = -V + V_{bi}$, completing the band diagram. As mentioned before, minor potential drops due to spatial extent of σ_C are at the moment neglected.

Plateau regime ($V \gtrsim 1.5V$)

In the *plateau regime* the roughly constant capacitance in Fig. 3.3(b) indicates almost constant $\varphi_i \approx 1.1V$, so that the rise in V must be fully compensated by a potential drop in GaN:C, i.e. $V_{GaN:C} \neq 0$, see Eq. (3.5) and extracted potential distributions in Fig. 3.4(b). Analogous to *depletion regime*, the positive charge of depleted donors in GaN:Si is compensated by accumulating negative charge in GaN:C near the GaN:Si/GaN:C interface (σ_C). However, in order to establish $V_{GaN:C} \neq 0$, an additional increase in σ_C is required. Due to non-negligible I_{SS} as shown in Fig. 3.3(a), equilibrium consideration is not sufficient anymore, impeding clear judgement on the location of the negative charge. Consequently, we consider the fraction y ($0 < y < 1$) of additional charge to accumulate near (in first approximation directly at) the GaN:Si/GaN:C interface and $(1 - y)$ to distribute homogeneously in the bulk. For reason of simplicity, Fig. 3.4(b) considers only interface charge ($y = 1$), leading to a linear potential drop in GaN:C, $y = 0$ would result in a parabolic φ . Details on the build-up of the potential barrier $\varphi_i = 1.1V$ are provided in Section 3.3.1.

Knowing the potential distribution enables the expression of C_{SS} as solution of the Poisson equation in depletion approximation for a structure of n-doped GaN (i.e. GaN:Si), semi-insulating GaN:C with a V -dependent equivalent sheet charge density σ_C and a top metal electrode [Kol+17b]:

$$C_{SS}(V) = \sqrt{\frac{q\epsilon N_{Si}}{2[V_{bi} - V + \frac{qd_{LUT}^2}{2\epsilon} N_{Si} + \frac{d_{LUT}}{\epsilon} \sigma_C(V)]}} \quad \text{for } V < 1.5V, \quad (3.8)$$

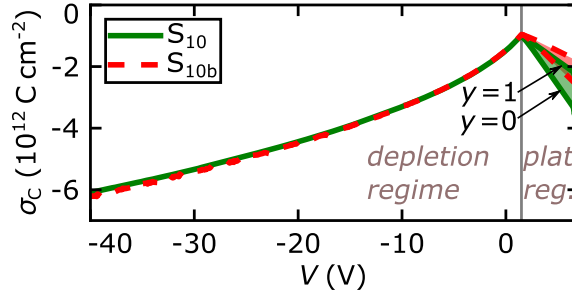


Fig. 3.5: Accumulated negative charge in GaN:C per area σ_C vs. V in S_{10} and S_{10b} with σ_C extracted from Eq. (3.8) and (3.9) with limiting lines for $y = 0$ (additional bulk charge in *plateau regime*) and $y = 1$ (only interface charge). Measurement data reused from [Kol+17b].

$$C_{SS}(V) = \sqrt{\frac{q\varepsilon N_{Si}}{2 \left[V_{bi} - V + \frac{q d_{LUT}^2}{2\varepsilon} N_{Si} + \frac{d_{LUT}}{\varepsilon} \left[\sigma_C(1.5 \text{ V}) + \frac{1+y}{2} [\sigma_C(V) - \sigma_C(1.5 \text{ V})] \right] \right]}} \quad \text{for } V > 1.5 \text{ V}. \quad (3.9)$$

In Eq. (3.9) the term $[\sigma_C(V) - \sigma_C(1.5 \text{ V})]$ represents the additional charge exceeding the value of $\sigma_C(1.5 \text{ V})$, with the latter extracted from Eq. (3.8). Fig. 3.5 shows extracted σ_C vs. V in SS, using Eq. (3.8) and Eq. (3.9). While in the *depletion regime* only interface charges are considered, in the *plateau regime* both interface and bulk charges are taken into account ($0 < y < 1$). From the maximum value of σ_C at -40 V , we can extract a minimum net acceptor concentration in GaN:C (i.e. $N_{acc}^* = N_{acc} - N_{don}$). In the most conservative estimation we consider all acceptors in GaN:C to be occupied, leading to $N_{acc}^* = \sigma_C / (q \times d_{LUT}) = 3 \times 10^{17} \text{ cm}^{-3}$. However, this conservative assumption would lead to major potential drop in GaN:C (i.e. $V_{GaN:C} = 11 \text{ V}$, which can be excluded from analysis of $1/C_{Si}^2 - V$). Detailed analysis of the tiny distortions in the $1/C_{Si}^2 - V$ curves of $S_{Schottky}$ and S_{10} shows that the slope in S_{10} is by 3.5% steeper than in $S_{Schottky}$. This can be explained by considering for N_{acc}^* a value of $3.5 \times 10^{18} \text{ cm}^{-3}$, which is a reasonable value, fitting also to reported values in literature [Rac+18a].

3.2.2 Fermi level pinning at dominant acceptor

From $V_{bi} = 2.7 \text{ V}$ we derived that E_F pins roughly at $E_{VB} + 0.7 \text{ eV}$ with low influence of T within the estimated measurement and analysis inaccuracy of $\pm 0.2 \text{ eV}$. Furthermore, we have evidence for the existence of acceptors and donors in GaN:C. We extracted that their densities N_{acc} (see Section 3.2.1) and N_{don} (see Section 3.6.1) must be in the most conservative assumption greater than 3 and $2 \times 10^{17} \text{ cm}^{-3}$, respectively, with less conservative and more likely values at least 10 times larger. Therefore, for rough estimations in the following we consider that all carbon defects are either acceptors with density N_{acc} and energy E_{acc} , or donors with density N_{don} and energy $E_{CB} - E_{don}$, i.e. $N_{acc} + N_{don} = [C]$. As shown in Fig. 3.6 the band gap E_{bg} and therefore also E_{CB} decreases with T , which is calculated by an empirically found expression by Levinshtein et al. [LRS01]:

$$E_{bg}(T) = E_{bg}(T = 0) - 7.7 \times 10^{-4} \frac{T^2}{T + 600}. \quad (3.10)$$

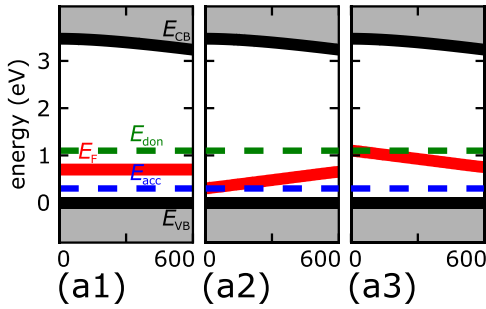
For matter of simplification and due to lack of better knowledge we consider that E_{acc} and E_{don} remain constant with T , as shown in Fig. 3.6. For the derivation of E_F we consider in equilibrium charge neutrality in GaN:C:

$$\begin{aligned} -N_{acc}(-) + N_{don}(+) - n + p &= 0, \\ N_{acc}(-) &= N_{acc} f_{FDD}(E_{acc} - E_F), \\ N_{don}(+) &= N_{don} f_{FDD}(E_F - E_{don}), \end{aligned} \quad (3.11)$$

with $N_{acc}(-)$ as negatively charged (i.e. occupied) acceptors and $N_{don}(+)$ as positively charged (i.e. unoccupied) donors. Maintaining Eq. (3.11) is only possible for a certain E_F , which depends on T , E_{acc} , E_{don} , N_{acc} and N_{don} . Knowledge that E_F pins at $E_{VB} + 0.7\text{eV}$ in combination with the boundary conditions for N_{acc} and N_{don} delivers further information about the defects, discussed in the following. Fig. 3.6 shows the decreasing band gap with T , the constant distances of E_{acc} and E_{don} from VB and the calculated E_F , using Eq. (3.11) and Eq. (3.10). E_{acc} , E_{don} , N_{acc} and N_{don} are chosen in order to achieve $E_F = 0.7\text{eV}$ in (a1) and (b), whereby two different concepts can be followed that both meet the requirements stated above and are both stated in literature to explain the semi-insulating behavior of GaN:C.

Autocompensation model (ACM) vs. dominant acceptor model (DAM)

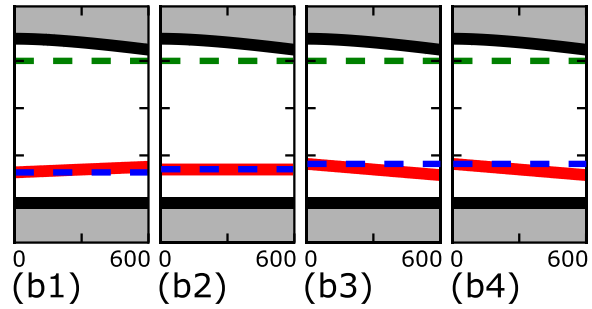
auto-compensation model:



energies in (eV)	T=0K	T=300K	T=600K
E_{CB}	3.47	3.39	3.24
(a1) $E_F(N_{acc}=N_{don})$	0.70	0.70	0.70
(a2) $E_F(N_{acc}=N_{don} \times 1.001)$	0.30	0.48	0.66
(a3) $E_F(N_{acc}=N_{don} \times 0.999)$	1.10	0.92	0.74

$$N_{acc} + N_{don} = 10^{19} \text{cm}^{-3}$$

dominant acceptor model:



energies in (eV)	T=0K	T=300K	T=600K
(b1) $E_F(N_{acc}=1.1 \times N_{don}, E_{acc}=0.64\text{eV})$	0.64	0.70	0.76
(b2) $E_F(N_{acc}=2 \times N_{don}, E_{acc}=0.70\text{eV})$	0.70	0.70	0.70
(b3) $E_F(N_{acc}=3 \times N_{don}, E_{acc}=0.72\text{eV})$	0.72	0.70	0.68
(b4) $E_F(N_{acc}=100 \times N_{don}, E_{acc}=0.82\text{eV})$	0.82	0.70	0.58

Fig. 3.6: Band gaps, defect levels and calculated E_F as function of T . (a1) Autocompensation model leads for $N_{acc} = N_{don}$ and $(E_{acc} + E_{don})/2 = 0.7\text{eV}$ to T independent $E_F = 0.7\text{eV}$. (a2,a3) However, tiny differences in N_{acc}/N_{don} ratios shift E_F dramatically and make it T -dependent. (b1-b4) In the dominant acceptor model E_{don} is irrelevant but E_F depends slightly on T for large variations in N_{acc}/N_{don} ; E_{acc} are chosen to establish $E_F = 0.7\text{eV}$ at $T = 300\text{K}$.

1. Fig. 3.6(a) demonstrates the “auto-compensation model” (ACM) as considered e.g. in [Ver+14; Wri02; Arm+06], in which $N_{don} = N_{acc}$ with $E_{acc} < E_{don}$. $E_F = 0.7\text{eV}$ can be achieved by: $E_{acc} = E_{VB} + 0.7\text{eV} - x$ and $E_{don} = E_{VB} + 0.7\text{eV} + x$ with $x \in (0, 0.7)\text{eV}$; for Fig. 3.6(a) $x = 0.4\text{eV}$ is used. Basically, all acceptors are occupied, while all donors are unoccupied. Due to their same density, charge neutrality is established by E_F pinning at

$(E_{\text{acc}} + E_{\text{don}})/2 = 0.7 \text{ eV}$, i.e. $N_{\text{acc}}(-) = N_{\text{acc}} = N_{\text{don}}(+)= N_{\text{don}}$. However, small fluctuations in N_{acc} and N_{don} have dramatic influence on E_{F} . E.g. for $x = 0.4 \text{ eV}$ as shown in Fig. 3.6(a2,a3), considering N_{acc} to be by only 1 ppm larger than N_{don} , E_{F} shifts at 300 K already by 0.22 eV. Therefore, exact same N_{acc} and N_{don} with tiny tolerances are crucial. In real GaN:C there are not only carbon defects but also other background donors such as Si, likely in the range of 10^{16} cm^{-3} and located near E_{CB} . In the ACM N_{don} is the sum of all donors, regardless of their physical and energetic nature. Important is only that the lowest donor above E_{acc} is considered to be equal to E_{don} .

2. Fig. 3.6(b) shows the ‘‘dominant acceptor model’’ (DAM) as considered e.g. in [Arm+06; LJW10], in which $N_{\text{don}} < N_{\text{acc}}$ with $E_{\text{acc}} < E_{\text{don}}$, whereby the exact location of E_{don} is irrelevant. Basically, all donors are unoccupied, i.e. positively charged $N_{\text{don}}(+)= N_{\text{don}}$, while acceptors are only partly occupied with $N_{\text{acc}}(-)= N_{\text{don}}$, satisfying charge neutrality. In order to establish this condition, E_{F} has to be located close to E_{acc} , with its exact level mainly depending on the ratio $N_{\text{acc}}/N_{\text{don}}$. Fig. 3.6(b1-b4) demonstrate that in order to establish $E_{\text{F}} = 0.7 \text{ eV}$, dependent on $N_{\text{acc}}/N_{\text{don}}$ E_{acc} has to be located slightly above (for $N_{\text{acc}}/N_{\text{don}} < 2$) or slightly below 0.7 eV (for $N_{\text{acc}}/N_{\text{don}} > 2$). For $N_{\text{acc}}/N_{\text{don}} = 2$ the following condition holds, independent of T : $E_{\text{acc}} \approx E_{\text{F}} = 0.7 \text{ eV}$. For $N_{\text{acc}}/N_{\text{don}} < 2$, E_{F} increases slightly with T , while for $N_{\text{acc}}/N_{\text{don}} > 2$, E_{F} decreases slightly with T . In theory, E_{F} vs. T would be measurable by extracting V_{bi} from $1/C_{\text{Si}}^2 - V$ measurements for various T , however this is practically impeded by several reasons: 1) Changes in V_{bi} are smaller than the measurement accuracy; 2) The decrease of E_{CB} is in the same range as the change in V_{bi} and cannot be distinguished from an increase in E_{F} ; 3) E_{acc} might shift with T and 4) E_{acc} is likely to be not discrete but show a certain unknown energy distribution that leads to a shift of E_{F} with T , especially due to the small $E_{\text{acc}} - E_{\text{F}}$. In sharp contrast to ACM, in DAM E_{F} pinning is very resilient against variations in $N_{\text{acc}}/N_{\text{don}}$ as demonstrated in the small effect of wide variations of $N_{\text{acc}}/N_{\text{don}}$ in Fig. 3.6(b).

Although in theory both ACM and DAM could explain the semi-insulating behavior of GaN:C by pushing E_{F} to 0.7 eV, Fig. 3.7 demonstrates that as soon as GaN:C is used in multilayer structures only the latter leads to E_{F} -pinning at 0.7 eV. Fig. 3.7(a,b) show the potential distribution of the lower part of the band gap next to the GaN:Si/GaN:C interface and (c,d) negatively charged acceptor and positively charged donor densities for $V = 0$ at 300 K for ACM (a,c) and DAM (b,d). Considering ACM, within about 3 nm next to GaN:Si the main part of N_{don} are occupied (i.e. neutral), while N_{acc} are within entire GaN:C occupied (i.e. neutral). This leads to a space charge and consequently band bending. For $E_{\text{don}} > E_{\text{F}}$ almost all donors are positively charged so that $N_{\text{don}}(+)- N_{\text{acc}}(-)$ becomes very small. Only after large distances E_{F} pins at $(E_{\text{acc}} + E_{\text{don}})/2$ as calculated in Fig. 3.6. Considering $E_{\text{acc}} = 0.4 \text{ eV}$, $E_{\text{don}} = 1.1 \text{ eV}$ and $N_{\text{acc}} = N_{\text{don}} = 5 \times 10^{18} \text{ cm}^{-3}$ E_{F} is on top of 200 nm GaN:C as in sample S₁₀ still roughly 200 meV above $(E_{\text{acc}} + E_{\text{don}})/2$ (i.e. at $E_{\text{VB}} + 1.1 \text{ eV}$). It would require 8 μm to push E_{F} in a 10 meV vicinity of $(E_{\text{acc}} + E_{\text{don}})/2$. This is not just valid for GaN:Si/GaN:C structures but also for example for a Schottky junction, an adjacent GaN:uid layer or any adjacent layer that requires band bending in GaN:C in order to push E_{F} to $E_{\text{VB}} + 0.7 \text{ eV}$. With applied bias the situation gets even worse, E_{F} is then even further away from $(E_{\text{acc}} + E_{\text{don}})/2$. In order to achieve stable E_{F} pinning, E_{acc} and E_{don} would have to be very close together, however there is no indication that this could be the case in GaN:C.

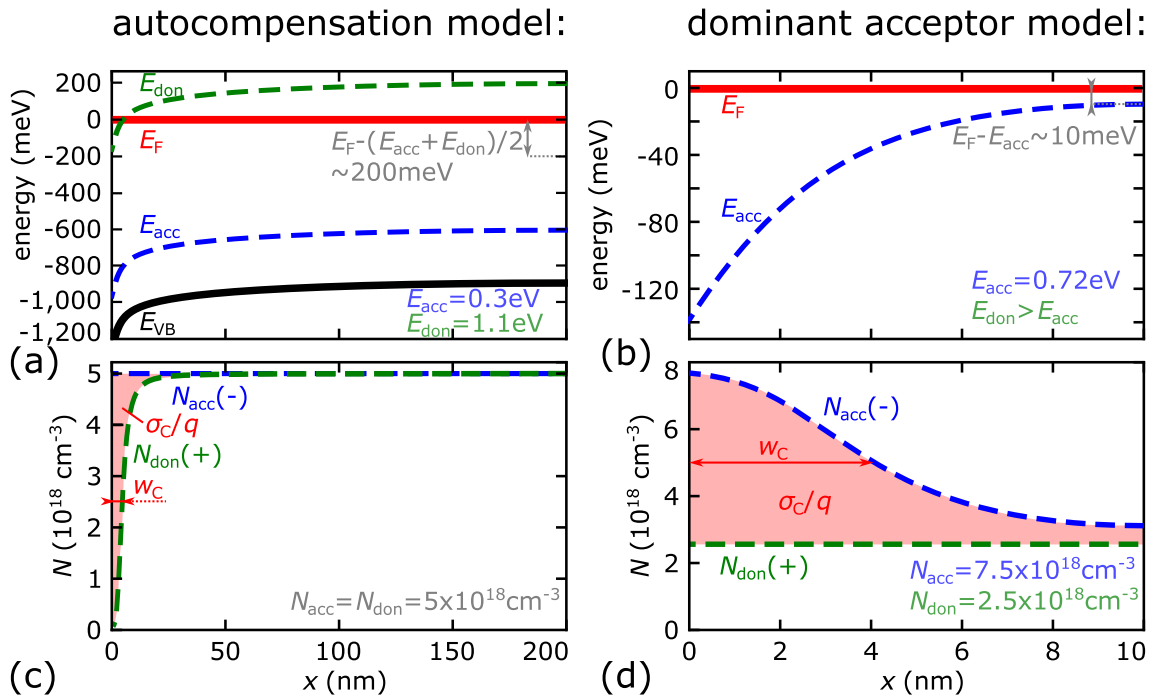


Fig. 3.7: Part of the band diagram calculated by Poisson equation in GaN:C as function of the distance from the GaN:Si interface for $V = 0$ V at 300 K, considering (a) auto-compensation model and (b) dominant acceptor model. The equivalent sheet charge density σ_C is the area between negatively charged acceptors and positive charged donors.

An alternative for the existence of acceptors and donors could be a single defect that can act as acceptor and donor. E.g. Lyons et al. [LJW14] report that C on N site acts in such a way with the difference that the acceptor transition is energetically higher than the donor transition and can consequently not explain the observed behavior.

Fig. 3.7(b) shows the potential distribution and (d) the negatively charged acceptors and positively charged donor densities for a GaN:C layer next to GaN:Si at 0 V and 300 K, considering DAM. In contrast to ACM in Fig. 3.7(a,c), E_F approaches E_{acc} within a much smaller distance so that for $E_{acc} = 0.7$ eV, $E_{don} > E_{acc}$, $N_{acc} = 7.5$ and $N_{don} = 2.5 \times 10^{18} \text{ cm}^{-3}$ in a distance 10 nm from the junction $E_F - E_{acc}$ is already smaller than 10 meV. Fig. 3.7(b) shows that all N_{don} are positively charged, while at $x = 0$ almost all N_{acc} are negatively charged and as $E_F - E_{acc}$ approaches 0, $N_{acc}(-)$ approaches $N_{don}(+)$. With increasing bias the width of the space charge region increases, represented by w_C which is the width when the space charge decreases to half of its maximum value. Even for $V = -40$ V with $w_{Si} \approx 730$ nm, w_C is only ≈ 8.3 nm, so that E_F is indeed pinned in the major part of GaN:C at 0.7 eV with small potential drops in GaN:C, which can be neglected for rough estimations.

Due to the experimentally observed E_F pinning which is further V independent, we conclude that only the DAM can explain results properly. Furthermore, from atomistic point of view it seems unlikely that carbon forms exactly $N_{acc} = N_{don}$ with fluctuations much smaller than 1 ppm and E_{acc} only slightly smaller than E_{don} (≈ 100 meV) at 0.7 eV. We consider it more likely that $N_{acc} > N_{don}$ with $E_{acc} = 0.7$ eV and any E_{don} that is greater than E_{acc} . Thus, we use for all following considerations within this thesis the DAM and if not stated explicitly we assume for

rough calculations $N_{\text{don}} = 0.25 \times [C]$, $N_{\text{acc}} = 0.75 \times [C]$, $E_{\text{acc}} = 0.72 \text{ eV}$ and $E_{\text{don}} > E_{\text{acc}}$ (see Fig. 3.6(b3)).

(No) donor occupation

For electrostatic considerations under following condition also donors can get occupied:

$$V_{\text{GaN:C}} \gtrsim (E_{\text{don}} - E_{\text{F,bulk}})/q, \quad (3.12)$$

with $E_{\text{F,bulk}}$ being E_{F} within the bulk; the occupation factor depends on E_{don} and T . However, for reverse bias considering e.g. $E_{\text{don}} = E_{\text{CB}} - 0.2 \text{ eV}$ and $[C] = 10^{19} \text{ cm}^{-3}$, Eq. (3.12) is only fulfilled for $w_{\text{C}} > 28 \text{ nm}$, for which w_{Si} must be greater than $1.65 \mu\text{m}$, which means that almost the entire GaN:Si is depleted. This happens only for $V < -220 \text{ V}$; as all investigations are done at much lower negative bias, occupied donors are neglected for equilibrium considerations. However, for forward bias $I_{\text{SS}} \neq 0$, so that equilibrium considerations have to be replaced by non-equilibrium considerations. As $V_{\text{GaN:C}} = V + \varphi_i - V_{\text{bi}}$, Eq. (3.12) is fulfilled for $V \gtrsim 4.1 \text{ V}$. But as E_{don} is assumed to be close to E_{CB} , electron emission from E_{acc} or E_{VB} to E_{don} is a much slower process than electron emission from E_{don} to E_{CB} , therefore E_{don} should be mainly unoccupied. As φ_i is supposed to be greater than $E_{\text{CB}} - E_{\text{don}}$, also injected electrons from GaN:Si cannot lead to relevant occupation rates, especially as the lifetime in the donor state is very short. Therefore, under all conditions donor states are considered as unoccupied.

Schottky barrier

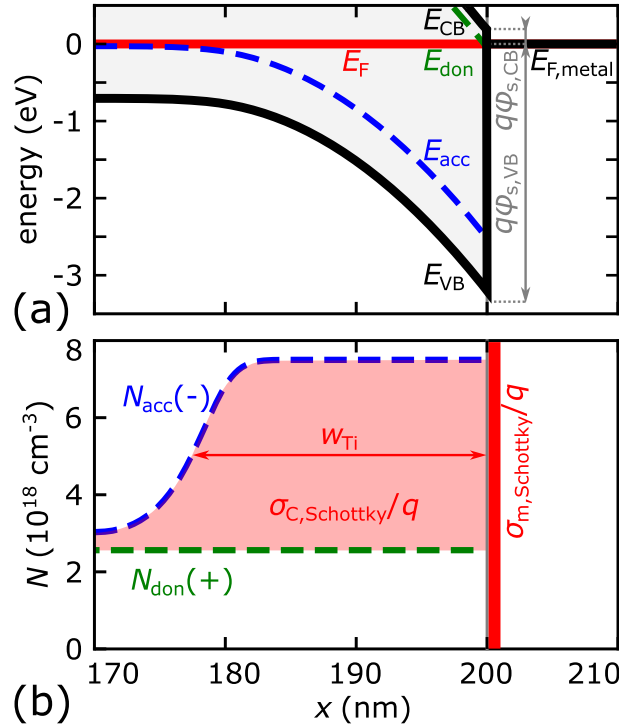


Fig. 3.8: (a) Calculated band diagram using Poisson equation at the GaN:C/metal junction and (b) negatively charged acceptor densities $N_{\text{acc}}(-)$, positively charged donor densities ($N_{\text{don}}(+)$) and equivalent sheet charge densities indicated by the red areas, whereby $\sigma_{\text{C,Schottky}} = \sigma_{\text{m,Schottky}}$.

We mentioned earlier that the top metal contact acts rather Ohmic than Schottky-like. In this section we will discuss this important statement in more detail. Using considerations of the dominant acceptor model from the previous Section 3.2.2, Fig. 3.8(a) shows the calculated band bending at the metal contact. Neglecting for rough estimations any surface states, the difference of the electron affinity of GaN (4.1 eV [LRS01]) and the work function of Ti (4.3 eV [Bin+94]) results in a potential difference of E_F in the metal ($E_{F,\text{metal}}$) and E_{CB} in GaN at the surface of $\varphi_{S,CB} \approx 0.2\text{ V}$ and therefore $\varphi_{s,VB} \approx 3.2\text{ V}$ as indicated in Fig. 3.8(a). From $1/C_{Si}^2 - V$ characteristic of S_{Schottky} we extracted $V_{bi} = 1.1\text{ V}$ which in theory has to be equal to $\varphi_{S,CB}$ but obviously is not. For samples with GaN:C on top we do not have any experimental information on the Schottky barrier, but we know that E_F pins in the GaN:C bulk at 0.7 eV. Therefore, in any case significant band bending is required in the surface vicinity. As explained in the following the exact value of $\varphi_{S,CB}$ is irrelevant, therefore we consider the theoretical value $\varphi_{S,CB} = 0.2\text{ V}$. As E_F is pinned in the bulk at E_{acc} , the bands have to be bent in the surface vicinity by $q \times \varphi_{s,VB} - E_{acc} \approx 2.5\text{ eV}$. Fig. 3.8(a) demonstrates that this is achieved as in this region E_{acc} is well below E_F , so that as shown in (b) $N_{acc}(-)$ rises in a width w_{Ti} of roughly 23 nm for sample S_{10} (72 nm for S_{01} , 9 nm for S_{70}). The negative equivalent sheet charge density in GaN:C ($\sigma_{C,\text{Schottky}}$) is compensated by a positive equivalent sheet charge density of $\sigma_{m,\text{Schottky}}$ in the metal (i.e. $\sigma_{C,\text{Schottky}} = \sigma_{m,\text{Schottky}}$) of roughly $12 \times 10^{12}\text{ C cm}^{-2}$ for S_{10} ($32 \times 10^{12}\text{ C cm}^{-2}$ for S_{01} and $4 \times 10^{12}\text{ C cm}^{-2}$ for S_{70}).

Ideal Schottky barriers would form an effective potential barrier, limiting leakage currents and charge injection. However, in the following we list a number of measurements that indicate that these Schottky barriers are instead rather leaky:

1. Sample S_{Schottky} in Fig. 3.3(a) shows already for small reverse biases high reverse leakage currents.
2. In a variation of sample S_{10} the Ti contacts are replaced by a few 100 nm thick p-type GaN layer with an annealed Ti contact on top. This standard process is known to establish Ohmic contacts. As these samples show insignificant change in $I_{SS}-V$ and trapping dynamics compared to standard S_{10} samples with Ti contact we conclude that the Ti contacts are actually quite Ohmic.
3. Thermionic emission or thermionic field emission would lead to an Arrhenius-like T dependence of the injected current. However, I_{SS} and trapping time constants show e^{aT} instead of $\exp(-q\varphi_{s,VB}/(k_B T))$ dependence (see Figs. 3.11 and 3.19), proving that throughout the entire investigated temperature range thermionic (field) emission is never determining I_{SS} .

These arguments prove that either the Schottky barrier must be much smaller or more likely it is very leaky, forming a good Ohmic contact. In any case it does not determine the electrical behavior (I_{SS} , trapping dynamics) of the test structures, hence we will neglect it for following considerations.

3.3 Transient behavior of LUT structures

In the previous section we discussed the SS behavior of S_{10} . During SS measurements we already discovered that slow ramp rates are required in order to reach thermal equilibrium. Furthermore, Fig. 3.5 reveals that the occupation of carbon acceptors changes as a function of V . As the

acceptors are deep in the band gap ($E_{\text{acc}} \approx 0.7 \text{ eV}$), they should cause dynamic trapping effects. In this section we will show that these dynamic effects are a great vehicle for characterization of the nature of carbon acceptors. Key elements of this section have been introduced in our publication in [Kol+17a], although in a very condensed way.

3.3.1 Dynamic characterization technique

The most straight-forward approach for transient characterization is to do bias steps and record the transient capacitance as a function of the time. In order to achieve good time resolution, we use a sophisticated capacitance measurement technique featuring lock-in-technique, detailed description of the setup is provided in [Stren; Str+16]. Measurements are performed with a small-signal frequency of 785 kHz, which ensures that even at high temperatures trap occupancy does not follow the small signal; this enables time resolution down to roughly 30 μs .

In order to determine the effect of the bias, we use a large matrix of 26 different initial biases, i.e. stress biases (V_{str}) and 26 different final biases, i.e. recovery biases (V_{rec}), resulting in a total of 676 transient capacitance measurements ($C(t)$). In order to decrease the measurement duration to feasible times, the temperature is increased for default measurements to 340 K. Due to the voltage limitation of the used lock-in amplifier, V_{str} and V_{rec} are limited between -9.5 and 9.5 V. This range is sufficient to cover a large part of the *depletion regime* and roughly the entire *plateau regime* for S_{10} . Dynamic measurements in the *Ohmic regime* are not possible but these are anyway inhibited by too large conductance.

Fig. 3.9 shows selected $C(t)$ for various bias steps with both V_{str} and V_{rec} in the *depletion regime*. In order to maximize amplitudes, in the first bias step $V_{\text{str}} = -9.5 \text{ V}$ is used and in order to reveal the effect of V_{rec} it is varied between -9.5 and 1.5 V, see (b)(I-III). In (b)(III-V) V_{str} and V_{rec} are swapped, i.e. $V_{\text{str}} \in (-9.5, 1.5) \text{ V}$ and $V_{\text{rec}} = -9.5 \text{ V}$. For deeper analysis in Fig. 3.9(c) we use Eq. (3.8) to derive from $C(t)$ the amount of charges in GaN:C as a function of the time ($\sigma_C(t)$). Additionally, the entire band diagram can be calculated using the formalism introduced in Section 3.2.1 at every point in time. Fig. 3.9(d) depicts band diagrams at several representative points in time for the bias steps $-9.5 \rightarrow 0 \text{ V}$ and $0 \rightarrow -9.5 \text{ V}$, indicated with black lines in (b,c). In the following we discuss the behavior of sample S_{10} in the different time ranges, indicated in Fig. 3.9:

- (I) A stress bias of $V_{\text{str}} = -9.5 \text{ V}$ is applied until thermal equilibrium (SS) is reached. This measurement also proves that for all transient characterizations the same initial condition (i.e. capacitance value) was established. In Section 3.2 we found that in SS \mathcal{E}_C is zero independent of V_{str} , as demonstrated in Fig. 3.9(d).
- (II) Immediately after the bias step to V_{rec} there is a "blind spot" of 30 μs that cannot be measured with the used equipment. By comparing the first measurement point at $t = 30 \mu\text{s}$ with C_{SS} at $V = -9.5 \text{ V}$, we find that the capacitance rose within the blind spot. Therefore, we conclude that there must be a process faster than 30 μs . For the sake of simplicity, Fig. 3.9(b,c) show dashed lines to indicate this fast capacitance increase, although these values are not measured. Interestingly, (c) reveals that σ_C stays constant during this capacitance increase, independent of V_{rec} . This means that in this ultrafast process only the depletion width in GaN:Si (w_{Si}) decreases. Comparison of band diagrams in Fig. 3.9(d) at the time points (I) and (II $_{\text{QS}}$) show this change of w_{Si} . Furthermore, it demonstrates that as σ_C did not change,

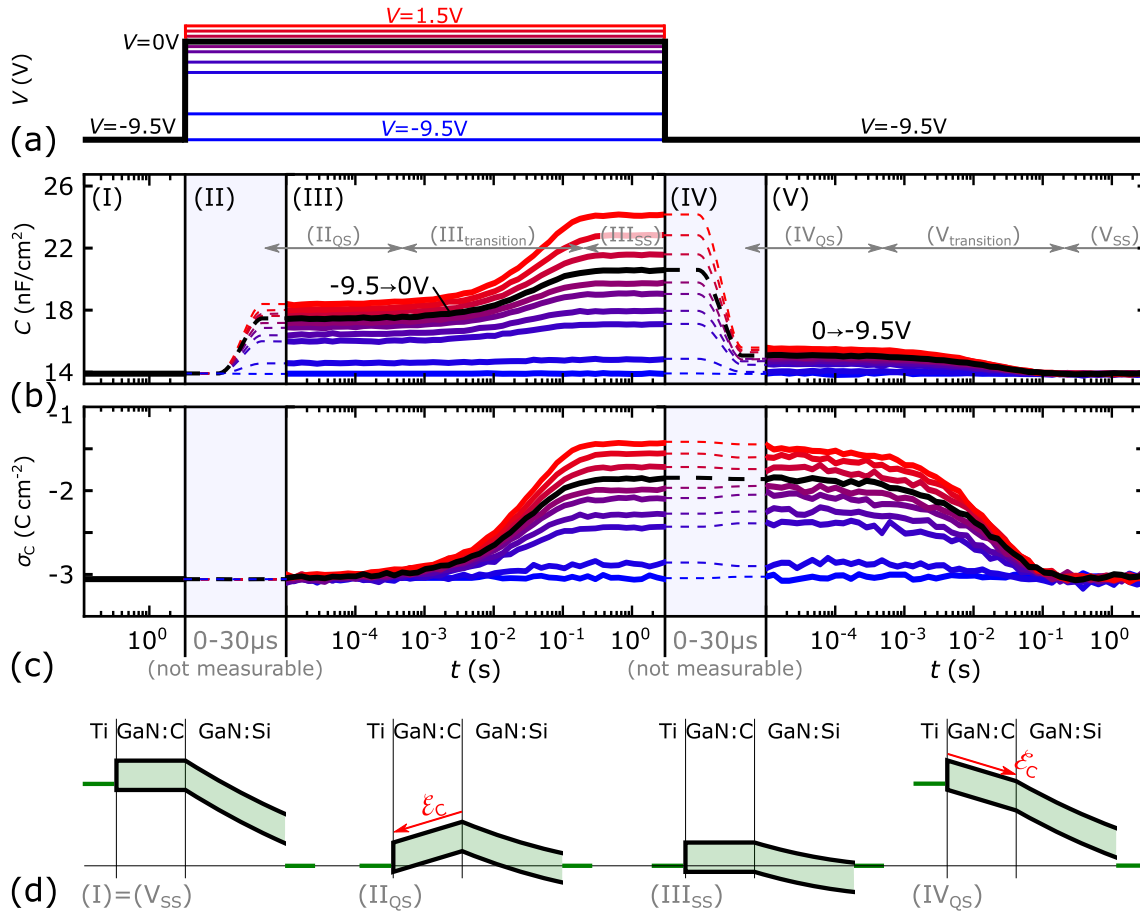


Fig. 3.9: (a) Schematic bias step from -9.5 V to various V within *depletion regime* (i.e. $V \leq 1.5$ V) and back to -9.5 V. (b) Corresponding measured transient capacitance and (c) calculated transient equivalent sheet charge density in GaN:C (σ_C), using Eq. (3.8). (d) Calculated band diagrams at points in time indicated in (b).

a non-equilibrium condition with $\mathcal{E}_C \neq 0$ establishes. However, as charges are trapped in deep carbon acceptors, change of σ_C requires times larger $30 \mu\text{s}$. Thus, we call (II_{QS}) a "quasistatic" or "metastable" condition.

- (III) After a certain time, \mathcal{E}_C causes an increase in σ_C by negative charges being transferred from carbon acceptors to the top electrode, indicated by (III_{transition}). The causative process is one of the major topics within this thesis and is discussed in detail in the following Sections (3.3.2-3.3.3). Anyway, a decrease in σ_C decreases also the potential at the GaN:Si/GaN:C interface and consequently decreases also w_{Si} and increases the capacitance, which is the actually measured physical property. The change in σ_C stops as soon as $\mathcal{E}_C = 0$ and the system reaches thermal equilibrium (III_{SS}). Surprisingly, the time constant of this transition does not depend on V_{rec} . The reason is that in the *depletion regime* independent of V in SS $\mathcal{E}_C = 0$. Therefore, one can consider that the last charge transported from a carbon acceptor to the top electrode is always exposed to the same vanishing small \mathcal{E}_C , independent of V_{str} and V_{rec} . In the discussions of dynamic processes in the following sections we will hence only use bias steps $-9.5 \rightarrow 0 \text{ V}$ as representatives for all dynamic processes in which σ_C increases within the *depletion regime*.
- (IV) After SS is established the bias is reduced again to the initial -9.5 V . The behavior is in this case identical with (II) with the only difference that the capacitance decreases instead of an increase.
- (V) Also ($V_{\text{transition}}$) is exactly analogous to (III_{transition}), only with opposite signs; even time constants are identical. Therefore, we will use in following analysis bias steps $-9.5 \rightarrow 0 \text{ V}$ as representatives for all dynamic process in which σ_C decreases within the *depletion regime*. Finally, SS is reached with the capacitance having the same value as initially in (I), i.e. no long term dynamic effects are observed.

While Fig. 3.9 covers bias steps within the *depletion regime*, Fig. 3.10 is analogous but for bias steps within the *plateau regime*. In the following we will again systematically analyze the transient behavior, for which we discuss bias steps from 8 to various V_{rec} between 1.5 and 8 V and vice versa. Biases above 8 V are avoided as in this range sometimes transitions to the *Ohmic regime* occur, which makes the behavior not comparable anymore.

- (I) A stress bias of $V_{\text{str}} = 8 \text{ V}$ is applied until SS establishes, whereby in the *plateau regime* in general $\mathcal{E}_C \neq 0$, as indicated in Fig. 3.10(d)(I). The reason why even with $\mathcal{E}_C \neq 0$ SS is reached, is the occurrence of I_{SS} , which creates a dynamic equilibrium for a certain \mathcal{E}_C as explained in detail in Section 3.3.3. This makes the dynamic behavior in the *plateau regime* more complex than for the *depletion regime*. Only in the limiting case of $V = 1.5 \text{ V}$, I_{SS} is still zero and therefore $\mathcal{E}_C \approx 0$, see Fig. 3.10(d)(III_{SS}).
- (II) Within the $30 \mu\text{s}$ blind spot the capacitance decreases due to increasing w_{Si} , while σ_C remains constant. Consequently, in the fast process only the depletion width in GaN:Si changed. Although after $30 \mu\text{s}$ the dynamic equilibrium is not established yet, due to the deep state of carbon acceptors a quasistatic dynamic equilibrium (II_{QS}) appears.
- (III) After a certain time, \mathcal{E}_C causes an increase in σ_C by negative charges being transferred from carbon acceptors to the top electrode, indicated by (III_{transition}). This leads to a decreasing

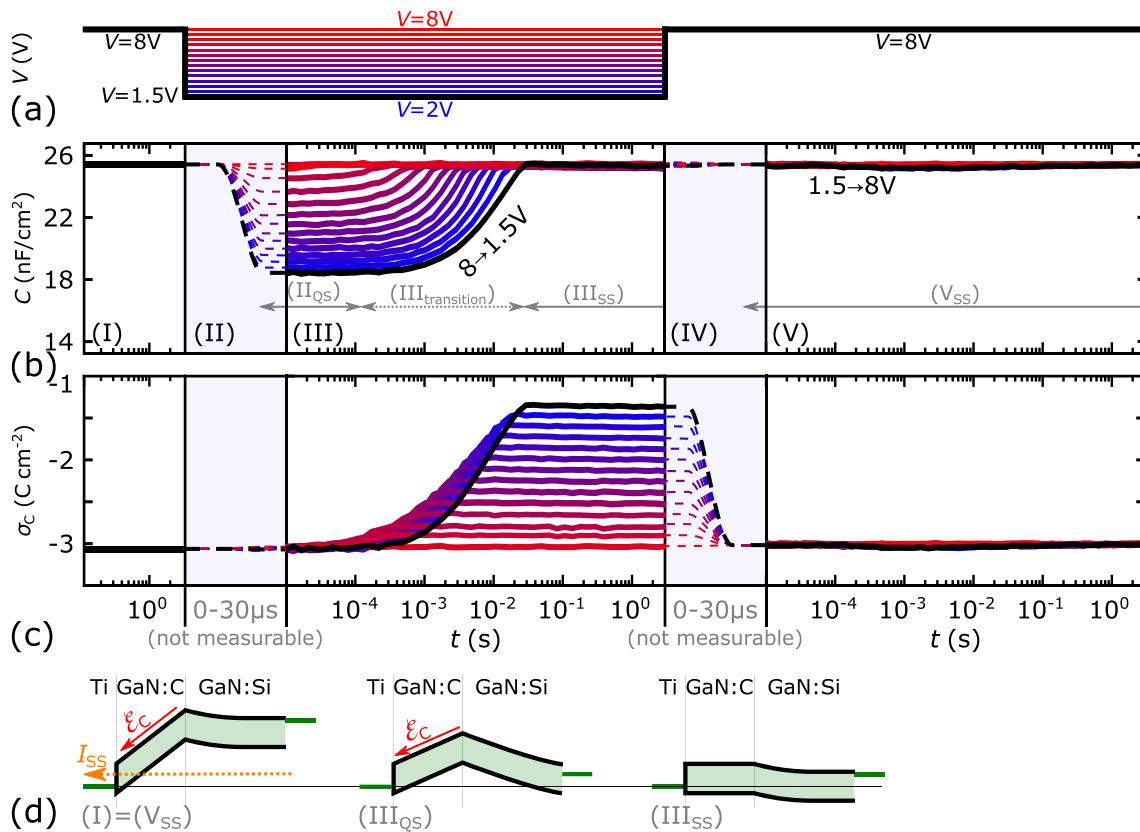


Fig. 3.10: (a) Schematic bias step from 8 V to various V within *plateau regime* (i.e. $V \geq 1.5$ V) and back to 8 V. (b) Corresponding measured transient capacitance and (c) calculated transient equivalent sheet charge density in GaN:C (σ_c), using Eq. (3.9) with $y = 1$ (i.e. considering no bulk charge). (d) Calculated band diagrams at points in time indicated in (b).

potential at the GaN:Si/GaN:C interface (φ_i) until the dynamic equilibrium establishes. For $V = 1.5\text{ V}$ $I_{SS} \approx 0$, in this border case the dynamic equilibrium becomes a static one with $\mathcal{E}_C = 0$. In general, with increasing V the SS \mathcal{E}_C increases, so that the last negative charge being transported from carbon acceptors to the top electrode is exposed to an increasing final \mathcal{E}_C . Considering an \mathcal{E}_C -dependent trapping process, this explains that with increasing V_{rec} the final time for reaching equilibrium decreases. The linear shift of this time with increasing V_{rec} in the logarithmic time-scale of Fig. 3.10 requires: $1/\tau \propto \mathcal{E}_C$, more detailed discussion follows in Section 3.3.3. While the end of the capacitance and σ_C change is determined by V_{rec} , the onset of the capacitance and σ_C change on the other hand depends on both V_{str} and V_{rec} , as their values determine the initial \mathcal{E} . For the sake of simplicity and comparativeness with the transient behavior in the *depletion regime* for all further analysis only bias steps from 8 to 1.5 V are used.

- (IV) After SS is established, the bias is raised again to the initial 8 V. Surprisingly, in this case the capacitance stays constant, while σ_C decreases immediately to the initial value at $V = 8\text{ V}$, for all V_{rec} . Understanding this behavior in detail requires discussion of the defect model, provided in Section 3.3.3 and illustrated in Fig. 3.14. Simplified described, the origin of this "ultrafast" decrease in σ_C is the fact that keeping σ_C constant and increasing V would result in decreasing φ_i , which would further result in an abrupt increase of electrons injected from the GaN:Si in the CB of GaN:C and thus ultrafast negative charge capture in carbon acceptors. Hence, σ_C and the capacitance are assumed to change basically with the speed of the voltage ramp. Experimentally proven is that even in low T experiments in cryostat ambient at 20 K, when the dynamics of the other relaxation processes are shifted to values more than six orders of magnitude larger, σ_C still changes faster than 30 μs . Therefore, analysis of σ_C -increases in the *plateau regime* are not possible utilizing LUT structures.
- (V) As SS is already reached in (IV) no transient behavior is observed anymore.

Table 3.2: All dynamic processes can be attributed to one of four representative bias steps.

	bias regime	ΔV	ΔC	$\Delta\sigma_C$	trans. process	repr. bias step
1	<i>depletion regime</i>	> 0	> 0	> 0	acc. discharging	$-9.5 \rightarrow 0\text{ V}$
2	<i>depletion regime</i>	< 0	< 0	< 0	acc. charging	$0 \rightarrow -9.5\text{ V}$
3	<i>plateau regime</i>	< 0	> 0	> 0	acc. discharging	$8 \rightarrow 1.5\text{ V}$
4	<i>plateau regime</i>	> 0	0	< 0	acc. ch. (fast)	$1.5 \rightarrow 8\text{ V}$

Summarizing, in this section we explained the dynamic behavior of LUT structures in very general without using any assumption on the nature of the trapping processes. We demonstrated that all dynamic processes can be associated with one of four representative bias steps as indicated in Tab. 3.2.

Yet, we did not discuss bias steps in which V_{str} and V_{rec} are in different regimes. In that case V_{rec} determines the representative regime, however instead of ΔV , $\Delta\sigma_C$ determines to which of the four representative processes in Tab. 3.2 the dynamic behavior is attributed to. E.g. for a bias step $-5 \rightarrow 5\text{ V}$ process 3 in Tab. 3.2 represents this process well, $C(t)$ is then e.g. equivalent to $8 \rightarrow 5\text{ V}$, as σ_C at -5 and 8 V are roughly identical.

3.3.2 Temperature dependence of relaxation processes in GaN:C

In the previous chapter the dynamic behavior of sample S₁₀ has been systematized and discussed in general without referring to the actual trapping/detrapping processes in GaN:C. In this chapter we analyze the temperature dependence of the four representative bias steps listed in Tab. 3.2 in a very wide temperature range between 130 and 560 K by using cryostat environment. Within this temperature range measurements are done at 187 different temperatures, whereby stress and recovery times were adapted in order to established SS after every bias step.

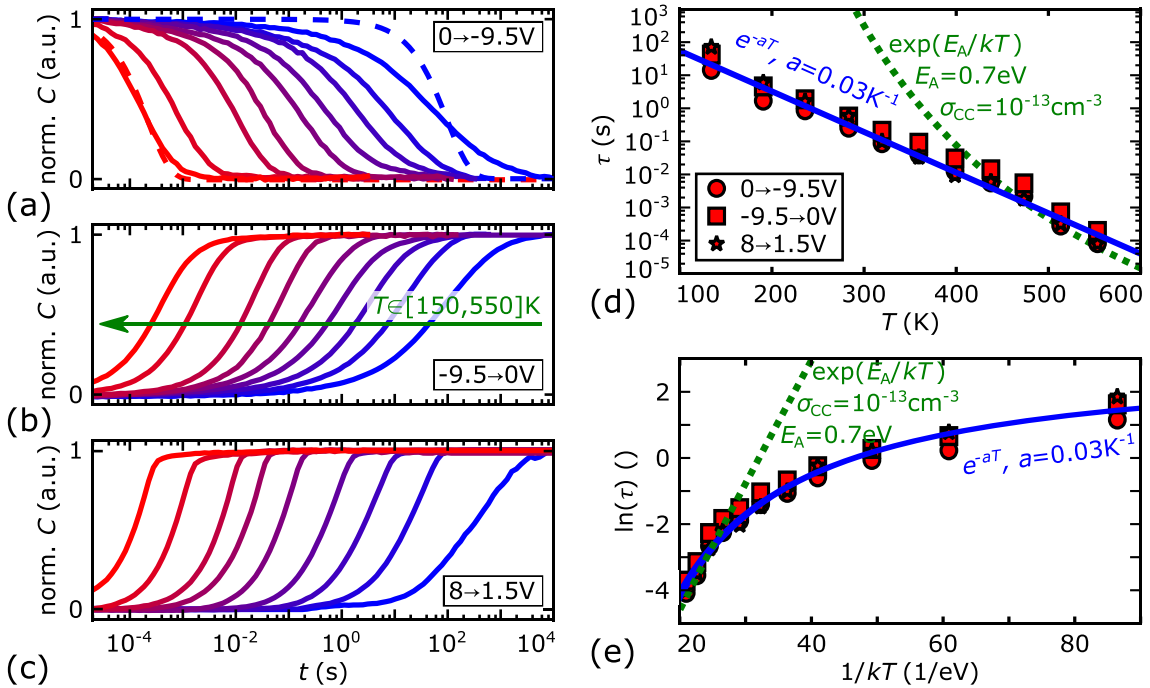


Fig. 3.11: Normalized $C(t)$ curves for S₁₀ for bias steps (a) $0 \rightarrow -9.5$ V, (b) $-9.5 \rightarrow 0$ V and (c) $8 \rightarrow 1.5$ V reveal faster processes with increasing T . Quantification of the T dependence for (d) linear T scale and (e) Arrhenius-plot clearly show exponential T dependence of charging/discharging time constants ($\tau \propto e^{aT}$, solid blue line). Arrhenius-dependence ($\tau \propto \exp(E_A/(k_B T))$), dashed green line) with reasonable action energies E_A and hole capture cross section σ_{CC} can clearly be ruled out. Dashed lines in (a) show fits of the data at 150 and 550 K to $\exp(-t/\tau)$.

Fig. 3.11(a-c) illustrates the shift of normalized $C(t)$ curves with increasing T to smaller times for three of the four representative bias steps. The fourth relaxation case ($1.5 \rightarrow 8$ V) is not shown as within the entire T range the transition of the capacitance has already finished at the first measurement point after 30 μs , confirming a different injection mechanism from GaN:Si. The dashed lines in Fig. 3.11(a) represent fits of the transient curves to $\exp(-t/\tau)$ for T of 150 and 550 K. While at high T measured data fits well to the exponential function, it broadens significantly with decreasing T , the origin of this broadening is yet unknown. Anyway, in order to compare the pace of processes at different T we will use points in time when the normalized capacitance changes by $1/e$, commonly referred to as "time constants" (τ). Fig. 3.11(d,e) show these time constants τ as function of T in linear scale (a) and in an Arrhenius-plot (b). It should also be mentioned that instead of analyzing $C(t)$, $\sigma_{CC}(t)$ as in Fig. 3.9(c) would be more appropriate. However, as the contact needle in the cryostat moves during the wide T measurement and has to be realigned several times, the absolute capacitance changes slightly. Unfortunately, these small changes in C

have large impact on extracted σ_{CC} , while normed C are resilient against these changes so that C values are used. Due to the logarithmic time-scale, differences in extracted τ from $C(t)$ vs. $\sigma_{CC}(t)$ are anyway negligibly small as can be seen by comparing (b) and (c) of Fig. 3.9 and Fig. 3.10

A surprising finding in Fig. 3.11 is that $C(t)$ curves are almost identical for all three bias steps, apart from the different sign in (a); despite the fact that in $0 \rightarrow -9.5$ V acceptors are being negatively charged, while in the $-9.5 \rightarrow 0$ V and $8 \rightarrow 1.5$ V acceptors are being discharged. A second surprising finding is that $\tau \propto e^{aT}$ dependence. As these findings are very different from the conventional defect model, in the next section we will introduce this conventional model and derive an adapted model that can explain our measurement data.

3.3.3 Necessity of defect bands

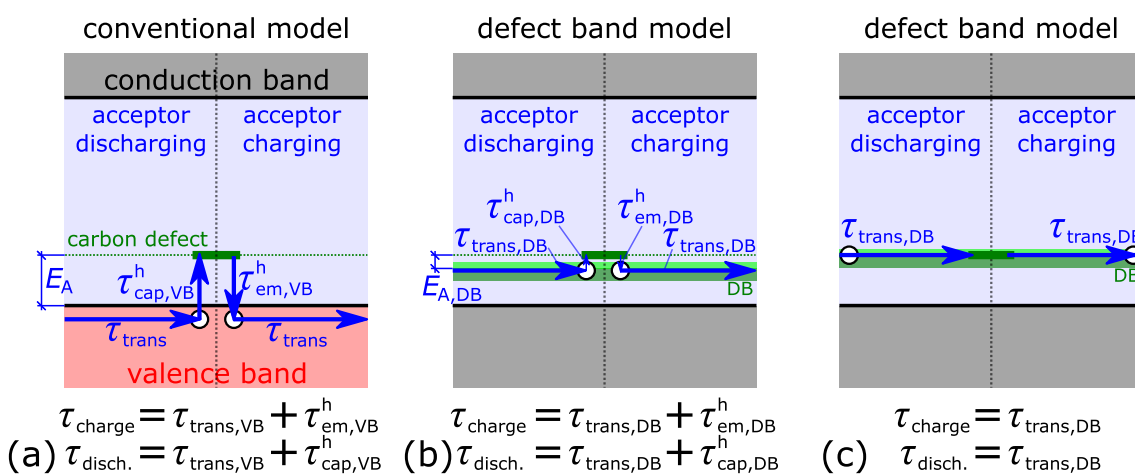


Fig. 3.12: Schematic band diagrams demonstrate the required processes for discharging (left half) and charging (right half) of acceptors in the (a) conventionally considered model with charge transport via valence band and in (b,c) the proposed model for GaN:C with charge transport via defect bands (DBs). In (b) the DB level is located below the carbon acceptor level while in (c) it surrounds the acceptor level. Figures reused from [Kol+17a; Kol+18a].

Fig. 3.12 shows schematic band diagrams with a dominant carbon acceptor energetically located 0.7 eV above VB as found in *dc* measurements, see Section 3.2.1. Donors are neglected and E_F is considered roughly pinned to the acceptor level. The conventional model in (a) is commonly considered for trapping in semiconductors, for GaN:C e.g. in [Bis+13; Bis+14b; Bis+14a; Bis+15; Ure+14a; Ure+14b; Moe+16; Tan+13; Chi+16; Zho+12; Ure+17]. To the author's knowledge there are no publications for GaN using a different defect model. However, the characterization technique introduced in this thesis questions the validity of known models far beyond state-of-the-art techniques, especially towards larger T ranges. We observe severe discrepancies when trying to explain gained measurement data with the conventional model. We eventually concluded that this requires the introduction of an adapted defect model. The first part of this section is dedicated to revision of the conventional defect model, while in the second part the adapted defect model is introduced.

Conventional defect model

Charging: In the conventional model, in order to charge an acceptor (Fig. 3.12(a), right side), a hole has to be emitted from the carbon acceptor to VB. For this process a potential barrier with height of $E_A \approx E_{\text{acc}} = 0.7 \text{ eV}$ has to be overcome, neglecting in first approximation ΔE_A (see Fig. 2.16). This process takes a certain amount of time ($\tau_{\text{em},\text{VB}}^{\text{h}}$) which depends crucially on T and can be described by Shockley-Read-Hall (SRH) theory [Hal52; SRJ52]:

$$\tau_{\text{em},\text{VB}}^{\text{h}} = \frac{1}{\nu_{\text{th}} \sigma_{\text{CC}} N_{\text{VB}}} \exp\left(\frac{E_A}{k_{\text{B}} T}\right) \propto T^2 \exp\left(\frac{E_A}{k_{\text{B}} T}\right), \quad (3.13)$$

where ν_{th} is the thermal velocity of holes in VB. As $\nu_{\text{th}} \propto \sqrt{T}$ and $N_{\text{VB}} \propto T^{3/2}$ the pre-factor delivers the T^2 factor on the right side of Eq. (3.13). Although in the great part of publications (e.g. [Bis+13; Bis+14b; Bis+14a; Men+14; Men+16; Men+04]) $\tau_{\text{charge}} = \tau_{\text{em},\text{VB}}^{\text{h}}$ is considered, in general also the time for the transport of the hole from the defect location to the electrode via VB $\tau_{\text{trans},\text{VB}}$ has to be included:

$$\tau_{\text{charge}} = \tau_{\text{em},\text{VB}}^{\text{h}} + \tau_{\text{trans},\text{VB}}. \quad (3.14)$$

In some publications (e.g. [Ure+17; Yac+17; Ure+15]) transport processes are considered, but they are explicitly mentioned only for discharging processes. For $\tau_{\text{trans},\text{VB}}$ e.g. Uren et al. describe in [Ure+15] that despite their assumed large E_A of 0.92 eV a small free hole concentration in VB (i.e. p) in the range of 10^4 cm^3 with a mobility $\mu = 8(T/373 \text{ K})^{-1.5} \text{ cm}^2 \text{ V}^{-1} \text{ s}^{-1}$ leads to a resistivity of $5 \times 10^{13} \Omega \text{ cm}$. $\tau_{\text{trans},\text{VB}}$ therefore shows following T dependence:

$$\tau_{\text{trans},\text{VB}} \propto \frac{1}{\mu p} \propto T^{3/2} \exp\left(\frac{E_A}{k_{\text{B}} T}\right). \quad (3.15)$$

The T dependence of $\tau_{\text{trans},\text{VB}}$ and $\tau_{\text{em},\text{VB}}^{\text{h}}$ are roughly identical with a slightly changed T exponent in the pre-exponential factor. However, this difference is observable only for very low T and is negligible at room temperature. The major difference is a multiplicative factor that leads to a different prefactor. Only if $\tau_{\text{trans},\text{VB}} > \tau_{\text{em},\text{VB}}^{\text{h}}$ the transport process determines τ_{charge} , which would be visible by an offset in logarithmic scale and by too small σ_{CC} for fitting data to Arrhenius-law; extracted E_A are roughly identical. For $\tau_{\text{trans},\text{VB}} < \tau_{\text{em},\text{VB}}^{\text{h}}$ the transport process can be neglected.

Discharging: For acceptor discharging with time constant $\tau_{\text{disch.}}$ a hole first has to be injected from the top electrode to the VB of GaN:C, however as explained in Section 3.2.2 this process is observed not to determine trapping processes, hence it is further neglected. Then the hole has to be transported within VB from the surface through GaN:C to the GaN:Si/GaN:C interface. This requires in general the same time as the transport for acceptor charging, i.e. $\tau_{\text{trans},\text{VB}}$. Additionally, the hole has to be captured from the acceptor, requiring a time of $\tau_{\text{cap},\text{VB}}^{\text{h}}$:

$$\tau_{\text{disch.}} = \tau_{\text{cap},\text{VB}}^{\text{h}} + \tau_{\text{trans},\text{VB}}. \quad (3.16)$$

In contrast to $\tau_{\text{em},\text{VB}}^{\text{h}}$, for $\tau_{\text{cap},\text{VB}}^{\text{h}}$ no significant energy barrier has to be overcome and can be described by:

$$\tau_{\text{cap},\text{VB}}^{\text{h}} = \frac{1}{\nu_{\text{th}} \sigma_{\text{CC}} p} \propto T^2 \exp\left(\frac{E_A}{k_{\text{B}} T}\right). \quad (3.17)$$

Although the actual capture process is rather T independent, p shows Arrhenius-like T dependence with the same E_A as in Eq. (3.13) and $\tau_{\text{trans,VB}}$ [Smi78]. However, there is an additional prefactor $(N_{\text{acc}}/N_{\text{don}} - 1)$ [Smi78] for $\tau_{\text{cap,VB}}^{\text{h}}$ compared to $\tau_{\text{em,VB}}^{\text{h}}$. For expected $N_{\text{acc}}/N_{\text{don}}$ ratios in the range of 2-3 this prefactor can get negligible so that capture and emission time constants could indeed show identical values.

Arguments against conventional defect model: In the following we will set the measurement data in Fig. 3.11 in perspective to this conventional model: The first thing we notice is that charging and discharging time constants are equal, unfortunately in a compensated semiconductor this does not directly reveal whether charging/discharging is determined by emission/capture processes or transport processes. As we know E_A from dc measurements, we can calculate $\tau_{\text{em,VB}}^{\text{h}}$ by using Eq. (3.13) with commonly used $\sigma_{\text{CC}} = 10^{-13} \text{ cm}^2$ [Ure+15] and compare it with measured τ_{charge} in Fig. 3.11(c,d). First of all, the figures undoubtedly reveal non-Arrhenius T behavior throughout the entire T range. While non-Arrhenius T behavior can be achieved by certain charge transport mechanisms or the interplay between different mechanisms [Kol+18a], it is impossible to receive this T behavior by capture and emission processes only. An even stronger argument that charging/discharging is determined by the transport mechanisms instead of capture/emission processes is provided by comparison of the absolute values of the experimental τ with the calculated Arrhenius-like τ in Fig. 3.11(d,e). It gets clear that $\tau_{\text{em,VB}}^{\text{h}}$ is in general larger than τ_{charge} , e.g. at 140 K it is even 14 orders of magnitude larger. This means that while the acceptor charging takes about 50 s, the emission of a hole from the acceptor to VB would require 5×10^{15} s. Therefore, this process can be definitely ruled out. In order to match the results, E_A would have to be significantly smaller. For matching the results in Fig. 3.11, E_A could be reduced to 0.4 eV. However, this is in direct contradiction to the dc measurements in Section 3.2 as well as the overwhelming majority of publications with results not only from electric characterization [Bis+13; Bis+14b; Bis+14a; Bis+15; Ure+14a; Ure+14b; Moe+16; Tan+13; Chi+16; Zho+12; Ure+17] but also from optical characterization techniques such as photoluminescence spectroscopy [Kne+16; Res+14]. Furthermore, the later introduced leakage current measurements strongly suggest that the observed e^{aT} dependence of τ continues at least down to 20 K, for which E_A would have to be considered lower than 60 meV in order to match the results. This would not just oppose all the before mentioned points but in this case GaN:C would even be very conductive, which be ruled out. We would like to emphasize that we spent much efforts to adapt the conventional model in order to match the results, but eventually we had to accept that it is impossible that holes can be emitted from carbon acceptors to VB with such short τ_{charge} . Thus, in the following section we introduce defect bands (DBs) within the band gap that can solve this issue.

Defect band model

From dc analysis in Section 3.2 we know that E_F and E_{acc} are located at roughly 0.7 eV, furthermore from low- T measurements we know that charges cannot overcome a potential barrier larger than about 60 meV at low T . In order to solve this apparent contradiction we introduce "defect bands" (DBs), also called "impurity bands" in e.g. [Rac+18b], within the GaN band gap close to the carbon acceptor with energy level E_{DB} , illustrated in Fig. 3.12(b). DBs can be considered as conductive band with limited carrier mobility, located $\Delta E_{\text{A,DB}}$ apart from the acceptor level, i.e. $\Delta E_{\text{A,DB}} = E_{\text{acc}} - E_{\text{DB}}$. Depending on the sign of $\Delta E_{\text{A,DB}}$ majority charge carriers are either

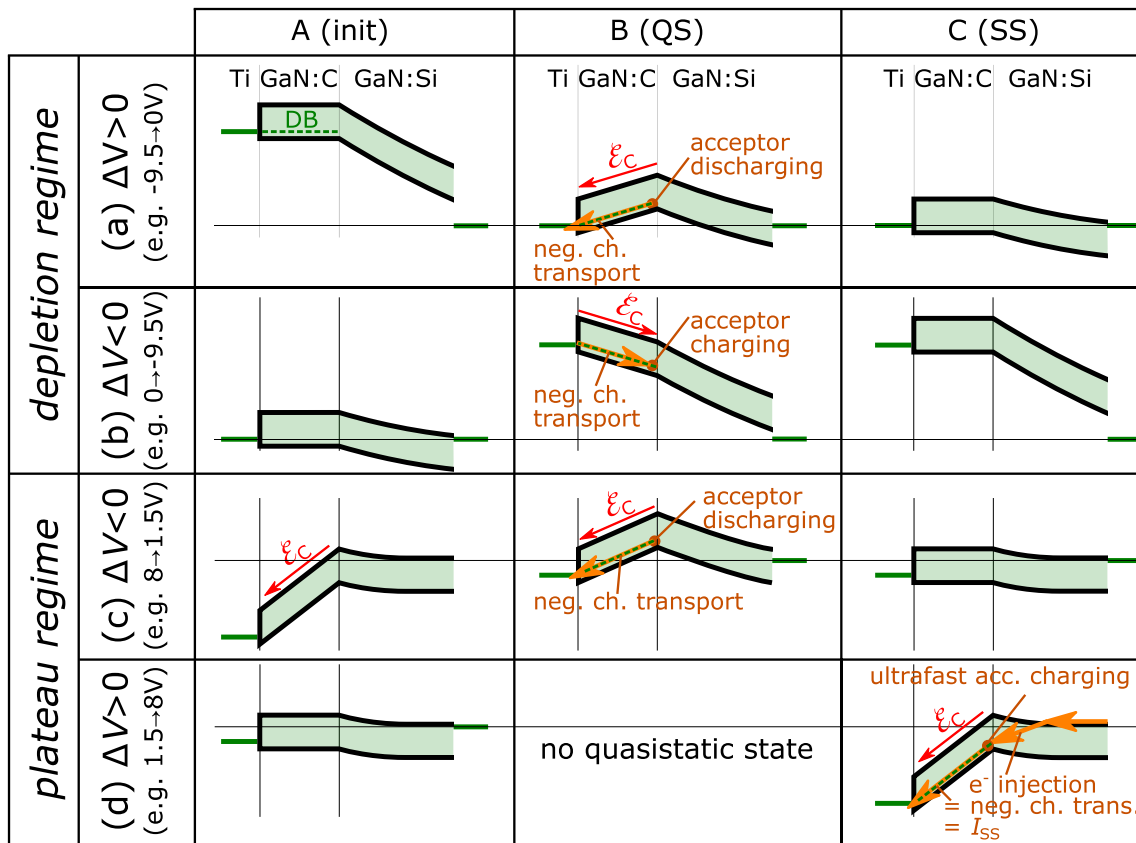


Fig. 3.13: Evolution of the band diagram in S_{10} after various bias steps (a-d): A) in state “A” SS condition is established for the initial bias; B) “B” shows the quasistatic (QS) condition 30 ns after the bias step; C) in “C” SS is established. Orange arrows indicate negative charge transport. Figure reused from [Kol+18a].

electrons (negative value; DBs above acceptor) or holes (positive values; DBs below acceptor). For the border case of $\Delta E_{A,DB} = 0$, shown in Fig. 3.12(c), a distinction between hole and electron conduction does not make sense anymore. In order to emphasize that we will speak in the following of negative charges instead of electrons or holes. For the nature of DBs we consider e.g. that preferential segregation of carbon atoms at threading dislocations cause wave function overlap for high carbon concentrations and hence the formation of defect bands, more detailed discussion of their nature follows later. We consider it very likely that DBs and acceptors storing the accumulated charge σ_C originate both from the very same carbon defects. Thus, we consider the case in Fig. 3.12(c) with $\Delta E_{A,DB} = 0$ most likely.

Fig. 3.13 shows calculated band diagrams for the four representative bias steps from Tab. 3.2, i.e. discharging (a,c) and charging (b,d) in *depletion regime* (a,b) and *plateau regime* (c,d). The three columns illustrate band diagrams for the initial bias condition "A", the quasistatic condition "B" (i.e. directly after applying the bias step, where the charge distribution in GaN:C is still the same as in "A") and final steady-state "C". The general explanation on the evolution of the band diagrams is given in Sec. 3.3 and in Figs. 3.9 and 3.10. Now we will extend the previous explanations by discussion of the actual charging and discharging processes, considering the peculiarities of the defect band model.

In Fig. 3.13(a) acceptor discharging is demonstrated after a bias step with $\Delta V > 0$ in the *depletion regime*. Therefore, the initial large depletion width in (A) decreases in a very fast ($\ll 30 \mu\text{s}$) process after the bias step, leading to the quasistatic state (QS) in (B). The apparent electric field \mathcal{E}_C drives negative charges from occupied (negatively charged) carbon acceptors into the defect band, i.e. acceptors get unoccupied (charge neutral). Due to \mathcal{E}_C negative charges in DBs propagate vertically through GaN:C to the top electrode. The decreasing negative charge in GaN:C decreases \mathcal{E}_C until it vanishes and SS establishes (C). The same happens in (b) for $\Delta V < 0$ in the *depletion regime*, but in this case \mathcal{E}_C is of opposite sign. This drives negative charges from the top metal into DBs down to the GaN:Si/GaN:C interface vicinity, where they are captured in carbon acceptors, i.e. occupying/charging them. The evolving charge decreases \mathcal{E}_C until SS is established.

For $\Delta V < 0$ in the *plateau regime* as illustrated in Fig. 3.13(c), acceptor discharging occurs similar to discharging in the *depletion regime*. A bias step results in a quasistatic condition analogous to (a) in which \mathcal{E}_C drives negative charges from carbon acceptors via DBs to the top electrode. The decreasing negative charge in GaN:C decreases φ_i until $\mathcal{E}_C = 0$ in SS.

With the defect band model we can finally explain how the dynamic equilibrium in the *plateau regime* establishes that makes the structure resistive, more experimental details on the leakage current follow in Section 3.3.5. Fig. 3.14 shows hypothetical band diagrams for stepwise increasing bias, as the occurring processes are faster than $30 \mu\text{s}$ we have no experimental data and can measure only SS conditions. Following points refer to the subfigures of Fig. 3.14:

- (a) At roughly $V = 1.5 - 1.7 \text{ V}$ the *plateau regime* starts, at this bias \mathcal{E}_C is still zero and no significant I_{SS} is observed, $\varphi_i \approx 1.1 \text{ eV}$.
- (b) Now we raise V by 0.6 V to 2.2 V . Dynamic measurements in the *depletion regime* revealed that carbon acceptor charging in GaN:C is a slow process while the change of the depletion width in GaN:Si is a fast process. Hence, φ_i would decrease fast by roughly 0.6 V . However, this massively decreased potential barrier would further result in large injection of electrons

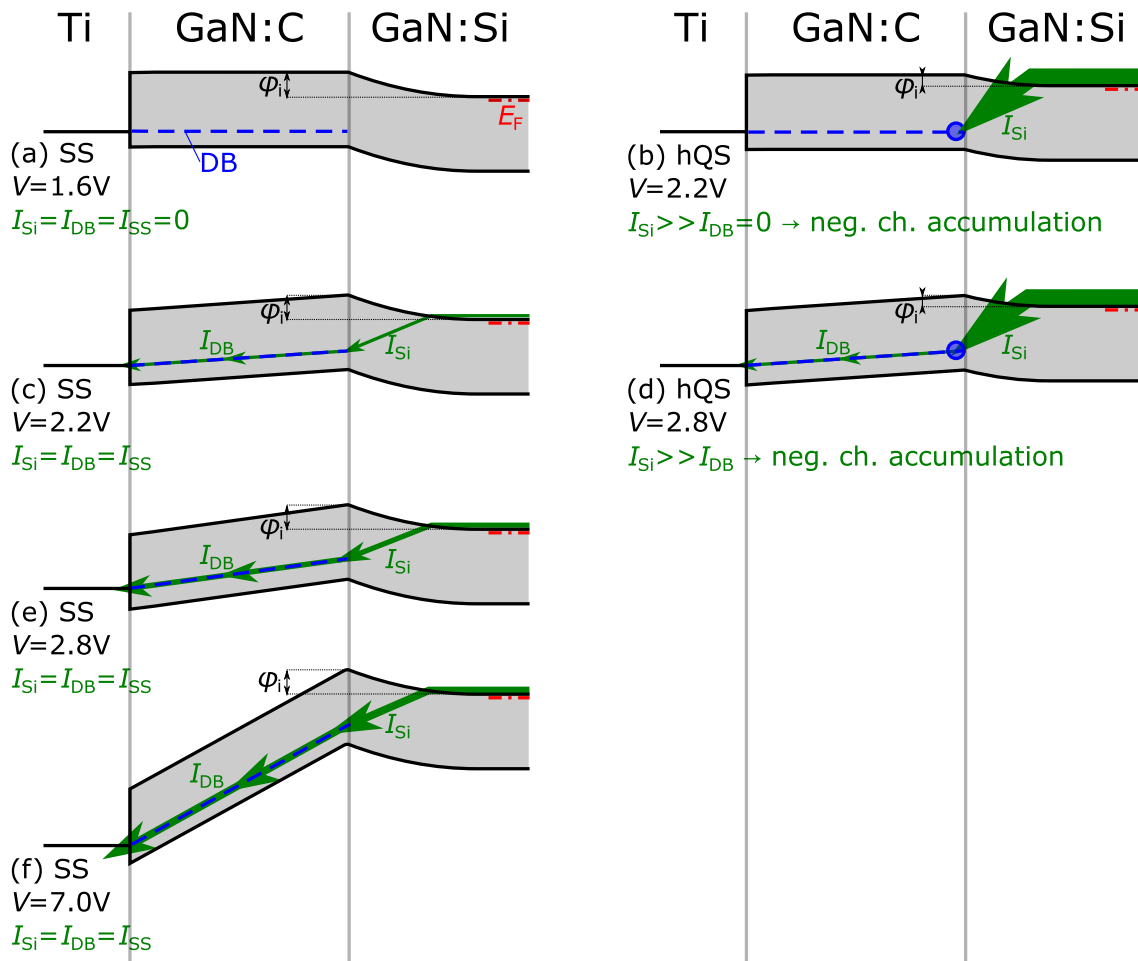


Fig. 3.14: Schematic band diagrams demonstrate how in the *plateau regime* charge accumulation in carbon acceptors in GaN:C establishes a potential barrier (φ_i) that prevents major charge injection into CB of GaN:C. Schematics in left half show SS cases while (b,d) in the right half illustrate hypothetical quasistatic states (hQS) after increasing the bias from (a,c) respectively and the according negative charge accumulation in blue circles. Green arrows represent negative charge transport. For simplicity, displacement current are not shown in hQS

from CB of GaN:Si to CB of GaN:C. For sufficiently thick GaN:C layers a great part of them is eventually captured by DBs or carbon acceptors, shallow donors can be neglected in first approximation. Thus, a large amount of electrons is injected into GaN:C within a very short time interval ($\ll 30 \mu\text{s}$). As obtained from dynamic characterization in the *depletion regime*, charges need e.g. at room temperature roughly 300 ms to propagate through GaN:C via DBs. Therefore, we can consider that the injection current from GaN:Si (I_{Si}) is much larger than the current through the defect band I_{DB} . This leads to "ultrafast" accumulation of negative charges in GaN:C and thus raising φ_i . With raising φ_i not only I_{Si} decreases but also \mathcal{E}_C and as a consequence I_{DB} increases. A so-called dynamic equilibrium establishes when $I_{\text{Si}} = I_{\text{DB}}$, which is then a SS vertical leakage current I_{SS} through the entire structure, see (c). This statement has wide-ranging consequences:

- (i) It demonstrates that charging of carbon acceptors effectively builds a potential barrier that prevents leakage current over the CB of GaN:C. In theory, same would apply for charge transport via VB, although due to E_{F} being located nearer to E_{VB} than to E_{CB} less effective. Without or with less carbon acceptors negative charge can not accumulate, hence no potential barrier can rise, as observed for samples with GaN:C with small carbon concentration, see Section 3.4.
- (ii) In case of an electric field in GaN:C, charges will always redistribute in GaN:C resulting in reduction of the field. This means that negative charges will propagate in direction of the electric field. Only a SS leakage current can maintain the supply and therefore only for $I_{\text{SS}} \neq 0$ potential drops in GaN:C (i.e. $I_{\text{SS}} \neq 0$), neglecting potential drops in space charge regions due to unoccupied or occupied acceptors. More details follow in the discussion of multilayer structures in Section 4

For a more realistic view we have to consider finite voltage ramp rates for the bias step, presumably slower than the charge accumulation rate in GaN:C. One can consider between (a) and (b) multiple steps, leading to a continuous process. Thus, φ_i will not change as significantly as in this simplified hypothetic scheme and therefore we consider only direct injection into carbon defects and no electron injection to the GaN:C CB. Anyway, the discussion of the physical mechanism of this capture process is rather speculative due to the lack of measurement data. However, the relevant point is that the pace of the process makes clear that captured charges must be electrons injected from GaN:Si, in very contrast to charges propagating through DBs as for all other charging/discharging processes in GaN:C.

- (c) In steady state $I_{\text{Si}} = I_{\text{DB}} = I_{\text{SS}}$, which shows that I_{SS} depends solely on the conductivity in DBs. We explicitly point out that I_{SS} depends not on φ_i or the injection mechanism. E.g. if there would be a faster injection mechanism, then in order to establish $I_{\text{Si}} = I_{\text{DB}}$ a larger φ_i would establish, but I_{SS} would not be harmed significantly. This is e.g. confirmed by T -dependent $C_{\text{SS}}-V$ measurements which show that with increasing T , φ_i increases slightly (not shown). As I_{Si} increases faster with T (probably Arrhenius-like but not proven) than I_{DB} ($\propto e^{aT}$), φ_i has to increase with T in order to keep $I_{\text{Si}} = I_{\text{DB}}$. Another indication is the slightly increasing C_{SS} with V in the *plateau regime*, as shown in Fig. 3.3(b): With increasing V also \mathcal{E}_C increases and as a consequence also I_{DB} (see the increased I_{SS} in Fig. 3.3(a)). In order to maintain $I_{\text{Si}} = I_{\text{DB}}$, also I_{Si} has to increase which is achieved by a decrease of

φ_i . Decreasing φ_i is accompanied by decreasing GaN:Si depletion width and increasing C_{SS} . Quantitative analysis follows in Section 3.3.5 (Fig. 3.22).

- (d) For further increasing V the same procedure as in (b) takes place.
- (e) This leads to SS with $I_{Si} = I_{DB} = I_{SS}$.
- (f) The introduced behavior is valid within the entire *plateau regime*, as shown here for $V = 7$ V.

Nature of defect band

Summarizing our knowledge, we have evidence for a conductive channel within the band gap very close (< 60 meV) to carbon acceptors that forms only for high carbon doping ($> (1-10)10^{19}$ cm $^{-3}$, see Section 3.4) and shows an unknown non-Arrhenius-like conduction mechanism. Based on this information we can speculate about the nature of this channel, which we call defect band:

- As DBs are energetically close to carbon acceptors and they form only for high $[C]$ it seems natural to consider carbon atoms as "building blocks" of DBs.
- The T dependence and its non-Arrhenius T behavior prove that charges do not interact with VB and CB. It suggests a charge transport mechanism that is not determined by overcoming a potential barrier, which would lead to Arrhenius-like T dependence. Instead, we consider quantum-mechanic tunneling between carbon defects, similar as hopping which is the only mechanism leading to the experimentally observed \mathcal{E}_C dependence, see Eq. 2.12 and Fig. 3.20. However, hopping should show different T dependence, possibly due to large $[C]$. In order to get reasonable conductivity as observed, carbon atoms have to be close enough to enable tunneling, justifying the term defect "band".

There are already publications claiming the existence of such bands in (not intentionally carbon-doped) GaN [Zha+15a; Rac+18b]. In these publications the leakage current in vertical GaN diodes is assigned to "mini-bands" [Zha+15a] or "impurity bands" [Rac+18b], which are assumed to rise in the vicinity of threading dislocations. In other semiconductors such as SiC, this phenomenon is more prominent, e.g. in Al-doped SiC (p-type) at very low T conduction via hopping between impurities has been reported (i.e. "impurity-band") [Kri05].

- Considering a carbon acceptor concentration of 5×10^{18} cm $^{-3}$ the average distance between neighboring carbon atoms is > 5 nm, which makes tunneling between them unlikely. Hence, we consider the existence of vertical paths in GaN:C where the carbon concentration is significantly enhanced. This could be near extended defects such as in GaN (especially in used GaN-on-Si) always existent grain boundaries or more likely threading dislocations. Zhou et al. [Zho+08] proved by atom probe tomography that Mg segregates preferentially at threading dislocations, similar could be the case for carbon. On the other hand optical spectroscopy studies [Kne+16] suggest that carbon does not segregate at dislocations but instead near dislocations the carbon concentration is even reduced. However, an increased concentration in the near vicinity could still be possible.
- Quantum-mechanic tunneling should show no major T dependence, however in DBs we find that conduction increases exponentially with T . We speculate that this originates from a T -

dependent tunnel parameter, but this is unclear yet. Similarly, the exponential dependence on the electric field (see Section 3.3.5) is not understood yet.

- An observation that is in line with the hypothesis of conduction via tunneling between carbon atoms is the increased conductivity in GaN:C with higher carbon concentration, see Section 3.4. For higher [C] smaller distances between carbon atoms and therefore higher tunnel current is expected and experimentally confirmed.
- Although the indications for a relation of DBs with carbon defects are strong, for the matter of completeness we also mention our speculations on the nature of DBs we introduced in [Kol+17b] at an earlier stage with less experimental data: Threading dislocations can cause local stress in their vicinity, which is known to reduce the band gap. This could cause conductive channels in the dislocation vicinity [CP58]. Such carrier localization in the dislocation vicinity is e.g. reported in InGaN [Mas+17]. Even separate channels for electrons and holes like in a quantum wire could exist [Rei+16].

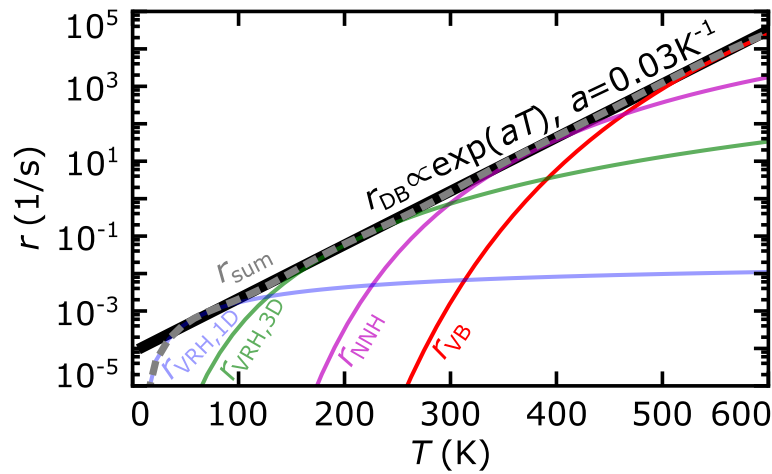


Fig. 3.15: Fitting of the observed exponential temperature dependence of the transport rate (i.e. r_{DB}), solid black line) by the sum of four contributions (r_{sum} , dashed grey line): r_{VB} , r_{NNH} , $r_{VRH,3D}$, $r_{VRH,1D}$ are the rate contributions due to charge transport in VB, nearest neighbor hopping, variable range hopping in 3D and in 1D, respectively. Simulation equations and parameters are given in Tab. 3.3. Figure reused from [Kol+18a].

- As we pointed out in [Kol+18a], instead of considering a single currently unknown mechanism that dominates the entire T range, several different mechanisms could be considered that dominate in different T ranges and result in total in an almost exponential T dependence. In the following we therefore tentatively consider the transport rate (r_{DB}) as sum of four parallel mechanisms with rates $r_{sum} = \sum_i r_i$, described in detail in Section 2.2.1 and recited with their T dependences in Tab. 3.3:

1. one-dimensional variable range hopping e.g. via dislocations ($r_{VRH,1D}$)
2. three-dimensional variable range hopping in the bulk ($r_{VRH,3D}$)
3. nearest neighbor hopping (r_{NNH})
4. charge transport via VB (r_{VB})

Fig. 3.15 demonstrates that by using simulation parameters given in Tab. 3.3, the exponential T dependence of r_{DB} can be reproduced. However, it has to be stated that the fitting parameters, especially the large E_A of 0.4 eV for r_{NNH} are hard to justify. Furthermore, we observe e^{aT} dependence independent of the bias and for all investigated samples featuring GaN:C layers. These samples are e.g. samples with different GaN:C layer thicknesses (S_{10} vs. S_{10b}), different carbon concentrations (S_{10} vs. S_{70}), with carbon-doped AlGaN (AlGaN:C) instead of GaN:C (S_{A1} vs. S_{10}) and even HEMT stacks (only leakage current measured). As different mechanisms should show different dependencies on these parameters, it is very unlikely that the exponential T dependence can be preserved [Kol+18a]. Hence, we consider a single unknown mechanism instead of multiple known mechanisms in parallel.

However, as also pointed out in [Kol+18a], charge transport via VB is supposed to occur always in parallel to charge transport via DBs, but is for $T < 600$ K negligible compared to transport via DBs. As shown later in the discussion of the influence of [C], Fig. 3.25(e) demonstrates that for S_{10} and S_{70} transport via VB should dominate already at 350 and 500 K, respectively. As this is experimentally not observed, we speculate that with increasing [C] the hole mobility in VB decreases due to increasing impurity scattering, shifting the T threshold to values exceeding 600 K [Kol+18a].

Table 3.3: Expressions for charge transport rates in Fig. 3.15 with simulation parameters. Table reused from [Kol+18a].

1. $r_{VRH,1D} = a_{VRH,1D} \exp\left(-\frac{A_{VRH,1D}}{T}\right)^{1/2}$ [MD12]
$a_{VRH,1D} = 4 \times 10^{-2} \text{ s}^{-1}$ $A_{VRH,1D} = 10^3 \text{ K}$
2. $r_{VRH,3D} = a_{VRH,3D} \exp\left(-\frac{A_{VRH,3D}}{T}\right)^{1/4}$ [MD12]
$a_{VRH,3D} = 2 \times 10^{-10} \text{ s}^{-1}$ $A_{VRH,3D} = 10^8 \text{ K}$
3. $r_{NNH} = a_{NNH} \exp\left(-\frac{E_{A,NNH}}{k_B T}\right)$ [MD12]
$a_{NNH} = 4 \times 10^6 \text{ s}^{-1}$ $E_{A,NNH} = 0.4 \text{ eV}$
4. $r_{VB} = a_{VB} T^2 \exp\left(-\frac{E_a}{k_B T}\right)$ [Smi78]
$a_{VB} = 4 \times 10^4 \text{ s}^{-1}$ $E_a = 0.7 \text{ eV}$

3.3.4 Comparison of defect band model with literature results

Fig. 3.11(d,e) prove well the non-Arrhenius T dependence that required the introduction of the defect band model. A question that immediately arises: If it is that obvious, why has it not been reported in literature yet? In order to give an answer we present in the following a literature study and compare it with our results.

As explained in Section 2.2.2 the by far most prominent characterization technique for investigating traps in GaN layers in HEMTs is current transient spectroscopy (CTS), which is supposed to deliver activation energies, i.e. trap levels of deep traps. In the introduction we already reported

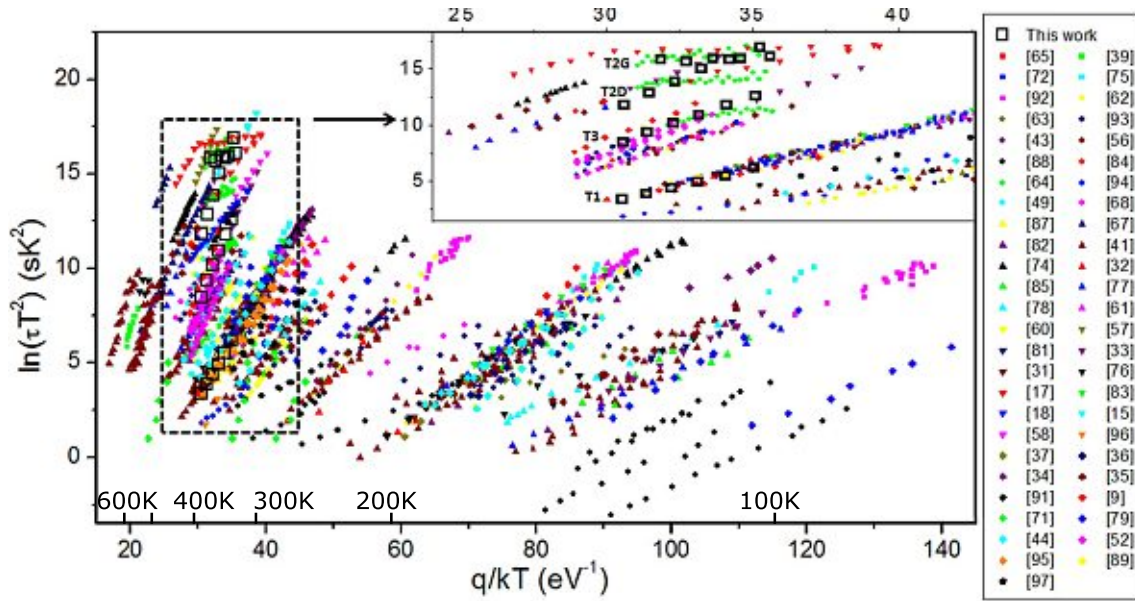


Fig. 3.16: Arrhenius plot with literature data from CTS measurements in literature from GaN- and AlGaN-based layers and devices with largely varying growth and doping conditions. Figure from [Bis+13].

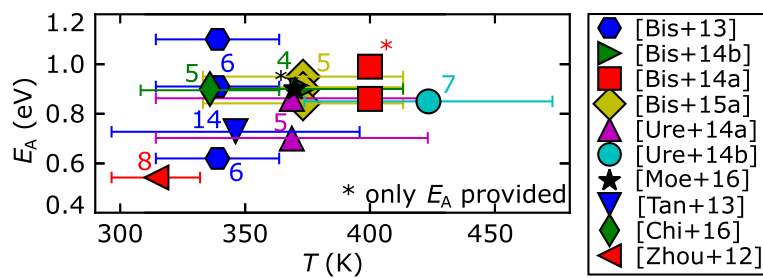


Fig. 3.17: E_A in literature related to carbon defects as function of the measurement temperature. Symbols indicate the central temperature, numbers the number of measurement points and bars the temperature ranges of the single studies. Figure reused from [Kol+17a].

that assigning trapping time constants directly to trap response times in HEMT stacks has large potential for misinterpretation if transport processes are not considered.

Fig. 3.16 shows an Arrhenius plot with datapoints from CTS measurements of more than 50 publications. Bisi et al. use this graph in [Bis+13] to extract E_A directly from the slope of a linear fit in the Arrhenius plot. The huge range of different slopes emphasizes the large range of reported E_A in literature for limited T intervals. However, data from GaN under a wide range of different growth parameters, dopants and doping concentrations is used. As the focus of this thesis lies on GaN:C, Fig. 3.17 shows extracted E_A only for studies in which trapping is related to carbon defects in GaN-based buffers. We notice still a very wide range of reported E_A between 0.5 and 1.1 eV. Remarkable is also the small temperature range, in which all experiments were performed. Central temperatures were all between 310 and 430 K with temperature ranges within single publications between 35 and 110 K. This means that the study with the largest range used only roughly a fifth of the range used e.g. in I_{SS} - V in Fig. 3.19 (20 to 560 K). Furthermore, for most studies only four to eight datapoints are used in the Arrhenius plot to derive E_A with only one study ([Tan+13]) using more than eight datapoints. In comparison in this thesis I_{SS} - V measurements in Fig. 3.19 are performed for 187 different temperatures, resulting in the same number of datapoints in an Arrhenius-plot. Transient $C(t)$ measurements in Fig. 3.11 are done for 88 different temperatures. We believe that these circumstances are the reason why we are the only group reporting on non-Arrhenius temperature behavior, demonstrated in detail in Fig. 3.18.

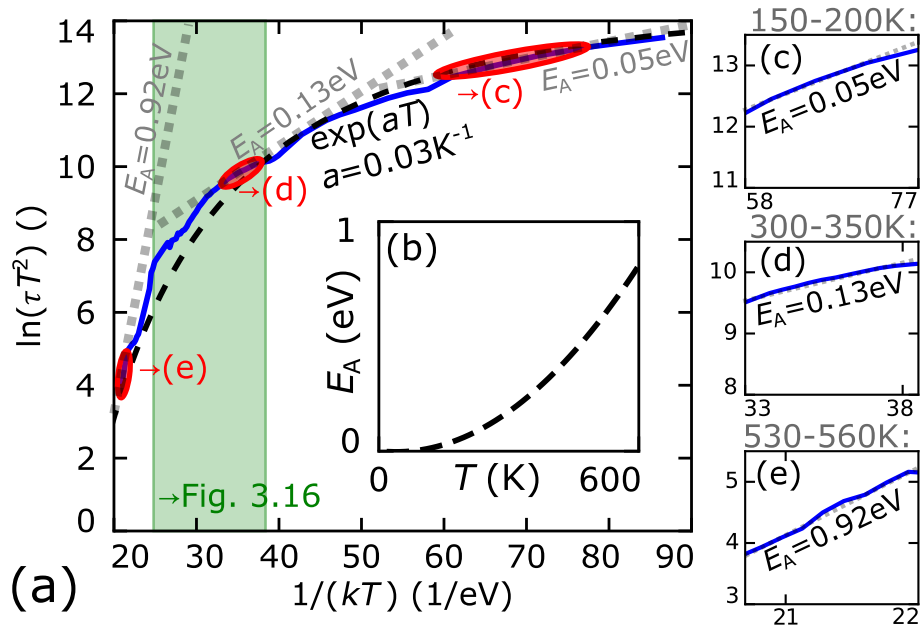


Fig. 3.18: (a) Arrhenius plot with discharging time constants after a bias step from $-9.5 \rightarrow 0$ V (blue solid line) and exponential fit (black dashed line). (b) Extracted activation energy E_A considering a classical SRH discharging process (Eq. (3.13)). (c-e) In small T ranges, processes appear Arrhenius-like, only large T ranges as in (a) reveal the non-Arrhenius-like T behavior.

The main figure (a) shows an Arrhenius-plot with trapping time constants derived after a bias step from -9.5 V to 0 V, i.e. discharging process. Charging processes are almost identical as shown in Fig. 3.11. Basically, it is analogous to Fig. 3.11(e) but with use of more datapoints, connected by the solid blue line. The black dashed curve shows a fit of the data to e^{aT} with $a = 0.033 \text{ K}^{-1}$.

In the large T range with the large amount of datapoints the non-Arrhenius behavior is obvious, however the green rectangle shows the small T range in which all experiments in literature were performed. As the T range of single studies is even much smaller and contains a very small amount of datapoints (see Fig. 3.17) it is practically impossible to distinguish between Arrhenius-like and e^{aT} behavior. This is also demonstrated in Fig. 3.18(c-e) where the data is only shown in Arrhenius-plots in limited T ranges. Even with the large amount of datapoints data falsely seems to follow Arrhenius law, i.e. forming a straight line. However, the consequence is that with decreasing extraction temperature the derived E_A increases, see (b). At room- and elevated temperature, in which all experiments in literature were performed, the extracted values for E_A are even close to the ones found in literature (0.1 to 0.9 eV) and to the actual carbon level. However, we explicitly point out that this is just a coincidence as E_A extracted from Arrhenius-plots have no physical meaning in the defect band model; there is no direct link to defect activation energies. Therefore, the commonly used CTS method cannot be used for determining carbon levels in GaN:C buffers. We have evidence for the non-Arrhenius e^{aT} behavior of the vertical leakage current not only in our LUT structures but also in multilayer buffers (Section 4.3.4) and even in HEMT structures (Fig. 3.23), indicating that the defect band model can probably be extended to buffer stacks used in HEMTs.

3.3.5 Leakage current in GaN:C

In this section we will discuss the nature of the leakage current through the GaN:C layer on basis of sample S_{10} , which has been published in [Kol+17a; Kol+18a]. The basic behavior of the LUT structures and especially the containing GaN:C layer is described in detail in Section 3.3.3 and sketched in Fig. 3.14. The key feature of GaN:C layers in general is that due to charge accumulation next to interfaces to adjacent layers, potential barriers form that inhibit injection of electrons to the GaN:C CB and injection of holes to the GaN:C VB. This feature becomes more clear when discussing multilayer structures in Section 4. Due to suppression of charge transport in CB/VB, I_{SS} is solely determined by the charge transport in DBs. As discussed in the previous chapters, the very same transport limits also all (dis-)charging processes. In order to prove this statement we compare the T and \mathcal{E}_C dependence of leakage current and (dis-)charging time constants, which should be identical according to the defect band model.

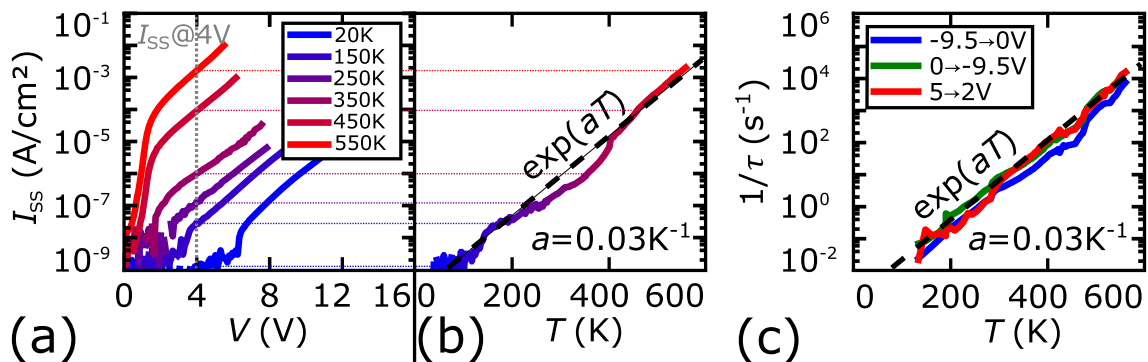


Fig. 3.19: (a) I_{SS} - V of S_{10} for selected temperatures and (b) extracted I_{SS} values at 4 V. Direct comparison of (b) with the trapping rate after various bias steps in (c) reveals the identical T dependence of leakage current and trapping. Figures reused from [Kol+17a].

SS current: First, we characterize the T dependence of I_{SS} by performing $I_{SS}-V$ measurements at various temperatures as shown in Fig. 3.19(a). In total 187 measurements are performed in a temperature range between 20 and 560 K. In Fig. 3.19(b) the I_{SS} values at $V = 4$ V are used and plotted against T , revealing a very good fit to e^{aT} . Subfigure (c) reveals the very same T dependence for $1/\tau$, independent of the bias step as represented by the three representative (dis-)charge processes in Tab. 3.2. It is remarkable that both $1/\tau$ and I_{SS} follow e^{aT} , even with the same factor a over the entire T range. This strongly indicates that indeed both processes are determined by the same process, i.e. the transport through the defect band. There is no sign for additional current flow via conduction or valence band.

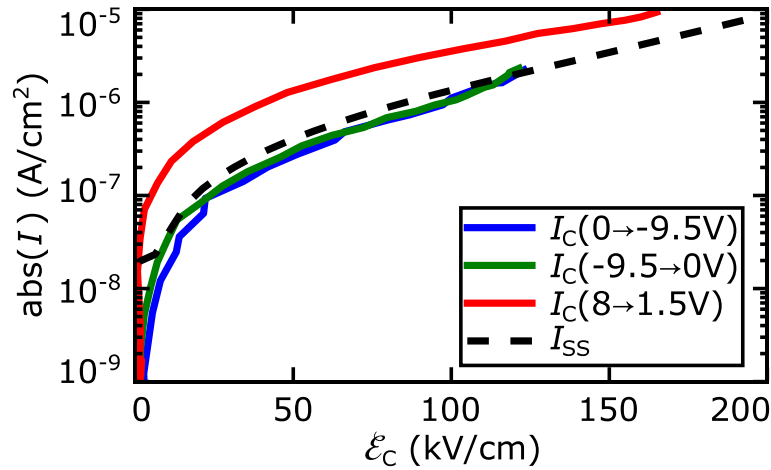


Fig. 3.20: I_{SS} (black dashed line) as function of \mathcal{E}_C with I_{SS} extracted from $I_{SS}-V$ and \mathcal{E}_C from $C_{SS}-V$. Transient currents after various bias steps (I_C , colored solid lines) are extracted from $C(t)$ analysis and fit well to $I_{SS} - \mathcal{E}_C$. Figure reused from [Kol+17a] and [Kol+18a].

Transient current: In a further step we can even check if the \mathcal{E}_C -dependencies and absolute values of I_{SS} and τ fit. Therefore, we compare the SS leakage current, that is propagating through the defect band (I_{SS}) and the transient flow of charges (i.e. current) through GaN:C that are subsequently captured by (or before emitted from) carbon acceptors (I_C). In general, both depend on T and \mathcal{E}_C ; as the T dependence has been already investigated well, we now perform analysis at a single $T = 340$ K, see Fig. 3.20. In order to get the \mathcal{E}_C dependence of I_{SS} we use the knowledge on the almost constant interface potential φ_i and V_{bi} (see Fig. 3.4), so that \mathcal{E}_C can be approximated directly from the applied bias V :

$$\mathcal{E}_C = \frac{V + \varphi_i - V_{bi}}{d_{LUT}}. \quad (3.18)$$

The black dashed line in Fig. 3.20 represents $I_{SS}(\mathcal{E}_C)$. For the \mathcal{E}_C dependence of I_C we first derive $I_C(t)$. From transient $C(t)$ measurements the transient amount of charge stored in carbon acceptors ($\sigma_C(t)$) can be derived, see Fig. 3.9 and Fig. 3.10. As a current density is per definition a change of charge per time and area, $I_C(t)$ can be calculated as:

$$I_C(t) = \frac{d\sigma_C}{dt}. \quad (3.19)$$

Furthermore, the transient $\mathcal{E}_C(t)$ can be calculated by using Eq. (3.18) but with φ_i being time-dependent. Linking $\mathcal{E}_C(t)$ with $I_C(t)$ allows extraction of $I_C(\mathcal{E}_C)$ where t is the independent

variable, as shown in Fig. 3.20 for three bias steps representing the three different (dis-)charging processes. As \mathcal{E}_C decreases after a bias step from a maximum value to 0, a full $I_C(\mathcal{E}_C)$ characteristic is gained from a single $C(t)$ measurement.

Fig. 3.20 proves same \mathcal{E}_C dependence and even a very good fit of the absolute values of I_{SS} and I_C , providing further evidence that not only for (dis-)charging processes charges propagate via DBs but also for SS leakage current. It should be mentioned that $I_{SS}-V$ characteristics in Fig. 3.19(a) are not in SS condition throughout the entire T range. Charging in the *plateau regime* is always faster than 30 μs , therefore for up-sweeps with increasing forward bias saturation is always reached, independent of the ramp rate. In contrast, discharging is at low T very slow, requiring e.g. times exceeding the lifetime of a PhD student significantly at 20 K. As such measurement times are unfeasible, shorter times are used and SS is not reached at every datapoint anymore. Hence, the charge condition of the maximum voltage before "breakdown" is frozen, resulting in a high φ_i and therefore higher \mathcal{E}_C . The measured current is then not I_{SS} but I_C instead, i.e. charges do not propagate from bottom to top electrode but only from carbon acceptors to the top electrode and from GaN:Si to bottom electrode, analogous to displacement current. Anyway as proven in Fig. 3.20 the current is determined by the charge flow in DBs and not by the injection current from GaN:Si to GaN:C, therefore this does not cause major differences. However, the slightly enhanced \mathcal{E}_C cause slightly enhanced current values. In the performed experiments we were interested not only in I_{SS} at $V = 4\text{ V}$ but also in $I_{SS}-V$ curves, but if I_{SS} at $V = 4\text{ V}$ would be the only point of interest, one could imagine an improved measurement: V could be kept at 4 V throughout the entire T sweep, resulting in a constant charge state. Even if the needle has to be re-adjusted as it is common for such large T ranges due to thermal expansion of the setup, V only returns to 0 and back to 4 V. As discharge is the much slower process, the charge state remains unchanged. It would change only for V exceeding 4 V.

Voltage dependence of defect band current I_{DB}

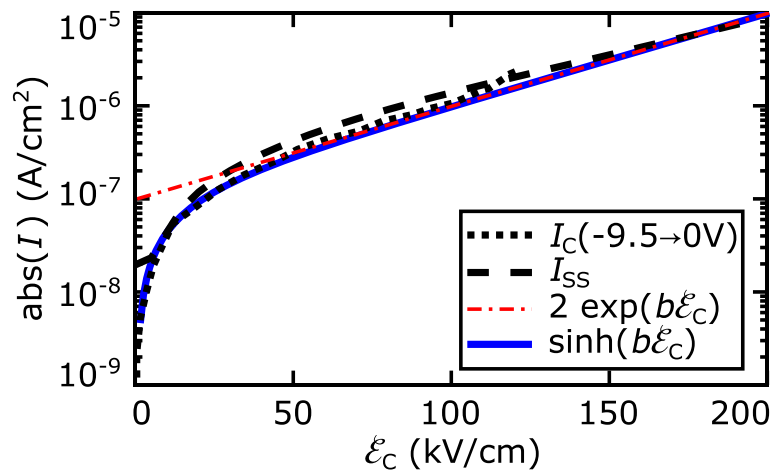


Fig. 3.21: Experimentally observed I_C and I_{SS} from Fig. 3.20 in black represent the current through defect bands, which can be fitted well by a \sinh -function (blue) in the entire \mathcal{E}_C regime and for high \mathcal{E}_C by an exponential function (red).

Fig. 3.20 reveals exponential \mathcal{E}_C dependence of the current that can propagate through defect band (I_{DB}) for high \mathcal{E}_C ($\gtrsim 50 \text{ kV cm}^{-3}$), i.e. $I_{DB}(\mathcal{E}_C) \propto e^{b\mathcal{E}_C}$ with $b = 2.3 \times 10^{-7} \text{ m V}^{-1}$. Fig. 3.20 demonstrates that while the exponential law describes I_{DB} for high \mathcal{E}_C well, it delivers for low fields too high currents. Furthermore, $I_{DB}(\mathcal{E}_C = 0) \neq 0$ which is unphysical. To solve this discrepancy we consider negative charge flow not only in opposite direction of \mathcal{E}_C but also in direction of \mathcal{E}_C :

$$I_{DB}(\mathcal{E}_C) \propto \text{sgn}(\mathcal{E}_C)(e^{b\mathcal{E}_C} - e^{-b\mathcal{E}_C}) = 1/2 \text{sgn}(\mathcal{E}_C) \sinh(b\mathcal{E}_C). \quad (3.20)$$

Obviously, this results in $I_{DB}(\mathcal{E}_C = 0) = 0$ and decreases I_{DB} for $\mathcal{E}_C \lesssim 50 \text{ kV cm}^{-3}$, leading to a well fit to the experimentally observed dependence, as shown in Fig. 3.21.

GaN:C/GaN:Si interface barrier, injection mechanism

In the description of the defect band model in Section 3.3.3 we explained that the injection current from GaN:Si to GaN:C (I_{Si}) does not determine the SS leakage current (I_{SS}), instead the conductivity of the defect band, i.e. the current that can propagate through the defect band (I_{DB}) does. The GaN:C/GaN:Si interface barrier (φ_i) always adapts to a level so that $I_{SS} = I_{DB} = I_{Si}$ and as we expect that small changes in φ_i have large impact on I_{Si} an almost constant φ_i and consequently roughly constant C_{SS} is observed in the *plateau regime*. However, as I_{SS} increases over several orders of magnitude, φ_i and therefore C_{SS} in the *plateau regime* should at least increase slightly.

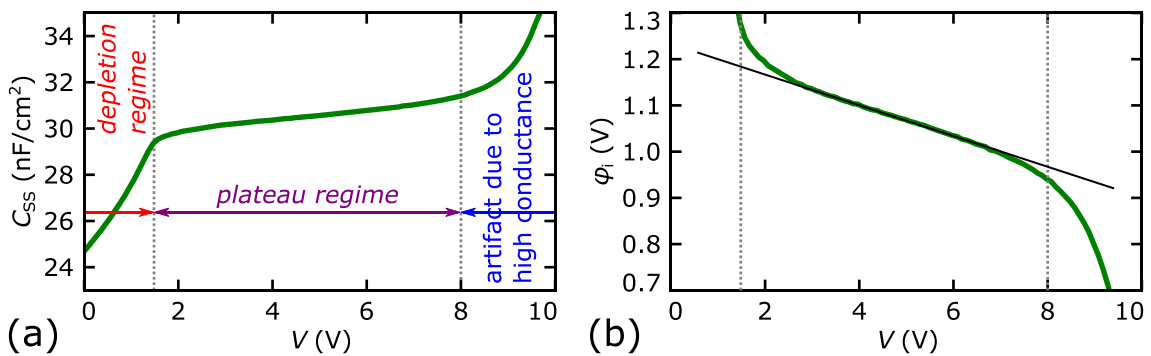


Fig. 3.22: (a) C_{SS} - V of S_{10} at 300 K and (b) calculated potential at the GaN:Si/GaN:C interface (φ_i) using Eq. (3.21).

Indeed, Fig. 3.22(a) demonstrates that the C_{SS} plateau is not entirely constant but shows a small increase with V . We mention that for these measurements highly precise capacitance measurements are crucial, e.g. absolute capacitances in Fig. 3.22(a) are roughly 3.5 pF with an increase in the *plateau regime* of only 20 fF V^{-1} . Significant increase of the alternating current (*ac*) conductance for biases above 7.5 to 8 V inhibits reliable capacitance measurements in this range. In Fig. 3.22(b) φ_i is calculated from C_{SS} values in (a) using Eq.s (3.1, 3.2, 3.4, 3.5, 3.7) for $x = 0$, i.e.:

$$\varphi_i = \frac{qN_{Si}w_{Si}^2}{2\varepsilon}. \quad (3.21)$$

Fig. 3.22(b) demonstrates that in the *plateau regime* φ_i decreases roughly linear with V from 1.2 to 1.0 V. Although there is a larger uncertainty on the absolute value of φ_i due to uncertainties in the exact values of e.g. N_{Si} , d_{LUT} , ε_r or there might be an offset in the measured C_{SS} due to insufficient

fixture compensation; the decrease of φ_i is rather resilient against before mentioned errors. The exponential increase of I_{SS} with linearly decreasing φ_i is found for all electrode-limited conduction mechanisms, in which charges have to overcome a potential barrier by thermal excitation [Chi14; MD12; LI15]. In order to learn more about the injection mechanism the temperature dependence of φ_i is discussed next.

We performed C_{SS} - V measurements at various T , however we did not find a clear shift in φ_i . Therefore, two major points have to be considered:

1. Performing C_{SS} - V measurements for $T \lesssim 300$ K is challenging as voltage ramps to establish SS condition have to be very slow and measurements require unfeasible long times. While this is not so important for e.g. I_{SS} - V measurements, in which I_{SS} increases by orders of magnitude, in C_{SS} - V measurements precise measurements are of utmost importance as parameters such as φ_i are very sensitive to small variations in C . Aggravating are the before discussed small absolute capacitances where it is challenging to get rid of artifacts from parasitics e.g. from cables. Unfortunately, not only small T are problematic but also measurements at high T . As the conductance rises exponentially with T , the border where high conductance prevents reliable C_{SS} measurements decreases roughly linearly with T and e.g. prevents C_{SS} measurements for $T \gtrsim 470$ K in the *plateau regime* completely. Within the observable T range no clear shift of φ_i with T has been observed.

For future measurements we would suggest measurement at higher frequency, where the conductance causes less artifacts. Additionally, different contact sizes could be tried in order to find a good compromise. Larger contact areas increase absolute capacitances and decrease parasitic effects e.g. from cables, both resulting in increased measurement precision; but they also increase artifacts from the conductance, which increase roughly linearly with the area.

2. Classical thermionic emission shows an Arrhenius-like T behavior. Fig. 3.18 in Section 3.3.4 demonstrate that within a T range of about 100 K Arrhenius-law ($\exp(-E_A/(k_B T))$) and conduction in DBs (e^{aT}) show same T dependence for E_A extracted from Fig. 3.18(b). This means that within the investigated T range I_{DB} follows approximately same T dependence as Arrhenius-law with $E_A \approx 0.5$ eV, with E_A corresponding to φ_i . Therefore, if we consider $\varphi_i \approx 0.5$ V, the injection current I_{Si} would increase with T in the same way as I_{DB} does, resulting in a T independent C_{SS} . However, in a larger T range φ_i has to follow roughly the T dependence of E_A , shown in Fig. 3.18(b), whereby it is likely that at very low T with low φ_i the emission process changes from thermionic emission to a different one. Otherwise e.g. at 20 K φ_i would be only ≈ 50 meV.

In order to enhance the knowledge on the injection current, first φ_i has to be measured more precisely. With current knowledge the uncertainty in φ_i is large enough so that φ_i might be indeed 0.5 V instead of the calculated 1.1 V. One of the major obstacles is the exact knowledge of the thickness of the GaN:C layer. Therefore, we suggest for future investigations to produce samples with a variation of different GaN:C thicknesses d_{LUT} . As the depletion width in GaN:Si depends not on d_{LUT} , the capacitance of GaN:Si also should not. On the other hand the measured capacitance C_{SS} does depend on d_{LUT} : $1/C_{Si} = 1/C_{SS} - d_{LUT}/\epsilon$. By comparing C_{Si} for all samples with different d_{LUT} they only fit if the right d_{LUT} is chosen. In that way precise values for φ_i could be gained. An easy way to manufacture a sample set with different d_{LUT} would be to use the existent samples and etch away part of the GaN:C

layer by using different exposure times. In order to expand the temperature range to lower T the above introduced technique can be used, where instead of entire C_{SS} - V characteristics only C_{SS} at a certain bias is measured. Furthermore, at higher T higher frequencies could be used in order to suppress artifacts from the ac conductance.

Leakage current in a HEMT with carbon-doped buffer

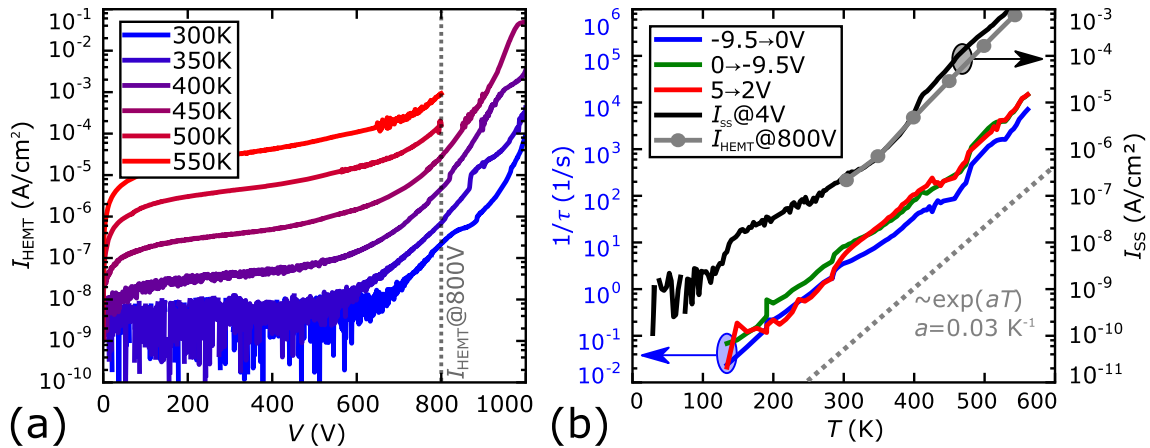


Fig. 3.23: (a) Vertical leakage current of a HEMT structure (raw data from [Arnen]) for various T and (b) quantitative comparison of its T dependence with I_{SS} and the charging/discharging rates after various bias steps in S_{10} .

Different from (dis-)charging processes the vertical leakage current through a HEMT-like test structure I_{HEMT} can be derived straight-forward. In order to avoid distribution of current in the 2DEG over a large undefined area, we use instead of HEMT-structures "HEMT-like test structures" without the top AlGa_N barrier so that no 2DEG can form. More details on the structures and characterization can be found in [Arnen].

Fig. 3.23(a) shows I_{HEMT} characteristics at various temperatures, from which the I_{SS} values are extracted for a top bias of $V = 800$ V and are plotted in (b) against T , see solid grey line. In (b) additionally (dis-)charging time constants and I_{SS} of S_{10} are shown. Remarkably, I_{HEMT} follows the same e^{aT} dependence as S_{10} , indicating that even in a HEMT the vertical leakage current might be limited by DBs and can be explained by the defect band model. As the scope of this thesis lies on discussion of GaN:C by usage of LUT structures, we did not do investigations in more details, results are intended as a teaser for the relevance of the defect band model for HEMT applications.

3.4 Influence of carbon concentration ([C]) for GaN:C

In the previous section we discussed the behavior of GaN:C on basis of samples with a carbon concentration ([C]) of 10^{19} cm^{-3} (S_{10} , S_{10b}), as determined by secondary ion mass spectroscopy. In order to extend the derived behavior towards GaN:C with varying [C], in this section we discuss LUT structures with GaN:C layers with three different [C] (S_{01} : 10^{18} cm^{-3} , S_{10} : 10^{19} cm^{-3} , S_{70} : $7 \times 10^{19} \text{ cm}^{-3}$, see Tab. 3.1). The outcome of this section has been the backbone for our publication in [Kol+18a].

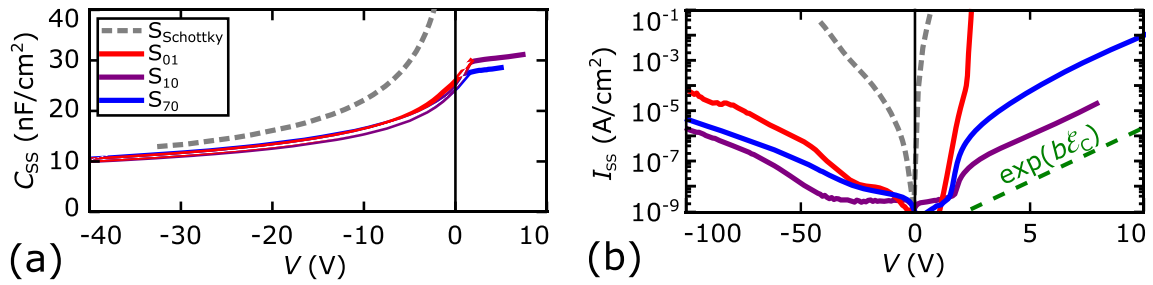


Fig. 3.24: (a) C_{SS} - V and (b) I_{SS} - V at 300 K for the four samples $S_{Schottky}$, S_{01} , S_{10} and S_{70} with the latter three being LUT structures with GaN:C layer with different $[C]$ (10^{18} cm^{-3} , 10^{19} cm^{-3} and $7 \times 10^{19} \text{ cm}^{-3}$, respectively). Figures reused from [Kol+18a].

Fig. 3.24(a) demonstrates that all LUT structures with GaN:C layer (S_{01} , S_{10} , S_{70}) show similar SS behavior in the *depletion regime* ($V < 1.5 \text{ V}$). A linear $1/C_{Si}^2 - V$ characteristic, from which the slope delivers $N_{Si} \approx 8.2 \times 10^{16} \text{ cm}^{-3}$ indicates that E_F -pinning at $E_{acc} \approx 0.7 \text{ eV}$ and flatband in the GaN:C bulk occur independent of $[C]$. Hence, GaN:C builds a block that prevents major leakage current for all three GaN:C samples, as a comparison with $S_{Schottky}$ in Fig. 3.24(b) confirms.

On the other hand in the *plateau regime* ($V > 1.5 \text{ V}$) the sample S_{01} behaves significantly different from S_{10} and S_{70} (i.e. samples with low and high $[C]$, respectively). For S_{70} , the C_{SS} plateau in Fig. 3.24(a) is analogous to S_{10} described before, only at slightly higher C_{SS} due to usage of a thinner GaN:C layer. The exponentially increasing I_{SS} with V in (b) is also analogous to S_{10} , even with the same slope but with a vertical offset: its origin is described in detail in Section 3.4.1. In very contrast, Fig. 3.24(a) reveals that S_{01} shows no C_{SS} plateau at all, corresponding to no formation of a stable GaN:Si/GaN:C interface barrier that prevents leakage current. Indeed Fig. 3.24(b) confirms this by an increase of I_{SS} by more than eight orders of magnitude within few volts. The structure transitions directly from the *depletion regime* to the *Ohmic regime*, in which the resistance is provided mainly by the base structure, for details see Section 3.1.3. We find that not only the SS behavior in the *plateau regime* is significantly different for S_{01} and S_{10}/S_{70} but also the (dis-)charging behavior. A summary is shown in Fig. 3.25, which depicts in (a-c) the T dependence of (dis-)charging processes represented by the three normalized $C(t)$ curves for S_{70} , S_{10} and S_{01} respectively. Fig. 3.25(d,e) show time constants extracted from (a-c) in $\log(\tau) - T$ scale and in an Arrhenius plot, respectively. Tab. 3.4 systematically quantifies the electrical behavior regarding leakage current and (dis-)charging processes. Details of Fig. 3.25 and Tab. 3.4 will be discussed in the following subsections, due to the significantly different behavior of S_{10}/S_{70} and S_{01} both sample groups are discussed in separate subsections and conclusions are drawn in a third subsection.

3.4.1 Highly carbon-doped GaN:C ($[C] \geq 10^{19} \text{ cm}^{-3}$)

The SS behavior in Fig. 3.24 shows qualitatively identical behavior of S_{10} and S_{70} in both, *depletion* and *plateau regime*, even with the same exponential factor b in (b). The only difference is that I_{SS} is in S_{70} roughly 30 larger than in S_{10} , resulting in the vertical offset in Fig. 3.24(b). Another observation is the higher transition/breakdown voltage (see Section 3.5) in S_{70} , which we assume to result from the higher achievable charge density in the space charge region in GaN:C and consequently the interface barrier can be hold up to higher V . In the defect band model the

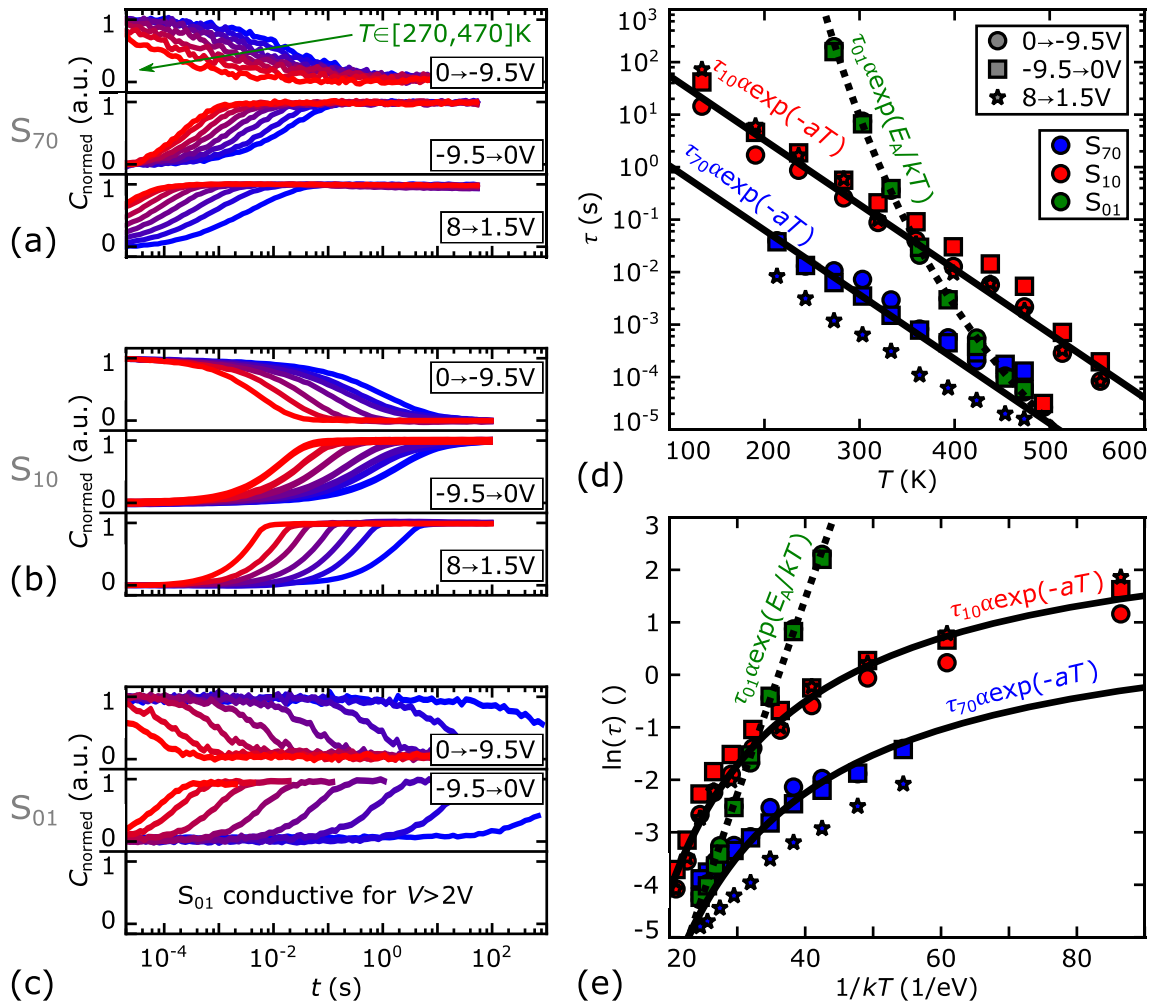


Fig. 3.25: Comparison of normalized $C(t)$ data for (a) S_{01} , (b) S_{10} and (c) S_{70} after various bias steps and for various T reveal the similar T dependence of S_{70} and S_{10} and the very different behavior of S_{01} . Quantification of the T dependence in (d) linear- T - and (e) Arrhenius-plots reveal for S_{70} and S_{10} $\tau \propto e^{-aT}$ (solid lines) in contrast to $\tau \propto \exp(E_A/(k_B T))$ with $E_A = 0.8 \text{ eV}$ for S_{01} [Kol+18a]. Figures reused from [Kol+18a].

Table 3.4: Summary of the T dependence of SS leakage currents I_{SS} and charging/discharging time constants τ after various bias steps as indicated in the index of τ for S_{01} , S_{10} and S_{70} with their different carbon concentrations [C] [Kol+18a].

	[C] (10^{18} cm^{-3})	I_{SS} for $V < 1.5\text{V}$	I_{SS} for $V > 2\text{V}$	$\tau_{0 \rightarrow -9.5\text{V}}$	$\tau_{-9.5 \rightarrow 0\text{V}}$	$\tau_{8 \rightarrow 1.5\text{V}}$	T -dep.
S_{01}	1	~ 0	conductive	$\tau_{01} \exp(E_A/(kT))$	$\tau_{01} \exp(E_A/(kT))$	not meas.	Arrhenius-like
S_{10}	10	~ 0	$I_{10} e^{aT}$	$\tau_{10} e^{-aT}$	$\tau_{10} e^{-aT}$	$\tau_{10} e^{-aT}$	non-Arrh.-like
S_{70}	70	~ 0	$I_{70} e^{aT}$	$\tau_{70} e^{-aT}$	$\tau_{70} e^{-aT}$	$\tau_{70} e^{-aT}$	non-Arrh.-like
parameters:							
[C] $\leq 1 \times 10^{18} \text{ cm}^{-3}$: $E_A = 0.8 \text{ eV}$							
[C] $\geq 1 \times 10^{19} \text{ cm}^{-3}$: [C]-independent: $a = 0.033 (\pm 0.005) \text{ K}^{-1}$							
[C]-dep.: $I_{10} = 5 \times 10^{-12} \text{ A/cm}^2$, $I_{70} = 150 \times 10^{-12} \text{ A/cm}^2$; $I_{70}/I_{10} = 30$							
$\tau_{10} = 2.5 \text{ s}$, $\tau_{70} = 0.08 \text{ s}$; $\tau_{10}/\tau_{70} \sim 30$							

30 times higher I_{SS} must correspond to a 30 times higher conductivity in the DBs in GaN:C in S_{70} . Consequently, this should result also in 30 times faster (dis-)charging processes. Dynamic characterization in Fig. 3.25(a,b) confirms this well: All transient $C(t)$ curves are shifted horizontally to smaller times. Quantification in Fig. 3.25(d,e) confirms $\tau \propto e^{aT}$ for both, S_{10} and S_{70} , with τ being roughly 30 times smaller in S_{70} . We speculate that the higher conductivity in DBs in S_{70} results from the smaller distances between neighboring carbon acceptors, leading e.g. to higher tunneling rate.

3.4.2 Moderately carbon-doped GaN:C ($[C] \leq 10^{18} \text{ cm}^{-3}$)

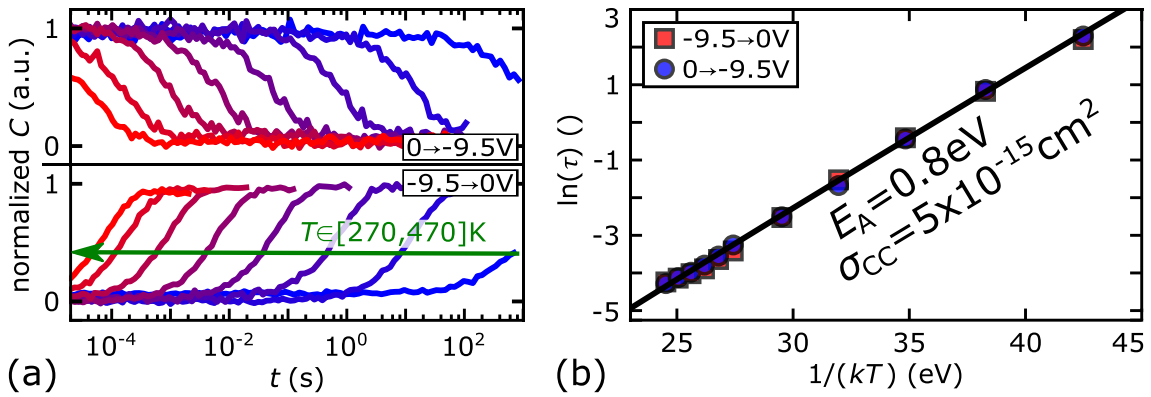


Fig. 3.26: (a) Normalized $C(t)$ after bias steps $-9.5 \rightarrow 0 \text{ V}$ and $0 \rightarrow -9.5 \text{ V}$ representing discharging and charging processes, respectively. (b) Quantification in Arrhenius-plot shows Arrhenius-like T dependence with identical time constants for both processes. Figures reused from [Kol+18a].

Fig. 3.24 demonstrates that besides similar behavior in the *depletion regime*, the *plateau regime* is missing for S_{01} . In order to find the origin of this different behavior we first analyze (dis-)charging processes in GaN:C. Fig. 3.26 shows only S_{01} -related datapoints from Fig. 3.25. The T range for dynamic characterization in S_{01} is practically limited by the (dis-)charging processes. While for $T > 470 \text{ K}$ the onset of the capacitance change starts within $30 \mu\text{s}$ after the bias step, which is below the time resolution of the used setup; for $T < 270 \text{ K}$ establishing SS requires relaxation times exceeding 10^4 s , making measurements unfeasible. Hence, the T range is limited to roughly 200 K . The Arrhenius-plot in Fig. 3.26(b) with time constants extracted from (a) reveals for S_{01} in contrast to S_{10}/S_{70} clear Arrhenius-like T dependence, indicated by the fit to a straight line in the Arrhenius-plot.

This indicates that the electrical behavior of S_{01} can be described by the conventional defect model with conduction via VB rather than by the proposed defect band model valid for $[C] \geq 10^{19} \text{ cm}^{-3}$ (see Section 3.3.3). In the conventional model, trapping time constants are in general determined by the sum of the transport time ($\tau_{\text{trans,VB}}$) and the time for negative charge capture (i.e. hole emission $\tau_{\text{em,VB}}^{\text{h}}$, Eq. (3.14)) or negative charge emission (i.e. hole capture $\tau_{\text{cap,VB}}^{\text{h}}$, Eq. (3.16)). Fig. 3.12(a) shows that charging ($0 \rightarrow -9.5 \text{ V}$) time constants are roughly identical to discharging ($-9.5 \rightarrow 0 \text{ V}$) time constants, however as we pointed out in Section 3.3.4 this information is not sufficient to distinguish whether capture/emission or transport processes dominate. In both cases τ is determined by the Boltzmann-term $\exp(-E_A/(k_B T))$ with E_A in first approximation being equivalent to the acceptor level E_{acc} [Smi78]. Fitting experimental data to the Boltzmann term delivers $E_{\text{acc}} = 0.8 \text{ eV}$ which fits well to the extracted E_{acc} of 0.7 eV

from SS analysis in Section 3.2, the 0.1 eV higher value could result from ΔE_A , see Fig. 2.16. Considering capture/emission as limiting processes, by using Eq. (3.14) for data in Fig. 3.24(b) a capture cross section σ_{CC} of $5 \times 10^{-15} \text{ cm}^2$ is extracted. As common literature values are in the range of $\sigma_{CC} = 10^{-13} \text{ cm}^2$ [Ure+15], expected capture and emission time constants are considered significantly smaller (factor 50) than the observed time constants. Although such a small cross section cannot be ruled out, we consider it more likely that the charge transport dominates in the (dis-)charging processes. For confirmation we suggest measurements as in Fig. 3.26 but for structures with different GaN:C thicknesses (d_{LUT}). If τ depends on d_{LUT} this would confirm that the transport process is the limiting factor, d_{LUT} -independent τ would indicate that capture/emission processes determine τ .

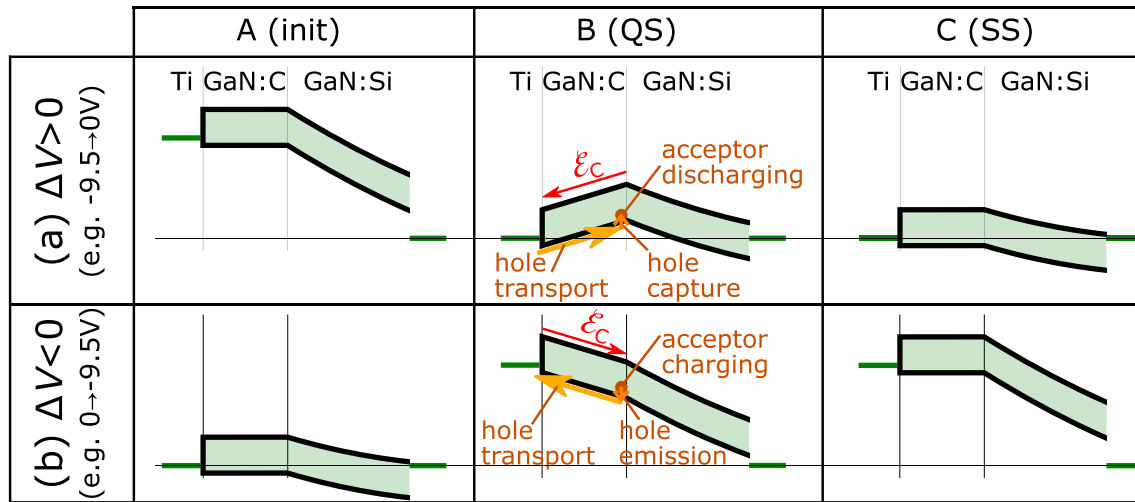


Fig. 3.27: Schematic band diagrams for bias steps with (a) $\Delta V > 0$ and (b) $\Delta V < 0$ within depletion regime at different points in time: (A) initial SS condition before bias step, (B) directly ($\approx 30 \mu\text{s}$) after bias step in quasistatic state, before charge redistribution occurs in GaN:C and (C) in SS. Orange arrows indicate the hole transport through GaN:C.

Fig. 3.27 shows schematically the entire discharging (a) and charging (b) processes on basis of the bias steps $-9.5 \rightarrow 0 \text{ V}$ and $0 \rightarrow -9.5 \text{ V}$. In (a) after the quiescent bias of -9.5 V in column A the bias is decreased to zero. In column B in the quasistatic state directly ($30 \mu\text{s}$) after the bias step the charge distribution in GaN:C has not changed yet, resulting in the increased potential at the GaN:Si/GaN:C interface. With increasing time the electric field in GaN:C leads to hole injection from the top electrode to the GaN:C VB, whereby the Schottky barrier can be considered leaky enough not to build a barrier that prevents hole injection, see Section 3.2.2. Subsequently, holes are transported via VB to the region next to the interface to GaN:Si, where they are captured by carbon acceptors, i.e. acceptors are discharged. This decreases the negative charge in GaN:C and decreases \mathcal{E}_C until SS is established in column C.

For charging processes in Fig. 3.27(b) after a rise of the bias from zero to -9.5 V , in the quasistatic state, \mathcal{E}_C with opposite polarity compared to (a) forms. This leads to emission of holes from carbon acceptors to VB, i.e. charging of acceptors. Holes then propagate via VB through GaN:C to the top electrode, whereby again the leaky Schottky barrier does not provide major resistance and flatband is established in SS.

An aspect we did not discuss yet is the injection mechanism from the top electrode to the GaN:C VB for the discharging process. Even if the Schottky barrier can be neglected, holes have to overcome a potential barrier of 0.8 eV with a time constant τ_{Schottky} . For thermionic emission this results in an Arrhenius-like process analogous to $\tau_{\text{em,VB}}^h$ (Eq. (3.13)). Consequently, the discharging process includes another Boltzmann-term from hole emission at the contact ($\tau_{\text{disch.}} = \tau_{\text{Schottky}} + \tau_{\text{trans,VB}} + \tau_{\text{cap,VB}}^h$). The charging process on the other hand is not affected ($\tau_{\text{charge}} = \tau_{\text{em,VB}}^h + \tau_{\text{trans,VB}}$). As discharging and charging show same time constants we consider τ_{Schottky} negligible.

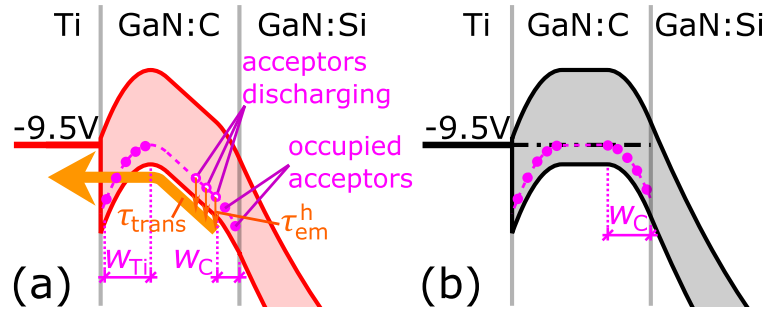


Fig. 3.28: Estimated band diagrams after bias step with $\Delta V > 0$ in (a) quasistatic state and (b) SS, considering an effective acceptor concentration $N_{\text{acc}}^* = 5 \times 10^{17} \text{ cm}^{-3}$. The finite carbon concentration leads to non-negligible space charge regions with finite widths next to top metal (w_{Ti}) and w_{C} next to the GaN:Si/GaN:C interface. Orange arrows illustrate the acceptor discharging process, leading to SS. Figures reused from [Kol+18a].

Another aspect we did not cover yet is band bending in S_{01} due to finite carbon concentration. For the sake of simplicity we have yet considered for the potential distribution that all negative charges accumulate directly at the GaN:Si/GaN:C interface and no Schottky barrier. As explained in Section 3.2 for $[C] = 10^{19} \text{ cm}^{-3}$ in S_{10} the widths in which carbon acceptors are occupied (i.e. space charge regions), are only in the range of few nm so that they can be neglected. However, in S_{01} due to its ten times smaller $[C]$ space charge region widths are ten times larger. Fig. 3.28 demonstrates the consequences for band diagrams after a bias step from 0 to -9.5 V in quasistatic state directly after the step (a) and in SS (b); but in contrast to Fig. 3.27 we consider $N_{\text{don}} = 2.5 \times 10^{17} \text{ cm}^{-3}$ and $N_{\text{acc}} = 7.5 \times 10^{17} \text{ cm}^{-3}$, resulting in $N_{\text{acc}}^* = 5 \times 10^{17} \text{ cm}^{-3}$. In GaN:C next to the top electrode and next to its interface to GaN:Si space charge regions with non-negligible widths (w_{Ti} and w_{C} , respectively) in the range of tens of nm form. This decreases the effective thickness of GaN:C with E_{F} pinned at E_{acc} , but as long as both space charge regions do not get close to joining, we expect minor effects.

Although we have evidence that in contrast to S_{10}/S_{70} with charge transport via DBs, in S_{01} charge transport occurs via VB instead. However, this does not deliver an explanation why the *plateau regime* does not exist in S_{01} , i.e. why no potential barrier rises at the GaN:Si/GaN:C interface due to electron capture in carbon acceptors. In theory, for $V > 1.5 \text{ V}$ we would expect behavior analogous to S_{10}/S_{70} as shown in Fig. 3.14 but instead of charge transport in GaN:C via DBs, the transport should occur via VB. Due to the high current we consider in the *Ohmic regime* conduction by electrons via CB, see also Section 3.5. This requires that the quasi- E_{F} for electrons moves up towards conduction band, which further requires high acceptor occupation rates. High acceptor occupation rates on the other hand raise a GaN:Si/GaN:C interface barrier, preventing major electron injection. Hence, it seems plausible that with a too low acceptor concentration

this interface barrier cannot form, explaining the absence of the *plateau regime* in S_{01} . Currently, we can only speculate about the exact reason for this interface barrier formation, also if DBs are required or not. We only have the empiric finding that if $[C]$ is sufficiently high to create DBs, structures establish the interface barrier and prevent major leakage current.

Transient behavior on longer time scale

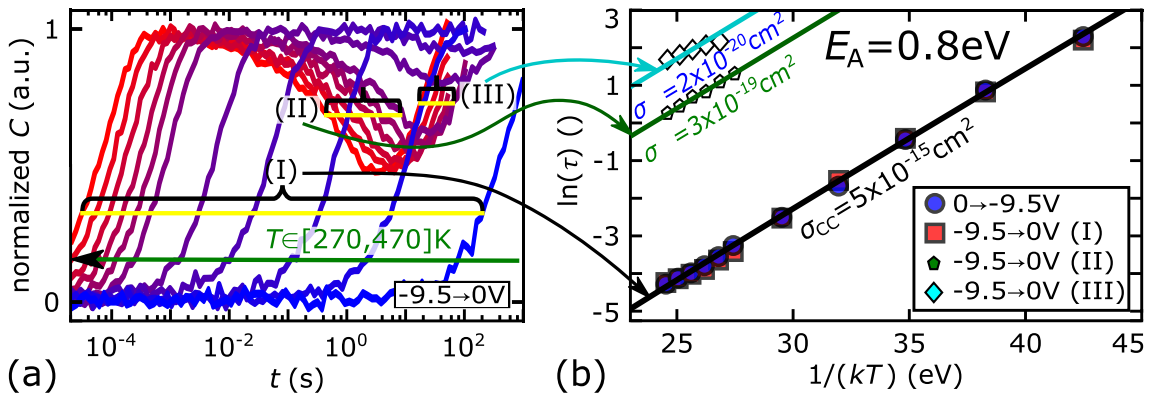


Fig. 3.29: Normalized $C(t)$ after bias step $-9.5 \rightarrow 0$ V reveal multiple capacitance rises/drops, all with same activation energies E_A but different prefactor.

To keep discussion simple, in Fig. 3.26(a) we showed only the part of the $C(t)$ curve with the major capacitance change. However, for the bias step from 0 to -9.5 V the full transient curves reveal more complex behavior as shown in Fig. 3.29. After the large capacitance increase for times roughly five orders of magnitude later C decreases slightly and increases again another order of magnitude later. Due to the large time constants of these additional features, they can be analyzed only at high T . Fig. 3.29(b) shows an Arrhenius-plot with extracted time constants of the falling (II) and second rising capacitance (III) together with the main capacitance rise (I). This reveals that all processes show Arrhenius-like temperature dependence and same E_A , the only difference is that curves for processes II and III are shifted vertically by roughly five and six orders of magnitude. Same E_A suggest that they are also related to charge transport in VB. E.g. (II) and/or (III) could be related to lateral charge transport, while (I) is related to vertical transport. This would fit to CTS measurements published in [Cha+17; Kar+16] showing transient $R_{ds,on}$ with two rising edges separated by several orders of magnitude in time but with same extracted E_A , which were also considered to originate from vertical and lateral conduction.

3.4.3 Synthesis of carbon doping effects in GaN:C layers

Our results show that DBs form in GaN:C only above a critical carbon concentration (N_{crit}) between 10^{18} cm^{-3} and 10^{19} cm^{-3} . Although DBs are additional conductive channels we assume that they are the reason why highly carbon-doped GaN:C layers can establish potential barriers at the interface to adjacent layers that prevent injection of electrons to GaN:C conduction band. We further assume that this behavior can be extended to the valence band, i.e. instead of injection of holes to VB and hole conduction via VB, a potential barrier would establish, preventing this. Instead of negative charge accumulation by occupied acceptors, positive charge accumulation can be

established by unoccupied (neutral) acceptors and occupied (positively charged) donors [Ure+17], leading to net positive space charge as demonstrated in Fig. 3.30. Electrical characterization under illumination in Section 3.6.1 (Fig. 3.58) demonstrate that positive charge accumulation is in general possible in GaN:C. As HEMT buffers should be as insulating as possible, such a behavior is desired. On the other hand the establishment of such potential barriers requires accumulation of charges, either injected charges from the electrode or only charge redistribution within GaN:C. While the establishment of such barriers are very fast in case of current flow, recovery can require long times, which can lead to dynamic effects such as dynamic $R_{ds,on}$, current collapse or threshold voltage shifts. Furthermore, if in *ac* devices charges have to flow through highly resistive defect bands within every switching cycle, this could result in severe switching losses. However, for high-frequency applications charge distribution might not follow the fast *ac* signal. Currently, too little is known in order to predict the behavior in complex application-relevant products. More details on the interaction of GaN:C with other layers or within multilayer structures are given in Section 4.

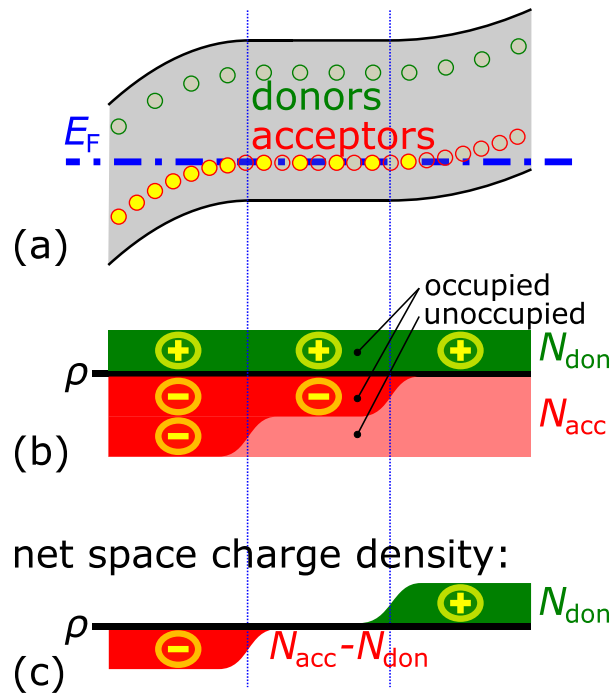


Fig. 3.30: (a) Band diagram, (b) occupation factor and (c) net space charge density density for cases when E_F is above E_{acc} , at E_{acc} and below E_{acc} , establishing respectively negative, zero and positive net space charge. N_{acc} is considered $2 \times N_{don}$.

Considering that the insulating properties of GaN:C featuring defect bands are desired, this requires not only high carbon doping but assuming that defect bands form at threading dislocations (see Section 3.3.3) also a certain dislocation density. We mention this explicitly as currently great effort is spent on reduction of dislocation density, which is supposed to reduce leakage current. Instead, it might even be detrimental if defect bands vanish.

For choosing the optimum carbon concentration one has to consider that $[C]$ should be larger than N_{crit} , however for concentrations beyond, the leakage current increases again. This fits well to experiments from Huber et al. [Hub+16], who found that the breakdown voltage of HEMTs increases with $[C]$ but saturates for values above roughly 10^{19} cm^{-3} . For special cases higher $[C]$ could still be beneficial, e.g. for GaN:C layers thinner than few tens of nm, where the regions of

occupied acceptors (w_{Ti} and w_C in Fig. 3.28) reach values in the range of the GaN:C thickness. In this case higher [C] reduces both, w_{Ti} and w_C .

3.5 Transition from "plateau" to "Ohmic regime" ("current filamentation")

The previous chapters covered *depletion* and *plateau regimes* (see Fig. 3.2), in which the electrical behavior is determined entirely by the features of the LUT. In contrast, in the *Ohmic regime* the electrical behavior is determined mainly by the impedance of the base structure. Fig. 3.2 shows that while I_{SS} in the *plateau regime* scales with the contact area, I_{SS} in the *Ohmic regime* is area-independent. Dependent on the contact area, in the abrupt transition from *plateau* to *Ohmic regime* the resistance can drop by several orders of magnitude. Although this abrupt transition looks like a breakdown, it is reversible; due to its physical nature explained later we refer to it as "current filamentation". This chapter covers the nature of this transition, which we focussed on in our recent publication in [Kol+18b].

3.5.1 Ohmic regime

In an ideal sample in *Ohmic regime* the impedance should be mainly determined by the impedance of the base structure with a resistance of R_{BS} defined by its resistivity (ρ_{BS}), its thickness (d_{BS}) and the wafer area (A_{wafer}): $R_{BS} = \rho_{BS}d_{BS}/A_{wafer}$. However, for real structures some additional points have to be considered:

1. The base structure is a complex multilayer structure consisting of many layers with various growth conditions, therefore ρ_{BS} is not homogeneous.
2. Lateral conductivity in GaN:Si is limited so that the current spreads not homogeneously over the entire wafer and for its proper description a two-dimensional model would be required.
3. Vertical leakage is probably enhanced in certain regions such as at the wafer edge or at largely extended defects, i.e. ρ_{BS} is laterally not homogeneous.

These points make it hard to judge what parameters determine R_{BS} . Comparison of I_{SS} - V measurements for different wafer fragments with the entire wafer reveals that R_{BS} can be reduced in fragments by factors up to 100. However, no clear correlation between R_{BS} and the position of the fragment in relation to the wafer, wafer size or any other parameter has been observed. Although we currently do not understand conduction through the base structure in detail, we remark that this has minor relevance for investigations on the electrical behavior of LUT structures, the main topic of this thesis. For our investigations the relevant point is that for every fragment or wafer R_{BS} is significantly lower than the resistance of the LUT (R_{LUT}) in the *depletion* and *plateau regime*. This is easily proven by the significant resistance drop between *plateau* and the *Ohmic regime*.

3.5.2 Electrostatic electrical characterization of current filamentation

Fig. 3.31(a) shows standard V -controlled I_{SS} - V characteristic for sweeping V from 0 to 12 V (up-sweep, red solid line) and vice versa from 12 to 0 V (down-sweep, blue dashed line) with a ramp

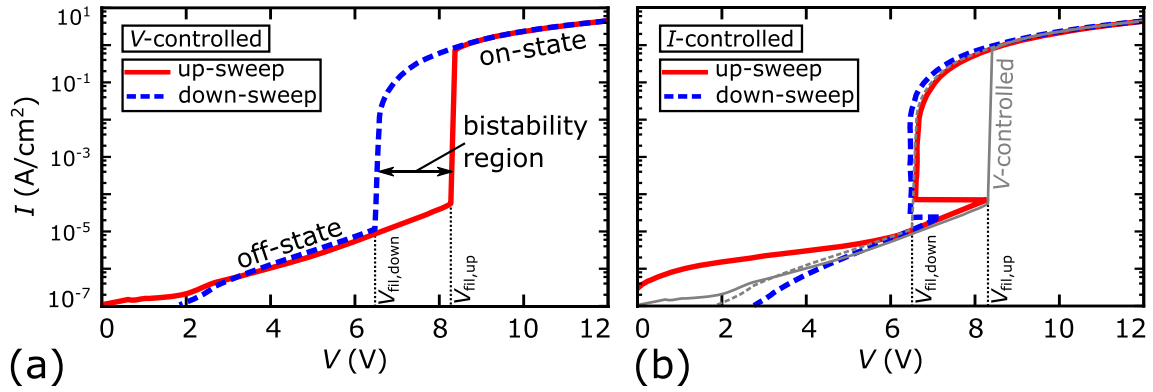


Fig. 3.31: I_{SS} - V characteristics for S_{10} in (a) voltage and (b) current controlled mode. Red and blue lines represent respective up- and down-sweeps. For comparison, in (b) voltage-controlled measurements from (a) are illustrated with light grey lines. Figures are reused from [Kol+18b].

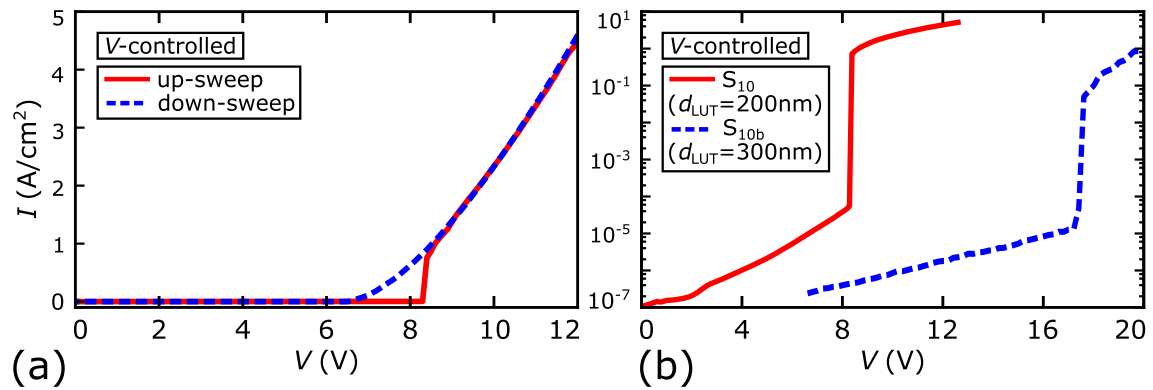


Fig. 3.32: (a) Voltage-controlled up- and down-sweep I_{SS} - V characteristics for S_{10} in linear scale. (b) I_{SS} - V characteristics for different d_{LUT} (i.e. S_{10}/S_{10b}). Figure (b) reused from [Kol+18b].

rate of 1.5 V s^{-1} . A resistance drop by several orders of magnitude accompanies the transition from *plateau* to *Ohmic regime*, which we labelled in [Kol+18b] due to the later discussed model also as off- and on-state. The bias where this transition occurs, depends significantly on the sweep direction with $V_{\text{fil,up}} \approx 8.5 \text{ V}$ and $V_{\text{fil,down}} \approx 6.5 \text{ V}$ for respective up- and down-sweeps, i.e. distinctive hysteresis behavior. The $I_{\text{SS}}-V$ characteristic in Fig. 3.32(a) with linear ordinate highlights the Ohmic behavior in *Ohmic regime* and that within *Ohmic regime* the structure's resistance is indeed dominated by the Ohmic resistance of the base structure (R_{BS}). Compared to a single Ohmic resistance, the $I_{\text{SS}}-V$ curve of the entire structure is shifted horizontally by approximately 6.5 V . This indicates a rather bias independent potential drop of 6.5 V in GaN:C within the *Ohmic regime*. The curvature between 6.5 and roughly 9 V could be a sign that in this bias range the potential drop in GaN:C still increases slightly. However, at higher biases R_{diff} saturates, indicating ideal Ohmic behavior, as shown in Fig. 3.2(d). $I_{\text{SS}}-V$ characteristics in Fig. 3.32(b) show increasing $V_{\text{fil,up}}$ with d_{LUT} .

In order to gain more knowledge on the bistability region, which we call the bias range between $V_{\text{fil,down}}$ and $V_{\text{fil,up}}$, current-controlled measurement as depicted in Fig. 3.31(b) are performed. Although they show almost identical V -controlled $I_{\text{SS}}-V$ characteristics within *plateau* and *Ohmic regime*, they reveal significantly different behavior within the bistability region. The shoulder for I -controlled up-sweeps for $V < 5 \text{ V}$ is a systematic measurement artifact of the used equipment. While V -controlled measurements already indicate in the bistability region an S-shape $I_{\text{SS}}-V$ characteristic with a negative differential resistance (NDR) region [Rid63; SS01], I -controlled measurements suggest a more complex than common S-shape characteristic. This points towards formation of spontaneous current filaments (CFs) in spatially extended homogeneous systems with S-shape I - \mathcal{E} characteristics [SS01; SMG13; VK69]. For such systems devices of various size can show different $I_{\text{SS}}-V$ characteristics, linked to homogeneous and inhomogeneous current flow, respectively, as explained in [Pog+11].

3.5.3 Emission microscopy (EMMI): Current filamentation during transition

In order to derive the distribution of the current underneath the contact, emission microscopy (EMMI) measurements are performed. As illustrated in the schematic in Fig. 3.33(a), vertical bias is applied to a LUT structure. As in forward bias electrons must be injected from GaN:Si to DBs or VB, their energy decreases in the GaN:Si/GaN:C junction area. This energy can be emitted as photon or phonon, whereby part of the emitted photons propagate through GaN:C, through the top semi-transparent metal and can then be recorded by a charge-coupled device (CCD), mounted above the sample. Hence, EMMI can measure where in the sample the current is located.

As the standard Ti contacts are optically opaque, adapted contacts with a 3 nm Ti layer and a 20 nm Au layer on top are used instead. As this might have effects on the electrical behavior, we label LUT structures with the same epitaxial stack as S_{10} but thin semi-transparent contacts in the following as $S_{10,\text{Au}}$. We further mention that for $S_{10,\text{Au}}$ small wafer fragments with areas of roughly 7 cm^2 (see Fig. 3.35) are used instead of entire wafers. Simple $I_{\text{SS}}-V$ characteristics prove that at least the static electrical behavior is identical for S_{10} and $S_{10,\text{Au}}$. Fig. 3.33(b) shows the transmissivity of the contacts (T_{metal}) as a function of the photon energy, which is throughout the entire band gap in the range of 20% . It further demonstrates that also the transmissivity of the used

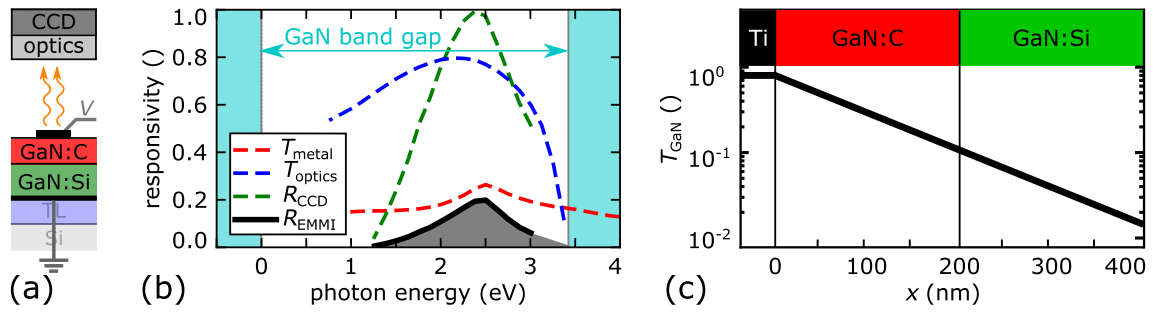


Fig. 3.33: (a) Schematic EMMI (and electro- and photoluminescence spectroscopy) setup. (b) Ratio of detected photons by CCD to emitted photons in GaN (i.e. responsivity R_{EMMI}) as function of the photon energy, the grey area under R_{EMMI} represents the measurable part of the signal. R_{EMMI} is determined by the transmissivity of the contact metals (T_{metal}), the optics (T_{optics}) and the responsivity of the CCD (R_{CCD}). (c) Transmissivity of GaN for light with energies above GaN band gap (T_{GaN}) as a function of the distance from the surface (x).

optics (T_{optics}) in order to focus emitted light on a CCD is limited. Additionally, the responsivity of the CCD (R_{CCD}) is considered, resulting in the total responsivity of the setup R_{EMMI} . A GaN monocrystal should be transparent for light with energies below band gap (< 3.4 eV). Dependent on the wavelength, doping increases the absorption, however for rough calculations within this thesis this is neglected. Fig. 3.33(c) demonstrates that the high absorption coefficient of roughly 10^5 cm^{-1} [Mut+97] leads to low transmissivity for energies above band gap. E.g. only about 13% of light emitted at the GaN:Si/GaN:C interface reaches the top of GaN:C. As R_{EMMI} is almost zero for light energies above band gap, the setup can be considered as completely blind for these light energies. Thus, light is only detected in a range between 1.5 and 3.4 eV as shown by the grey area under the black curve in Fig. 3.33(b).

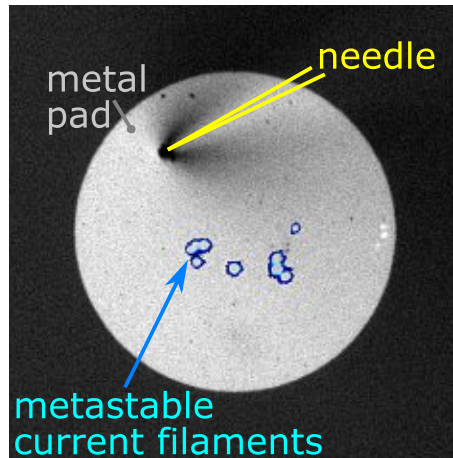


Fig. 3.34: Optical image of the top electrode, superimposed with the EMMI signal for $V = 14$ V with $I_{SS} = 10 \mu\text{A}$. Yellow lines indicate the position of the contacting needle forming a black spot, the light grey area represents the top contact and blue circles the superimposed EMMI signal.

In order to perform EMMI, first the CCD is aligned and focused on the top contact. An optical image is taken while the chamber is illuminated with white light, as illustrated in Fig. 3.34 in grey. Subsequently, EMMI is performed under dark condition and in order to localize the position of the EMMI signal in respect to the contact, this signal is in Fig. 3.34 superimposed in color to the grey

optical image. As we found that the EMMI signal originates solely from underneath the contact with no tendency to formation at the edges, we will in the following show in most cases only the EMMI signal without superimposed optical image.

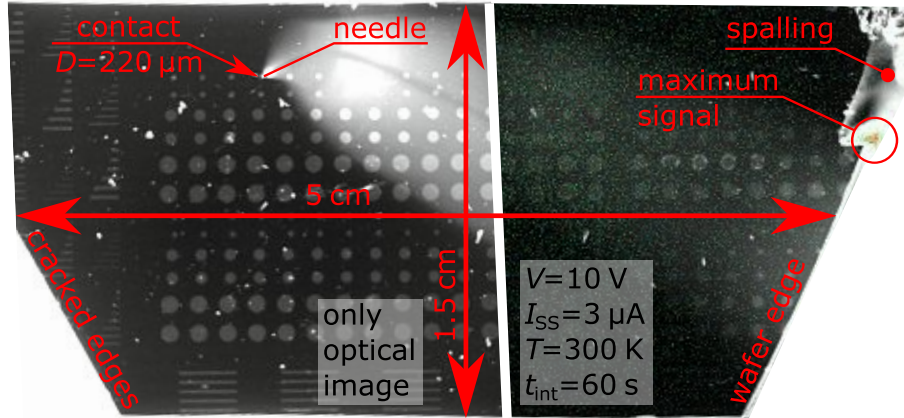


Fig. 3.35: EMMI images of parts of the used fragment with the left part unbiased, showing the contacted device and the right part when bias is applied via the needle on the left side. The EMMI spot at the spalled edge shows enhanced current flow centimeters away from the contact.

Fig. 3.35 shows part of a fragment and the used contact. The left part of the figure shows only the optical image for $V = 0$ while on the right part the EMMI signal for $V = 10$ V is overlaid. It reveals at the spalled wafer edge a significant EMMI spot, although the contacting needle is roughly 3 cm away. This provides further evidence for the existence of a laterally conductive layer, likely to be GaN:Si. It indicates that current does not propagate homogeneously through the base structure but can propagate in localized spots such as the wafer edge, proving the concept of the LUT structures described in Section 3.1.3.

Fig. 3.36 demonstrates the evolution of the EMMI signal with increasing bias. At room temperature in the entire off-state region no EMMI signal is found, a possibly existing signal is below the signal-to-noise ratio. In order to increase the EMMI signal we perform measurements at elevated temperatures with long integration times (t_{int}) and indeed above approximately 400 K the signal exceeds the noise. EMMI measurements in Fig. 3.36(a) at 475 K clearly reveal an increased EMMI signal, uniformly distributed under the entire contact area, marked by the black dotted line. This indicates homogeneous light emission under the contact and consequently homogeneous charge distribution in off-state, at least in the μm range. For voltages exceeding $V_{\text{fil,up}}$, i.e. on-state, the homogeneous distributed EMMI signal is replaced by distinct emission spots, which increase in general in number and size with V and/or I_{SS} . These emission spots correspond to localized current filaments (CFs). Figs. 3.36(b-f) demonstrate the increasing spot size from diameters of 1 – 2 μm at 9 V to roughly 10 μm at 20 V. We remark that although Fig. 3.36 shows only a single CF, this behavior is rather rare as in general CFs are unstable and split after certain times.

In order to investigate the stability of CFs over time, EMMI videos with a time resolution of 100 ms are recorded. Fig. 3.37 shows frames of the video at chosen points in time within such a video. It illustrates movements, splits and merges of CFs at constant $V = 10$ V and $I_{\text{SS}} = 3$ μA over time. While in (a) directly after switching to on-state ($t = 0$) only one CF exists, it splits within the first 2 s into two CFs of comparable size but with sizes being smaller than the first one (Fig. 3.37(b)). In (c) after 3 s the second CF has moved left while the first, indicated as "CF1" stays

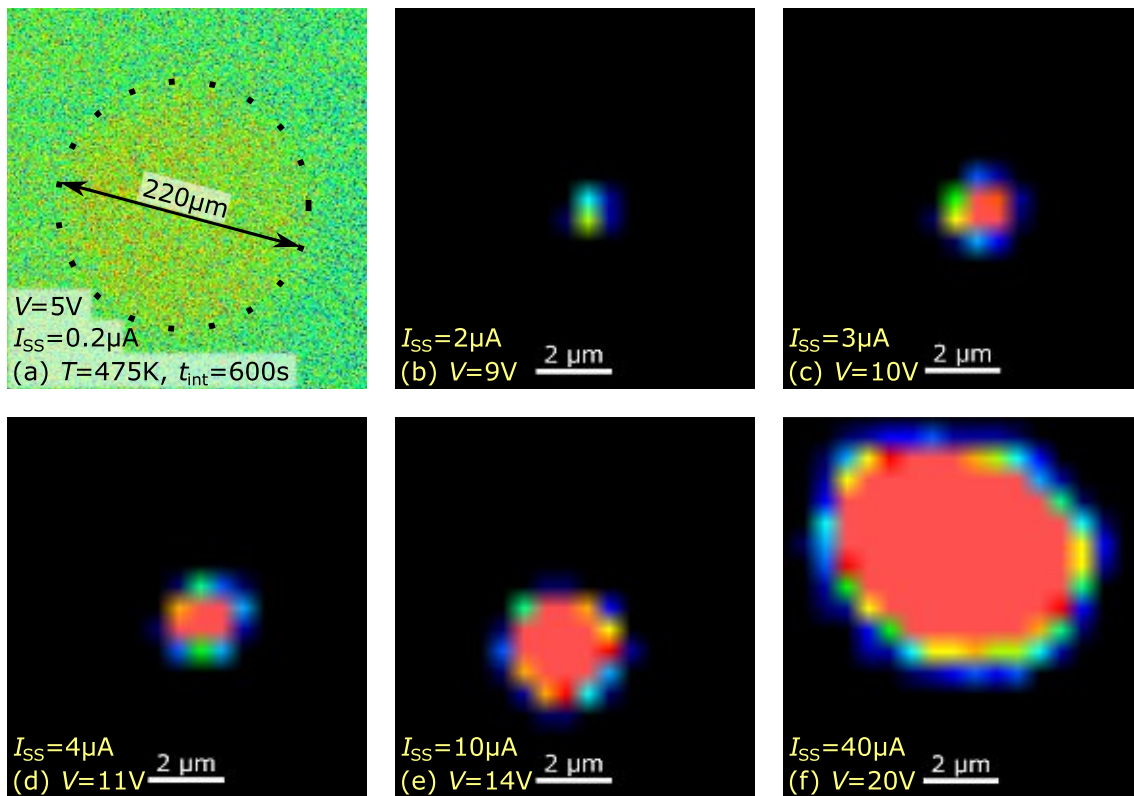


Fig. 3.36: (a) EMMI image in off-state at $T = 475\text{ K}$ with an integration time $t_{\text{int}} = 600\text{ s}$. The location of the electrode is indicated by a black dotted line at its perimeter. (b-f) EMMI images in on-state at room temperature with $t_{\text{int}} = 1\text{ s}$ and different V as labeled in the figures. For better visibility (b-f) show only $10\text{ }\mu\text{m} \times 10\text{ }\mu\text{m}$ excerpts of the contact area, in outer regions no significant EMMI signal is found. Figures reused from [Kol+18b].

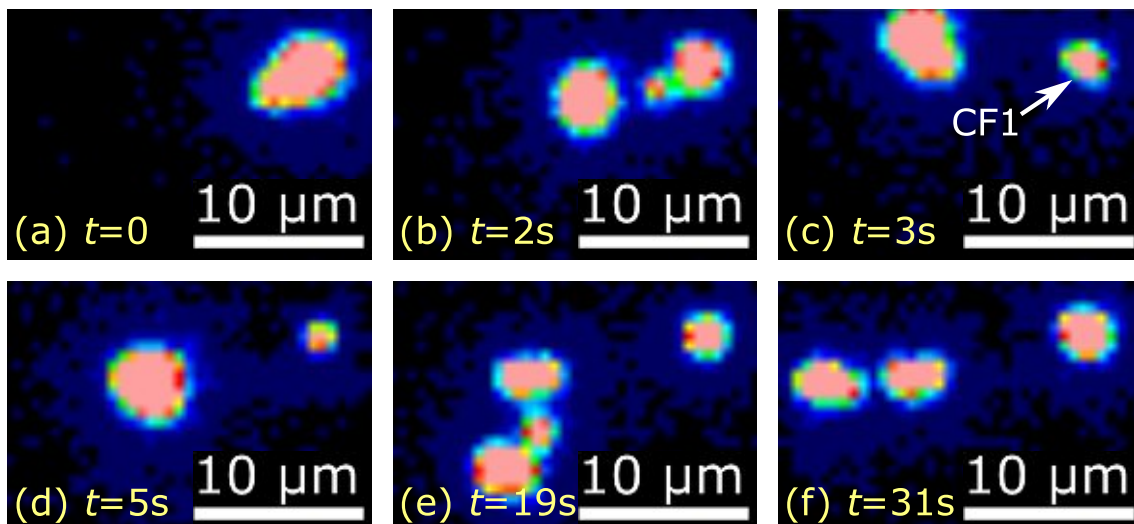


Fig. 3.37: Frames of an EMMI video at six chosen moments in time for $V = 10\text{ V}$ with $I_{\text{SS}} = 3\text{ }\mu\text{A}$ demonstrate current filament splitting, moving and merging. For better visibility only $22\text{ }\mu\text{m} \times 15\text{ }\mu\text{m}$ excerpts, including the only apparent EMMI spots, are shown. "CF1" in (c) marks a pinned filament. Figures reused from [Kol+18b].

pinned to its original position. In Fig. 3.37(d) after 5 s the second CF has moved further away from CF1 and its intensity exceeds the one from CF1, indicating current redistribution between both filaments. These CFs are pinned for a rather long time until shortly before $t = 19$ s the second CF splits again so that in Fig. 3.37(e) at $t = 19$ s three smaller CFs exist. Between $t = 19$ s and $t = 31$ s in (f) the two left CFs merged and split again into two CFs. In conclusion, Fig. 3.37 points out that CFs can be pinned more or less stable at certain positions, however they usually split and move to different positions. After switching to off- and back to on-state, even with times of a fraction of a second in off-state, CFs form in general at different positions. The videos further reveal that CFs do not move continuously but rather jump between metastable spots with distances in the μm -range within time intervals smaller than the time resolution of 100 ms. The empiric findings suggest that there is a maximum stable size of CFs, while their number can fluctuate. In contrast to the special case of a single CF shown in Fig. 3.36, in most cases at higher biases the number of CFs increases, as shown in Fig. 3.38.

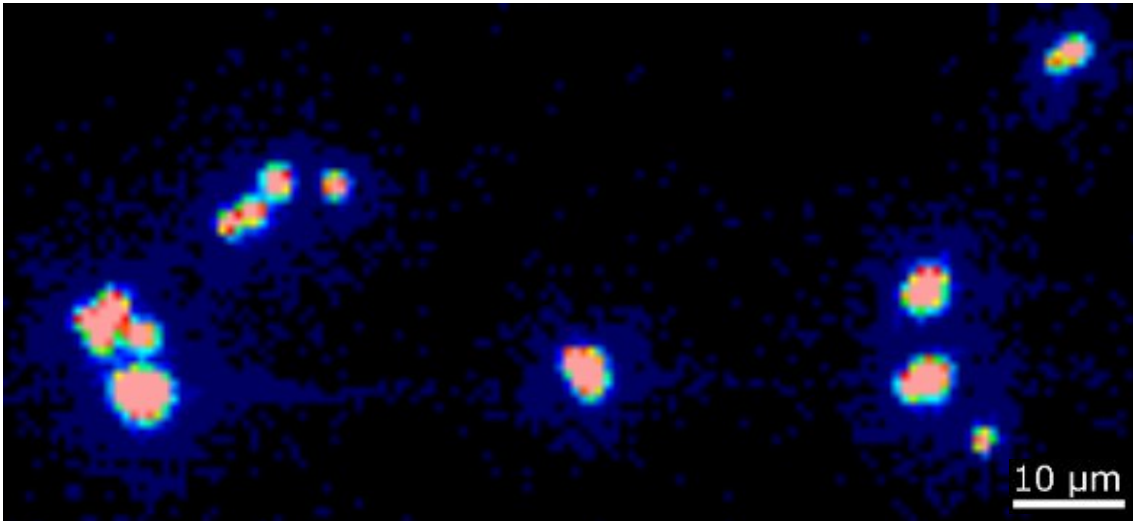


Fig. 3.38: An EMMI image recorded at $V = 14$ V and $I_{SS} = 10$ μA demonstrates the existence of multiple current filaments. Figure reused from [Kol+18b].

3.5.4 Luminescence spectroscopy

As introduced in Section 2.2.2, defects do not only influence the electrical behavior of semiconductors but also their optical properties. The emitted light of a biased sample as in EMMI or after its illumination as in photoluminescence spectroscopy (PL) contains information on the defects in the sample. Spectral analysis of the emitted light enables detection of the defect energy within the band gap. In the following we discuss spectrally resolved EMMI (further referred to as electroluminescence spectroscopy (EL)) and PL on LUT structures $S_{10,Au}$.

Electroluminescence spectroscopy (EL)

Fig. 3.39 shows a schematic of the used setup for EL and PL. For EL a top bias of 10 V is applied, which results in on-state behavior and light emission from CFs. In contrast to standard EMMI analysis, a rectangular aperture with a grating with 500 lines/mm is inserted into the optical path. The sample is positioned in such way that a thin stripe with one EMMI-spot is visible as indicated

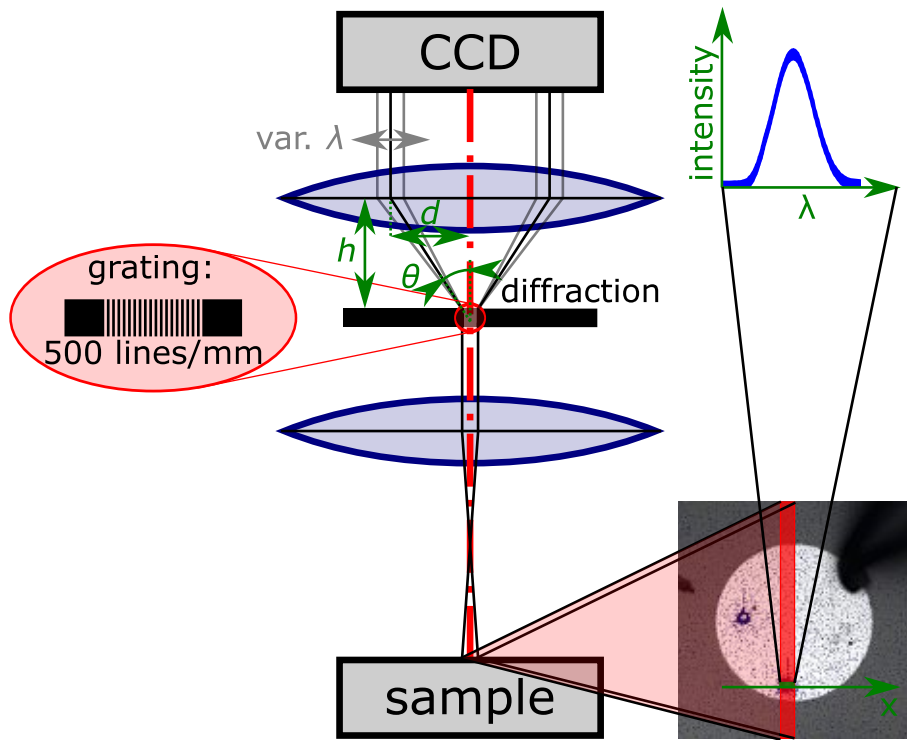


Fig. 3.39: Schematic setup for electroluminescence and photoluminescence spectroscopy (EL and PL).

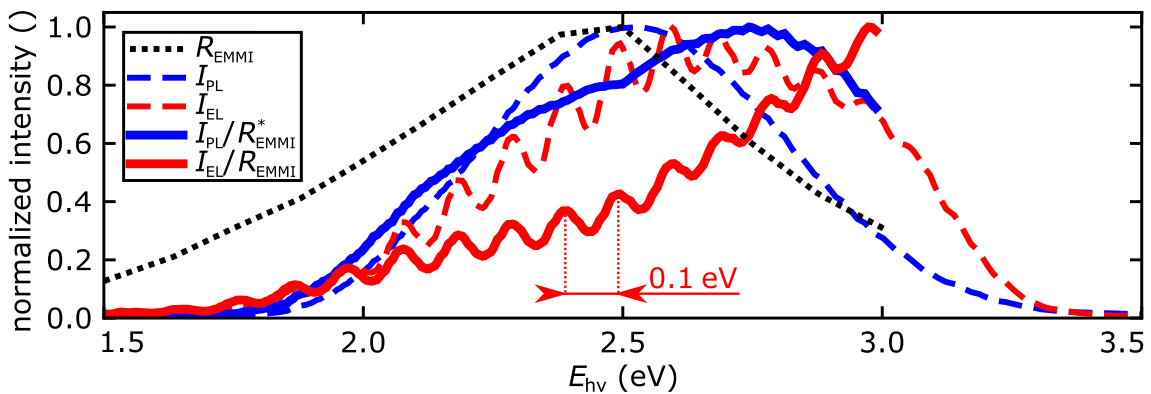


Fig. 3.40: Normalized spectra (I_{PL} , I_{EL}) and corrected spectra (I_{PL}/R_{EMMI}^* , I_{EL}/R_{EMMI}) for EL and PL, respectively. R_{EMMI} considers the wavelength-dependent responsivity of the optical setup, whereby it has to be considered that as for PL no metal contact is required, so that $R_{EMMI}^* = R_{EMMI}/T_{metal}$. The "ringing" signal in EL is assumed to result from interference due to reflections at bottom (and top) interfaces of the GaN stack.

in the bottom right EMMI figure in Fig. 3.39. It is crucial to find a CF which is pinned for sufficiently long times at the same position to align the setup and perform the measurement. The grating diffracts then emitted light of the CF, whereby the diffraction distance (d) depends on the wavelength of the emitted light (λ) and can be derived by Bragg's law:

$$2d \sin(\theta) = n_0 \lambda, \quad (3.22)$$

with $d \sin(\theta) = \sqrt{d^2 + h^2}$, n_0 being an arbitrary positive integer and d , h and θ as indicated in Fig. 3.39. The schematic demonstrates that the emitted light from the CF is diffracted only in x -direction perpendicular to the long side of the slit. Using Bragg's law, d can directly be translated into the wavelength, i.e. photon energy ($E_{h\nu} = hc/\lambda$) of the emitted light. The result is a spectrum with the intensity (I_{EL}) vs. $E_{h\nu}$ as shown in Fig. 3.40 by the dashed red line. In order to correct the measured intensity for the wavelength-dependent responsivity of the EMMI setup (R_{EMMI}), I_{EL} is divided by R_{EMMI} , giving the red solid line.

Photoluminescence spectroscopy

Instead of applying bias as in EL, for PL the setup is extended by a custom-built ring of light emitting diodes (LEDs) with a wavelength of 325 nm (i.e. photon energy $E_{\text{LED}} = 3.8$ eV), which irradiate the sample. As the photon energy is larger than the GaN band gap, this creates electron-hole pairs and possibly also leads to electron emission from carbon acceptors. After illumination, LEDs are turned off, so that electron-hole pairs recombine again, either by direct recombination or by defect-assisted recombination. For the latter process holes from VB and electrons from CB are captured in carbon acceptors and thereby emit photons with energies $E_{\text{acc}} - E_{\text{VB}} = 2.7$ eV and $E_{\text{don}} - E_{\text{CB}} = 0.7$ eV, respectively. As explained in the next section due to Franck-Condon shift [Con28] actually emitted photons have energies with values roughly 0.5 eV lower. Anyway, due to the wavelength-limitation of the used setup, only electron capture can be detected. Part of the emitted photons leave the sample and are detected by the identical optical setup, used for EL. As E_{LED} exceeds E_{bg} , the low transmissivity of GaN has to be considered as shown in Fig. 3.33(c). Therefore, about 87% of all photons are already absorbed in the top GaN:C layer. The resulting normalized spectrum is shown by blue lines in Fig. 3.40.

Interpretation of spectroscopy results

For interpretation of the derived spectra it is crucial to consider that $E_{h\nu}$ does not directly relate to the defect ionization energy $E_{\text{A}}^{\text{ion}}$. Fig. 3.41 demonstrates this in a schematic configuration coordinate diagram. As e.g. carbon acceptors can slightly change their position within the GaN crystal when becoming negatively charged, the minima of neutral and negatively charged states in the configuration coordinate diagram are horizontally shifted. While for thermal ionization the energy difference between their minima is $E_{\text{th}} = E_{\text{CB}} - E_{\text{acc}} = 2.7$ eV, for photon-induced electron capture an additional energy has to be overcome. This additional energy is commonly referred to as Franck-Condon shift ($d_{\text{FC},2}$) and values for carbon defects in GaN:C of about 0.5 eV are reported [Arm06; MB17], leading to optical excitation energies (E_{opt}) of roughly 3.2 eV. For the opposite process (i.e. electron capture), emitted photons have energies which are reduced by the Franck-Condon shift $d_{\text{FC},1}$, which has similar values as $d_{\text{FC},2}$ [Arm06; MB17]. Resulting photon

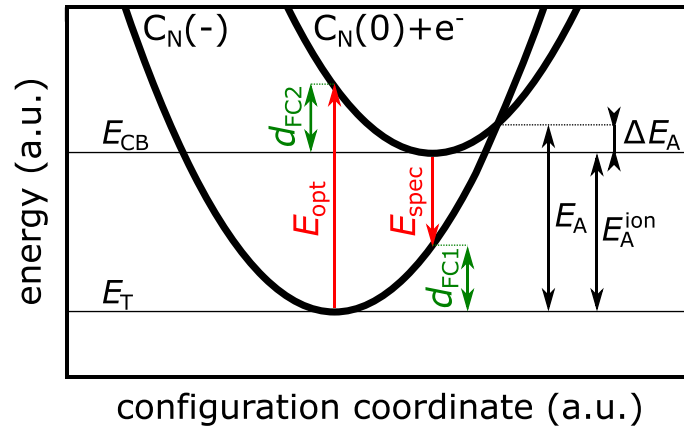


Fig. 3.41: Schematic configuration coordinate diagram comparing the capture and emission energies for thermal (E_A) and optical (E_{opt} , E_{spec}) transitions between negatively charged and neutral acceptor charge states ($C_N(-)$, $C_N(0)$). E_{opt} and E_{spec} are shifted compared to E_{th} by the Franck-Condon shifts $d_{FC,1}$ and $d_{FC,2}$, respectively.

emission energies (E_{spec}) are in the range of 2.2 eV, which would fit to "yellow luminescence", see Fig. 2.18. As both EL and PL analyze photon emission, $d_{FC,1}$ has to be considered.

In this perspective, the derived corrected spectra from PL and EMMI in Fig. 3.40 are rather surprising. Instead of a peak at 2.2 eV, the PL spectrum reveals a peak at roughly 2.7 eV, while the intensity in EL increases steadily with energy without a peak. In the following we discuss several factors that might contribute to understanding these observation:

- First of all, we have to mention that the experimental setup has been in a development stage and therefore systematic errors cannot be excluded. The limited availability of the setup prevented deeper investigations resulting in more reliable data, for the sake of completeness data is shown but has to be treated with caution.
- Although it seems unlikely due to the large carbon defect densities, the intensity from band-to-band recombination could exceed the intensity from defect-assisted recombination via carbon defects so significantly that the observed spectra show only the tail of the band-to-band process, especially for EL.
- Fig. 3.42 demonstrates that in forward bias the energy of the emitted light (E_{spec}) might differ significantly from the classical E_{spec} , derived from the configuration coordinate diagram in Fig. 3.41. If the potential barrier built by depleted GaN:Si is overcome not by a thermal process, as indicated by the T dependence of I_{SS} (see Fig. 3.19), but by e.g. by trap-assisted-tunneling [VCB79], then E_{spec} could decrease by $q \times \varphi_i$. Furthermore, if electrons are not captured directly at the GaN:Si/GaN:C interface but deeper in GaN:C, the electric field causes E_{spec} to increase. This might result in a smeared out spectrum without clear peak as observed in Fig. 3.40.
- The EL spectrum in Fig. 3.40 shows distinct "ringing" signal with equidistant peaks and valleys with an energetic distance $\Delta E_{int} = 0.1$ eV. We suppose that its origin is that light is emitted in the GaN:Si/GaN:C vicinity, but not only towards the metal contact but in all directions. Part of the light dissipates into the GaN stack and is then reflected at its interface to Si as the refractive index of GaN for energies between 1.5 and 3 eV is with $n_{GaN} \approx 2.4$ [BI73]

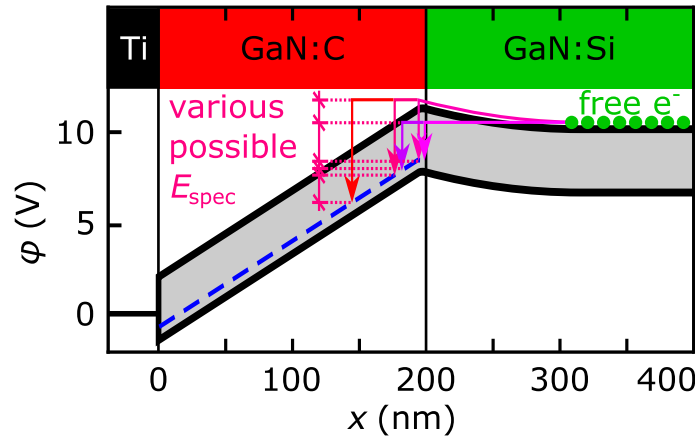


Fig. 3.42: Schematic band diagram of S_{10} for $V = 10$ V showing that the energy of the emitted light (E_{spec}) might differ from classically expected values in Fig. 3.41.

significantly lower than of Si with 4.1 [AS83]. The reflected and the directly towards the metal dissipated beam interfere and when their phase shift is $2n\pi$ constructive interference occurs, while for $(2n + 1)\pi$ destructive interference occurs, with n being any positive integer. The thickness for the GaN stack d_{stack} can then be calculated by $d_{\text{stack}} = (hc)/(2\Delta E_{\text{int}}n_{\text{GaN}}) = 2.6 \mu\text{m}$. The value is indeed in the range of the nominal stack thickness, suggesting that light is emitted at the GaN:Si/GaN:C interface. Interference effects, resulting in ringing is known in literature and described e.g. in [Bra+16].

- In PL there is no external bias applied and therefore there is flatband in GaN:C, which simplifies interpretation. As the photon energy of the irradiating LEDs exceeds the GaN band gap, 87% of the photons are absorbed in GaN:C and do not reach GaN:Si. Considering that in GaN:Si the major part of emitted photons have energies above band gap, also 87% of the emitted photons from GaN:Si are absorbed in GaN:C. Therefore, signal from GaN:Si is completely neglected. Emitted light originates mainly from bulk GaN:C, directly related to capture of free electrons in carbon acceptors. This might lead to the clearer peak at 2.7 eV. However, to explain the peak energy either a very shallow acceptor level or a negligible small $d_{\text{FC},1}$ has to be considered. While a shallow acceptor can be excluded from electrical characterization, a negligible $d_{\text{FC},1}$ could be related to the formation of the defect band, which is yet not understood.

3.5.5 Time dependence of filamentation

In Section 3.5.2 we discussed the electrical behavior of filamentation by slow $I_{\text{SS}}-V$ measurements but we did not discuss its time dependence yet. In general, $V_{\text{fil,up}}$ is not fixed but depends for $I_{\text{SS}}-V$ sweeps significantly on the ramp rate. A better way to characterize the time dependence of $V_{\text{fil,up}}$ is to do bias steps from unstressed condition (i.e. $V = 0$) to V within the bistability regime, i.e. $V_{\text{fil,down}} > V > V_{\text{fil,up}}$. Fig. 3.43(a) shows that filamentation event, corresponding to the transition from off- to on-state, occurs only after a certain time (t_{fil}). t_{fil} decreases significantly with V , whereby Fig. 3.43(b) demonstrates for $V = 9.5$ V large statistical distribution over several orders of magnitude. More detailed statistical assessment is provided in Fig. 3.44(a), showing 100 consecutive bias steps from 0 to 9.5 V. Quantitative analysis in (b) shows very broad time

distribution of t_{fil} over the measurable time range between 20 ms and 100 s. Additionally, after 20 ms in 35 % of the measurements the device is already in on-state and after 100 s in 15 % the device is still in off-state. This means that in only 50 % of measurements the filamentation event occurs between 20 ms and 100 s. One could even put the data in a Weibull plot, as commonly used for characterization of e.g. time-dependent dielectric breakdown [McP10], which even gives a good fit. The extracted β value of 0.17 is very low, however meaningful interpretation of the statistical distribution would require further investigations. The main information from the time-dependent measurements are the large statistical distribution of t_{fil} and that its value decreases with V .

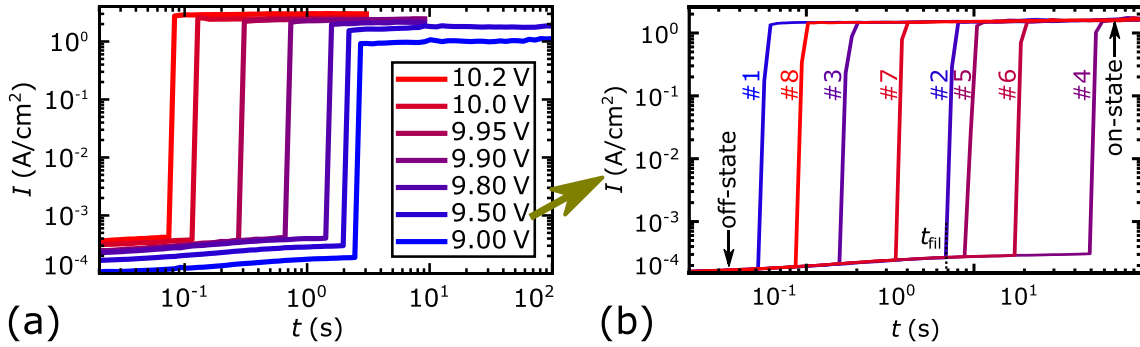


Fig. 3.43: (a) Transient $I(t)$ measurements after bias steps from 0 to various V and (b) several consecutive measurements for steps to $V = 9.5$ V, indicating statistical distribution of time-to-filamentation (t_{fil}). Stress times in (b) are 100 s with 10 s recovery time between measurements, numbers indicate the sweep number. Figure (b) reused from [Kol+18b].

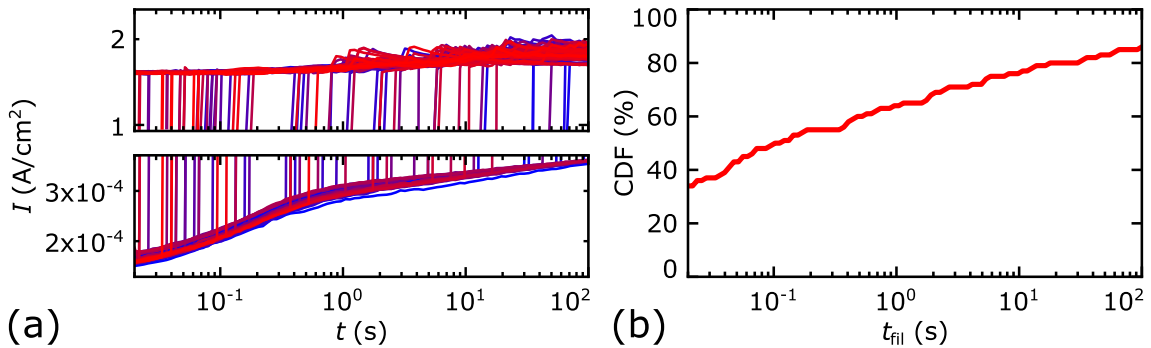


Fig. 3.44: (a) 100 consecutive bias steps from 0 to 9.5 V with stress times of 100 s and recovery times of 10 s, scales for I are logarithmic. (b) Cumulative distribution function (CDF) for devices in on-state vs. t_{fil} .

3.5.6 Statistical distribution of filamentation voltage

In the previous section we found that t_{fil} decreases with V in the bistability region. This means that $V_{\text{fil,up}}$ should decrease with slower ramp rates, which is indeed experimentally confirmed. However, the large statistical distribution in t_{fil} should also result in large statistical distribution of $V_{\text{fil,up}}$. As V_{fil} (i.e. $V_{\text{fil,up}}$ and $V_{\text{fil,down}}$) shows besides this intrinsic statistical distribution large dependences on the position on the wafer (wafer center vs. wafer edge), stress history, temperature and large device-to-device variation, these parameters cannot be treated separately. E.g. if $V_{\text{fil,up}}$ depends significantly on the position of the wafer, statistical analysis of $V_{\text{fil,up}}$ for 100 devices from

different regions of the wafer would not give the intrinsic statistical distribution. In the following we will discuss these influences in more detail.

V_{fil} as function of the stress history

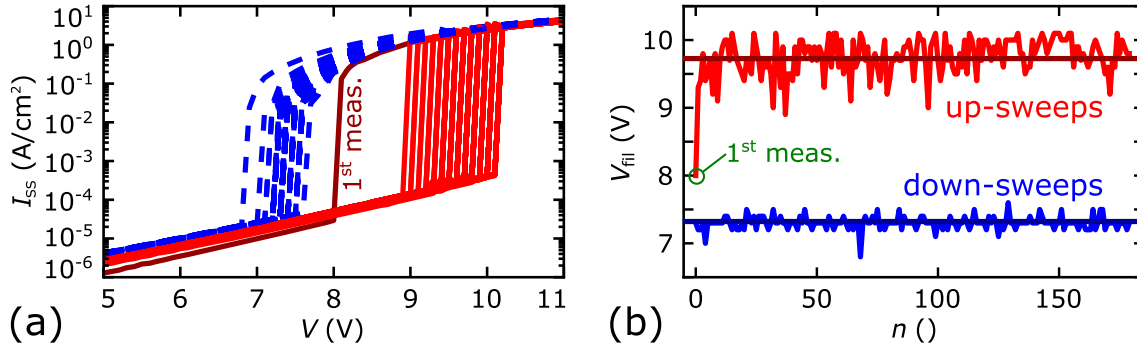


Fig. 3.45: (a) $I_{\text{SS}}-V$ characteristics (up- and down-sweeps) of 180 consecutive measurements on a single device with a ramp rate of 1.5 V s^{-1} at 300 K. (b) Evolution of $V_{\text{fil,up}}$ and $V_{\text{fil,down}}$ with number of up-/down-cycles (n).

Fig. 3.45(a) shows $I_{\text{SS}}-V$ characteristics of 180 consecutive up- and down-sweeps, (b) shows the evolution of $V_{\text{fil,up}}$ and $V_{\text{fil,down}}$ with number of measurement cycles. While for a virgin device $V_{\text{fil,up}}$ is significantly lower, after the first measurement the value fluctuates strongly. While $V_{\text{fil,down}}$ is independent of the recovery time between up- and down-cycles, $V_{\text{fil,up}}$ decreases with increasing recovery time between measurement cycles. E.g. at 300 K after approximately two day recovery, $V_{\text{fil,up}}$ reaches again values comparable to a virgin device. As expected due to the large distribution in t_{fil} , $V_{\text{fil,up}}$ also shows large statistical distribution for consecutive measurements with values roughly between 9 and 10.2 V. Interestingly also $V_{\text{fil,down}}$ shows a certain distribution, however much smaller than for $V_{\text{fil,up}}$.

V_{fil} as function of the device position on the wafer

Fig. 3.46(a) shows $I_{\text{SS}}-V$ characteristics for 100 equidistant located devices between the wafer center and locations about 5 cm towards the wafer edge as shown in Fig. 3.46(b), z is the distance from the wafer center. Fig. 3.46(a) reveals that I_{SS} within the off- and on-state varies by a factor of up to five, however much more distinctive is the large statistical distribution of $V_{\text{fil,up}}$ ($V_{\text{fil,down}}$) within about 6.6-10.3 V (5.2-7.5 V), respectively. We mention that as virgin devices often show different unreproducible behavior, for analysis always the second up- and down-sweeps are used. Quantification of V_{fil} dependent on z in Fig. 3.46(c) reveals that averaged $V_{\text{fil,up}}$ and $V_{\text{fil,down}}$ are separated by approximately 1.8 V and remarkably, both show a decrease of roughly 1.1 V when approaching the wafer edge. The superimposed noise is in the same range as the fluctuations for consecutive measurements, therefore we assume that its origin is the same and also the same as of t_{fil} fluctuations. However, besides fluctuations there is a significant decrease of V_{fil} from wafer center to wafer edge, which we cannot explain yet. A possibly decreasing GaN:C thickness towards the wafer edge could result in decreasing V_{fil} , however this should lead to a significant compression of the $I_{\text{SS}}-V$ characteristic and therefore increased $I_{\text{SS}}-V$ slopes, which is not observed. Another

explanation approach could be an increased extended defect density in outer regions of the wafer, causing decreased V_{fil} , however this is speculative and not supported by experiments yet.

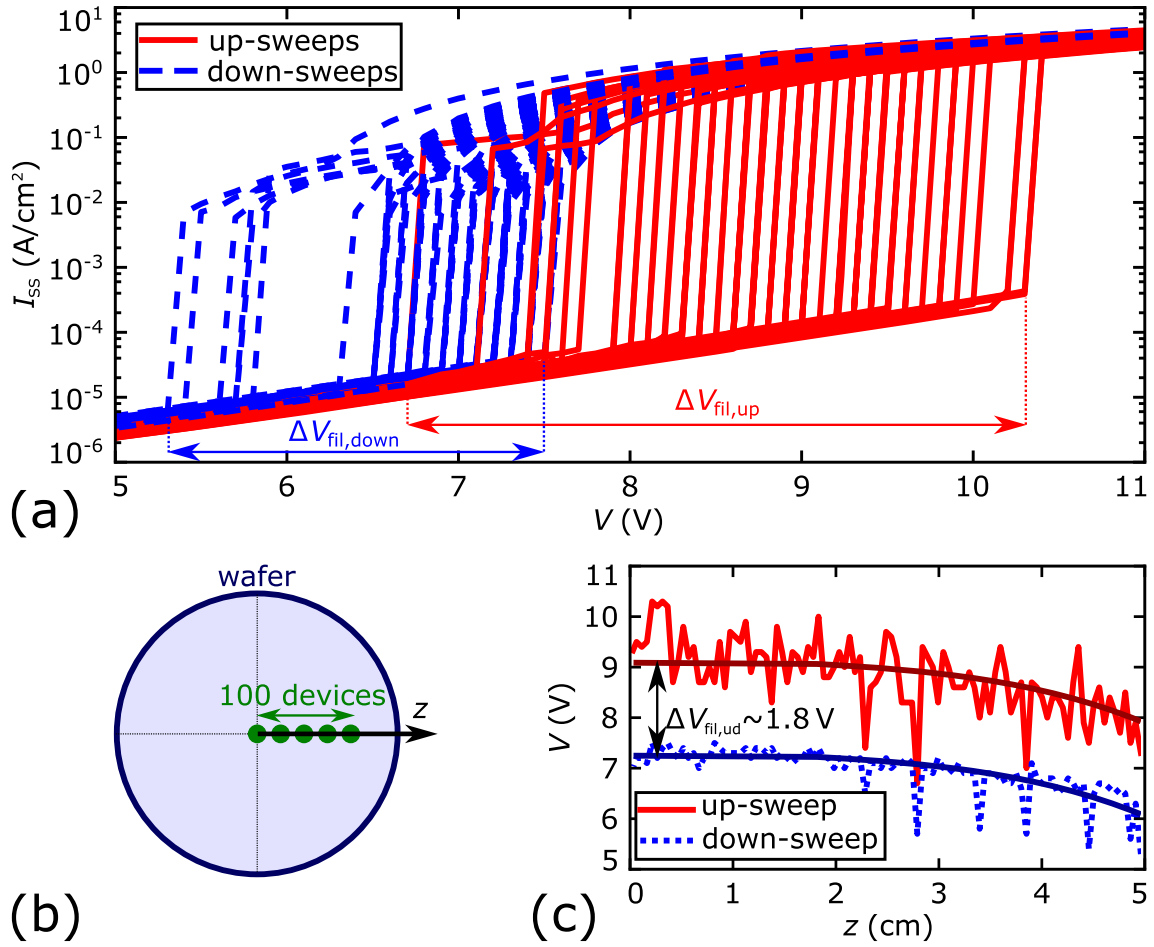


Fig. 3.46: (a) $I_{\text{SS}}-V$ characteristics (up- and down-sweeps) of 100 devices on the same wafer on sample S_{10} with a ramp rate of 1.5 V s^{-1} at 300 K. (b,c) Dependence of V_{fil} on the distance of the measured wafer from the wafer center (z).

V_{fil} as function of the temperature

Fig. 3.47(a) shows $I_{\text{SS}}-V$ characteristics within a wide T range between 20 and 560 K for up- and down-sweeps. Quantitative analysis of V_{fil} in (b) reveals a linear decrease of V_{fil} with T . Remarkably, the hysteresis between up- and down-sweeps occurs only in a limited T range between 180 and 350 K. We speculate that this observation is linked to the time dependence of the off-on transition in combination with the fixed ramp rate, a link to trapping time constants could also be possible.

Filamentation under illumination

Fig. 3.48(a) illustrates $I_{\text{SS}}-V$ characteristics measured in dark condition vs. conditions in which the samples are illuminated by monochromatic light with various $E_{h\nu}$. Illumination shifts I_{SS} to

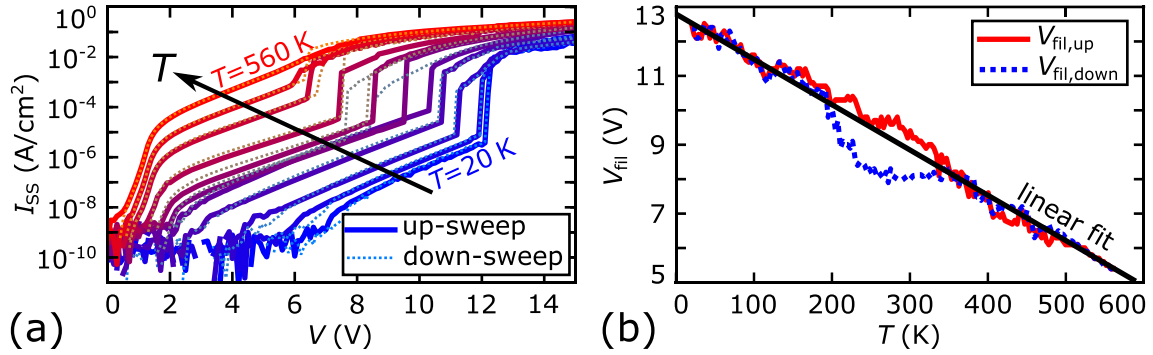


Fig. 3.47: (a) I_{SS} - V for various T with a fixed ramp rate of 0.3 V s^{-1} and (b) V_{fil} vs. T , revealing a mainly linear relation.

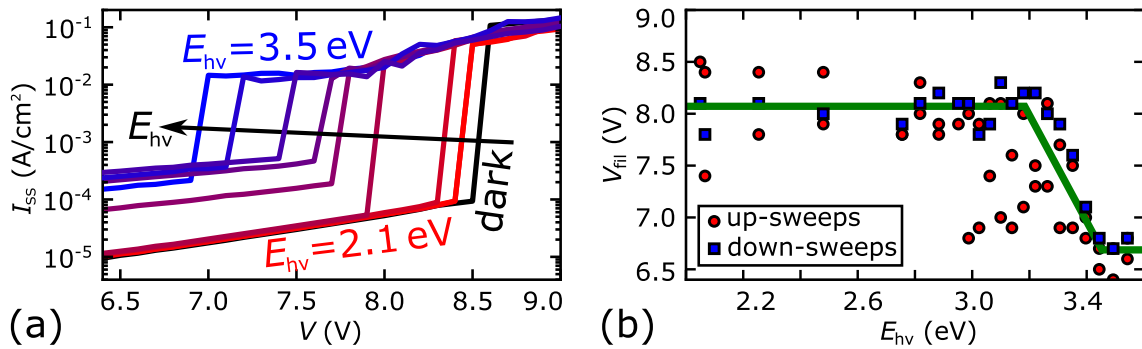


Fig. 3.48: (a) I_{SS} - V characterization at 340 K with a ramp rate of 0.3 V s^{-1} in dark condition ("dark") and with the device being illuminated with monochromatic light with varying photon energies (E_{hv}). (b) Analysis of V_{fil} as function of E_{hv} reveals significant decrease of V_{fil} above roughly 3.2 eV .

higher values (see also Section 3.6.1) and decreases V_{fil} . Quantitative analysis in Fig. 3.48(b) reveals that this happens only if $E_{\text{h}\nu}$ gets close to the band gap energy ($E_{\text{bg}} \approx 3.4 \text{ eV}$). Large fluctuation between consecutive measurements complicate quantitative analysis, especially for $V_{\text{fil,up}}$. Due to the smaller fluctuations in $V_{\text{fil,down}}$, analysis of down-sweeps gives a clearer $E_{\text{h}\nu}$ dependence.

For physical understanding of the filamentation the most interesting features are that V_{fil} decreases and that this happens only for $E_{\text{h}\nu} \gtrsim 3.2 \text{ eV}$. Considering a Franck-Condon-Shift of 0.5 eV the reason for the smaller V_{fil} could be negative charge emission from negatively charged acceptors and therefore an earlier vanishing interface barrier (φ_i). However, 3.2 eV is already close to E_{bg} , where electron-hole pair generation increases I_{SS} significantly, which might also decrease V_{fil} . For clearer judgement larger amount of data would be required in order to decrease the large uncertainties in Fig. 3.48(b).

3.5.7 Current filamentation model

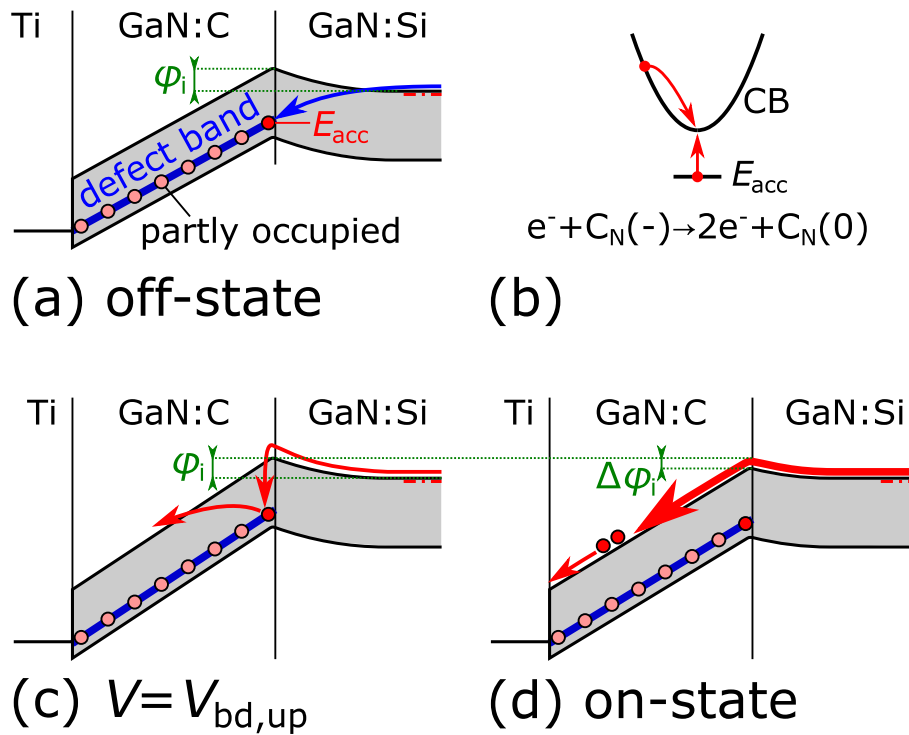


Fig. 3.49: (a) Band diagram in off-state, the blue arrow indicates negative charge injection from CB of GaN:Si to DBs in GaN:C. (b) Schematic energy - wave vector (k) diagram with equation describing impurity impact ionization with $C_{\text{N}}(-)$ and $C_{\text{N}}(0)$ as respective occupied and unoccupied carbon acceptors. (c,d) Band diagrams demonstrate impurity impact ionization at the filamentation onset and in on-state, respectively. An injected electron from GaN:Si can impact an electron in a carbon acceptor and eventually excite it to the conduction band, leaving a neutrally charged acceptor. (d) This results in decreased σ_{C} and consequently a decrease of φ_i by $\Delta\varphi_i$. The thick red arrow in (d) indicates the resulting massive electron injection, the two red dots represent the two electrons from (c). Figure reused from [Kol+18b].

In the following we combine the previous results in order to derive a model for the observed current filamentation. Due to the small leakage current in off-state, $C_{\text{SS}}-V$ characterization delivers reliable band diagrams, as shown in Fig. 3.49(a), the evaluation is described in Section 3.2.1 and

[Kol+17b]. In off-state negative charge accumulation in carbon acceptors in GaN:C next to the GaN:Si interface raises φ_i , which prevents major electron injection from CB of GaN:Si to CB of GaN:C. However, minor electron injection to DBs in GaN:C, in which they can propagate to the top electrode, causes a leakage current I_{SS} [Kol+17b; Kol+17a; Kol+18a]. In contrast to off-state, the largely increased I_{SS} in on-state prevents reliable capacitance measurements and consequently derivation of band diagrams; providing more room for interpretation. Despite missing experimental prove, we consider it inevitable that in the transition from off- to on-state and the resulting dramatic increase in I_{SS} , φ_i has to decrease. We further consider the decrease in φ_i as reason for the transition, which requires also a decrease in σ_C and therefore involves discharging processes. Due to the small power dissipation of roughly 1 mW per CF, the estimated temperature rise does not exceed few degrees so that significant self-heating effects can be excluded. Furthermore, electric fields at $V_{fil,up}$ of 0.4-0.5 MV cm⁻¹ are only a fraction of the field of roughly 3-5 MV cm⁻¹, reported for impact ionization in GaN [Zha+14; Dic+16]. Hence, electron-hole pair generation due to impact ionization can also be excluded. We mention that for matter of simplicity we consider only linear electric field in GaN:C, although this might be slightly modified we do not expect extreme changes as reported e.g. in [LKV05] due to strong injection effects.

In literature there are many nonlinear generation-recombination processes known that cause due to a non-equilibrium phase transition of first order S-shape I_{SS} - V curves [Sch12]. E.g. Schöll [Sch79] and Landsberg [Lan80] propose that the generation process could be determined by impurity impact ionization and electron-hole annihilation could then result in the observed S-shape I_{SS} - V characteristic. Fig. 3.49(b) illustrates the impurity impact ionization process which can be imagined as Auger-like process in which a free electron from CB impacts an occupied carbon acceptor. If the energy of the first electron is sufficient, it can excite the electron in the acceptor, making it charge neutral [Sch79; San+10]. This results in two electrons propagating via CB in GaN:C towards the top electrode as depicted in Fig. 3.49(c,d). This would reduce σ_C and consequently φ_i by $\Delta\varphi_i$. The reduced φ_i further increases electron injection from GaN:Si to the GaN:C CB. This forms a closed positive feedback loop, resulting in the sudden current increase during filamentation. The increasing $V_{fil,up}$ with d_{LUT} , observed in Fig. 3.32(b) suggests a field-controlled mechanism, fitting to the proposed model [Sch79; San+10]. Emission of light with energies below band gap is supposed to originate from recombination of electrons from GaN:C CB in unoccupied carbon acceptors. Required positive charges can either be provided by hole transport from the top electrode via VB or charge transport within DBs.

The small increase of I over time in off-state, as shown in Fig. 3.44(a), suggests slightly decreasing φ_i due to negative charge emission from carbon acceptors. We expect that below a certain threshold the positive feedback is initiated, resulting in filamentation. This can be considered equivalently to a decreasing $V_{fil,up}$ with time. Fig. 3.50 shows with a solid line a schematic S-shape I_{SS} - V characteristic in the "initial" case, i.e. unstressed. With increasing stress time $V_{fil,up}$ decreases, as demonstrated in Fig. 3.50 by dashed lines and a black arrow. For applying a certain voltage V within the bistability region, $V_{fil,up}$ decreases and after a certain time $V_{fil,up}$ reaches V . We introduced this time as t_{fil} , where the transition from off- to on-state occurs. Fig. 3.50 shows that for a voltage-controlled measurement this leads to a sudden increase in I . Concluding, in our proposed model slow negative charge emission causes the time dependence of $V_{fil,up}$, while fast emission due to impurity impact ionization causes the actual filamentation, i.e. transition from off- to on-state.

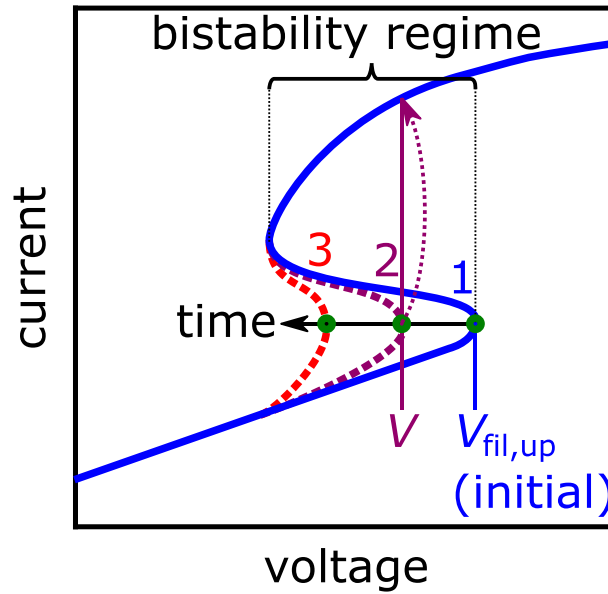


Fig. 3.50: The schematic S-shape I_{SS} - V characteristic demonstrates the decrease of $V_{fil,up}$ with stress time from curves marked with "1" to the one marked with "3". For curve "2" the moment of filamentation is shown. When the decreasing $V_{fil,up}$ becomes smaller than the applied bias V , transition from off- to on-state occurs with the abrupt current jump marked with the dashed arrow. Figure reused from [Kol+18b].

Until now, the model does not predict the existence of multiple CFs. Therefore, we have to expand our model in the following to the second dimension. We tentatively consider a spatially homogeneous systems with S-shape $I-\mathcal{E}$ characteristic, device size large enough, and the operation within the bistability region. As an alternative, small devices obtaining homogeneous current distribution and an S-shape I_{SS} - V characteristic can be considered. In such systems it is reported that spatially homogeneous current flow is unstable against fluctuations in I and \mathcal{E} [VK69; SS01; SMG13]. Therefore, regions in on- and off-state and corresponding high and low current densities separate, i.e. a CF is formed. In a single active layer one CF would rise with its size increasing with I [VK69; Pog+11]. In contrast, for an active region in series with a passive Ohmic layer, the formation of multiple CFs is favored over one large CF [Pur+89; JBS86; GN02; KO89; MHR90; Mam+09]. Fig. 3.51(a) shows schematically by yellow arrows the localized current flow in CFs in GaN:C and its distribution in GaN:Si. Subfigures (b,c,d) illustrate how we expect E_{CB} , I and σ_C to distribute as a function of the lateral coordinate x . The formation of multiple CFs is energetically favored due to lateral spreading of I in GaN:Si, i.e. the passive Ohmic layer, at the edges of CFs and the hence decreased voltage drop in GaN:Si in comparison to a single large CF. CFs are only stable within a certain size range [MHR90]. While larger CFs split to smaller CFs, smaller ones can merge or completely disappear, as observed in EMMI videos discussed in Section 3.5.3. Due to the finite size range of CFs, their size and number can vary for identical biases and currents [Mam+09].

Fig. 3.51(e) shows a simplified equivalent circuit, in which the active GaN:C layer, represented by current sources in the CFs, is in series to resistances of the passive layer and the base structure. The decreased resistance due to lateral current flow in GaN:Si is represented by additional paths in GaN:Si, marked with black arrows. In [JBS86; Mam+09] it has been reported that I_{SS} - V

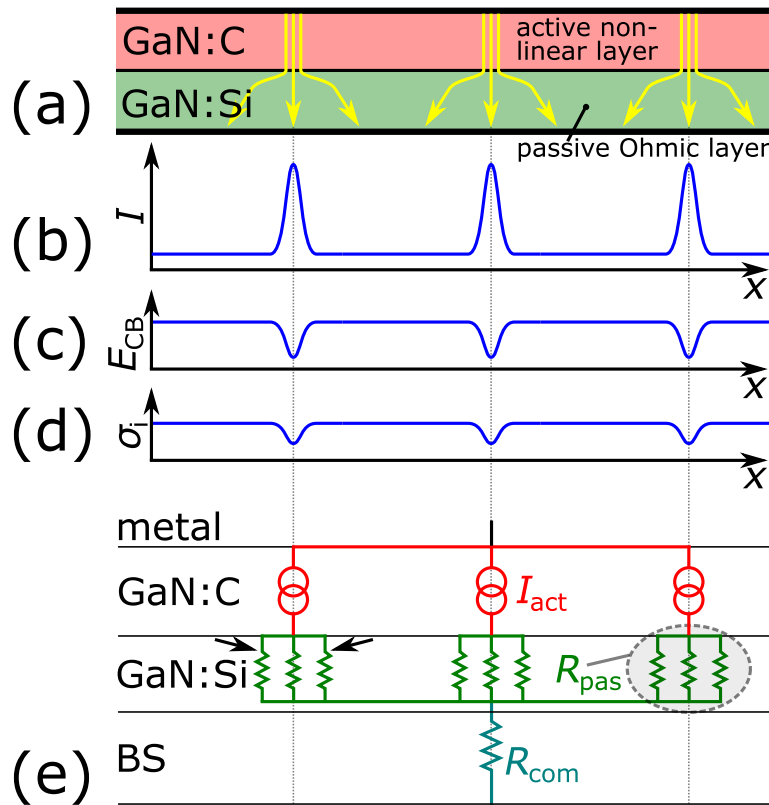


Fig. 3.51: (a) Schematic model of the LUT with current flow lines represented by yellow arrows. The LUT can be represented with GaN:C as active non-linear layer and GaN:Si as passive Ohmic layer. (b,c,d) show respective I , E_{CB} and σ_C distributions in GaN:C with x as lateral coordinate. (e) Simplified equivalent circuit with the active GaN:C layer represented by current sources in CFs (I_{act}), the passive GaN:Si layer represented by R_{pas} and the base structure represented by R_{com} . Two black arrows demonstrate the parallel components of R_{pas} due to lateral current flow in GaN:Si. Figure reused from [Kol+18b].

characteristics for different number of CFs result in zig-zag behavior due to the changing potential drop in the passive Ohmic layer. This behavior is not observed in our experiments, we suppose that this could be due to the additional series resistance of the base structure which could exceed the GaN:Si resistance by far so that changes in I due to different number of CFs are below the noise level.

Due to the expected important role of dislocations for leakage current (e.g. defect bands), in the following we discuss a possible link between dislocations and CFs. EMMI analysis in reverse biased InGaN/GaN light emitting diodes (LEDs) reveals also localized current filaments [Men+09; Usa+18b]. It has further been reported that these filaments occur at the position of screw and mixed dislocations [Usa+18b; Usa+18a], indicating current flow via the dislocations [Li+04]. Our EMMI analysis reveals spontaneous formation of multiple CFs, therefore we do not consider extended defects as mandatory for CF formation. However, we consider that pinning of CFs, e.g. shown in Fig. 3.37, could take place indeed at extended defects such as dislocations. Pinning of spontaneously formed CFs at defects has already been reported in other systems in [Ale+98]. We suppose that in our structures local charge in the vicinity of extended defects could result in local reduction of $V_{\text{fil,up}}$ and hence metastable pinning. The movement of CFs could result from lateral inhomogeneities in σ_C , driving CFs in random directions.

3.6 LUT structures under illumination

Illuminating LUT structures with light can have two major effects: 1) For photon energies above band gap energy (i.e. $E_{h\nu} > E_{\text{bg}}$) photons generate electron-hole pairs, resulting in photo-current, free electrons in CB, free holes in VB and can change the occupation of carbon defects due to capture of these charges. 2) For photon energies exceeding optical excitation energies (see Fig. 3.41) defects can change their charge state. In the following section we discuss the effect of illumination on basis of sample $S_{10,\text{Au}}$ in detail, experimental details on the optical setup are provided in Appendix A.

3.6.1 Static behavior

This section is dedicated to discussion of the change of the SS behavior of the LUT structure $S_{10,\text{Au}}$ by illuminating it. Besides spectroscopic analysis and deriving the influence of the light intensity, the main discussion bases on $C_{\text{SS}}-V$ measurements, from which potential, electric field and charge distributions are derived for dark and illuminated conditions, using the formalism introduced in Section 3.2.1.

Spectroscopy

Fig. 3.52(a,b) show $I_{\text{SS}}-V$ of $S_{10,\text{Au}}$ in dark condition and with monochromatic light focused onto the contact. For reverse bias up to -40 V in dark condition the leakage current is well below the measurement resolution. Quantitative analysis of I_{SS} vs. $E_{h\nu}$ in Fig. 3.52(c) for $V = -10\text{ V}$ reveals that for light with $E_{h\nu} > 3\text{ eV}$ significant photocurrent (I_{photo}) rises with a maximum approximately at E_{bg} . This photocurrent originates from electron (e^-) - hole (h^+) pair generation in GaN:C and depleted GaN:Si. Possibly existing defect-assisted generation processes at carbon acceptors should result in a peak at $E_{\text{opt}} \approx 3.2\text{ eV}$ (see Fig. 3.41), its absence in

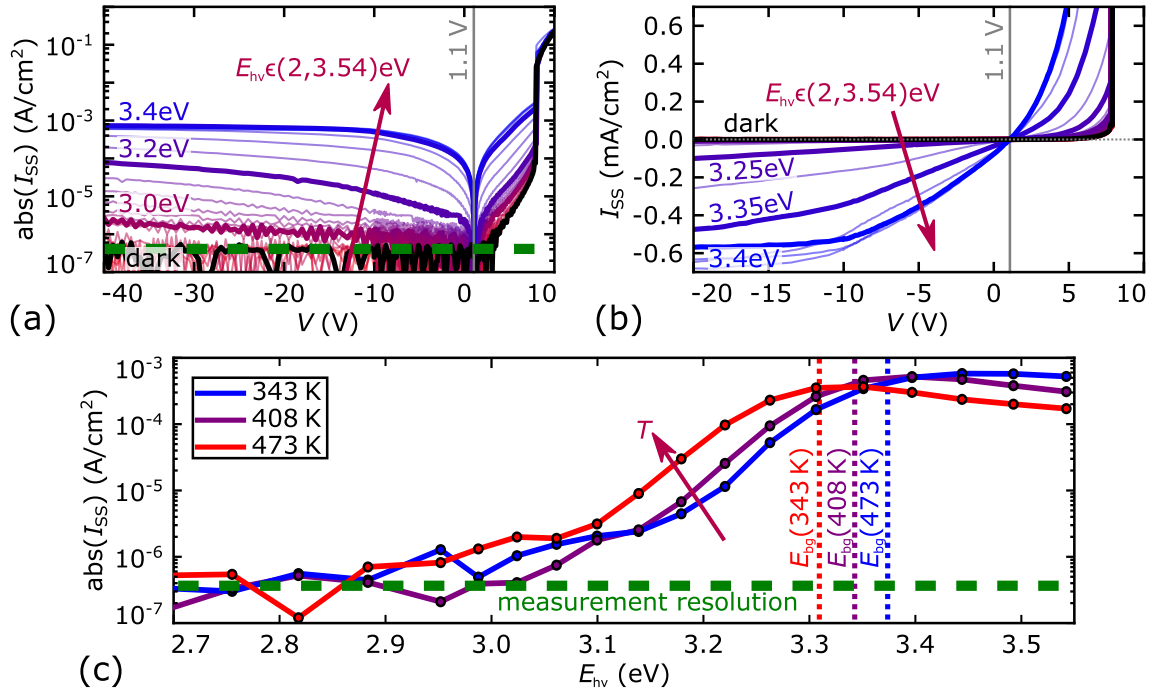


Fig. 3.52: (a,b) I_{SS} - V characteristics without illumination (“dark”) and illuminated with various E_{hv} . (c) Quantitative analysis of the spectral dependence of I_{SS} at $V = -10$ V.

Fig. 3.52(c) indicates that its rate is by orders of magnitude smaller than the band-to-band generation rate. For $E_{hv} > E_{bg}$ the photocurrent decreases again which is probably related to the setup-related significantly decreasing photon irradiance (E_e) as illustrated in Fig. A.4. In order to keep experiments at different T comparable we use for all further investigations $E_{hv} = 3.54$ eV ($\lambda = 360$ nm). Comparing light induced maximum charge flow per area and time interval (i.e. $I_{photo} \approx 2 \times 10^{15} \text{ cm}^{-2} \text{ s}^{-1}$) with the flow of photons irradiating the GaN sample per area and time interval (i.e. $E_e \times T_{metal} \approx 5 \times 10^{16} \text{ cm}^{-2} \text{ s}^{-1}$) reveals a conversion factor of 4%. This means that roughly 4% of all photons are translated into free charges reaching the electrodes.

Influence of light power

Fig. 3.53(a) shows I_{SS} - V in dark condition as well as illuminated with $E_{hv} = 3.45$ eV with the light power (P_{lamp}) varying between 240 and 330 W. Fig. 3.53(b) demonstrates that at all three representative biases (0, -10 and 7 V) I_{SS} scales roughly linear with P_{lamp} , which further scales roughly with E_e .

The linear scaling of I_{SS} with E_e suggests that within the entire bias range (excluding *Ohmic regime*) practically the entire current is photocurrent, generated by band-to-band electron-hole pair generation; dark I_{SS} is orders of magnitude smaller.

Analysis of illuminated LUT structures based on potential distributions

Fig. 3.54(a) shows C_{SS} - V , once in dark condition and once illuminated with light with $E_{hv} = 3.54$ eV at 343 K. Fig. 3.54(b) demonstrates that $1/C_{Si}^2$ scales linear with V not only in dark but also in illuminated condition, even with identical slope. The illuminated curve is only shifted horizontally by 12.4 V, resulting in a root value of $V_{bi,lighted} = -9.7$ V.

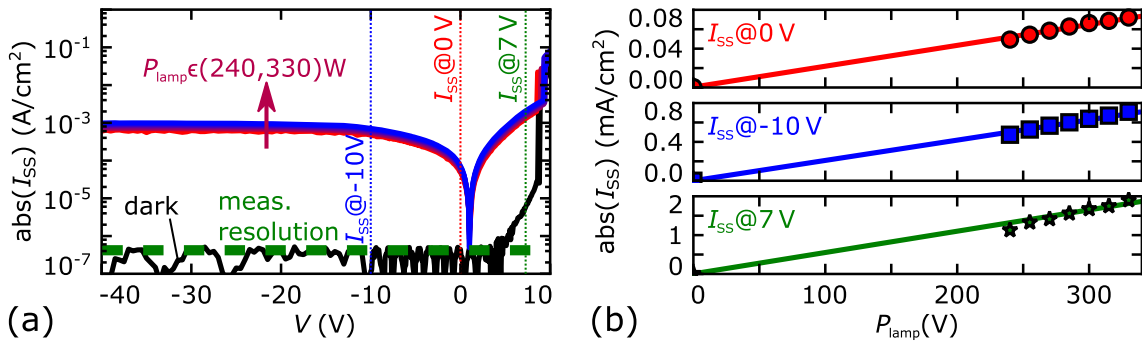


Fig. 3.53: (a) I_{SS} - V characteristics in dark condition and under illumination with $E_{h\nu} = 3.54 \text{ eV}$ ($\lambda = 350 \text{ nm}$) and various P_{lamp} (i.e. various E_e). (b) I_{SS} vs. P_{lamp} at various V as indicated in (a).

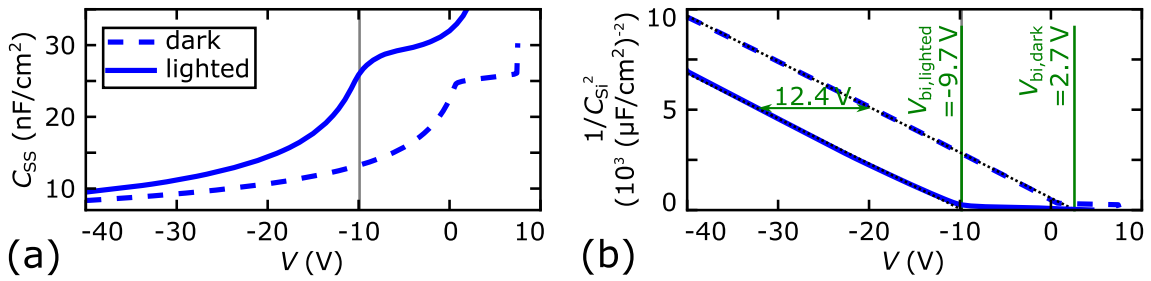


Fig. 3.54: (a) C_{SS} - V and (b) $1/C_{Si}^2 - V$ for $S_{10, \text{Au}}$ at 343K reveal a horizontal shift by 12.4 V to lower V for characterization under illumination with $E_{h\nu} = 3.54 \text{ eV}$ ($\lambda = 360 \text{ nm}$).

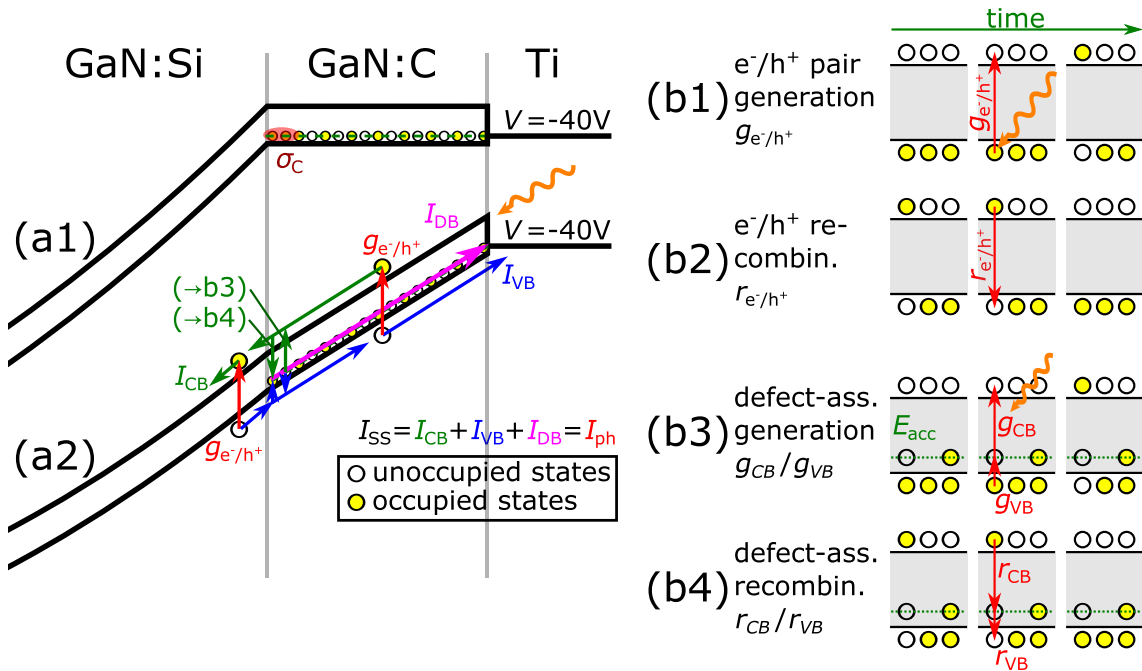


Fig. 3.55: (a) Calculated band diagrams for $S_{10, \text{Au}}$ at 343K in (a1) dark and (a2) illuminated condition, derived from data in Fig. 3.54. (b1-b4) illustrate schematically the main generation and recombination processes indicated in (a2). Orange wavy arrows represent photons.

Fig. 3.55(a1) shows calculated band diagrams in dark condition, as discussed in detail in Section 3.2.1, for the sake of simplicity charges in GaN:C are considered directly at the GaN:Si/GaN:C interface and the Schottky barrier is neglected. While in dark condition bands in GaN:C are flat, illumination generates an electric field in GaN:C (\mathcal{E}_C), as can be seen in Fig. 3.55(a2). Light with $E_{h\nu} > E_{bg}$ generates e^-h^+ pairs with a rate of $g_{e^-h^+}$ (b1); although part of the generated charges recombine again with a rate $r_{e^-h^+}$ (b2), a great part is accelerated by \mathcal{E}_C and reaches the related electrode, contributing to the measured current in Fig. 3.52. As the major part of photons are absorbed in GaN:C, carbon defects have to be considered too; whereby for the sake of simplicity we only discuss the effect of light on acceptors and ignore donors. Carbon acceptors act as recombination centers (see Fig. 3.55(b4)) with electron capture rates r_{CB} from CB and hole capture rates r_{VB} from VB. As $E_{h\nu} > E_{CB} - E_{acc} + d_{FC,1}$, photons can also excite e^- from occupied acceptors to CB (g_{CB} , (b3)). Similarly, h^+ could be excited from E_{acc} to E_{VB} , but as $E_{h\nu} \gg E_{acc}$, this process is unlikely. As discussed in Section 3.5.4, significant current starts to rise only for $E_{h\nu}$ close to E_{bg} , so that for I_{SS} defect-assisted carrier generation can be neglected. However, although $g_{CB} \ll g_{e^-h^+}$, it could still play a role by changing the occupation of acceptors. The band diagram in Fig. 3.55(a2) reveals that the generated e^-h^+ pairs generate an \mathcal{E}_C that drives e^- to GaN:Si and consequently to the bottom electrode, while h^+ drift to the top electrode. The total current in GaN:C is the sum of charges propagating in CB, VB and DBs.

Yet, we did not explain how \mathcal{E}_C forms, in the following we propose a model therefore. If in dark condition in Fig. 3.55(a1) light is switched on, e^-h^+ pairs are generated, e^- drift towards GaN:Si and h^+ towards the top electrode. However, some e^- and h^+ are captured by carbon acceptors on their way and if more e^- are captured a net negative space charge occurs, for more captured h^+ a net positive space charge occurs. In theory, net negative charge could also result from a difference in free charges, i.e. different p and n due to reasons discussed below. However, transient C measurements show that relaxation after switching light off can take many seconds. As free charges in CB and VB are expected to reach associated electrodes many orders of magnitude faster, we consider the contribution of n and p for the net charge density negligible. We define the amount net charge capture (captured h^+ minus e^-) per time interval and area as I_h , which can be calculated as:

$$I_h = (p \times r_{VB} - n \times r_{CB})d_{LUT}. \quad (3.23)$$

In general, n , r_{CB} , p and r_{VB} are unknown, but we are mainly interested in the sign of I_h , which we will estimate in the following:

- Capture rates r_{CB} and r_{VB} depend mainly on capture cross sections and thermal velocity. The capture cross section for h^+ is roughly 100 times larger than for e^- [Ure+15], while its thermal velocity is roughly two times smaller [LRS01; Pan75]. This results in approximately 50 times larger r_{VB} than r_{CB} .
- Due to the high photocurrent we consider for p and n only photo-induced charges. e^- and h^+ are generated in same amounts, however the densities n and p can differ significantly. First of all, due to the roughly four times higher effective mass of h^+ compared to e^- , generated h^+ are longer in the GaN:C layer, increasing p compared to n . Furthermore, generated h^+ in GaN:Si also have to propagate through GaN:C and contribute to p while generated e^- in GaN:Si propagate to the bottom electrode without passing the GaN:C layer. On the opposite side, due to decreasing light intensity with depth because of absorption, the amount

of generated e^-h^+ pairs also decreases. Consequently, h^+ propagate in average over shorter distances in GaN:C than e^- . Also p and n decrease due to trap-related recombination and as $r_{VB} > r_{CB}$ this decreases p more than n . In total without experimental support we cannot judge whether p or n is larger, however we consider it unlikely that n exceeds p by a factor greater than 50.

Concluding, we expect $n \times r_{CB}$ to be smaller than $p \times r_{VB}$, making I_h positive and resulting in a net positive space charge in GaN:C.

Let us discuss once more in a phenomenological way what happens when at -40 V (Fig. 3.55(a)) light is switched on: I_h results in positive charge accumulation in GaN:C. The decreasing negative charge in GaN:C (σ_C) results in decreasing potential and consequently an electric field in GaN:C (\mathcal{E}_C). \mathcal{E}_C causes negative charge transport from the top electrode via defect bands (I_{DB}). As I_{DB} increases with \mathcal{E}_C , after a certain amount of captured positive charges a value for \mathcal{E}_C establishes at which $I_{DB} = I_h$, i.e. thermal equilibrium (SS) establishes.

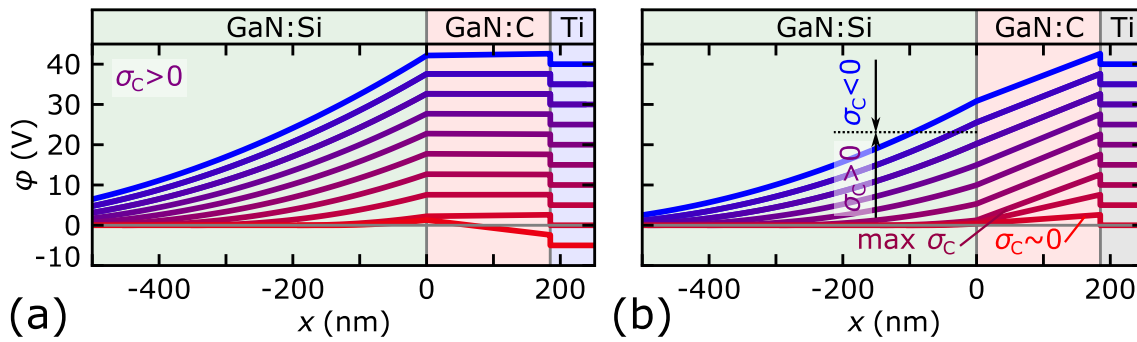


Fig. 3.56: Potential distributions calculated from data in Fig. 3.54(a) under (a) dark and (b) illuminated condition. Comments in (b) indicate bias regions with maximum, positive and negative charge in GaN:C (σ_C), quantified in Fig. 3.58.

Fig. 3.56 depicts potentials and band diagrams for various V , dark (a) and illuminated (b). $1/C_{Si}^2 - V$ shows a shift of V_{bi} to more negative values, indicating a shift of the transition voltage between *depletion* and *plateau regime* by 12.4 V to -9.7 V. In addition, illumination changes features of both regimes slightly. In *depletion regime* instead of zero, $\mathcal{E}_C = const. > 0$ with its value determined by the light intensity and the conductivity in DBs. This is demonstrated well in Fig. 3.57, where in (a) φ_i is V independent but shifted in illuminated condition by 12.4 V to lower values; consequently in (b) $\mathcal{E}_C = const > 0$. In *plateau regime* φ_i is constant in both, dark and illuminated condition, but in the latter it is significantly smaller with a value of roughly 0.5 V, compared to 1.1 V in dark condition. As the *plateau regime* starts already at roughly -10 V, I_{SS} is negative, until at $V = 1.1$ V (Fig. 3.52) the sign changes. The large I_{SS} at 0 V is a direct evidence that its nature is light induced charges. The sign change at 1.1 V suggests flatband at this value with a change of sign of \mathcal{E}_C at this value. In forward bias $I_{SS}-V$ in Fig. 3.52 shows qualitatively equivalent behavior of dark and illuminated devices with only a vertical shift to higher I_{SS} . Due to lack of better knowledge we speculate that this might be related to parallel charge transport via CB besides DBs.

Band diagrams for dark condition in Fig. 3.56(a) show independent of V a concave kink at the GaN:Si/GaN:C interface, corresponding to negative charge accumulation in GaN:C, i.e. $\sigma_C < 0$. In contrast, under illuminated condition in (b) \mathcal{E}_C stays constant but not zero, resulting in concave

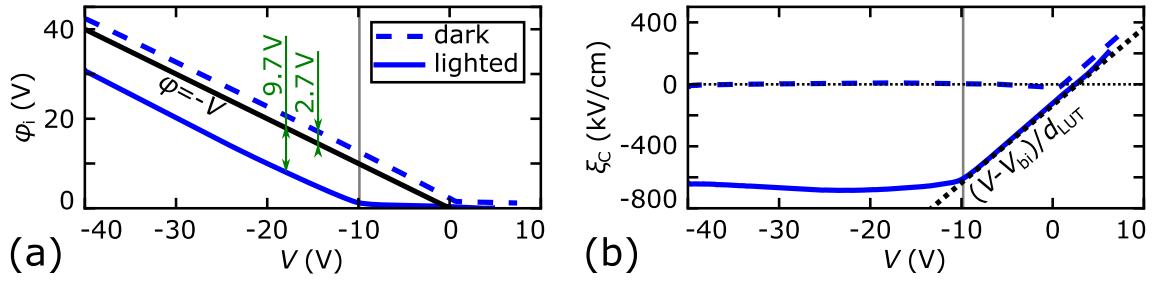


Fig. 3.57: (a) Interface potential (φ_i) and (b) electric field in GaN:C (ξ_C) as function of V under dark and illuminated condition. Calculations base on data in Fig. 3.54(a).

and convex kinks, depending on the bias. Fig. 3.58(a) shows calculated σ_C , using Eq. (3.8) and (3.9), whereby for illuminated conditions, equations have to be slightly adapted. As the transition voltage between *depletion* and *plateau regime* shift from 1.5 V to -9.7 V, the values 1.5 V in the equations have to be replaced by -9.7 V, whereby we mention that this value is only valid for this light intensity and temperature. Fig. 3.58(a) demonstrates that for high negative and for positive biases negative charge accumulates, but for -29 V $< V < 0$ positive charge appears. (b) shows schematically how the occupation of acceptors and donors change for changing sign of σ_C :

1. For $\sigma_C = 0$ donors are unoccupied and acceptors partly occupied with $N_{acc}(-) = N_{don}(+) = N_{don}$.
2. For $\sigma_C < 0$ donors are unoccupied and acceptors occupied with $N_{acc}(-) > N_{don}(+) = N_{don}$, resulting in a maximum space charge density of $N_{acc}^* = N_{acc} - N_{don}$.
3. For $\sigma_C > 0$ donors are unoccupied and acceptors less occupied, i.e. $N_{acc}(-) < N_{don}(+) = N_{don}$, resulting in a maximum space charge density of N_{don} when all acceptors are unoccupied.

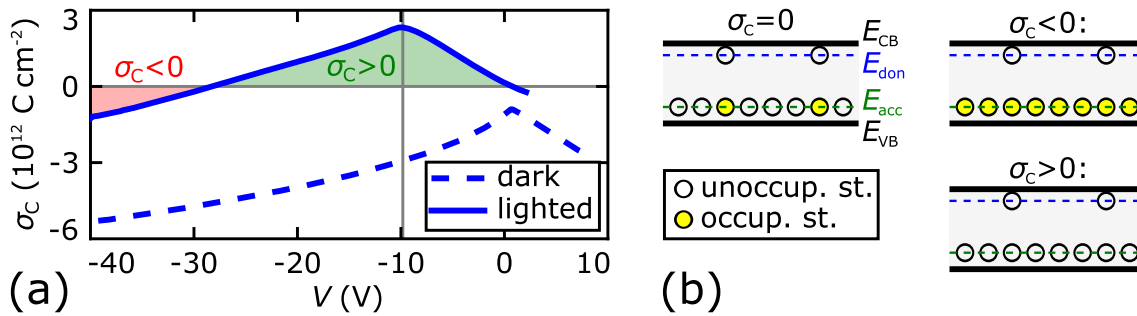


Fig. 3.58: (a) Bias-dependent equivalent sheet charge in GaN:C (σ_C) and (b) schematic band diagrams indicating the charge states in the different bias ranges in (a). Calculations base on data in Fig. 3.54(a).

Although the existence of donors has been evidenced indirectly by proving the validity of the dominant acceptor model, these electric measurements under illumination are to the author's knowledge the first direct evidence for the existence of donors. From the maximum σ_C at -10 V of 2.5×10^{12} cm $^{-2}$ a minimum N_{don} can be estimated. Considering all charges at the interface, N_{don} must exceed $\sigma_C(10 \text{ V})/(q \times d_{LUT}) = 1.4 \times 10^{17}$ cm $^{-3}$, for homogeneous distribution in GaN:C $N_{don} > 0.7 \times 10^{17}$ cm $^{-3}$. As at least a major part of σ_C is located close to the interface, even

under conservative consideration the lower boundary for N_{don} is 10^{17} cm^{-3} . As $[C] = 10^{19} \text{ cm}^{-3}$, this means that at least 1% of $[C]$ act as donors.

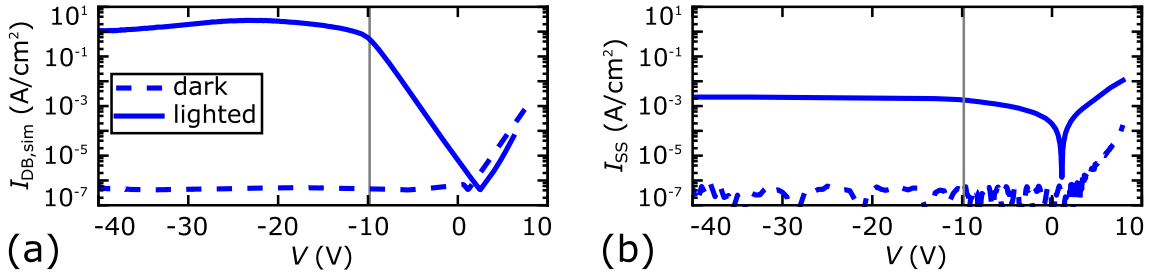


Fig. 3.59: (a) Simulated current flow through defect bands in GaN:C ($I_{\text{DB,sim}}$) based on extracted \mathcal{E}_C from Fig. 3.54(a) and $I_{\text{DB}}(\mathcal{E}_C)$ -relations shown in Fig. 3.20. (b) Measured $I_{\text{SS}}-V$ characteristics.

The current flow in the DBs for a given $[C]$ is fully determined by \mathcal{E}_C and T (see Eq. 4.1). As both parameters are known from $C_{\text{SS}}-V$ measurements, we can simulate this current flow ($I_{\text{DB,sim}}$) as function of V for dark and illuminated cases in Fig. 3.59(a). Comparison of $I_{\text{DB,sim}}$ with the actually measured I_{SS} in Fig. 3.59(b) reveals that $I_{\text{DB,sim}} \gg I_{\text{SS}}$. In this non-equilibrium condition e^- would accumulate in GaN:C, reducing \mathcal{E}_C and I_{DB} until $I_{\text{DB}} \approx I_{\text{SS}}$. The discrepancy could be explained by considering that under illumination the conductivity in DBs decreases. This could result from a changing occupation level as it is proposed for impurity bands in [Rac+18b]. Another reason could be systematic errors, e.g. small errors in the measured capacitances have large impact on the extracted fields. Also shortcomings in the proposed model are conceivable, however deeper investigations would go beyond the scope of this thesis.

Temperature-dependent illumination measurements

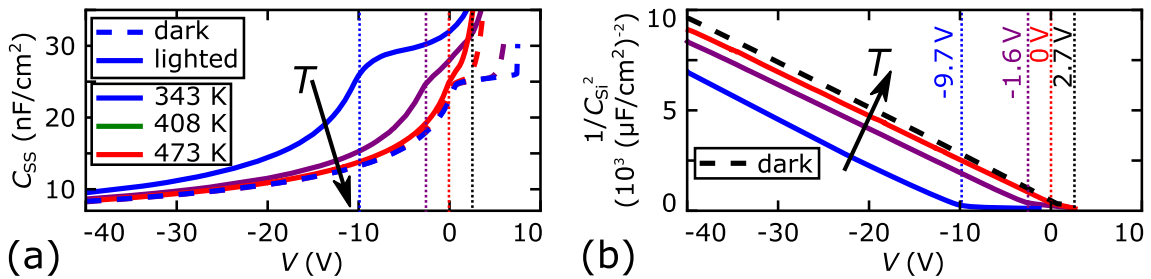


Fig. 3.60: (a) $C_{\text{SS}}-V$ and (b) $1/C_{\text{Si}}^2 - V$ for $S_{10,\text{Au}}$ reveal T independence under dark and a horizontal shift to lower V with decreasing T under illuminated condition with $E_{\text{h}\nu} = 3.54 \text{ eV}$ ($\lambda = 360 \text{ nm}$).

Fig. 3.60(a) shows dark and illuminated $C_{\text{SS}}-V$ measurements for various T . Dark characteristics are for $V \lesssim 2 \text{ V}$ roughly T independent, therefore for following analysis of the dark behavior only the measurement at 343 K is illustrated. Under illumination the horizontal shift of $C_{\text{SS}}-V$ characteristics decreases until at 473 K dark and illuminated measurements are almost identical (for the used light intensity). The horizontal shift is well recognizable in the $1/C_{\text{Si}}^2 - V$ characteristic in Fig. 3.60(b), which also shows the same slope but different V_{bi} for all T , hence we use again the LUT characterization technique.

Fig. 3.61 demonstrates that with decreasing T the transition between *depletion* and *plateau regime* shifts to more negative V , but the behavior within the regimes remains qualitatively unchanged. Quantitatively the absolute \mathcal{E}_C as well as σ_C in the *depletion regime* decreases with increasing T . We suppose that the root of the T dependence is mainly the large T dependence of I_{DB} . In contrast, I_{photo} and therefore I_h show no significant T dependence. As a consequence at low T large \mathcal{E}_C are required in order to ensure $I_{DB} = I_h$ while with increasing T \mathcal{E}_C can decrease in order to achieve same I_{DB} . At $T = 473$ K already negligible \mathcal{E}_C is sufficient, thus C_{SS-V} characteristics in Fig. 3.61 show almost no discrepancies to dark C_{SS-V} characteristics.

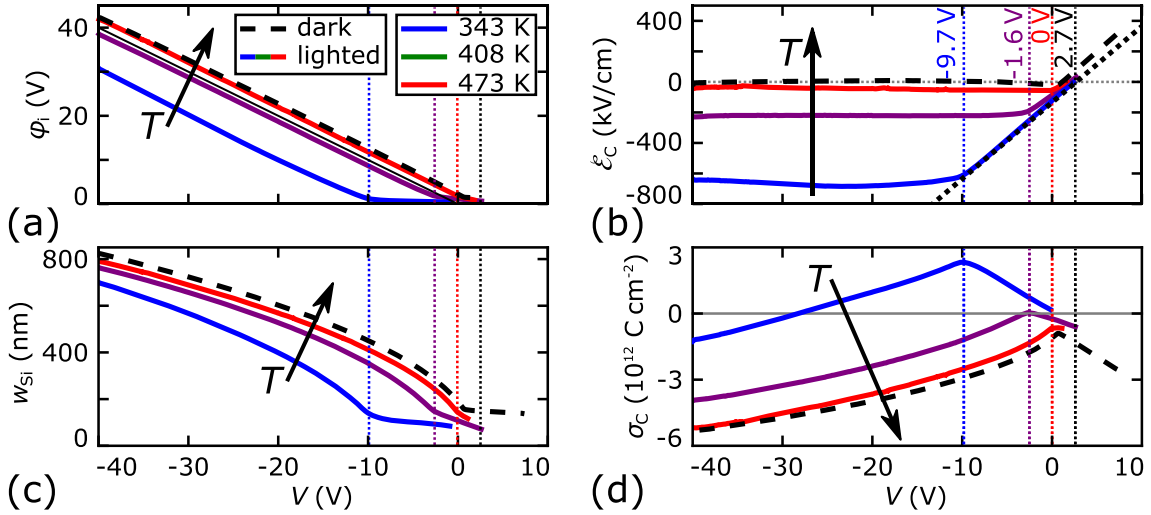


Fig. 3.61: (a) Interface potential (φ_i), (b) electric field in GaN:C (\mathcal{E}_C), (c) depletion width in GaN:Si (w_{Si}) and equivalent sheet charge density in GaN:C (σ_C) as function of V under dark and illuminated condition for various T , whereby in dark condition the parameters are approximately T independent. Calculations base on data in Fig. 3.60(a).

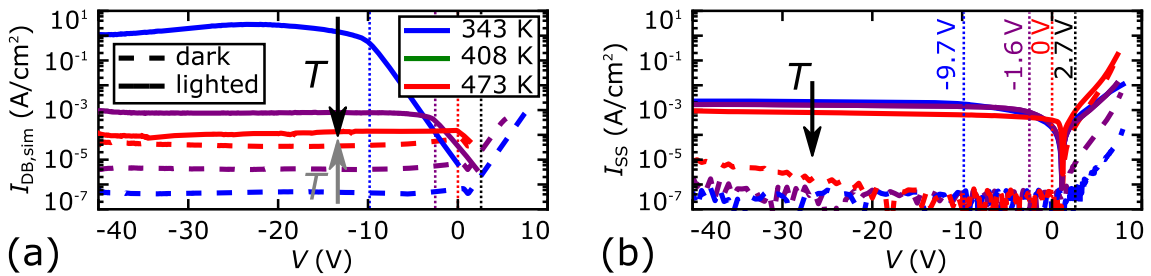


Fig. 3.62: (a) Simulated current flow through defect bands in GaN:C ($I_{DB,sim}$) based on extracted \mathcal{E}_C from Fig. 3.60(a) and $I_{DB}(\mathcal{E}_C)$ -relations shown in Fig. 3.20 with T dependence extracted from Fig. 3.19. (b) Measured I_{SS-V} characteristics.

While the proposed hypothesis can explain the results qualitatively correct, quantitative comparison of $I_{DB,sim}$ and I_{SS} in Fig. 3.62 show major discrepancies which cannot be explained yet.

3.6.2 Dynamic behavior

Analysis of the static behavior has delivered a model describing the interaction of GaN:C layers with light. In this section we verify and extend this model by performing and comparing dynamic characterization of GaN:C layers in dark and under illumination.

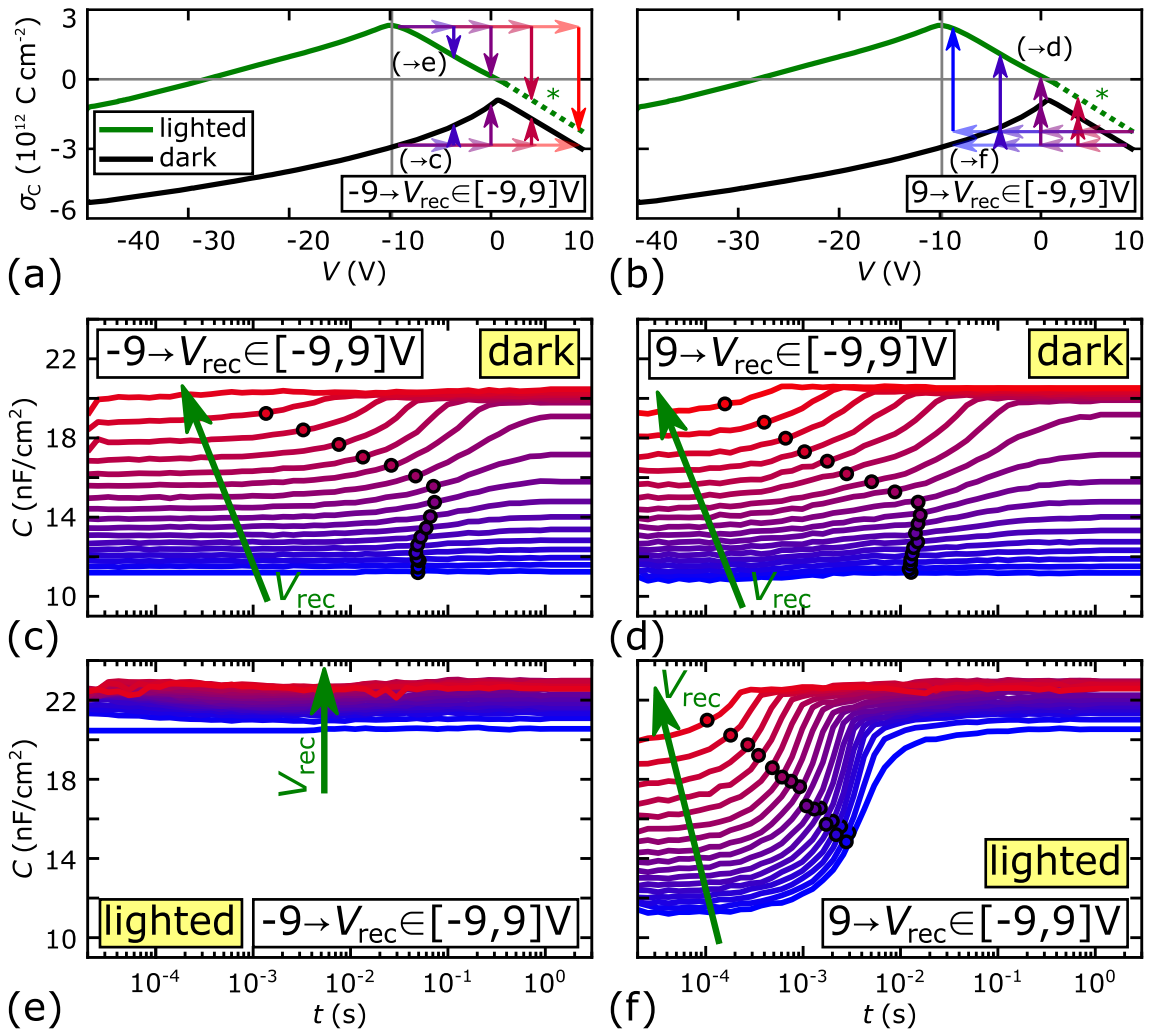


Fig. 3.63: (a,b) σ_C - V in dark and illuminated condition for $S_{10,\text{Au}}$ at 343K, derived from data in Fig. 3.54. (a) Change of σ_C after bias steps from -9 V to various V_{rec} , indicated with different colors, the corresponding color map is used in $C(t)$ in (c) and (e). (b,d,f) are analogous to (a,c,e) but show bias steps from 9 V to various V_{rec} , i.e. the vice versa process. *Data from dotted green lines could not be derived from SS measurements due to artifacts from high conductance, instead data is gained from high-frequency $C(t)$ measurements using lock-in technique.

Fig. 3.63(a) shows steady-state σ_C - V curves in dark (black) and illuminated (green) condition as well as the expected charge being captured after bias steps from $V_{\text{str}} = -9$ V to various V_{rec} ($\Delta\sigma_C$), indicated by colored arrows. The arrows for dark condition demonstrate that with increasing V_{rec} from -9 V to 1.5 V $\Delta\sigma_C$ increases, but decreases again for $V_{\text{rec}} > 1.5$ V so that for $-9 \rightarrow 9$ V $\Delta\sigma_C \approx 0$. The corresponding $C(t)$ curves in Fig. 3.63(c) demonstrate this well, the top red line corresponds to the last mentioned process. In lighted condition σ_C decreases approximately linear in the entire range between -9 and 9 V. However, Fig. 3.63(e) shows no transient behavior at all. The reason is that the entire accessible bias range is in the *plateau regime* and as explained in detail in Section 3.3.3 negative charge capture in the *plateau regime* occurs "ultrafast", i.e. faster than the time resolution of 30 μs . Fig. 3.63(b,d,f) are analogous to (a,c,e) but for $V_{\text{str}} = 9$ V instead of $V_{\text{str}} = -9$ V. As positive charge capture is not ultrafast but shows well characterizable $C(t)$ transients, we will focus for quantification mainly on this process.

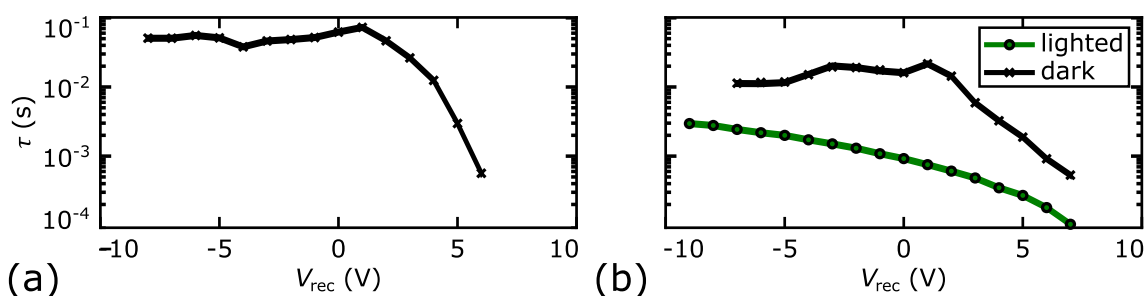


Fig. 3.64: Acceptor discharging (negative charge emission) time constants τ as a function of V_{rec} after (a) $V_{\text{str}} = -9$ V and (b) $V_{\text{str}} = 9$ V in dark and lighted condition, derived from data in Fig. 3.63. τ in lighted condition for $V_{\text{rec}} = -9$ V are too small to be measured, see Fig. 3.63(e).

Fig. 3.64 illustrates τ derived from Fig. 3.63. In dark condition τ remains roughly constant for $V_{\text{rec}} < 1.5$ V as all these processes end in $\mathcal{E}_C = 0$. Only for $V_{\text{rec}} > 1.5$ V the final \mathcal{E}_C increases and therefore τ decreases. In lighted condition τ surprisingly depends not only on \mathcal{E}_C , which would lead to a maximum at $V_{\text{rec}} = 1.1$ V, where the final \mathcal{E}_C is zero. Instead, it decreases with V_{rec} throughout the entire bias range.

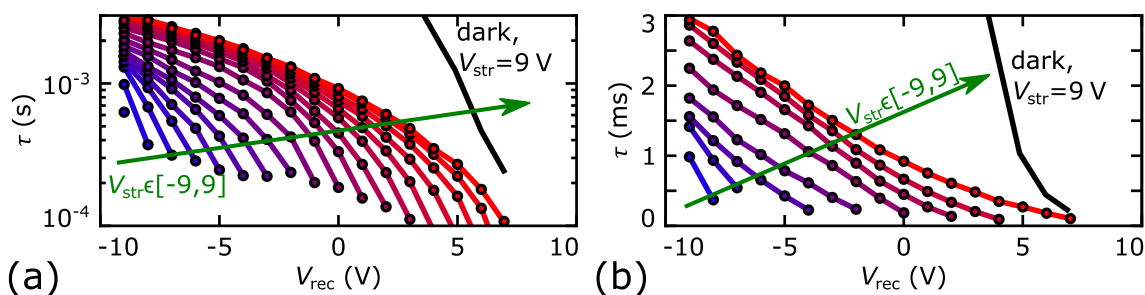


Fig. 3.65: τ - V_{rec} with (a) logarithmic and (b) linear ordinate in dark (black) and lighted condition (colored) with various V_{str} ; derived from data in Fig. 3.63.

This observation can be best understood by extracting τ for a large matrix of V_{str} and V_{rec} , as illustrated in Fig. 3.65. Especially in linear scale in (b) it gets obvious that τ decreases roughly linear with V_{rec} and increases roughly linear with V_{str} . We can simplify this and state that $\tau \propto |V_{\text{str}} - V_{\text{rec}}|$ with minor disturbances from the linear relation for large V_{rec} , presumably due to SS leakage current. Fig. 3.63 shows that $|V_{\text{str}} - V_{\text{rec}}|$ is proportional to $\Delta\sigma_C$, so that $\tau \propto \Delta\sigma_C$. This

is only reasonable if we consider a constant bias-independent injection current which fits perfectly to the model proposed for SS analysis. The injection current is the proposed I_h and can easily be calculated by:

$$I_h = q \times \Delta\sigma_C / \tau. \quad (3.24)$$

The value of I_h is approximately $200 \mu\text{A cm}^{-2}$ and therefore in the range of the SS photo-current (I_{photo}) with few mA cm^{-2} as depicted in Fig. 3.62. That indicates that at least until SS is established, a great part of the photo-generated holes are captured in GaN:C.

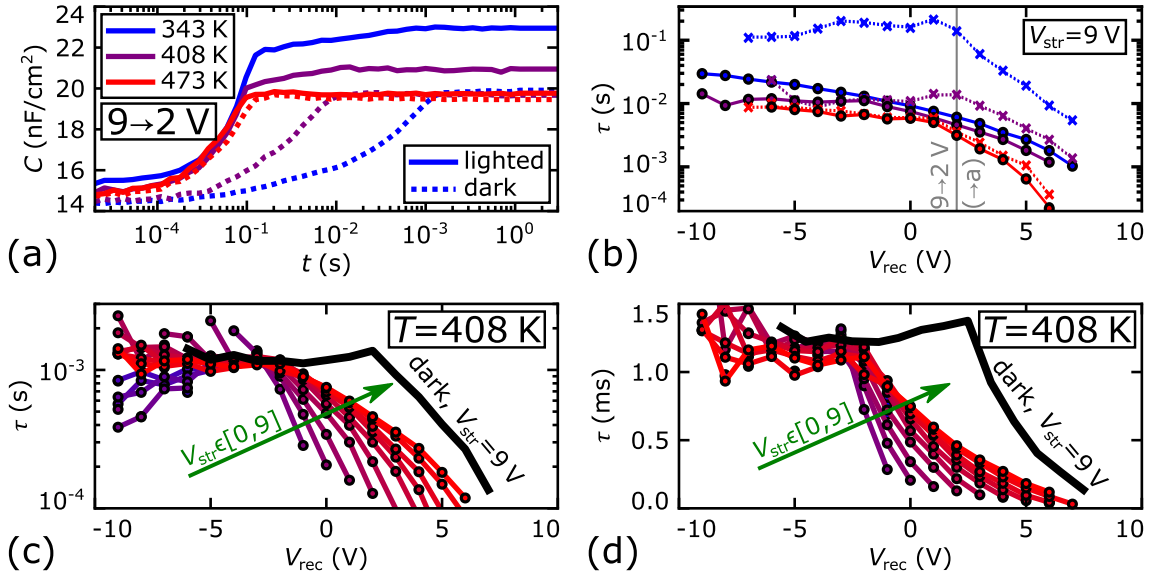


Fig. 3.66: (a) $C(t)$ after bias steps $9 \rightarrow 2$ V in dark and lighted condition for various T . (b) Quantitative analysis of trapping time constants τ for $V_{\text{str}} = 9$ V as a function of V_{rec} for various T . (c,d) τ for various V_{str} vs. V_{rec} at $T = 408$ K demonstrates that τ under light cannot exceed τ in dark.

Fig. 3.66(a) shows $C(t)$ after the bias step $9 \rightarrow 2$ V in dark and illuminated condition for various T . In dark environment τ is solely determined by the conductivity in DBs and consequently decreases with increasing T . In contrast, under illuminated condition τ is independent of T , although the amplitude is not. This makes it inevitable that there is a threshold T at which charge capture/emission via DBs is faster than photo-induced hole capture, i.e. $I_h < I_{\text{DB}}$. We find that this is given for 473 K, which means that above this T light has no influence on the potential distribution anymore as confirmed by SS measurements shown in Fig. 3.60. Due to the different V dependences of I_h and I_{DB} it is also possible that for certain bias steps I_h determines τ while for others I_{DB} does. This is demonstrated in Fig. 3.66(c,d), which shows for 408 K that as soon as τ derived from Eq. (3.24) would become larger than τ in dark condition, I_{DB} becomes dominant. This V dependence is further considered to be the reason for the horizontal shift of the $C_{\text{SS}}-V$ characteristics. The transition from *depletion* to *plateau regime*, which defines this shift, is the bias at which $I_h = I_{\text{DB}}$. For higher biases \mathcal{E}_C and consequently I_{DB} are smaller so that I_h dominates.

In summary, investigations of LUT structures under illumination gave evidence for the existence of donors in GaN:C with a lower boundary of 10^{17} cm^{-3} , solely based on electrical measurements. We found that illumination with $E_{h\nu} > E_{\text{bg}}$ results in significant capture of holes and consequently

positive charge accumulation in GaN:C. As SS and dynamic measurements can only be understood by the defect band model, these measurements provide further evidence for the proposed defect bands.

4

Extension of LUT concept to multilayer structures and AlGaN:C: Interaction of (Al)GaN:C with other layers

In Chapter 3 we discussed in very detail how GaN:C behaves within simple LUT structures in every condition regarding temperature and bias. The reason why we want to understand GaN:C is to understand and predict the behavior of multilayer stacks containing GaN:C layers as used in HEMT buffers. Consequently, the next step is to verify if the proposed physical model is capable of explaining the electrical behavior of simple multilayer structures. Therefore, we use the LUT approach but instead of the single GaN:C layer we use different multilayer stacks. In order to simplify discussion we present in the first section the physical GaN:C model in a simplified way. In order to demonstrate its peculiarities and effects we will apply it in the first part to simple hypothetical, i.e. not existing, structures as shown in Fig. 4.1(a-d) and describe their hypothetical electrical behavior. Additionally, we discuss the standard GaN:C LUT structure S_{10} (Fig. 4.1(e)) using the simplified model. In the second part, samples analogous to S_{10} but with an additional GaN:uid layer on top as schematically depicted in Fig. 4.1(f) are investigated. Finally, the third part is dedicated to discussion of AlGaN:C layers and the effects at GaN:C/AlGaN:C and AlGaN:C/GaN:C interfaces, based on samples shown in Fig. 4.1(g,h).

4.1 Simplification of GaN:C model and application to simple fictive multilayer structures

First, we simplify the complexity of the electrical behavior of GaN:C, explained in detail in Section 3 to a slightly more phenomenological picture. Fig. 4.2 shows band diagrams for the simplest possible

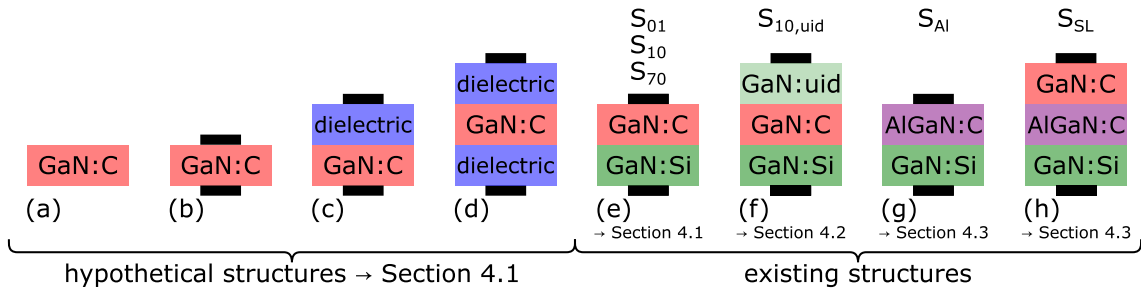
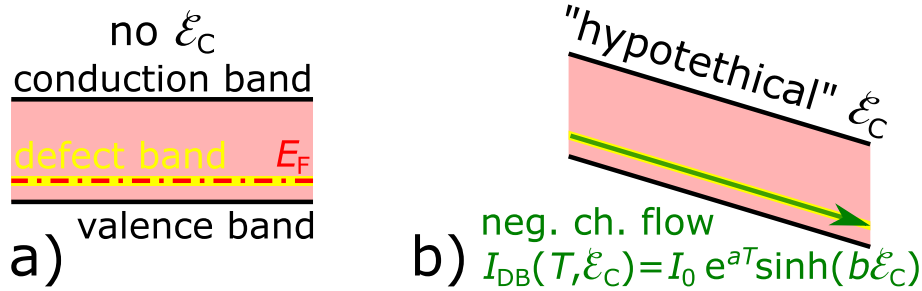


Fig. 4.1: Schematic set of LUT structures discussed within this chapter.


 Fig. 4.2: Simplified model of a hypothetical GaN:C layer with (a) no electric field \mathcal{E}_C and (b) with a hypothetical \mathcal{E}_C , which causes charge flow, indicated by the green arrow.

structure, which is a GaN:C layer without any contacts or adjacent layers. E_F is pinned to $E_{acc} = 0.7 \text{ eV}$. Due to this deep pinning level (i.e. large $|E_{CB} - E_{acc}|$ and $|E_{acc} - E_{VB}|$) we completely ignore conduction in CB and VB so that charge transport through GaN:C can occur only via DBs. The DB energy level is also considered at E_{acc} and currents via DBs follow (see Tab. 3.4 and Eq. 3.20):

$$I_{DB}(T, \mathcal{E}_C) = \text{sgn}(\mathcal{E}_C) I_0 e^{aT} \sinh(b\mathcal{E}_C), \quad (4.1)$$

with values for GaN:C with $[C] = 10^{19} \text{ cm}^{-3}$ derived from S_{10} of $I_0 = 2.5 \times 10^{-4} \text{ A cm}^{-2}$, $a = 0.033 \text{ K}^{-1}$ and $b = 2.3 \times 10^{-7} \text{ m V}^{-1}$.

Apart from the low conductivity, GaN:C could also be imagined as a metal instead of a semiconductor. Like in a metal, in case of $\mathcal{E}_C \neq 0$ negative charges flow in DBs in opposite direction of \mathcal{E}_C as depicted in Fig. 4.2(b). Within this thesis we consider in DBs propagation of negative charges, but this is only arbitrary convention. We cannot distinguish between holes propagating in one or electrons propagating towards the opposite direction. For the DOS in DBs we consider N_{acc} and for rough estimations $N_{acc} = 0.75 \times [C]$. To take into account the unoccupied donors, we consider a positive fixed space charge of $N_{don} \times q$ and for rough estimations $N_{don} = 0.25 \times [C]$. In neutral state this fixed charge is compensated by the same density of acceptors being occupied, i.e. $N_{acc}(-) = N_{don}(+) = N_{don}$ and E_F pins approximately at E_{acc} . Consequently, for $E_F \ll E_{acc}$ and completely unoccupied DBs a positive space charge density of N_{don} forms, while for $E_F \gg E_{acc}$ and completely occupied DBs a negative space charge density of $N_{acc}^* = N_{acc} - N_{don}$ forms.

Ohmic contact/GaN:C/Ohmic contact

In the simplest case we put "ideal barrier-free" contacts on both sides of GaN:C as shown in Fig. 4.3(a), resulting for $V = 0$ in no charge accumulation. As "ideal barrier-free" contacts we

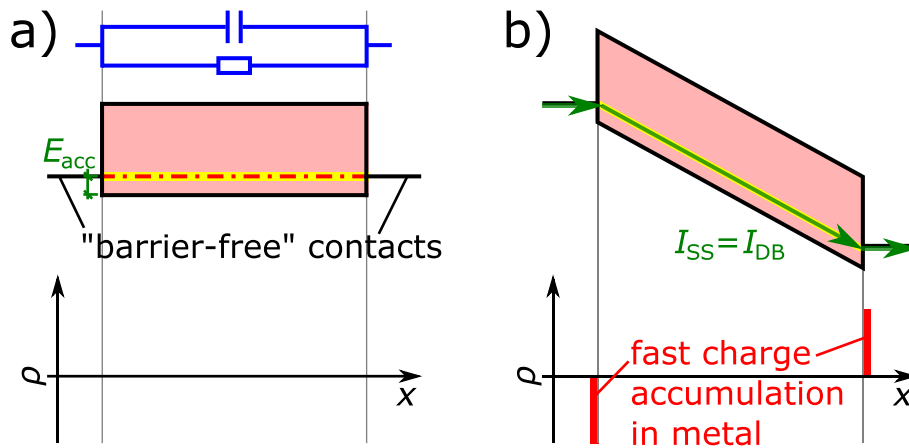


Fig. 4.3: Schematic band diagrams and equivalent circuit on top and space charge density (ρ) distribution on bottom for a hypothetical GaN:C layer between two ideal "barrier-free" contacts for (a) $V = 0$ and (b) $V \neq 0$.

consider contacts that do not form any band bending at the metal/GaN:C interface for $V = 0$, i.e. no surface states and the work function of the metal being by $(E_{bg} - E_{acc})$ larger than the electron affinity in GaN. After applying bias in (b), negative charges from the left side propagate towards the right side, resulting in SS current $I_{SS} = I_{DB}$, determined solely by the conduction in DBs. As there are 1) no energy barriers for negative charge injection from the left metal into defect bands in GaN:C, 2) no barriers for negative charge injection from the defect bands to the right electrode, and 3) the metals are more conductive than the defect bands; charge accumulates only in the metals as shown in Fig. 4.3(b). This phenomenon is known as Maxwell-Wagner effect and describes that at the interface of two layers with different resistances charge accumulates, for details see [Jam+06].

Ohmic contact/GaN:C/dielectric

Next, we insert an "ideal" dielectric between contact and GaN:C on the right side, see Fig. 4.4(a). As "ideal" we define a dielectric without defects and leakage current, with large conduction and valence band offsets and a dielectric's permittivity equal to GaN:C's permittivity. Consequently, directly after applying bias in (b) the same electric field occurs in both layers. The equal permittivity is only for simplification reasons, for different values electric fields in GaN:C and dielectric would be different. Anyway, in quasistatic state (QS) in Fig. 4.4(b) charges have accumulated in the metal and an electric field \mathcal{E}_C exists in GaN:C, resulting in negative charge transport from its left side towards its right side. For every charge propagating towards the right side, another negative charge is injected from the left contact. On the right side however, charges have to overcome a large potential barrier to pass the dielectric and get to the right electrode. Either electrons have to overcome φ_{CB} or holes can be injected from the right contact by overcoming φ_{VB} . Due to the negligible probability of these processes we can ignore leakage current through the dielectric and therefore through the entire structure completely. As a consequence, negative charge accumulates in GaN:C next to the interface with the dielectric by occupying all carbon acceptors next to the interface, resulting in a space charge density of N_{acc}^* . The accumulating negative charge decreases \mathcal{E}_C and therefore I_{DB} until in SS in Fig. 4.4(c) $\mathcal{E}_C = 0$, the transient current $I_{DB} = 0$ and the entire

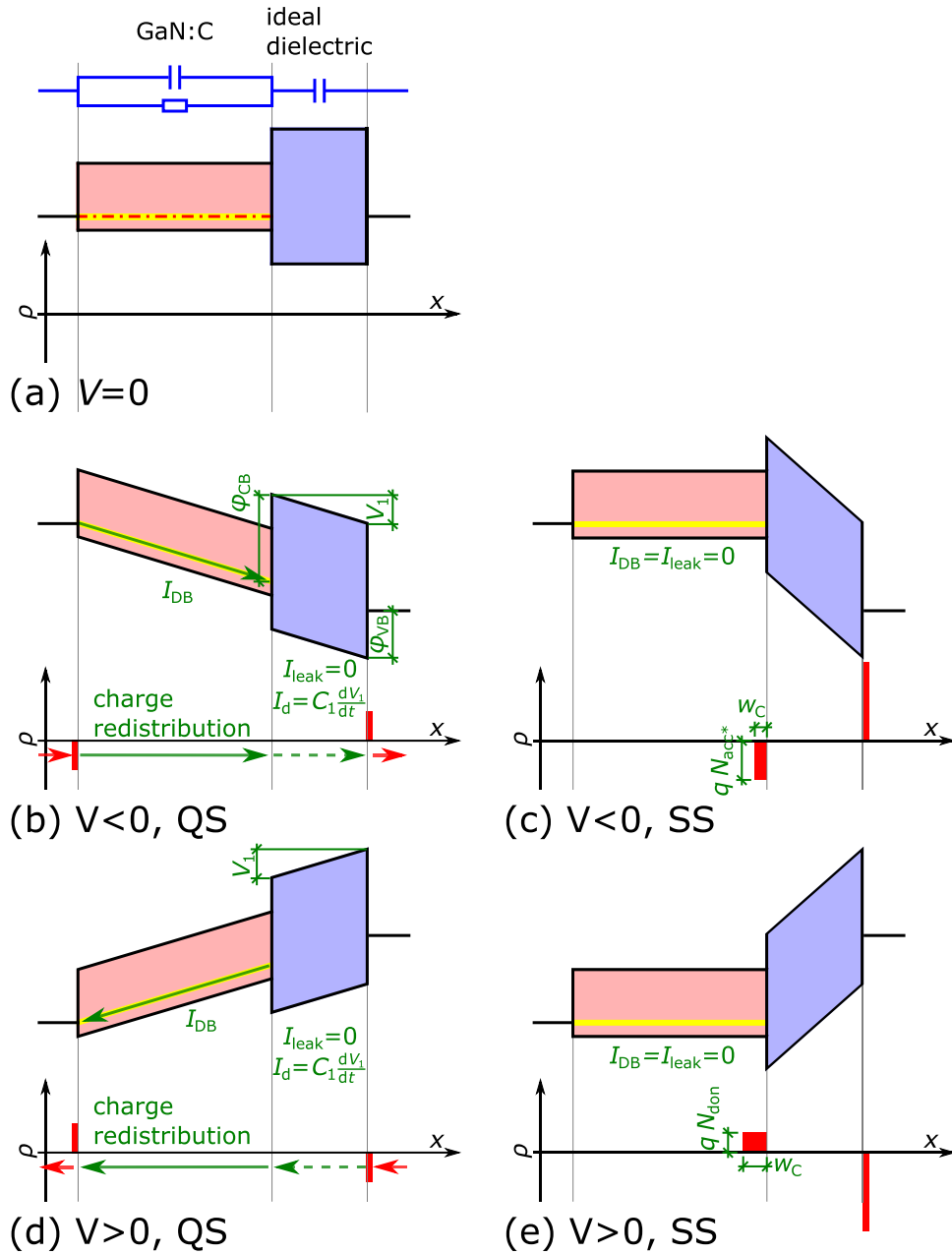


Fig. 4.4: Schematic band diagrams and equivalent circuit on top and charge distribution on bottom for a hypothetical structure consisting of a GaN:C layer and an "ideal" dielectric (with same permittivity as GaN:C) between two ideal "barrier-free" contacts. After $V = 0$ in (a) a negative bias is applied on the left contact. (b) As charge transport is many orders of magnitude faster in the metal than in GaN:C, there is a quasistatic state (QS), in which charges already accumulated in the metal but no charge transport through GaN:C occurred yet. (c) After longer recovery time also charge transport through GaN:C occurred, resulting in SS. (d,e) are analogous to (b,c) but for positive bias on the left contact. Arrows indicate apparent (transient) negative charge transport, whereby solid lines represent "real" charge transport (i.e. "conduction current") while dashed lines represent displacement current I_d ; C_1 is the capacitance of ideal dielectric.

potential drops in the dielectric. The width of occupied acceptors next to the GaN:C/dielectric interface w_C establishes at a level so that the equivalent sheet charge density $N_{acc}^* \times q \times w_C$ equals the sheet charge density in the right metal. As discussed in Section 3.2.2 and 3.4.2 the finite N_{acc}^* results in finite w_C and therefore a finite potential drop in GaN:C ($V_{GaN:C}$), however for sufficiently high carbon concentration $V_{GaN:C}$ should be small. For the sake of simplicity we neglect w_C and $V_{GaN:C}$ in the schematic band diagrams within this section.

Fig. 4.4(d,e) are analogous to (b,c) but for positive bias. In this case, in QS condition \mathcal{E}_C causes negative charge transport from the GaN:C/dielectric interface towards the left electrode, leaving carbon acceptors unoccupied and therefore generating a positive space charge of $N_{don} \times q$ due to the still positively charged unoccupied donors. As N_{don} is in general different from N_{acc}^* the width w_C is different for positive and negative bias.

Dielectric/GaN:C/dielectric

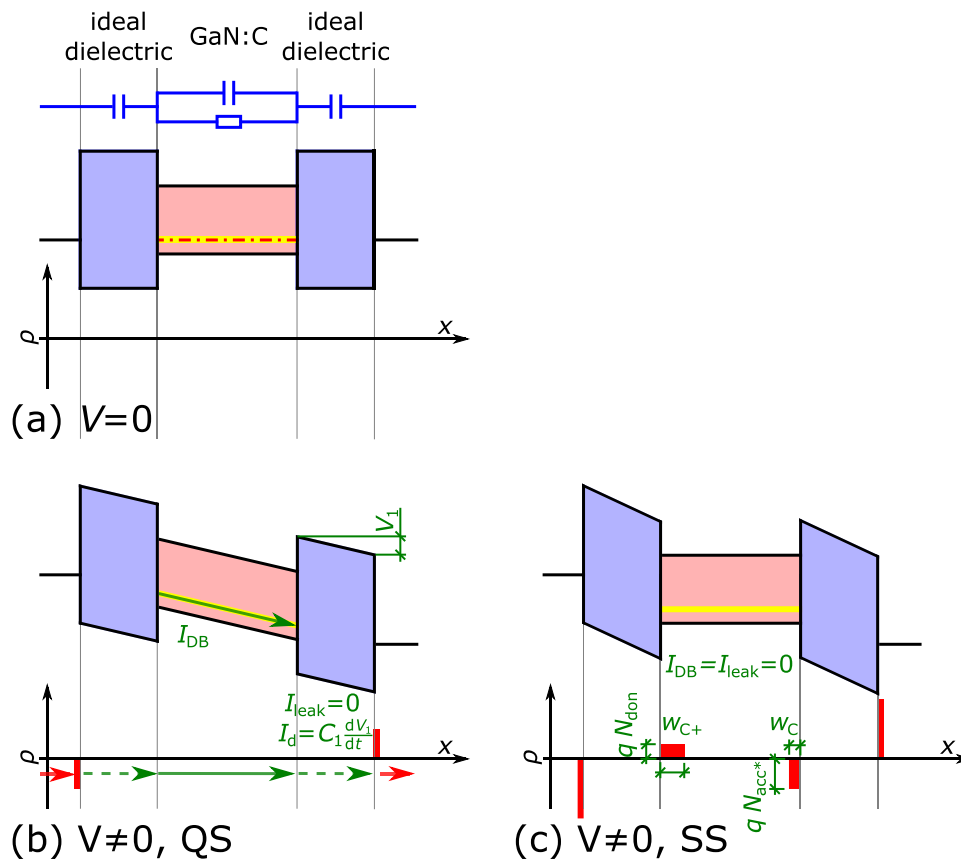


Fig. 4.5: Schematic band diagrams and equivalent circuit on top and charge distribution on bottom for a hypothetical structure consisting of a GaN:C layer sandwiched between ideal dielectrics and ideal "barrier-free" contacts. After (a) $V = 0$ a bias is applied, leading to (b) QS condition and finally (c) SS condition (for definition see caption Fig. 4.4). Arrows indicate apparent (transient) negative charge transport, whereby solid lines represent "conduction current" while dashed lines represent displacement current I_d ; C_1 is the capacitance of ideal dielectric.

In the next structure in Fig. 4.5, GaN:C is sandwiched between two dielectrics of same thickness. Due to the symmetry of the structure, positive and negative bias are symmetric. In QS state in

Fig. 4.5(b), \mathcal{E}_C causes negative charge transport in GaN:C from left to right. The dielectrics prevent any charge injection from the electrodes, so that the charge transport in GaN:C leaves unoccupied acceptors on the left side and fully occupied acceptors on the right side. SS is reached in Fig. 4.5(c) when $\mathcal{E}_C = 0$. Due to the missing charge injection the total charge in GaN:C has to be 0, i.e. $N_{\text{don}}w_{C+} = N_{\text{acc}}^*w_C$.

GaN:Si/GaN:C (S_{10})

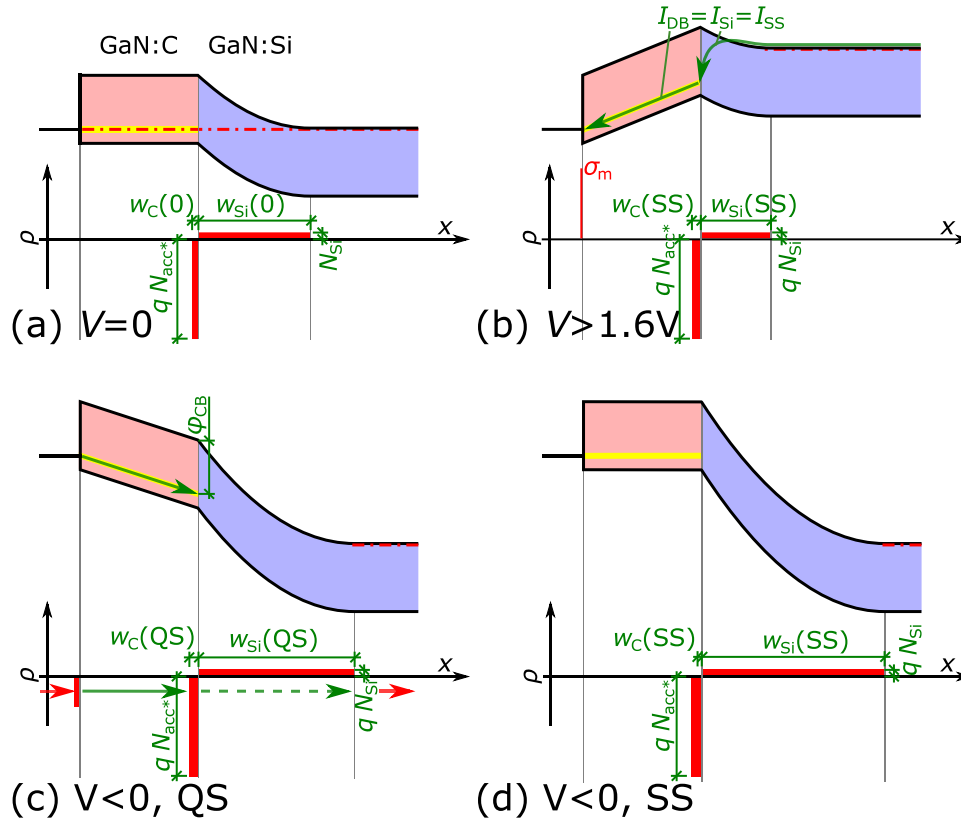


Fig. 4.6: Schematic band diagrams on top and charge distribution on bottom for S_{10} . (a) SS condition for the quiescent bias $V = 0$. (b) Increasing the bias from the quiescent to a more positive value results in "ultrafast" electron injection from GaN:Si to GaN:C acceptors, establishing SS. Increasing the bias from the quiescent to a more negative value results first in (c) QS condition, in which charges already redistributed in GaN:Si but not in GaN:C and finally in (d) SS condition, in which charges also redistributed in GaN:C. For better readability, values of w_C and N_{Si} are multiplied by a factor of 3. Arrows indicate apparent (transient) negative charge transport, whereby solid lines represent "conduction current" while dashed lines represent displacement current I_d

Although discussed in detail in Section 3 we briefly show the application of the proposed simplified model to S_{10} as it demonstrates well its simplicity. Fig. 4.6(a) shows the 0 V band diagram and charge distribution. In contrast to the structures before, this one is not charge-free for $V = 0$. As E_F is pinned in bulk GaN:C 2.7 eV below E_{CB} and in bulk GaN:Si few tens of meV below E_{CB} , charge occurs in their interface region that bends CB and VB. As N_{acc}^* is by a factor of roughly 50 larger than the donor concentration in GaN:Si (N_{Si}), depletion widths in GaN:Si (w_{Si}) are by the same factor larger than w_C .

For a bias step to positive values exceeding roughly 1.6 V (see Section 3.3.3), as shown in Fig. 4.6(b), w_{Si} and φ_i decrease, resulting in a substantial increase of the injection current I_{Si} . As the increase of I_{DB} is compared to I_{Si} negligible, all injected carriers have to accumulate in GaN:C acceptors next to the GaN:Si/GaN:C interface. Thus, φ_i rises and I_{Si} decreases until $I_{\text{Si}} = I_{\text{DB}}$. Considering e.g. a thermal injection mechanism, I_{Si} increases roughly exponentially with decreasing φ_i , leading to the observed "ultrafast" charge accumulation.

A bias step to negative values is similar to the GaN:C/dielectric structure, shown in Fig. 4.4(b,c). w_{Si} and therefore the positive charge in GaN:Si rises, which is compensated by accumulation of negative charge in the top metal, QS establishes as shown in Fig. 4.6(c). The apparent $\mathcal{E}_C \neq 0$ results in negative charge propagation from left side of GaN:C towards the right side. As charges can effectively be injected from the metal to GaN:C but they cannot overcome the barrier φ_{CB} , $I_{\text{DB}} \gg I_{\text{Si}} \approx 0$. Consequently, negative charge accumulates in acceptors in GaN:C next to its interface to GaN:Si, SS is established when $\mathcal{E}_C = 0$.

4.2 Electrical behavior of GaN:C/GaN:uid multilayers (sample S_{10,uid})

After discussion of the electrical behavior of fictive multilayer structures and the already well-known sample S₁₀, we investigate a structure analogous to S₁₀ but with an additional 110 nm thick unintentionally doped GaN (GaN:uid) layer on top (i.e. S_{10,uid}). Although the term "unintentionally doped" conjectures no doping, in reality there are always background donors. Most prominent are Si impurities, which act as shallow donors and make GaN:uid slightly n-type. Concentrations (N_{uid}) are expected to be in the range of 10^{16} cm^{-3} . GaN:C/GaN:uid multilayer stacks are widely used in HEMT stacks, e.g. the GaN channel below the 2DEG is commonly GaN:uid with the GaN:C buffer below. This bilayer has been the topic of several publications [Ure+17; Ure+14b], which emphasize the importance of considering the GaN:uid layer in addition to the GaN:C stack for the discussion of detrimental dynamic effects. For example, Uren et al. [Ure+17] claim that in order to suppress CC, GaN:uid with a certain "leakiness" is required. The LUT principle enables for the first time investigation of simple GaN:C/GaN:uid bilayers separated from the rest of the HEMT stack. Analogous to the previous chapter, static analysis of these structures in the first part is followed by dynamic characterization in the second part.

4.2.1 Static behavior of sample S_{10,uid}

Fig. 4.7 compares the SS electrical behavior of S_{Schottky} , S₁₀ and S_{10,uid}. The general electrical behavior is similar to S₁₀ with distinctive *depletion* ($V \lesssim 1.5 \text{ V}$), *plateau* ($1.5 \text{ V} \lesssim V \lesssim 35 \text{ V}$) and *Ohmic regimes* ($V \gtrsim 35 \text{ V}$). Fig. 4.7(c) demonstrates that also $1/C_{\text{Si}}^2 - V$ is mainly linear in the *depletion regime*, indicating that all potential drops in GaN:Si, which is increasingly depleted, as in S₁₀. Below roughly -30 V distortions from the linear relation start, we suppose that then some potential starts to drop in GaN:C or GaN:uid. Fig. 4.7(c) reveals a significantly steeper slope for S_{10,uid}, resulting in an extracted donor concentration of $2 \times 10^{16} \text{ cm}^{-3}$, which is more than a factor 4 less than in S₁₀. This leads to largely increased depletion widths and together with the additional GaN:uid layer to the significantly lower capacitance in Fig. 4.7(b). We further observe in S_{10,uid} much smaller currents than in S₁₀; with $e^{b\mathcal{E}_C}$ dependence but a significantly smaller slope b . The

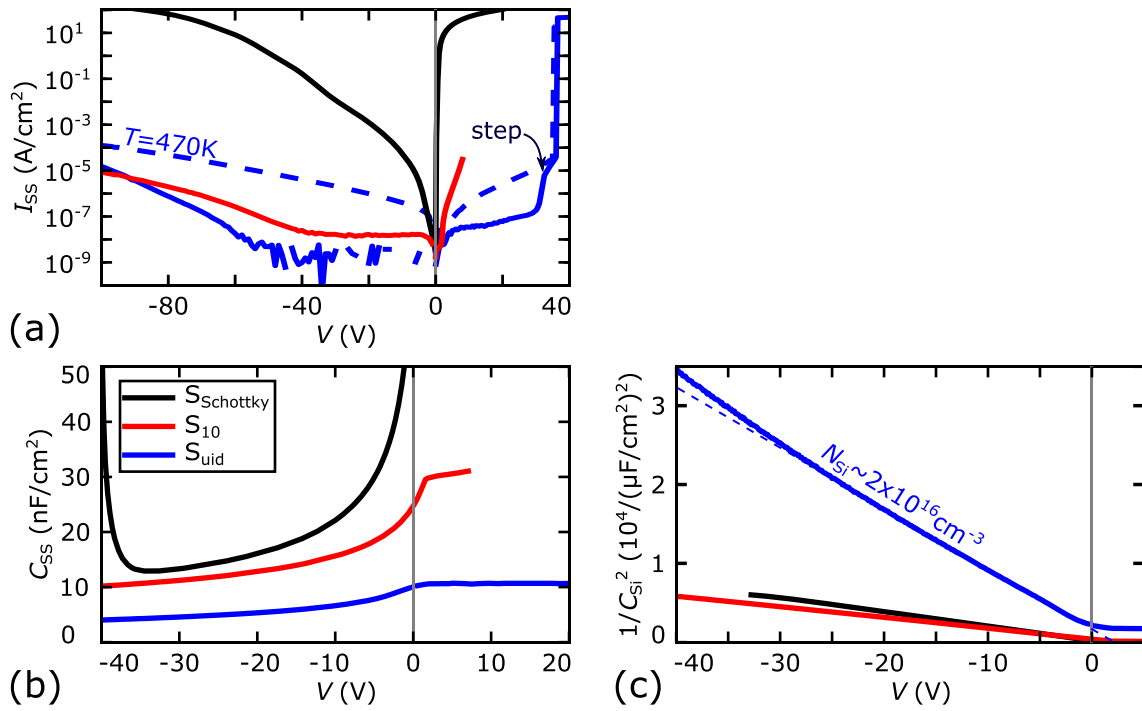


Fig. 4.7: (a) I_{SS} - V and (b) C_{SS} - V characteristics as well as extracted $1/C_{Si}^2 - V$ for $S_{Schottky}$, S_{10} and $S_{10,uid}$ at room temperature. The dashed line in (a) additionally shows $S_{10,uid}$ under elevated T .

transition to the *Ohmic regime* occurs at a similar I_{SS} but at much higher biases of roughly 35 V. In the following we explain these empiric findings using the simple GaN:C model.

Fig. 4.8 shows band diagram and charge distribution for $V = 0$, extracted similar as in sample S_{10} , described in detail in Section 3.2.1. The potential in GaN:Si until the GaN:Si/GaN:C interface potential (φ_i) can simply be extracted from the C_{SS} - V characteristics. A potential drop in GaN:C ($V_{GaN:C}$) is only stable in case of current flow, hence for $I_{SS} = 0$ at $V = 0$ also $V_{GaN:C}$ has to be zero, resulting in flatband in GaN:C. Further, the potential at the top of GaN:uid ($\varphi_{S,CB}$) can be calculated from the difference of the electron affinity of GaN and the work function of the metal, giving a value of roughly 0.2 V, as described in Section 3.2.2. In reality, the exact value of $\varphi_{S,CB}$ might differ significantly but as this has no influence on qualitative statements, for the sake of simplicity in the following we consider $\varphi_{S,CB} = 0.2$ V. This requires significant voltage drop in GaN:uid of $V_{GaN:uid} = E_{bg} - E_{acc} - \varphi_{S,CB} = 2.5$ V. Fig. 4.8 demonstrates that consequently E_F in GaN:uid is between 0.2 and 2.7 eV below E_{CB} , resulting in GaN:uid being completely depleted (i.e. donors are unoccupied, hence positively charged), and no free electrons exist. The low N_{uid} in the range of $\lesssim 10^{16} \text{ cm}^{-3}$ leads to such a small space charge that the resulting potential drop is less than 0.1 V. N_{acc}^* is more than 500 times larger, hence space charge regions in GaN:C lead to much larger band bending. Consequently, the charge required to establish the electric field and potential drop in GaN:uid ($V_{GaN:uid}$) has to be located in GaN:C and the top metal as demonstrated in Fig. 4.8. The sum of the positive charge in the metal σ_{Ti} , the negative charge in GaN:C ($N_{don} \times q \times w_{C+}$) and the negligible positive charge in GaN:uid has to be zero. Analogous, the sum of negative charge in the bottom area of GaN:C ($N_{acc}^* w_C$) and the positive charge from depleted GaN:Si ($N_{Si} \times q \times w_{Si}$) has to be zero.

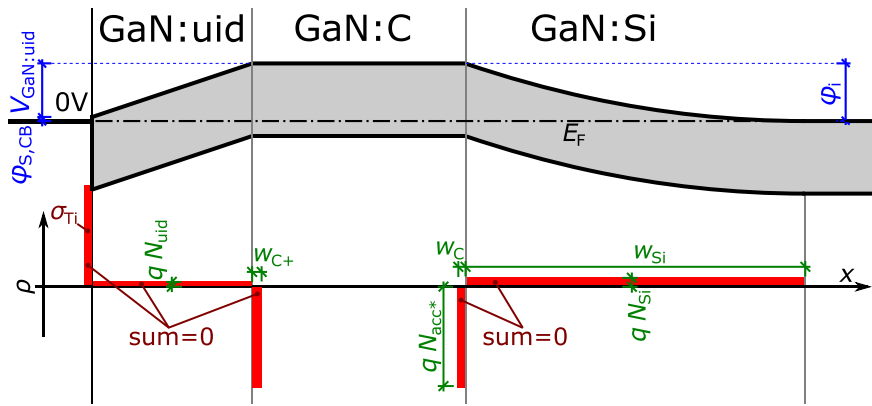


Fig. 4.8: Calculated band diagram on top and charge distribution on bottom for S_{10,uid} at $V = 0$. For better readability N_{uid} and N_{Si} are magnified by a factor of 20 and w_{C+} and w_C by a factor of 5. Calculations base on data shown in Fig. 4.7.

In a next step, we derive band diagrams dependent on the bias, as shown in Fig. 4.9. As long as $I_{SS} = 0$ as in the *depletion regime*, also $V_{GaN:C} = 0$. Consequently, the voltage has to drop either in GaN:uid or in GaN:Si by an increasing w_{Si} . In theory, for low biases $V_{GaN:uid}$ could decrease slightly, but only to a value where it is still sufficiently high to prevent major charge injection to GaN:C, clearer understanding is gained from dynamic measurements in Section 4.2.2. Anyway, this would result in a constant w_{Si} and corresponding constant capacitance for low reverse bias. Its absence in Fig. 4.7(b) proves that $V_{GaN:uid}$ does not change significantly and we further consider that in the *depletion regime* only φ_i increases with negative V , see the representative case of $V = -10$ V in Fig. 4.9.

In contrast to *depletion regime*, in the *plateau regime* for 1.5 V $\lesssim V \lesssim 35$ V the value of φ_i stays roughly constant and the major part of the voltage drops in GaN:C and GaN:uid. As I_{SS} is not zero anymore, the flatband-condition in GaN:C does not hold anymore. As the capacitance delivers only φ_i there is no direct way to distinguish how much of the voltage drops in GaN:C ($V_{GaN:C}$) and how much in GaN:uid ($V_{GaN:uid}$). However, from S₁₀ we know $I_{SS} = I_{DB} = I_0 e^{aT} \sinh(b\mathcal{E}_C)$ with values for the constants I_0 , a and b . Consequently, if we know I_{SS} we can indirectly derive $V_{GaN:C}$. Band diagrams in *plateau regime* in Fig. 4.9 base on this assumption. They reveal that for low biases the major part of the voltage drops in GaN:uid up to a value of roughly 30 V. Above this value I_{SS} in S_{10,uid} shown in Fig. 4.7(a) significantly increases. Between 30 and 35 V I_{SS} increased in a way so that mainly $V_{GaN:C}$ increases while $V_{GaN:uid}$ remains constant. We speculate that the electric field in GaN:uid reaches a critical value (≈ 2 MV cm⁻¹), above which the current increases significantly. This could be related e.g. to a trap-assisted-tunneling mechanism that enables injection of charges from DBs to GaN:uid CB. Trap-assisted-tunneling is in literature frequently considered (explicitly or implicitly) as conduction mechanism, enabling current flow between 2DEG and GaN:C VB through a GaN:uid layer [Li+04; Sha+11; Ure+14b; Ure+17], however no details on its nature were provided yet. Above 35 V the transition to the *Ohmic regime* occurs in the same way as in S₁₀, described in Section 3.5.

An interesting finding is that this current step at roughly 30 V occurs only for $T \lesssim 400$ K; Fig. 4.7(a) shows $I_{SS}-V$ also for $T = 470$ K without the step but with steeper slope. This can be understood by the different T dependences of conduction via DBs in GaN:C and the conduction mechanism in GaN:uid. For higher T an increasing amount of the potential drops in GaN:C rather

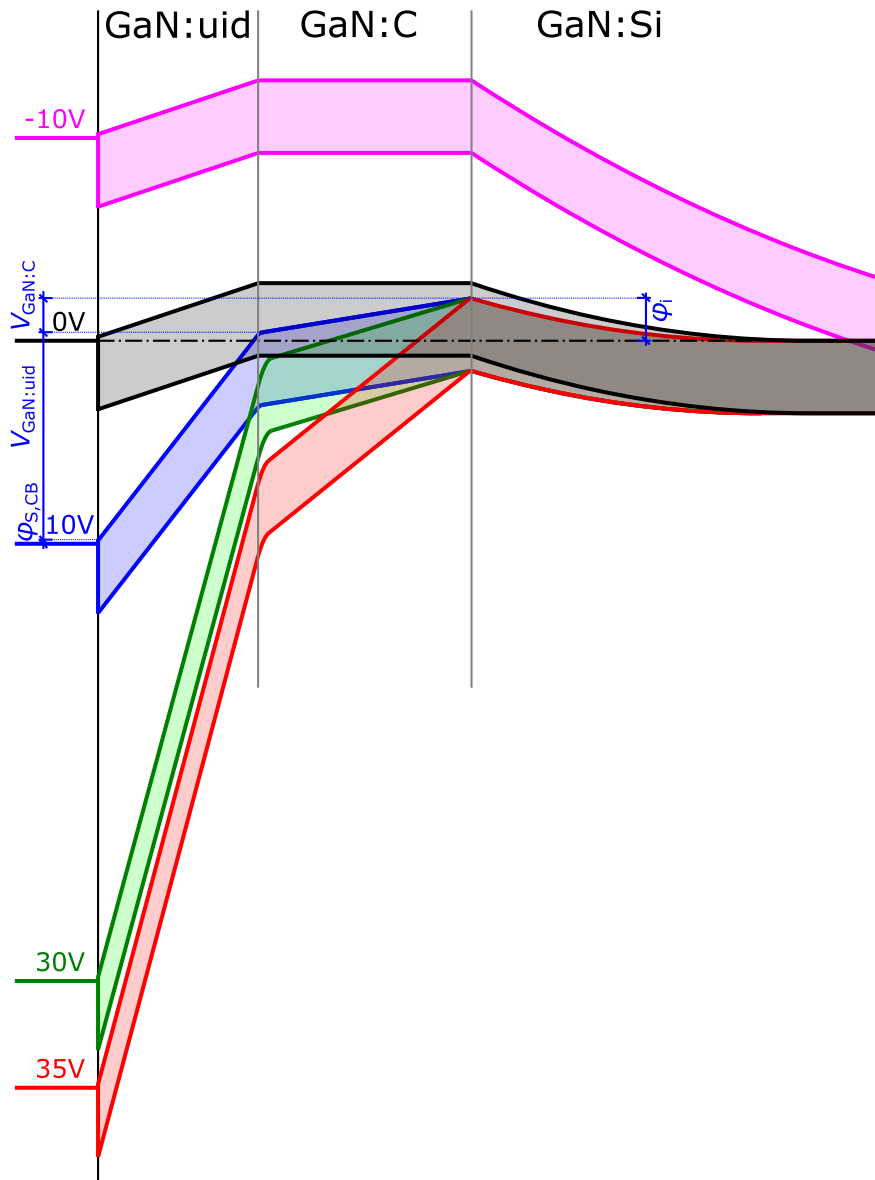


Fig. 4.9: Calculated band diagrams for S_{10,uid} at 300 K for several bias conditions. Calculations base on data shown in Fig. 4.7.

than in GaN:uid, resulting in higher I_{SS} and therefore steeper slope in $I_{SS}-V$. Hence, for $T = 470$ K the critical electric field in GaN:uid is not reached before the transition to the *Ohmic regime*.

In summary, static analysis of S_{10,uid} confirmed that GaN:C layers effectively suppress charge transport in CB and VB. However, once this is ensured, a depleted GaN layer such as GaN:uid is a better insulator as it does not feature conductive DBs. This suggests that multilayer structures with alternating carbon-doped and not-carbon-doped layers should provide good insulating properties, even in both polarities. Furthermore, the current filamentation/”breakdown”, i.e. the transition to the *Ohmic regime* occurs for the GaN:C/GaN:uid bilayer at much higher biases than it would occur in a pure GaN:C layer of same thickness. E.g. S_{10b} is of comparable thickness as S_{10,uid} but shows a filamentation voltage of only ≈ 15 V which is a factor 2 less than in S_{10,uid}.

4.2.2 Dynamic behavior of S_{10,uid}

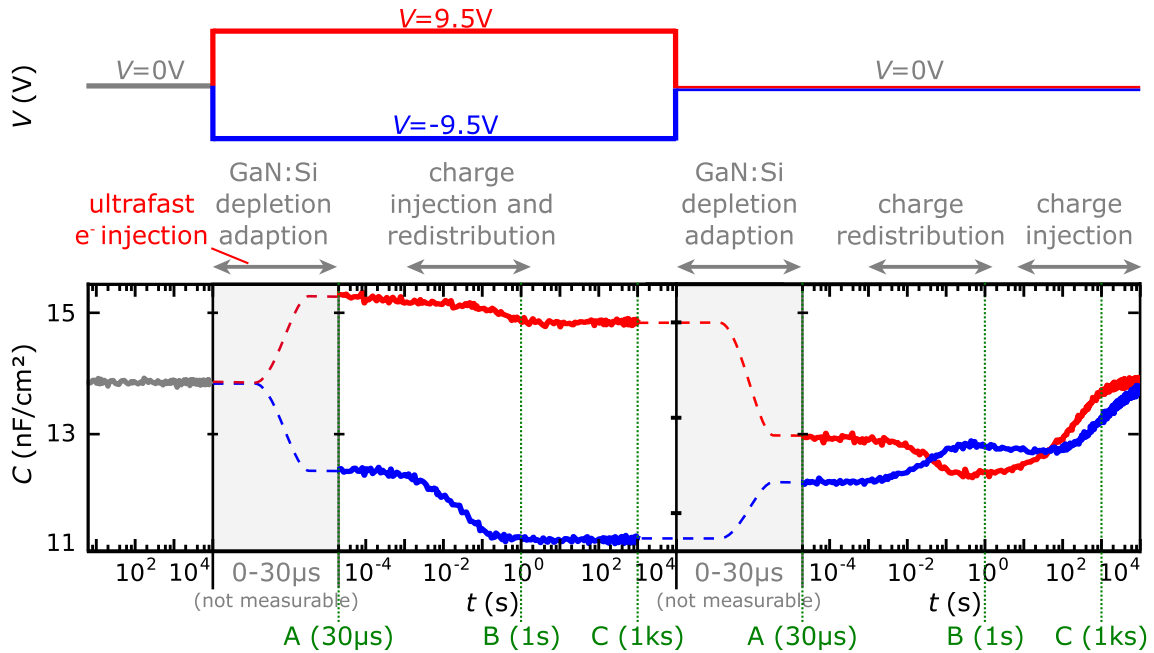


Fig. 4.10: Transient capacitance for S_{10,uid} during bias step from 0 to ± 9.5 V and back with description of occurring processes in every time range. For points in time marked with green letters 'A'-'C' band diagrams and potential distributions are calculated and shown in Fig. 4.11-4.15.

After investigation of the SS behavior of S_{10,uid} we are interested in the processes that lead to SS, i.e. the transport of charges through the single layers and their accumulation. Therefore, we perform bias steps and measure the transient capacitance as illustrated in Fig. 4.10. We observe that $C(t)$ after applying positive or negative biases are similar to the ones for sample S₁₀, even with identical time constants. For returning to 0 V there is also a capacitance change with same time constant as in S₁₀, but in addition there is a second much slower capacitance change. In order to understand the transient behavior, we will discuss the relevant processes for all four representative bias steps in the following:

a) Bias step $0 \rightarrow -9.5$ V:

We start with detailed discussion for the bias step from 0 to -9.5 V. Additionally to the SS band diagram in Fig. 4.11(b), we derive also the band diagram in the quasistatic state (QS) in (a), where the depletion width in GaN:Si already adapted to the new bias but charge distribution in GaN:C (i.e. charge transport in DBs) did not take place yet. In theory, one could calculate the charge distribution at 0 V, calculate φ_i in QS at -9.5 V from the capacitance and use the unaltered charge distribution in order to calculate the exact band diagram in the entire structure. However, there are much larger uncertainties in $S_{10,uid}$ concerning the thickness of the GaN:uid layer and N_{Si} than in S_{10} . In combination with the significantly reduced capacitance values down to 1 pF and the worse precision of transient measurements compared to SS measurements, the quantitative analysis with measured capacitances might give an inaccurate result. We instead use only the qualitative evolution of C and refer to the band diagrams as "schematic", see Fig. 4.11.

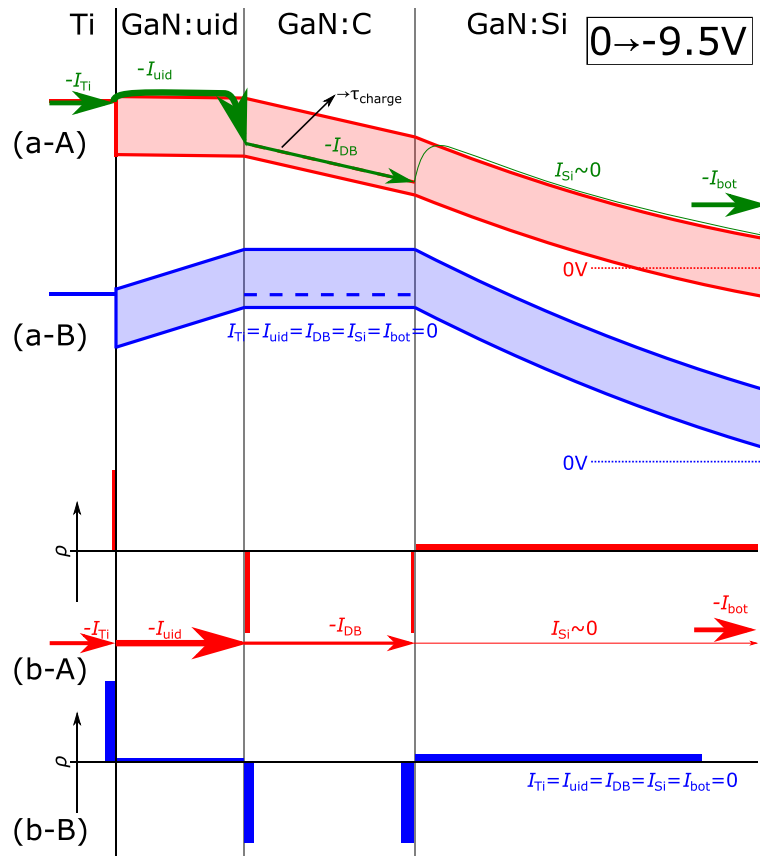


Fig. 4.11: (a) Schematic band diagrams and (b) charge distributions in every layer of $S_{10,uid}$ after a bias step from 0 to -9.5 V. Arrows represent (transient) current flow, whereby their thickness scales with the current; for simplicity displacement currents are not shown. 'A' represents a quasistatic state before charge redistribution occurred in GaN:C while 'B' represents SS. Estimations base on data from Fig. 4.10.

Fig. 4.11(b-A) shows the schematic charge distribution and additionally (a-A) and (b-A) show schematically transient currents through the structure. As throughout the thesis we describe current as flux of negative charges, the arrows in Fig. 4.11 indicate negative charge flow. As this flow is opposite to the electrical current direction they are labeled with a minus-sign. (a-A)

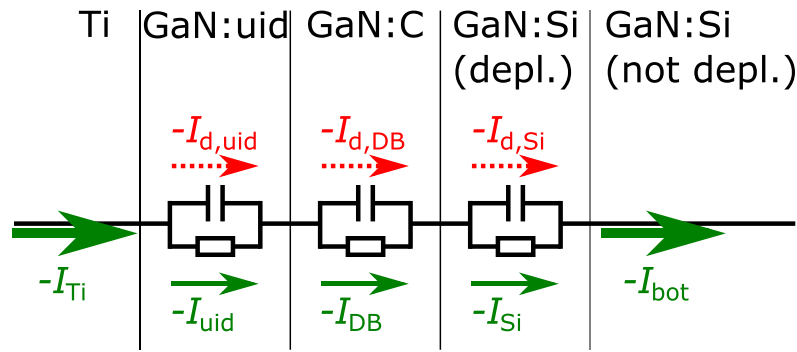


Fig. 4.12: Equivalent circuit of sample $S_{10,uid}$ in QS with "conduction currents" indicated by solid green arrows and displacement currents indicated by dashed red lines.

shows in QS different currents in every layer as displacement currents are not depicted. Fig. 4.12 illustrates an equivalent circuit of $S_{10,uid}$. GaN:uid, GaN:C and (depleted) GaN:Si layers can be considered as three in series connected layers, whereby each can be represented by a capacitance in parallel with a resistor. In QS every layer has a "conduction current" term and a displacement current term ($I_d = C \frac{dV}{dt}$, see also Fig. 4.4) which have to be in sum equal in all layers. As apparent in GaN:uid in Fig. 4.11 this can even lead to displacement currents in opposite directions of the "conduction current", which will in the following be referred to as "current" again.

As in QS in Fig. 4.11(b-A) no charge redistribution took place in GaN:C yet, there is an electric field which determines the current through the defect band (I_{DB}). Due to the large potential barrier of 2.7 eV there is practically no charge injection to GaN:Si, so that the current through GaN:Si (I_{Si}) is negligible. The decreased bias step $|V_{GaN:uid}|$ enables larger current through GaN:uid (I_{uid}). Neglecting a possible Schottky barrier, this leads to substantial I_{uid} and therefore ultrafast negative charge injection into GaN:C until the therefore raised potential barrier decreases I_{uid} to a value in the range of I_{DB} . This process is supposed to be analogous to the ultrafast charge injection for steps to more positive biases in the *plateau regime* in sample S_{10} . I_{Ti} and I_{bot} are equal transient currents at the top and bottom electrodes. The thickness of the arrows in every layer in Fig. 4.11(b-A) scale with the current through this layer. The negative current (I_{Ti}) propagates through Ti, an even larger negative current (I_{uid}) then propagates through GaN:uid. Therefore, not only I_{Ti} is injected into GaN:uid but additionally free electrons from Ti are injected, leaving a more positive charge in Ti, as can be seen by comparison of the charge distributions in (b-A) and (b-B) (i.e. blue area in Ti representing equivalent sheet charge density is larger in (b-B)). As $|I_{uid}| > |I_{DB}|$, analogously in GaN:C near its interface with GaN:uid negative charges accumulate. However, also a great part of the injected carriers propagates through GaN:C (I_{DB}). As $|I_{DB}| > |I_{Si}| \approx 0$ all remaining charges accumulate in GaN:C near its bottom interface with GaN:Si. As $|I_{bot}| > 0$, negative charges have to be emitted from GaN:Si. This happens by an increasing w_{Si} , i.e. in the newly depleted GaN:Si free electrons propagate towards the bottom electrode, leaving behind a positive space charge. Finally, in SS a charge distribution as in Fig. 4.11(b-B) establishes and no transient currents are present anymore.

As for charge injection from Ti via GaN:uid conduction band into GaN:C defect bands no major potential barriers have to be overcome, charge transport in DBs limits charging/discharging processes. This explains the same time constants in the transient capacitance analysis for $S_{10,uid}$ and S_{10} .

b) Bias step $-9.5 \rightarrow 0$ V:

In the following we use the same analysis procedure as before but for stepping the bias back from -9.5 to 0 V. The band diagram in Fig. 4.13(a-A) shows a high φ_i and slightly enhanced $V_{\text{GaN:uid}}$ due to the captured negative charge at -9.5 V. The electric field causes $I_{\text{DB}} \neq 0$ in GaN:C, while I_{Si} and I_{uid} are due to the large potential barriers φ_{Si} and φ_{uid} for electron injection to CB of respective GaN:Si and GaN:uid negligible. Although these barriers are lowered by Poole-Frenkel effect due to electric fields in GaN:Si and GaN:uid, the remaining barrier is still well above $2eV$. Thus, charges first only redistribute within GaN:C until the electric field is almost zero, which is labeled as second quasistatic state 'B'. Although I_{uid} does not increase significantly compared to 'A', for large enough durations the "negligible" current transports a sufficient amount of negative charges from GaN:C via GaN:uid to the top electrode. Due to the long durations also a minor electric field in GaN:C is sufficient to transport also negative charges from the GaN:Si/GaN:C interface to the GaN:C/GaN:uid interface. In theory, we cannot rule out current over GaN:Si but as the w_{Si} is substantially larger in GaN:uid we consider $|I_{\text{uid}}| > |I_{\text{Si}}|$; finally SS establishes.

Concluding, charge redistribution in GaN:C is determined again by I_{DB} . However, due to the absence of DBs in GaN:uid, for charge transport between GaN:C and Ti, negative charges have to be excited from DBs to CB which is a many orders of magnitude slower process than conduction in DBs. Consequently, this process ultimately limits discharging time constants and explains why a combination of GaN:uid and GaN:C layers is substantially more insulating than single GaN:C or GaN:uid layers.

c) Bias step $0 \rightarrow 9.5$ V:

For a bias step from 0 to 9.5 V, shown in Fig. 4.14, analogous to S₁₀ ultrafast electron injection occurs, leading to quasistatic state 'A'. However, while in S₁₀ charge mainly accumulates in GaN:C next to its interface to GaN:Si, in S_{10,uid} some charge also accumulates in GaN:C next to its interface to GaN:uid. For this process negative charges have to propagate through DBs in GaN:C, which explains the observed time constant of DBs, i.e. same τ as in S₁₀. The potential at the upper interface rises and the potential at the bottom interface decreases until all currents finally match and SS is established.

d) Bias step $9.5 \rightarrow 0$ V:

For the bias returning from 9.5 to 0 V, shown in Fig. 4.15, all processes are analogous to returning from -9.5 to 0 V with the only difference that in quasistatic state 'A' the majority of negative charge in GaN:C is stored at its top instead of its bottom. This leads to an electric field in 'A' with opposite sign. Quasi-static states 'B' and SS are again analogous to Fig. 4.13.

Temperature dependence of dynamic behavior of S_{10,uid}

As indicated in Fig. 4.11(a-A) and Fig. 4.13(a-A) we proposed that the charging time constants (τ_{charge}) as well as the fast discharging time constant ($\tau_{\text{disch.,1}}$) are determined by I_{DB} . The slow discharging time constant ($\tau_{\text{disch.,2}}$) on the other hand is determined by the injection of negative charges from GaN:C DBs to the GaN:uid CB, see Fig. 4.13(a-B). In order to verify these statements we perform T -dependent $C(t)$ measurements as depicted in Fig. 4.16(a,b). The T range is limited

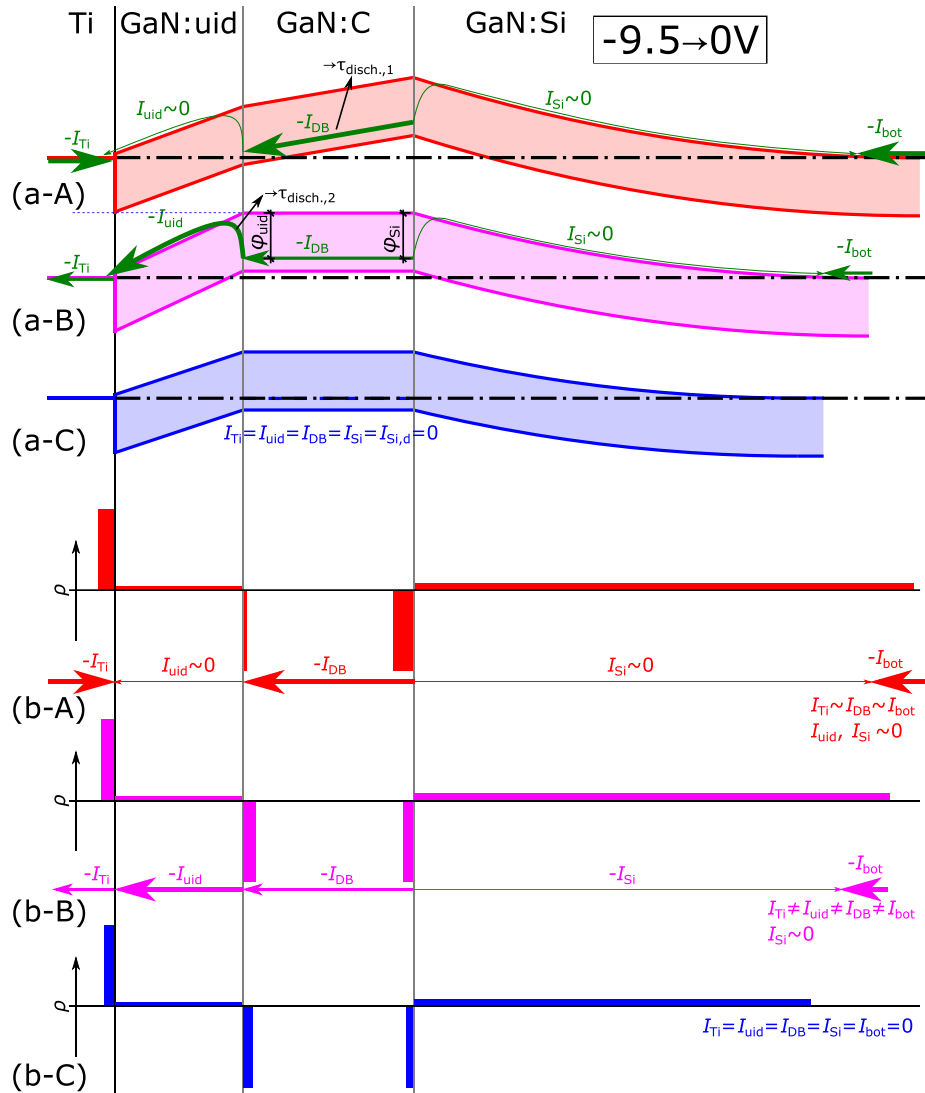


Fig. 4.13: (a) Schematic band diagrams, (b) charge distributions and transient "conduction currents" (represented by arrows) in every layer of S_{10,uid} after a bias step from -9.5 to 0 V. 'A' represents a quasistatic state before charge redistribution occurred in GaN:C, 'B' a quasistatic state in which charge redistribution in GaN:C finished but no charge exchange with electrodes occurred yet. Finally, in 'C' the structure is in SS, details on the evolution in time are provided in Fig. 4.10. Estimations base on data from Fig. 4.10.

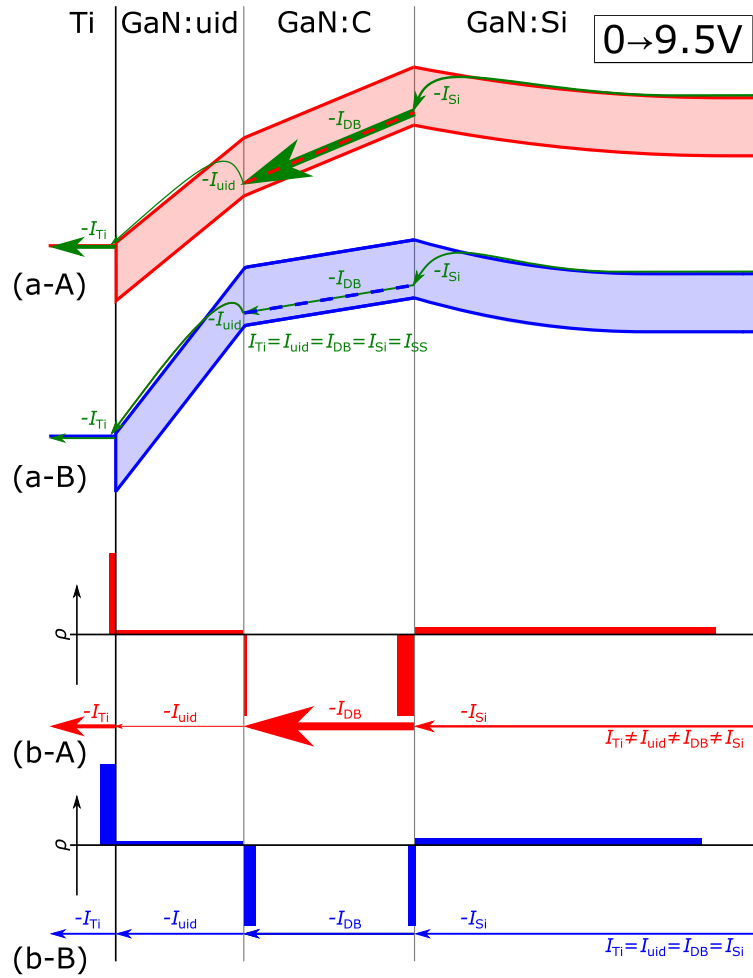


Fig. 4.14: (a) Schematic band diagrams, (b) charge distributions and "conduction currents" (represented by arrows) in every layer of S_{10,uid} after a bias step from 0 to 9.5 V. 'A' represents a quasistatic state before charge redistribution occurred in GaN:C while 'B' represents SS, see also Fig. 4.10. Estimations base on data from Fig. 4.10.

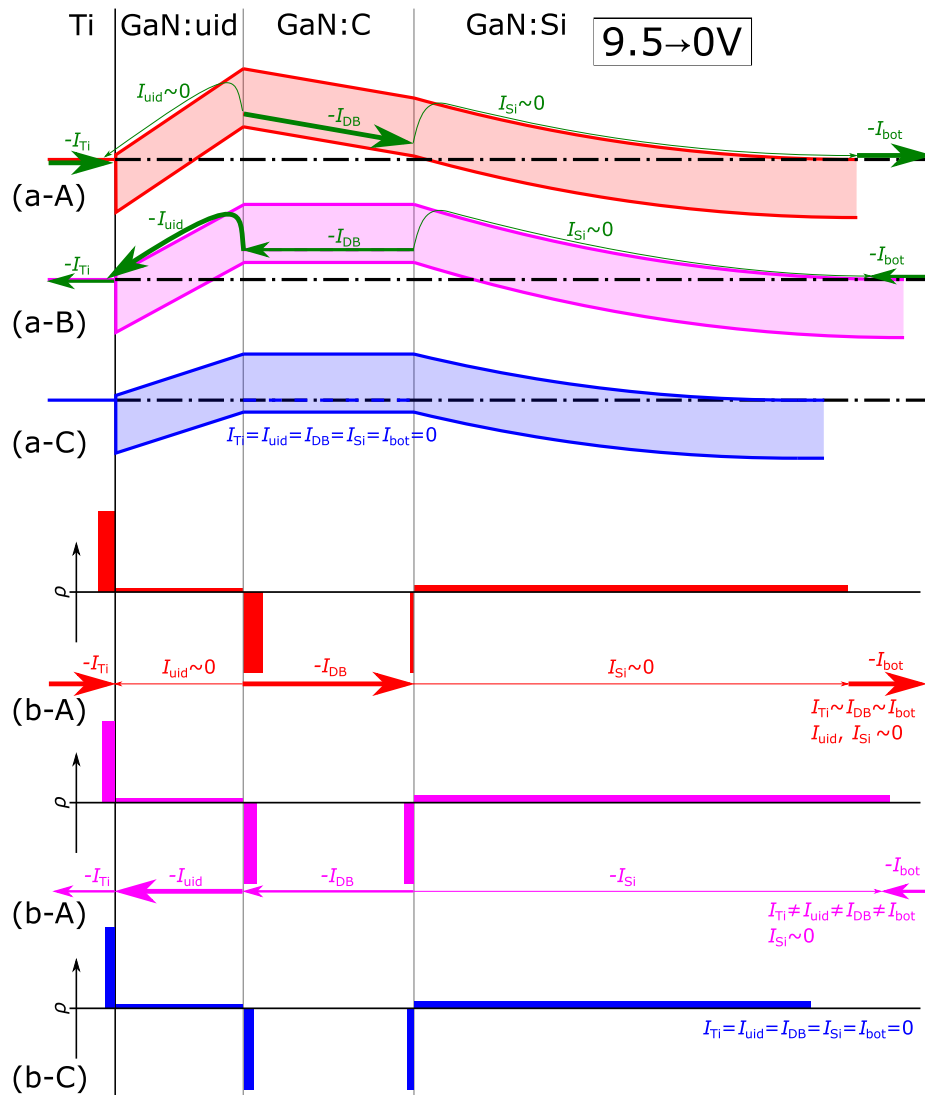


Fig. 4.15: (a) Schematic band diagrams, (b) charge distributions and transient "conduction currents" (represented by arrows) in every layer of $S_{10,uid}$ after a bias step from 9.5 to 0V. 'A' represents a quasistatic state before charge redistribution occurred in GaN:C, 'B' a quasistatic state in which charge redistribution in GaN:C finished but no charge exchange with electrodes occurred yet. Finally, in 'C' the structure is in SS, details on the evolution in time are provided in Fig. 4.10. Estimations base on data from Fig. 4.10.

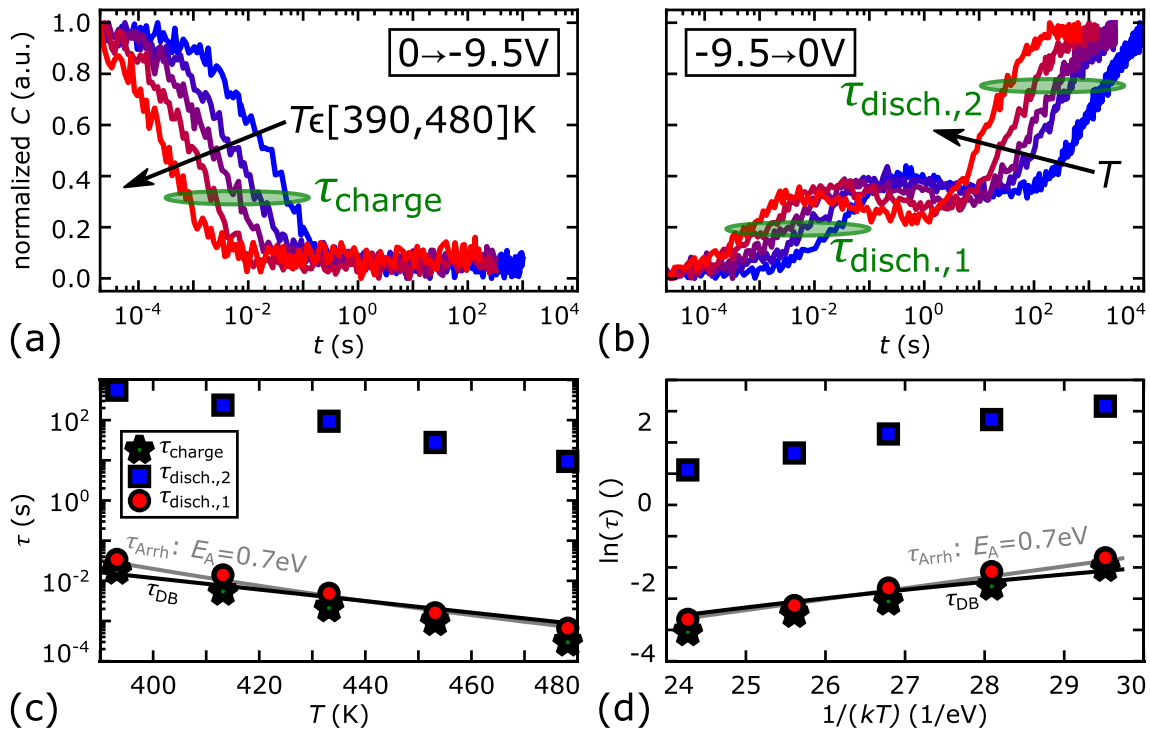


Fig. 4.16: Normalized transient capacitances for S_{10,uid} after bias steps (a) from 0 to -9.5 V and (b) back to 0 at various T . (c,d) Time constants τ as function of T , (d) representing an Arrhenius-plot. Grey lines represent fits to Arrhenius law with $E_A = 0.7 \text{ eV}$ and black lines show τ according to the defect band model, derived from S₁₀ (i.e. $\tau \propto e^{-aT}$) with $a = 0.03 \text{ K}^{-1}$).

by the large time difference between $\tau_{\text{disch.,1}}$ and $\tau_{\text{disch.,2}}$ of roughly five orders of magnitude. The full transient behavior stretches over roughly eight orders of magnitude. In combination with the feasible time range for measurements between 30 μs and 10 ks, this limits measurements to a temperature range between 390 and 480 K.

Fig. 4.16(c,d) show extracted time constants from (a,b) as a function of T and in an Arrhenius-plot, respectively. The graphs further show fits to Arrhenius-law with $E_A = 0.7 \text{ eV}$ and time constants according to the defect band model (Tab. 3.4). τ_{charge} and $\tau_{\text{disch.,1}}$ fit well to calculated values using the defect band model, apparently confirming DB conduction as dominant process. However, we want to remark that due to the small available T range the results could in theory also result from an Arrhenius-like process with $E_A = 0.7 \text{ eV}$. $\tau_{\text{disch.,2}}$ seems to be only shifted by roughly five orders of magnitude to larger values, hence they could be fitted by Arrhenius-law but as well by the defect band model with a larger pre-exponential factor. If the slow discharging would be determined by an Arrhenius-like process it would be very unlikely that its activation energy is equivalent to E_{acc} . If thermal excitation was responsible, we would expect $E_A = E_{\text{bg}} - E_{\text{acc}} = 2.7 \text{ eV}$, as this is the energy barrier that has to be overcome (neglecting a possibly decreased barrier due to electric field in GaN:uid). On the other hand it seems also unlikely that discharging follows the relations of the defect band model, as we expect no DBs in GaN:uid. Therefore, we speculate that there might be weakly pronounced DBs in GaN:uid, where the transport is superimposed by conduction in the CB. However, if the potential barrier for the latter mechanism is large enough and conduction via CB inhibited, conduction via the weakly pronounced DBs might dominate.

Concluding, the small T range prohibits clear statements concerning the injection mechanism into GaN:uid as we cannot clearly distinguish between DB and Arrhenius-like conduction.

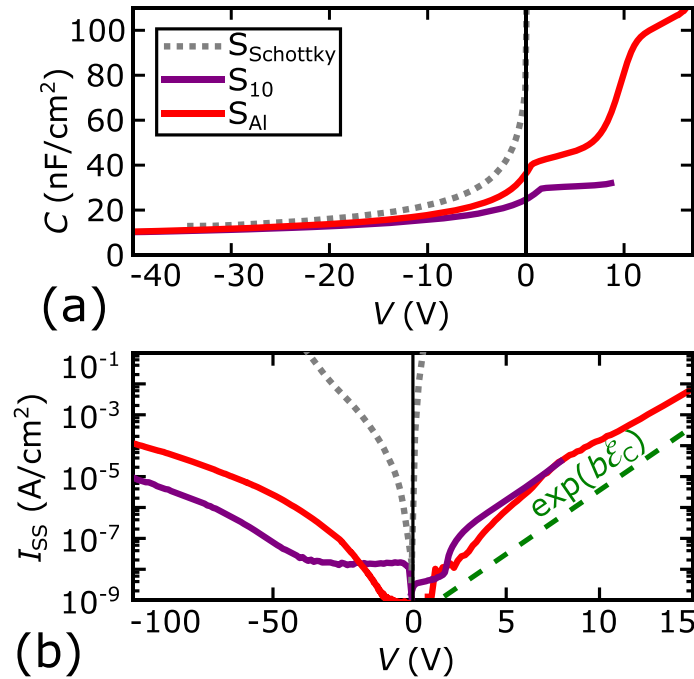
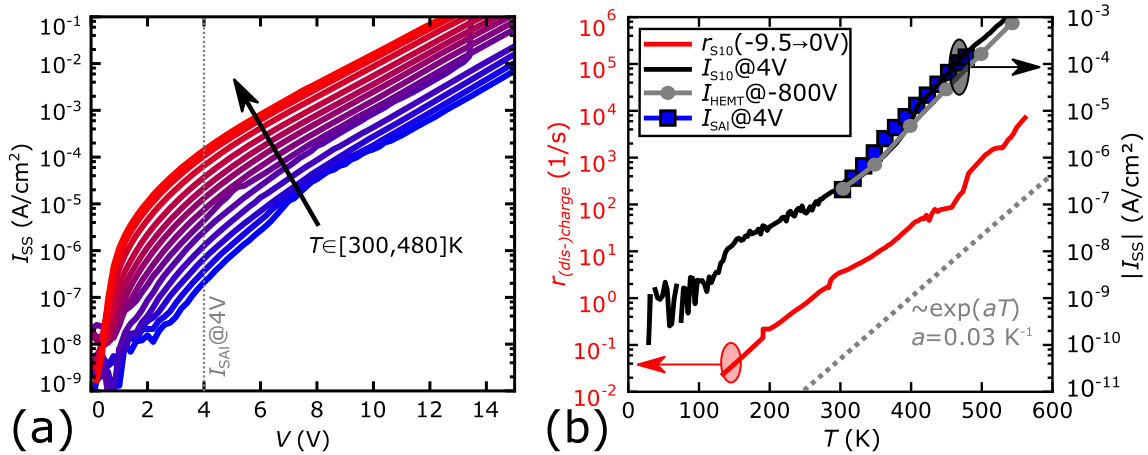
In summary, static analysis reveals great insulation properties of GaN:C/GaN:uid multilayer structures. Dynamic characterization provide additional evidence that DBs determine charge transport in GaN:C. GaN:C/GaN:uid/metal multilayer structures allow for fast negative charge injection from metal to GaN:C, however for the vice versa process of transporting negative charges from GaN:C acceptors to the top metal, a large energy barrier between E_{acc} and E_{CB} has to be overcome. This requires times that are by several orders of magnitude larger. This observation is relevant for HEMT stacks containing GaN:C/GaN:uid/2DEG layers acting similar to the investigated GaN:C/GaN:uid/metal multilayer stacks. Applying our findings to the HEMT stack this would mean that after negative charge accumulation e.g. in off-state, for its depletion in on-state negative charges have to overcome the energy barrier between DBs and CB, resulting in the corresponding long time constants, i.e. severe CC. In order to avoid this we agree to Uren et al. suggesting that leaky GaN:uid layers would significantly decrease CC [Ure+17]. Another technical solution is to inject holes from a p-doped structure next to the drain that reduce negative charge accumulation in GaN:C [Tan+15]. Similarly, accumulated negative charge can be depleted by photo-induced holes generated by a photonic drain as in photonic-Ohmic drain field-effect transistors (PODFETs), demonstrated to reduce CC in [Tan+18].

4.3 Electrical behavior of AlGa_N:C and GaN:C/AlGa_N:C multilayers

In order to study the behavior of carbon-doped AlGa_N (AlGa_N:C) we study samples (S_{A1}) analogous to S_{10} but exchange the 200 nm thick GaN:C layer by a roughly 100 nm thick AlGa_N:C layer with comparable carbon concentration (see Tab. 3.1). Besides static and dynamic characterization we analyze theoretically and experimentally the influence of polarization on AlGa_N/Ga_N and Ga_N/AlGa_N interfaces. We further point out the importance of the understanding of this interface for superlattice structures, widely used in transition and buffer layers of HEMT structures [Fel+01; SSE09; Sel+12; Che+02; XWW16; Sto+15].

I_{SS} - V and C_{SS} - V characteristics in Fig. 4.17 reveal almost identical behavior for S_{10} and S_{A1} for $V < 7$ V: depletion of GaN:Si for $V < 1.5$ V and a slightly increasing capacitance plateau above. As the AlGa_N:C layer in S_{A1} is only half as thick as GaN:C in S_{10} , the capacitance in S_{A1} is significantly larger. The capacitance plateau as well as the qualitatively similar (dis-)charging dynamics of S_{10} and S_{A1} described later, suggest the existence of DBs. As a consequence we describe AlGa_N:C analogous to GaN:C using the dominant acceptor model and DBs. Considering an $[Al]/([Al]+[Ga])$ ratio of 30 % with $[Al]$ being the aluminum concentration, the band gap increases at room temperature from ≈ 3.4 to ≈ 4 eV [Lag14]. For the offset of CBM and VBM between AlGa_N and Ga_N we consider 0.36 and 0.24 eV, respectively. At AlGa_N/Ga_N interfaces for Ga-polar growth the sum of different spontaneous polarization of Ga_N and AlGa_N, and the piezoelectric polarization in AlGa_N, which is supposed to grow at least in the bottom part pseudomorphically on Ga_N, causes a polarization sheet charge density (σ_{pol}) of 1.4×10^{13} C cm⁻² [Lag14; Amb+02].

Considering σ_{pol} at the GaN:Si/AlGa_N:C interface, we would expect at first sight the formation of a 2DEG as for the AlGa_N/Ga_N bilayer in HEMTs. Hence, GaN:Si should be only insignificantly depleted leading to a capacitance of $C = \epsilon/d \approx 100$ nF cm⁻² with d being the AlGa_N:C thickness.


 Fig. 4.17: Comparison of (a) C_{SS} - V and (b) I_{SS} - V for $S_{Schottky}$, S_{10} and S_{Al} at room temperature.

 Fig. 4.18: (a) I_{SS} - V for S_{Al} at various T and (b) I_{SS} at 4 V compared for S_{Al} ($I_{SAl@4V}$) and S_{10} ($I_{S10@4V}$) as well as I_{SS} at 800 V for a HEMT structure ($I_{HEMT@800V}$) and trapping rate in S_{10} ($r_{S10}(-9.5 \rightarrow 0V)$). Remarkably, all currents as well as the trapping rate follow same T dependence, even with same constant a .

Instead, GaN:Si is substantially depleted for $V < 8$ V, just as in S_{10} , giving clear evidence for the absence of a 2DEG. In order to understand this behavior in the following we first discuss theoretically polarization effects in GaN, AlGaN and at AlGaN:C/GaN:Si interfaces and afterwards apply that knowledge in order to describe the electrical behavior of the sample S_{A1} .

4.3.1 Polarization in (Al)GaN

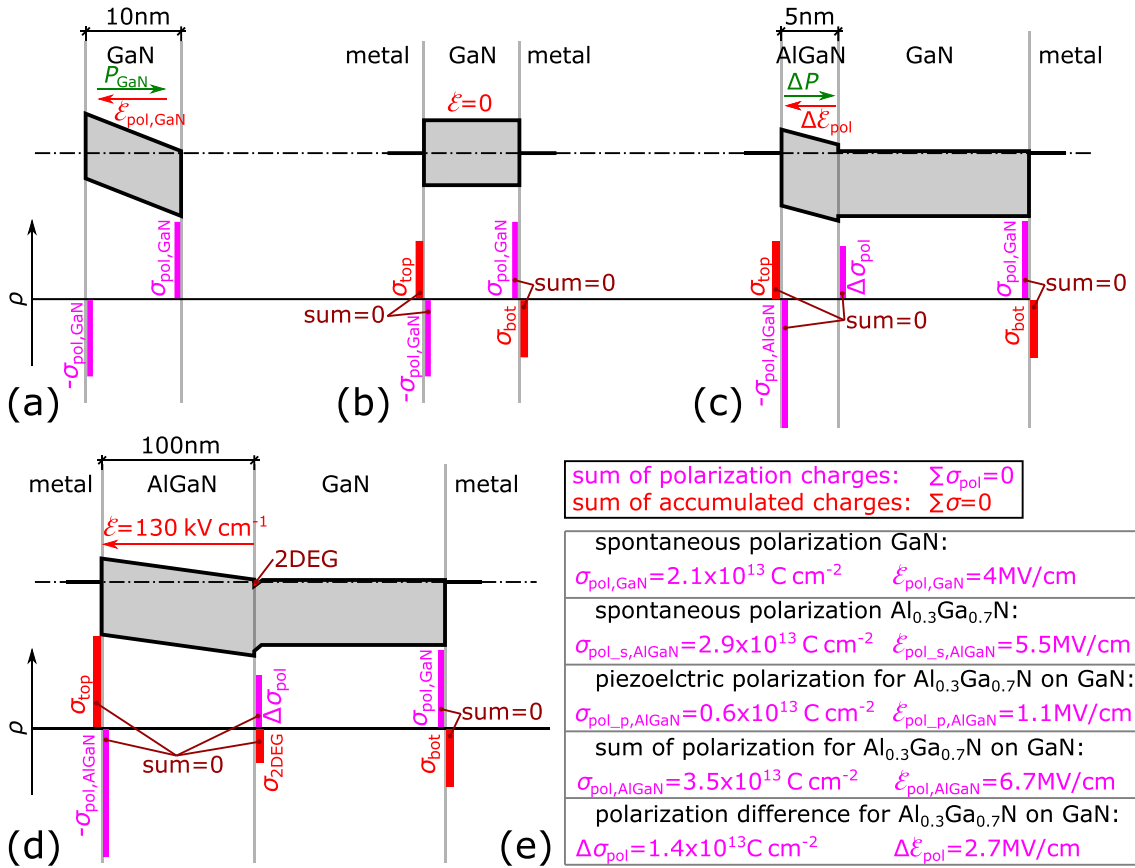


Fig. 4.19: (a-d) Schematic band diagrams (top) and charge distributions (bottom) for various hypothetical structures demonstrate the effect of polarization in (Al)GaN which leads for sufficiently thick AlGaN layers as in (d) to the formation of a 2DEG. (e) Values for spontaneous and piezoelectric polarization (polarization charge σ_{pol} and polarization field \mathcal{E}_{pol}) in (Al)GaN [WJ07; Lag14].

Fig. 4.19(a) shows a hypothetical 10 nm thin freestanding GaN layer, i.e. without contacts or adjacent layers. Spontaneous polarization in GaN can be described by polarization charges at the surfaces with densities (σ_{pol}) of $2.1 \times 10^{13} \text{ C cm}^{-2}$ (see Fig. 4.19(e)) [WJ07]. Neglecting surface states, for the thin freestanding GaN layer this results in a large electric field (\mathcal{E}_{pol}) of 4 MV cm^{-1} , which can be calculated by $\sigma_{pol} = \mathcal{E}_{pol} \times \epsilon$.

For thicker GaN layers with surface states [WJ07; Lag14] or for GaN layers embedded between hypothetical metal contacts as in Fig. 4.19(b), charges will accumulate in the metal or surface states and compensate the electrical field in GaN.

In the next step in Fig. 4.19(c) we add an additional thin AlGaN layer on top of GaN. The GaN layer on bottom (right) forms a flatband as $\sigma_{bot} = \sigma_{pol,GaN}$. For the AlGaN/GaN interface we

have to consider that AlGaN shows higher spontaneous polarization and additionally piezoelectric polarization as thin AlGaN layers grow pseudomorphically on GaN. The difference of the GaN and AlGaN polarization charge ($\Delta\sigma_{\text{pol}}$, see (e)) can be considered as fixed charge at the GaN/AlGaN interface. This leads to the electric field ($\Delta\mathcal{E}_{\text{pol}} = 2.7 \text{ MV cm}^{-1}$) in AlGaN. At the AlGaN surface the full AlGaN polarization charge appears, which is partly compensated by σ_{top} .

If the AlGaN layer exceeds a certain thickness as shown in Fig. 4.19(d), $\Delta\mathcal{E}_{\text{pol}}$ cannot establish anymore. E.g. for a 100 nm thick AlGaN layer ΔE_{pol} would require a potential drop in the AlGaN layer of 27 V which is only for extreme bias conditions achievable. In general, the electric field in AlGaN is determined by the adjacent layer, in (d) by the metal (and Schottky barrier). In the presented example $\mathcal{E} = 130 \text{ kV cm}^{-1}$ which is a factor 20 smaller than ΔE_{pol} . This requires negative charge accumulation at the GaN/AlGaN interface, compensating 95% of $\Delta\sigma_{\text{pol}}$. This is provided by the 2DEG (σ_{2DEG}), which establishes as the CBM in GaN next to the GaN/AlGaN interface drops below E_{F} , creating a high amount of occupied states in CB.

For matter of simplicity, within this thesis we usually do not explicitly mention polarization charge at interfaces to metals and their compensation as in Fig. 4.19(b) by a sheet charge density in the metal of opposite sign. If metal sheet charge densities are considered as e.g. in Fig. 4.3 this sheet charge density has the meaning of an additional charge to the polarization-charge compensating charge.

4.3.2 Polarization in AlGaN:C/GaN:Si bilayers

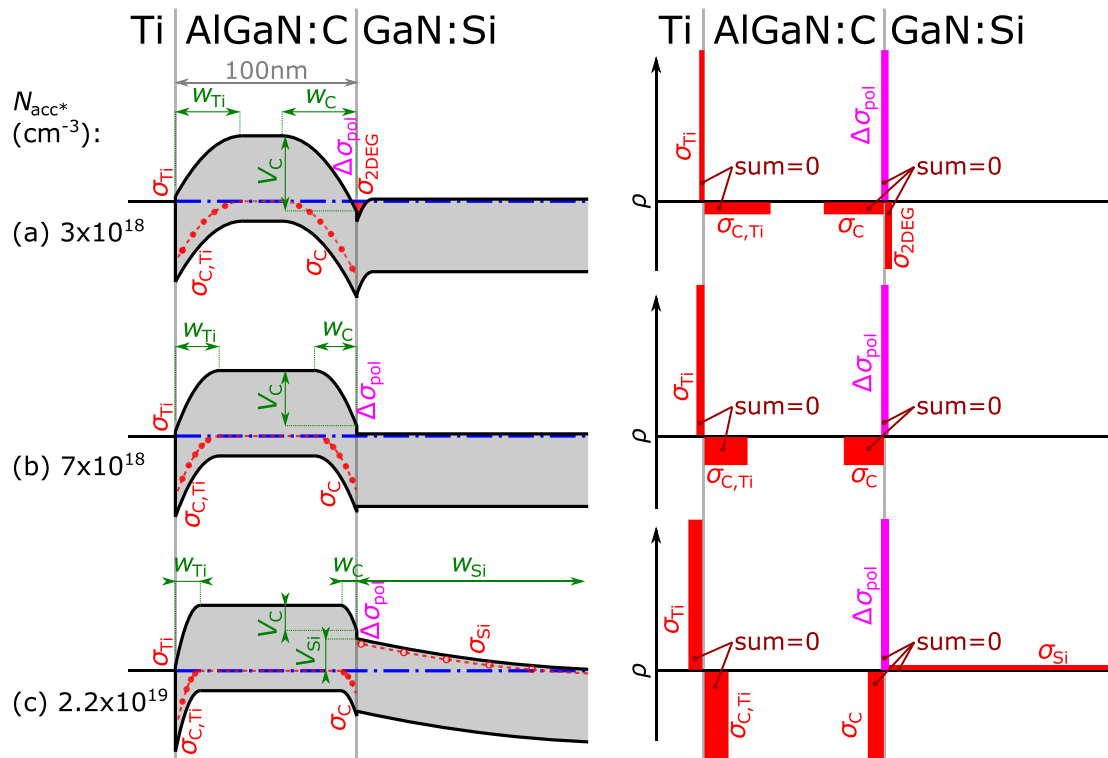


Fig. 4.20: Theoretical calculation of band diagrams (left) and charge distributions (right) for S_{A1} considering the dominant acceptor model (see Section 3.2.2), a polarization sheet charge (σ_{pol}) of $1.4 \times 10^{13} \text{ C cm}^{-2}$ and for varying effective acceptor concentration (N_{acc}^*) as indicated in (a-c).

In a next step, we consider that the AlGa_N:C layer from Fig. 4.19(d) is doped with carbon, as in S_{Al}. Using the dominant acceptor model with different net acceptor concentrations (N_{acc}^*) we calculate band diagrams and charge distributions in Fig. 4.20. As explained in detail in Section 3.2.2, in AlGa_N:C next to the surface in a width of w_{Ti} carbon acceptors are below E_{F} and therefore fully occupied. This results in a space charge region that bends the potential so that in the bulk E_{F} pins near E_{acc} . As we consider AlGa_N:C analogous to GaN:C, an electric field in AlGa_N:C would cause current flow which is not possible in SS at 0 V, hence \mathcal{E} in the bulk has to be zero. For "connecting" AlGa_N:C and GaN:Si we have to consider two main aspects:

1. As E_{F} in bulk AlGa_N:C is pinned at E_{acc} and in GaN:Si roughly at CB, the potential in the interface vicinity has to drop by approximately 2.7 V. Therefore, we consider that E_{acc} is located in AlGa_N:C 2.7 V plus the conduction band offset (0.36 V) below E_{CB} . In general, there are three possibilities where the potential can drop:

- (a) The potential can drop in AlGa_N:C (V_{C}) by the formation of a space charge region of width w_{C} with a resulting negative equivalent sheet charge density of σ_{C} :

$$w_{\text{C}} = \sqrt{\frac{2\varepsilon V_{\text{C}}}{N_{\text{acc}}^* q}}, \quad (4.2)$$

$$\sigma_{\text{C}} = N_{\text{acc}}^* q w_{\text{C}}. \quad (4.3)$$

- (b) The potential can drop in GaN:Si (V_{Si}) by depleting GaN:Si in a width of w_{Si} , resulting in a positive effective sheet charge density of σ_{Si} :

$$w_{\text{Si}} = \sqrt{\frac{2\varepsilon V_{\text{Si}}}{N_{\text{Si}} q}}, \quad (4.4)$$

$$\sigma_{\text{Si}} = N_{\text{Si}} q w_{\text{Si}}. \quad (4.5)$$

- (c) The potential can partly drop in GaN:Si and partly in GaN:C.

In conclusion, following relation has to hold:

$$V_{\text{Si}} + V_{\text{C}} = 2.7 \text{ V}. \quad (4.6)$$

2. Due to flatband in the bulk of AlGa_N:C and GaN:Si the sum of charges in the AlGa_N:C/GaN:Si vicinity including $\Delta\sigma_{\text{pol}}$ has to be zero:

$$\sigma_{\text{C}} + \sigma_{\text{Si}} + \Delta\sigma_{\text{pol}} = 0. \quad (4.7)$$

As demonstrated in Fig. 4.20(c) for N_{acc}^* above a critical value ($N_{\text{acc,crit}}^*$) Eq. (4.6, 4.7) unambiguously determine V_{Si} and V_{C} . Considering constant V_{C} , w_{C} decreases linearly with N_{acc}^* , however, σ_{C} increases with its square ($\sigma_{\text{C}} = \sqrt{2\varepsilon V_{\text{C}} N_{\text{acc}}^* q}$). Hence, with decreasing N_{acc}^* , V_{C} increases while V_{Si} decreases. Obviously, there must exist a critical N_{acc}^* ($N_{\text{acc,crit}}^*$), at which $V_{\text{C}} = 2.7 \text{ V}$ and $V_{\text{Si}} = 0$, as shown in Fig. 4.20(b). In this condition, $\Delta\sigma_{\text{pol}} = \sigma_{\text{C}}$ and $N_{\text{acc,crit}}^*$ can be calculated by:

$$N_{\text{acc,crit}}^* = \frac{\Delta\sigma_{\text{pol}}^2}{2\varepsilon q V_{\text{C,crit}}}, \quad (4.8)$$

with $V_{C,crit} = 2.7\text{ V}$, resulting in $N_{acc,crit}^* = 7 \times 10^{18}\text{ cm}^{-3}$. For $N_{acc}^* < N_{acc,crit}^*$ as in Fig. 4.20(a), even if the entire 2.7 V drop in AlGa_N:C, $\sigma_C < \Delta\sigma_{pol}$. In that case V_C increases slightly further, which results in a V_{Si} of opposite sign, pushing CB below E_F , leading to formation of a 2DEG as explained in Section 4.3.2. Therefore, an additional negative sheet charge density (σ_{2DEG}) replaces positive σ_{Si} in Eq. 4.7 and following relation applies:

$$\sigma_C + \sigma_{2DEG} + \Delta\sigma_{pol} = 0. \quad (4.9)$$

It becomes clear that with decreasing N_{acc}^* , σ_{2DEG} increases. In conclusion, for negligible N_{acc}^* , $\Delta\sigma_{pol}$ has to be almost entirely compensated by σ_{2DEG} , i.e. σ_{2DEG} has the maximum value. With increasing N_{acc}^* , σ_C increases so that σ_{2DEG} decreases until for N_{acc}^* the 2DEG vanishes entirely. With further increasing N_{acc}^* , V_C decreases and V_{Si} increases.

Yet, the discussion considered only the $V = 0\text{ V}$ case, however from band diagrams in Fig. 4.20 it also gets clear what happens for $V \neq 0$. With increasing negative bias the potential on the left side is raised so that even for $N_{acc}^* < N_{acc,crit}^*$, σ_{2DEG} decreases and can eventually vanish. Even for undoped AlGa_N above a certain threshold voltage (V_{th}) the 2DEG vanishes which is analogous to the AlGa_N/GaN bilayer in HEMT structures. Alternatively, one could postulate that carbon doping shifts V_{th} to more positive values whereby at $N_{acc,crit}^*$, V_{th} passes 0 V and becomes positive. With increasing N_{acc}^* , V_{th} shifts more and more to positive values. Hence, in theory by carbon-doping of the AlGa_N barrier, normally-off (i.e. enhancement mode) transistors could be built, by adjusting [C] and consequently N_{acc}^* even the desired V_{th} could be chosen. However, a carbon-doped barrier would have substantial detrimental effects such as higher impurity scattering resulting in lower electron mobility and greater dynamic effects as carbon traps are located directly next to the 2DEG.

4.3.3 Electrical behavior of AlGa_N:C

Static behavior of sample S_{A1}

With the insights from the theoretical considerations of the previous two sections we can eventually explain the absence of the 2DEG at 0 V and its appearance above 10 V as depicted in Fig. 4.17(a). It is a direct result of N_{acc}^* being greater than $N_{acc,crit}^*$ in the AlGa_N:C layer. From the capacitance value at 0 V we can extract w_{Si} , σ_{Si} and further the required V_C and σ_C (Eq. 4.6, 4.7), from which we derive an estimated value for N_{acc}^* (Eq. 4.2, 4.3) of roughly $2.2 \times 10^{19}\text{ cm}^{-3}$.

Fig. 4.21 shows band diagrams calculated from data of Fig. 4.17(a). The behavior in the *depletion* and *plateau regime* ($V < 7\text{ V}$) is analogous to S₁₀ and not discussed separately. Mentionable is only the good fit of $I_{SS}-V$ of sample S₁₀ and S_{A1} despite the fact that the AlGa_N:C layer in S_{A1} is significantly thinner than the GaN:C layer in S₁₀. We suppose that the reason is decreased conductivity in DBs in AlGa_N:C compared to GaN:C. This is supported by dynamic measurements, revealing that time constants for S_{A1} are roughly ten times smaller than in S₁₀. For $V > 7\text{ V}$ the increasing capacitance corresponds to a decreasing GaN:Si depletion width until it vanishes completely at roughly 11 V, indicating the formation of a 2DEG. Surprisingly, this is not accompanied by substantial current increase, for exceeding biases I_{SS} still increases roughly exponentially with V as demonstrated in Fig. 4.17(b). We suppose that the reason is that $\Delta\sigma_{pol}$ is only partly compensated by σ_{2DEG} , while the remaining part is compensated by σ_C , which bends the potential

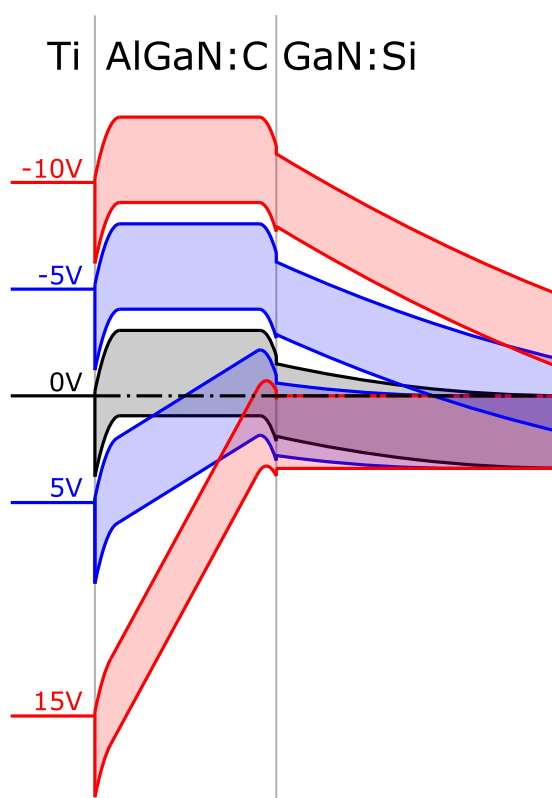


Fig. 4.21: Calculated band diagrams for S_{A1} for various bias conditions, based on $C_{SS}-V$ data depicted in Fig. 4.17(a).

as demonstrated for biases of 5 and 15 V in Fig. 4.21. This bending in addition to the conduction band offset is assumed to provide a potential barrier sufficient to prevent major electron injection into the AlGaN:C CB. As a consequence, leakage current is still determined by I_{DB} , resulting in the still exponential V dependence. Above roughly 15 V the transition from *plateau* to *Ohmic regime* occurs, analogous to S_{10} .

Dynamic behavior of S_{A1}

Due to the time-consuming nature of dynamic characterization, these measurements have been performed only for a single temperature of 390 K, where SS is reached after 30 s. Fig. 4.22 shows $C(t)$ after various bias steps, whereby the dynamic behavior is indeed qualitatively equivalent to S_{10} with time constants at 390 K being roughly ten times larger than in S_{10} , presumably due to ten times smaller conductivity in DBs.

4.3.4 GaN:C/AlGaN:C vs. AlGaN:C/GaN:C interfaces

After discussion of GaN:Si/AlGaN:C bilayers in the previous section, this section is dedicated to theoretical discussion of GaN:C/AlGaN:C and AlGaN:C/GaN:C bilayers. Possibly surprising at first sight, we point out that due to the polar nature of III-N materials both bilayers behave significantly different. Eventually, we investigate LUT structures featuring a GaN:Si/AlGaN:C/GaN:C multilayer stack and discuss its relevance for superlattice structures.

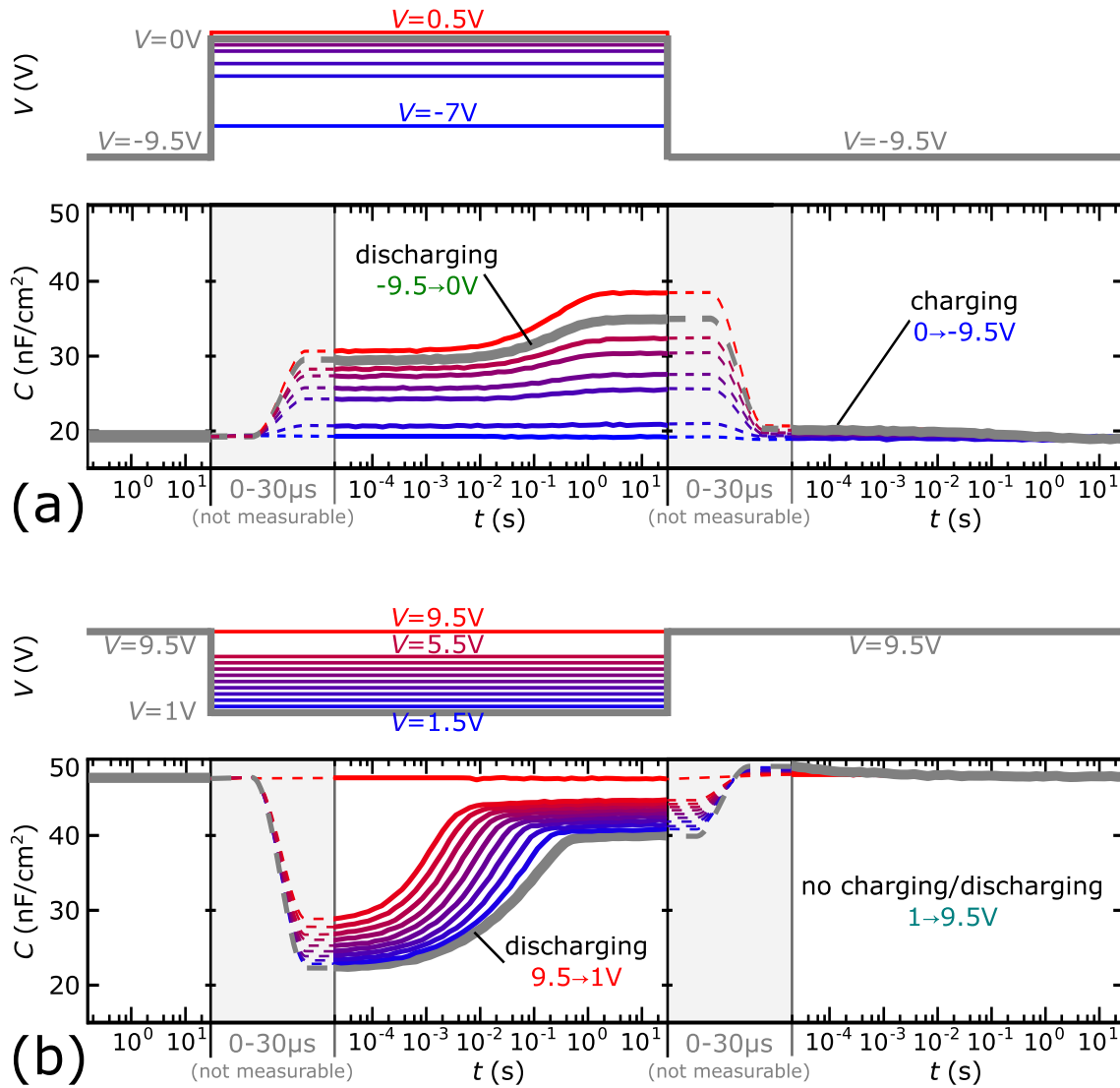


Fig. 4.22: Transient capacitance analysis at 390 K after various bias steps in (a) *depletion regime* and (b) *plateau regime* with indicated carbon acceptor charging/discharging processes.

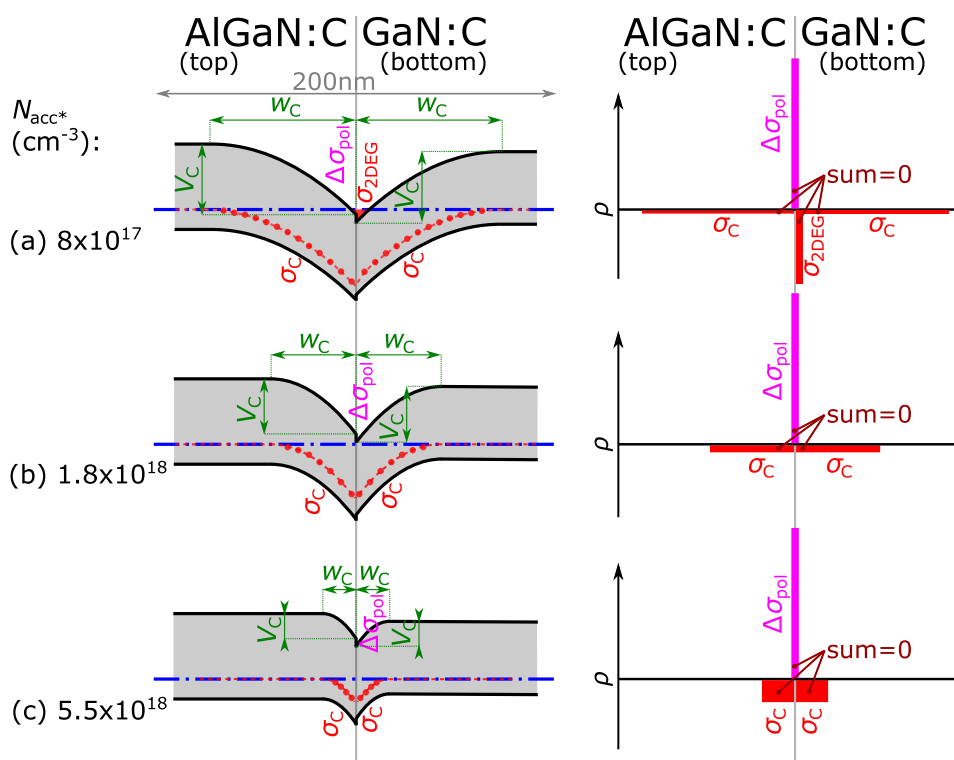
Theoretical discussion of GaN:C/AlGa_N:C and GaN:C/AlGa_N:C interfaces

Fig. 4.23: Theoretically calculated band diagrams (left) and charge distributions (right) for an AlGa_N:C/GaN:C interface with AlGa_N:C on top, considering same effective acceptor concentrations (N_{acc}^* ; varying for (a-c)) in GaN:C and AlGa_N:C.

Fig. 4.23 shows theoretically calculated GaN:C/AlGa_N:C bilayers using same considerations as in Fig. 4.20 for AlGa_N:C. In contrast to the GaN:Si/AlGa_N:C bilayer, in the GaN:C/AlGa_N:C bilayer the potential is bent not only in AlGa_N:C. Instead, in both GaN:C and AlGa_N:C carbon acceptors fall below E_F and consequently get fully occupied, forming two space charge regions with density N_{acc}^* and an equivalent sheet charge density σ_C . Analogous to the GaN:Si/AlGa_N:C interface for low N_{acc}^* as in Fig. 4.23(a), σ_C is insufficient to compensate $\Delta\sigma_{\text{pol}}$ and a 2DEG forms. With increasing N_{acc}^* , σ_{2DEG} decreases until at a certain threshold, shown in Fig. 4.23(b), it eventually vanishes. For further increasing N_{acc}^* the potential drop in GaN:C and AlGa_N:C (V_C) decreases just as for GaN:Si/AlGa_N:C bilayer. The obviously major difference between GaN:Si/AlGa_N:C and GaN:C/AlGa_N:C bilayers is that space charge regions form at both sides of the interface. For the calculation of $N_{\text{acc,crit}}^*$ Eq. (4.8) can be used but due to the space charge regions at both sides only half of the value for $\Delta\sigma_{\text{pol}}$ must be used. As $N_{\text{acc,crit}}^* \propto \Delta\sigma_{\text{pol}}^2$ this results in $N_{\text{acc,crit}}^*$ being only a fourth of the value for the GaN:Si/AlGa_N:C bilayer. The resulting value of $1.8 \times 10^{18} \text{ cm}^{-3}$ is presumably lower or at least in the range of N_{acc}^* is typical for GaN:C buffers in HEMTs. This finding is relevant as GaN:C/AlGa_N(:C) bilayers are used in HEMT buffers and suppression of 2DEGs desired in order to avoid increased vertical and horizontal leakage current within the HEMT stack.

After GaN:C/AlGa_N:C bilayers we study AlGa_N:C/GaN:C layers with GaN:C on top. In these layers the difference of the polarization of GaN and AlGa_N leads to negative polarization charge

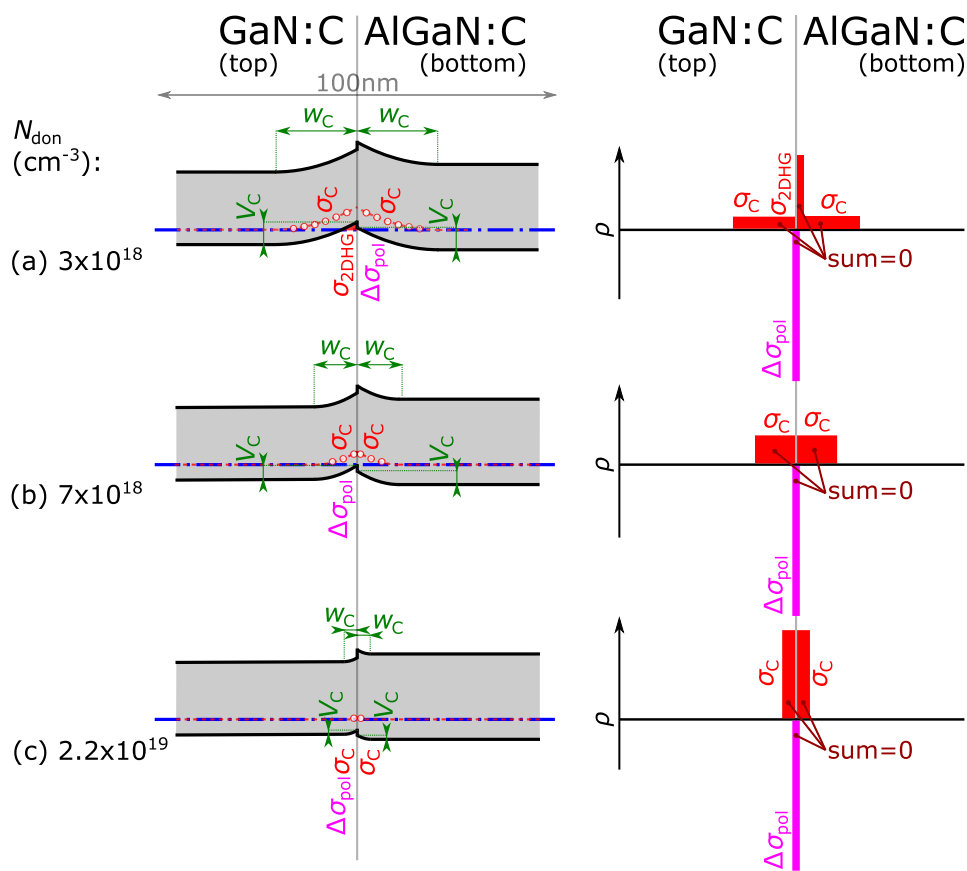


Fig. 4.24: Theoretically calculated band diagrams (left) and charge distributions (right) for an AlGaIn:C/GaN:C interface with GaIn:C on top, considering same donor concentrations (N_{don} ; varying values in (a-c)) in AlGaIn:C and GaIn:C.

at the interface, roughly identical to $\Delta\sigma_{\text{pol}}$ in GaN/AlGaN bilayers but of opposite sign. This pushes the potentials at the GaN:C/AlGaN:C interface upwards, resulting in unoccupied carbon acceptors and consequently positive space charge regions with charge densities of N_{don} due to still unoccupied donors in the upper half of the band gap as demonstrated in Fig. 4.24. For small N_{don} this is insufficient for compensating $\Delta\sigma_{\text{pol}}$ and a two-dimensional hole gas (2DHG) forms in GaN:C at the interface. However, analogous to the GaN:C/AlGaN:C bilayer above a critical donor concentration the 2DHG vanishes and the potential drop V_C decreases. For the critical concentration it has to be considered that much smaller band bending (0.7 V) is sufficient to form a 2DHG at AlGaN/GaN interfaces compared to the formation of a 2DEG at GaN/AlGaN interfaces (2.7 V). For the calculation of the critical donor concentration again Eq. (4.8) can be used but with $V_{C,\text{crit}} = 0.7 \text{ V}$ and half value of $\Delta\sigma_{\text{pol}}$. As $2.7 \text{ V}/0.7 \text{ V} \approx 4$ the critical donor concentration is $7 \times 10^{18} \text{ cm}^{-3}$ and therefore roughly four times higher than $N_{\text{acc,crit}}^*$ in AlGaN:C/GaN:C and comparable to the value of the AlGaN:C/GaN:Si bilayer. As N_{don} is assumed to be smaller than N_{acc}^* and smaller than the critical donor concentration, 2DHGs are likely to be formed at GaN:C/AlGaN:C interfaces, possibly detrimental for the insulating properties of HEMT stacks.

We remark that for all calculated critical values we used the nominal value for $\Delta\sigma_{\text{pol}}$ of $1.4 \times 10^{13} \text{ C cm}^{-2}$ [Lag14; Amb+02], which holds for ideal pseudomorphic growth of GaN on relaxed AlGaN and vice versa. In reality, the full stack is under mechanical stress and the actual values might differ significantly from theoretical values.

Electrical characterization of GaN:Si/AlGaN:C/GaN:C multilayers (2DHG formation)

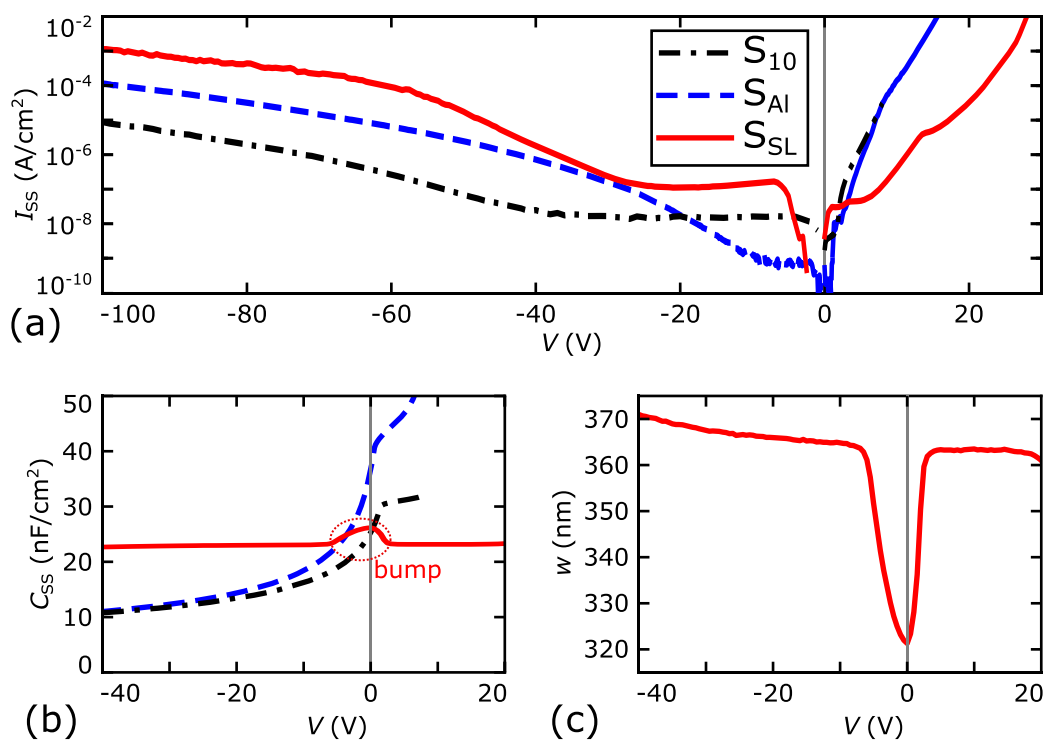


Fig. 4.25: Comparison of (a) $I_{\text{SS}}-V$ and (b) $C_{\text{SS}}-V$ for samples S_{10} , S_{Al} and S_{SL} . (c) Calculated total depletion width w based on data from (b).

In order to experimentally investigate AlGaN:C/GaN:C bilayers with the latter on top we use LUT structures with GaN:Si/AlGaN:C/GaN:C multilayer stacks as in sample S_{SL} , details can be found in Tab. 3.1. SS electrical characterization in Fig. 4.25 reveals slightly higher I_{SS} in reverse bias compared to S_{10} and S_{A1} , while in forward bias the current increases roughly exponentially, but due to the larger thickness with smaller slope. In contrast to all other investigated LUT structures, S_{SL} shows no *depletion regime*, indicated by the roughly constant C_{SS} in the entire measured V range with only a small "bump" for $-8\text{ V} < V < 3\text{ V}$. C_{SS} refers to a total depletion width ($w = \epsilon/C_{SS}$) shown in Fig. 4.25(c) of approximately 365 nm outside of the bump region. This indicates that part of GaN:Si is depleted, i.e. no 2DEG exists at the GaN:Si/AlGaN:C interface, in line with results from S_{A1} .

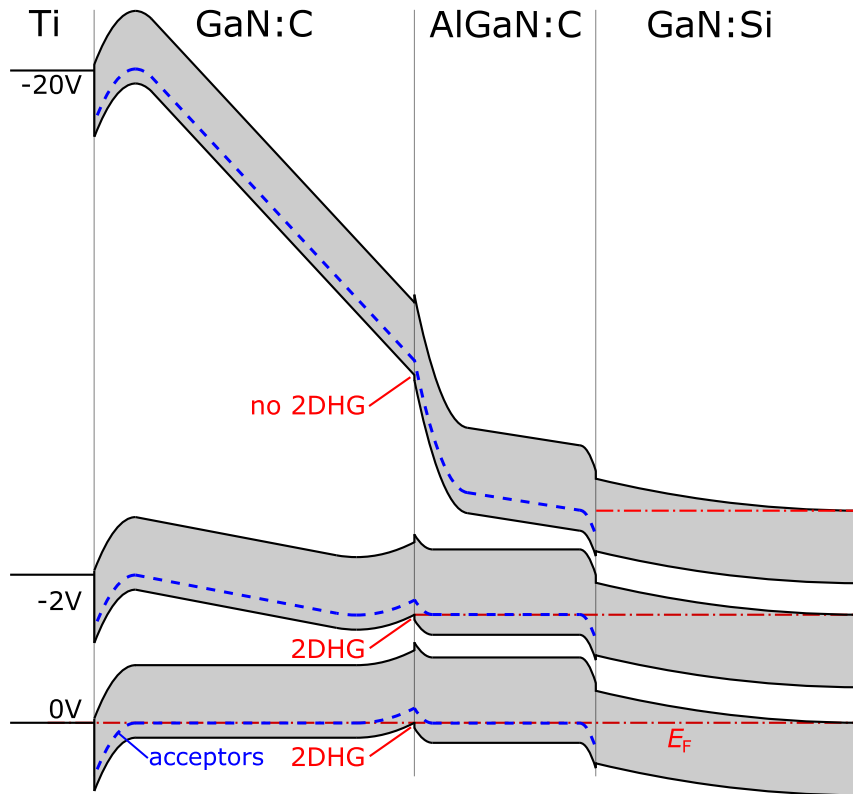


Fig. 4.26: Speculative schematic SS band diagrams for reverse biased S_{SL} structures based on $C_{SS}-V$ and $I_{SS}-V$ characteristics shown in Fig. 4.25(a,b).

Due to the complex multilayer nature and the large amount of unknown parameters such as acceptor and donor concentrations in every layer and polarization charges, we calculated band diagrams as shown in Fig. 4.26 and 4.27 but we remark that they have to be considered as very "speculative". We suppose that for $V = 0$ a 2DHG forms at the AlGaN:C/GaN:C interface which fits to the theoretical considerations considering $N_{don} < 7 \times 10^{18} \text{ cm}^{-3}$. This is supported by observed significantly larger equivalent parallel (ac) conductance within the bump- V range as well as by the observation that the peak of this capacitance bump decreases with increasing frequency. We assume that with increasing reverse bias the voltage mainly drops in the top GaN:C layer as shown for $V = -2\text{ V}$ in Fig. 4.26, resulting in the steep increase of I_{SS} . However, for $V \lesssim -7\text{ V}$ C_{SS} and I_{SS} saturate, which we suppose is due to depletion of the 2DHG. As shown in Fig. 4.26 for high reverse bias the space charge region in AlGaN:C next to its interface to GaN:C can get sufficiently

large to compensate $\Delta\sigma_{\text{pol}}$, resulting in the absence of the 2DHG. As a result the potential drops in GaN:C and AlGaN:C. However, it is unclear why GaN:Si does not get depleted.

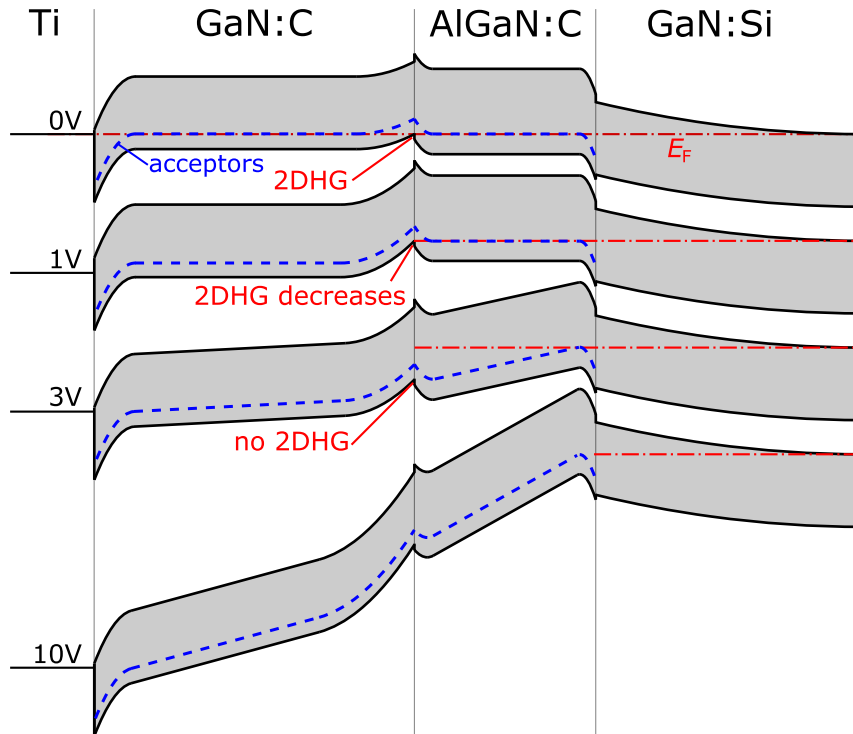


Fig. 4.27: Speculative schematic SS band diagrams for forward biased S_{SL} structures based on $C_{\text{SS}}-V$ and $I_{\text{SS}}-V$ characteristics shown in Fig. 4.25(a,b).

With increasing forward bias the 2DHG seems to slowly vanish. We assume that as demonstrated in 4.27 for low forward biases the potential drops mainly in an increasing space charge region in GaN:C at its interface to AlGaN:C until the positive charge in this space charge region is sufficient to compensate $\Delta\sigma_{\text{pol}}$ so that the 2DHG vanishes at roughly 2V. For further increasing bias the potential drops in GaN:C and AlGaN:C layers. Similar to reverse bias it is not understood why the depletion width in GaN:Si does not decrease as we would expect from the behavior in sample S_{10} .

In conclusion, sample S_{SL} gave hints for the formation of a 2DHG at the GaN:C/AlGaN:C interface. It further demonstrates how complex the characterization of multilayer structures becomes and how important the approach for investigation of single layers instead of entire HEMT stacks as used within this thesis was.

5

Conclusion

The scope of this thesis was to understand the electrical behavior of carbon-doped GaN (GaN:C). In chapter 3 we elaborated that already in an early stage of the work we realized that the commonly followed approach of extracting the electrical behavior of GaN:C layers from complex multilayers of HEMTs is not feasible. To a great part the behavior is determined by the interfaces between the single layers and even if considering them negligible it is impossible to determine which layers determine the behavior in which way. In contrast, our approach included first the characterization of single GaN layers and only after understanding every aspect of single layers extend the knowledge to structures with a stepwise increasing number of layers, with the final goal of understanding the principles of complex HEMT stacks. The great obstacle therefore is that GaN is commonly grown on substrates of a different material, in our case Si, with different lattice constant and thermal expansion coefficient. Hence, high-quality GaN layers featuring low number of extended defects require a thick transition layer separating them from the Si substrate. The apparent problem for investigation of single GaN layers is that its electrical behavior cannot be investigated separated from the transition layer.

The solution and novelty in our work is to include a highly Si-doped GaN (GaN:Si) layer on top of the transition layer that distributes due to its n-type nature current horizontally over the entire wafer and therefore acts as backside electrode, i.e. negligible impedance of the transition layer. Consequently, single or also multiple high-quality GaN layers on top of GaN:Si with a metal contact on top can be characterized without influence of the transition layer, we therefore call these layers "layer-under-test" (LUT). In the main part of the thesis we use as LUT single GaN:C layers with varying carbon concentration ($[C]$), additional Al (AlGaN:C), different layer thickness and also different top contacts; in order to derive a physical model of every single layer used in a GaN HEMT. In chapter 4 we use as LUT various simple multilayers as a first attempt to close

the knowledge gap between the understanding of single layers and macroscopic empirically found electrical behavior of multilayers such as HEMT stacks step by step.

In the following we present deeper insight we gained during the course of this thesis about single (Al)GaN:C layers:

- Electrical characterization of single GaN:C layers in LUT structures delivered for the first time evidence that in GaN:C the Fermi level (E_F) is pinned roughly 0.7 eV above the valence band maximum (VBM). This energy level is very close to carbon acceptors for which we derived for $[C] = 10^{19} \text{ cm}^{-3}$ a minimum concentration of $3 \times 10^{17} \text{ cm}^{-3}$. We further demonstrated the necessity of carbon donors in the upper half of the band gap with concentrations smaller than the one from acceptors but with a minimum of 10^{17} cm^{-3} . Less conservative and more realistic estimations suggest that acceptors and donors account for roughly 2/3 and 1/3 of $[C]$, respectively.
- We proved that in GaN:C both leakage current as well as trapping processes, i.e. charging and discharging time constants, are determined solely by the charge transport through GaN:C. Leakage currents through GaN:C layers are of interest because in HEMTs vertical leakage between two dimensional electron gas (2DEG) and Si substrate decrease e.g. the off-state resistance and have to be suppressed by carbon-doped layers. Trapping in GaN:C layers of HEMTs cause dynamic on-resistance and current collapse which are severe performance issues that have to be suppressed. In literature it is speculated that charge transport occurs via valence band; we can confirm that hypothesis, but only for moderate $[C]$ ($< (1 - 10) \times 10^{18} \text{ cm}^{-3}$).
- $[C]$ in GaN:C layers in HEMTs commonly exceed $10 \times 10^{18} \text{ cm}^{-3}$. We found that in this case charge transport does not occur via valence or conduction band but instead via "defect bands" (DBs). These bands are located energetically near carbon acceptors and it seems likely that they arise from carbon acceptors accumulating in the vicinity of threading dislocations, which always exist in GaN, especially when grown on Si. The strongest evidence for the existence of DBs is provided by the fact that at negligible electric fields and cryogenic temperatures, where charge emission from carbon acceptors to conduction and valence bands can be entirely suppressed, emission and capture still takes place. Furthermore, Arrhenius-like temperature dependence of transport processes can be ruled out in a wide temperature range between roughly 20 and 560 K; instead e^{aT} dependence was found. Yet, no satisfactory physical model could be found to explain this charge transport and its T dependence, only speculative mechanisms were provided, their confirmation is pending. Interestingly, we observed for the vertical leakage current in HEMTs the same T dependence, suggesting the applicability of the proposed model also for HEMT structures.
- For charge transport in DBs, the energy difference between acceptors and valence band does not determine charge transport or trapping events, resulting in non-Arrhenius T dependence. As a consequence, the T dependence of trapping events cannot deliver the energetic position of defects which is the basis of classical defect parameter evaluation performed in literature. We demonstrated that possibly the only reason why Arrhenius plots in literature appear reasonable is the fact that in all previous investigations of GaN:C without exception small T ranges were used, in which e^{aT} cannot be distinguished from $\exp(-E_A/(k_B T))$. We suggest

that for future investigations first Arrhenius-like T dependence has to be proved in a wide T range before trusting extracted activation energies E_A .

- Introduction of conductive channels (i.e. defect bands) seems at first sight detrimental to achieve the desired insulating properties of GaN:C. However, we revealed that in combination with the high carbon acceptor concentration, effective space charge regions can form. These raise potential barriers in GaN:C next to adjacent layers that effectively suppresses injection of free electrons/holes from adjacent layers to the conduction/valence band of GaN:C, respectively. Hence, conduction through GaN:C layers is in general determined by the electrical properties of DBs. We revealed that increasing $[C]$ above the critical value of $(1 - 10) \times 10^{18} \text{ cm}^{-3}$ increased the conductivity in DBs and therefore the leakage current through GaN:C.
- Another investigated aspect is a "breakdown-like" feature similar to time-dependent dielectric breakdown (TDDB) with a negative differential resistance (NDR) regime, which occurs for applying high positive biases to GaN:C/GaN:Si multilayers. We found that for biases below the breakdown voltage, current through GaN:C is distributed homogeneously under the contact, while it localizes in current filaments for exceeding biases. With increasing bias the number and size of these filaments increases and in general they are not stable but move around. We introduced a physical model explaining this phenomenon and proposed in contrast to available literature that current filaments do not form at dislocations, however they are likely to pin these filaments for a certain time.
- We further proved that single AlGaN:C layers behave analogous to GaN:C layers and also contain DBs. We demonstrated that with increasing $[C]$ the threshold voltage for the formation of a 2DEG at GaN:C/AlGaN:C interfaces with the latter on top, increases. We showed experimentally that large positive threshold voltages of 7 V can be achieved. Analogous, two dimensional hole gases (2DHGs) at AlGaN:C/GaN:C interfaces with the latter on top, could in theory be suppressed by large donor concentrations but theoretical considerations as well as experimental investigations suggest that required donor concentrations would be probably unfeasibly high.

We further presented a simplified DB model and demonstrated how it can describe the electrical behavior of some fictive multilayers as well as of some real multilayers that were characterized using the LUT principle. For example we investigated bilayers consisting of an unintentionally doped GaN (GaN:uid) layer and a GaN:C layer, as existing in HEMTs directly below the 2DEG. We found that in these structures electrons can easily propagate via the conduction band of GaN:uid and be injected into GaN:C acceptors without overcoming significant energy barriers. However, for the emission of electrons from GaN:C acceptors to the conduction band of GaN:uid a large energy barrier has to be overcome, leading to fast electron capture and extremely slow emission. Although this might be detrimental for HEMTs concerning trapping dynamics, it can be beneficial for suppressing leakage current. While we observed large conductivity of single GaN:uid layers and intermediate conductivity of GaN:C layer, their combination outperformed single layers significantly.

6

Outlook

In a nutshell, we developed novel test structures that enabled electrical characterization of single GaN layers, from which we derived a physical model that describes the electrical behavior of GaN:C. In order to extend the physical model to explain the macroscopic behavior of complex HEMT structures we also investigated simple multilayers. Although the foundation has been laid, there are still important points missing in both, the physical model and even more in the macroscopic considerations as we point out in the following.

Concerning the physical model we consider it as most important to gain more knowledge on the nature of the DBs, especially the conduction mechanism that leads to the observed e^{aT} dependence of charge transport has never been reported and requires a theoretical model for its explanation. A more practical aspect is that DBs are supposed to arise not at every dislocation but instead only e.g. at ones with screw character. First of all, evidence is required that carbon segregates at dislocations, which could be provided by molecular dynamic simulation but stronger evidence would be delivered by physical analysis, e.g. by atom probe tomography (APT). Due to the severe challenge of manufacturing APT specimens including threading dislocations, we follow a more indirect but more practical electrical approach. We manufacture contacts with diameters smaller than the distance between two neighboring dislocations so that we can compare if DBs only form under contacts with dislocations or under under all contacts. Expected obstacles arise from required contact diameters smaller than 400 nm, which require not only sophisticated lithography technique but also high-resolution measurement equipment due to the expected small signal. In order to prevent such small contacts, in parallel we use instead of Si, GaN as substrate which results in several orders of magnitude smaller dislocation densities.

In order to close the gap between knowledge of electrical behavior of single layers and HEMT stacks, two approaches are followed in parallel:

-
1. The LUT structure concept is used with multilayers of increasing complexity, i.e. the number of layers in multilayers is steadily increased and electrically analyzed.
 2. The physical model is incorporated in a TCAD model of GaN in order to simulate the electrical behavior of HEMT stacks. In intermediate steps the multilayers with increasing complexity of the upper approach are simulated and the model parameters adjusted.

We are optimistic that with this approach we can describe currently lacking macroscopic understanding of HEMT stacks and provide insights how to enhance device performance concerning vertical leakage current, breakdown and dynamic properties determined by trapping in GaN defects. With a proper TCAD model development cycles could effectively be shortened.

A

Appendix A: Experimental details of optical setup

In order to investigate the influence of light on the electrical behavior of devices, the mechanical probe station is extended by an optical bench. This features a light source emitting light in a broad spectrum, from which a monochromator filters light with the desired wavelength, i.e. E_{hv} . The light beam is then fed into a light guide, directing it into the probe station surrounding darkbox, and focusing it on the desired part of the sample. This section is dedicated to the description of the single components, more details of the used setup are provided in [Stren].

A.1 Light source

A high-pressure, short-arc discharge Xenon lamp with an adjustable power of up to 330 W is used as light source. Fig. A.1 shows its broad spectrum from near infrared (NIR) over the visible (VIS) into the near ultraviolet (UV) range with feasible irradiance down to roughly 250-300 nm.

A.2 Monochromator

The light beam is directed from the light source through a flange to the monochromator (Cornerstone 260), in which the broad spectrum is filtered so that only light in a small energy window is ejected from the monochromator. Fig. A.2 demonstrates that the core element of the monochromator is the rotatable grating in the center; all other components only serve to focus the beam to the grating and to the ejecting slit. Incoming light is diffracted at the grating, whereby the angle between the incoming and the maximum of the ejected beam depends on the wavelength and the angle between grating and incoming beam. These relations are defined by Bragg's law (Eq. (3.22)) and ensure that only light of a certain wavelength enters the exit slit. In order to change this wavelength, the grating is rotated.

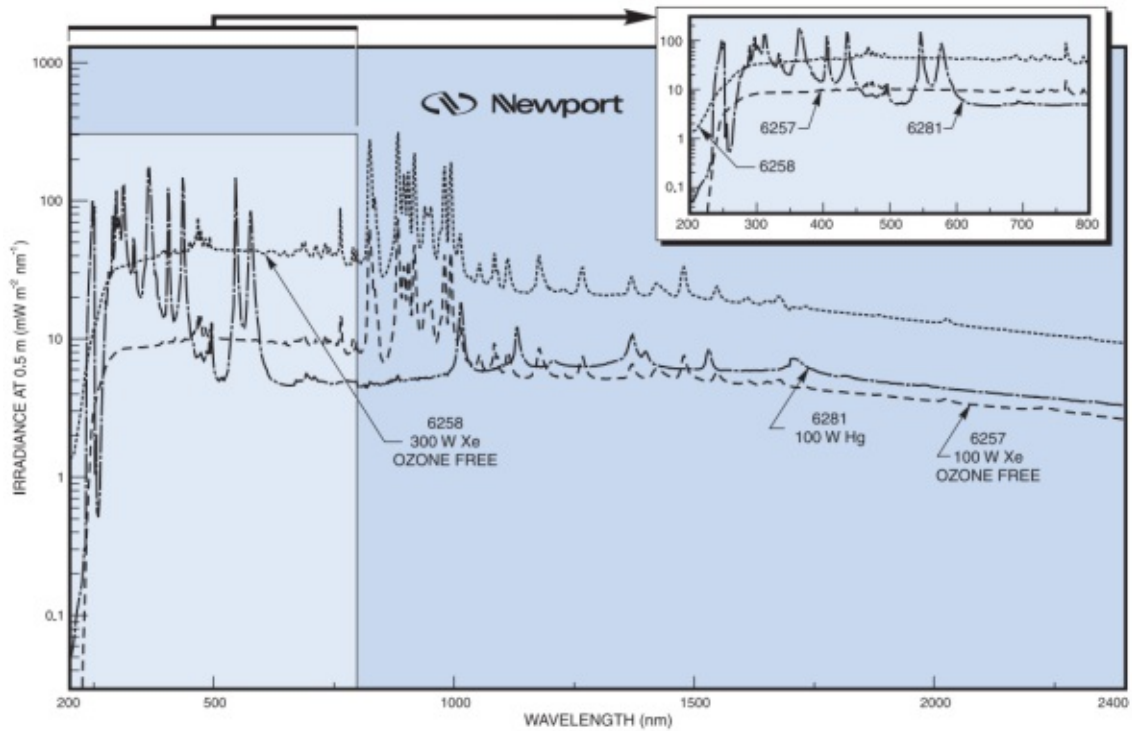


Fig. A.1: Spectra of various discharge lamps, whereby the upper one (“6258 300 W Xe OZON FREE”) is used. Figure from [NC06b].

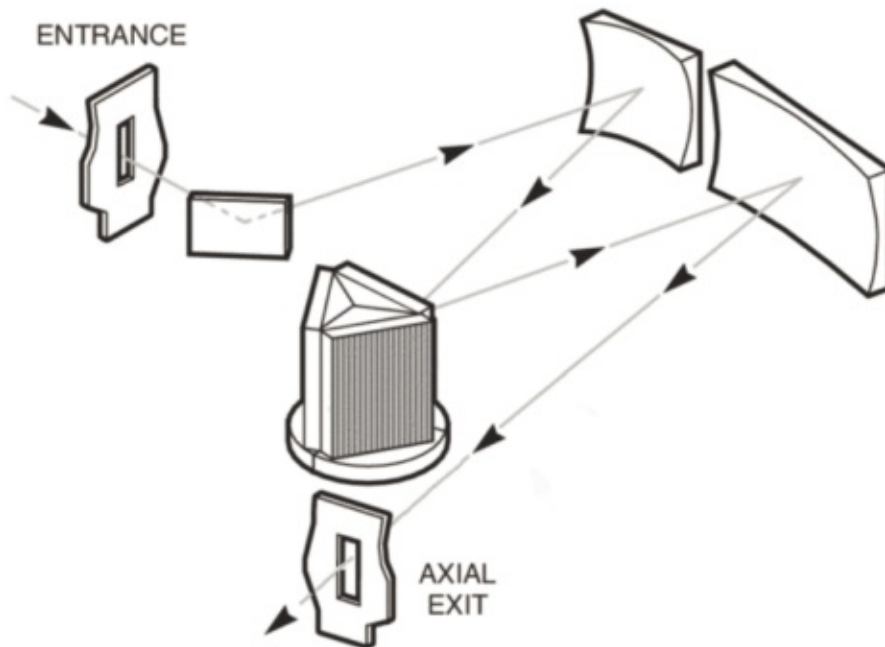


Fig. A.2: Inner workings of the monochromator with gratings as wavelength-filtering part. Figure from [NC06a].

Due to the finite width of entrance and exit slits, emitted light has also a finite spectrum with a certain distribution around the desired center wavelength. The width of the exit slit, which can be adjusted between $4\mu\text{m}$ and 3mm , defines its bandpass with thinner slits corresponding to a narrower bandpass (with lower intensity).

In the used setup two gratings with different lines per millimeter (150 and 1200mm^{-1}) can be used. Denser grooves result in smaller bandpass and higher intensity, but due to the smaller bandpass the absolute flux becomes smaller. As experiments show that the flux is not critical, we only use the grating with denser grooves. The bandpass dependence on d_{slit} can be calculated by $6.7\text{nm}\text{mm}^{-1} \times d_{\text{slit}}$ [NC06b]. Although in theory with $d_{\text{slit}} = 4\mu\text{m}$ a resolution of 0.03nm could be achieved, this is broadened by practical aspects such as aberrations. A well-working compromise is found with $d_{\text{slit}} = 1.5\text{mm}$, resulting in a bandpass of 9nm . E.g. at 3eV this results in light with $E_{\text{h}\nu} \approx (3 \pm 0.035)\text{eV}$.

The output efficiency is not uniform over the entire spectrum, but has a maximum at the so-called blaze wavelength. For the used grating it has a value of 350nm (i.e. $E_{\text{h}\nu} = 3.54\text{eV}$) and is therefore close to the energy range of interest for experiments in this thesis ($\approx 2.5\text{-}3.5\text{eV}$).

Yet, we considered Bragg's law (Eq. (3.22)) only in first order, i.e. $n_0 = 1$. For higher orders not only light with λ but also with λ/n_0 is emitted, with n_0 being the order, i.e. any positive integer. As the light source emits only light with $\lambda > 200\text{nm}$, second order reflections appear only for $\lambda > 400\text{nm}$. In order to avoid that, for $\lambda > 400\text{nm}$ a cut-off filter with a cut-off wavelength of 400nm is inserted. As we are not interested in $\lambda > 800\text{nm}$ this is sufficient to neglect all higher-order effects.

A.3 Light transmission

The light beam is guided from the exit slit of the monochromator into the blackbox of the probe station and onto the device-under-test by a 2m long Newport liquid light guide. Fig. A.3 demonstrates that the light guide is designed for wavelength in the ultraviolet and visible range. A focusing lens at the end of the light guide focuses the light beam to a spot size down to roughly 1mm .

A.4 Light on sample surface

In general, the photon irradiance (E_e , i.e. number of photons per time interval and area) depends on the wavelength as all optical components show wavelength-dependent transmissivity/responsivity. In theory, the photon irradiance at the sample could be calculated by considering the wavelength-dependent output power of the light source (P_{lamp}) and all wavelength-dependent losses due to condenser lens, monochromator (grating, cut-off filter, focusing lenses), light guide (absorption, illuminated area) and the contact (absorption, contact size). However, there are always unknown losses, e.g. from not perfectly aligned lenses, slits, gratings, etc. Hence, for calibration the light output is analyzed by focusing the beam on a Thorlabs SM1PD2A photodiode and measuring the photocurrent (I_{photo}), see Fig. A.4(a). Considering the responsivity of the photo diode ($R_{\text{photodiode}}$, Fig. A.4(b)), the light power (P_{lamp}) can be calculated (see Fig. A.4(c)):

$$P_{\text{lamp}} = I_{\text{photo}}/R_{\text{photodiode}}. \quad (\text{A.1})$$

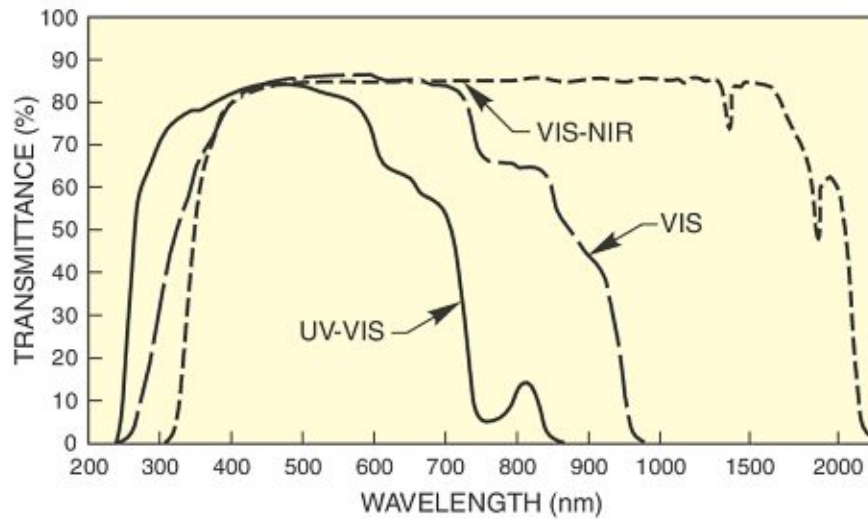


Fig. A.3: Spectral transmittance of the light guide, whereby the one labelled “UV-VIS” has been used. Figure from Newport datasheet.

From P_{lamp} then E_e can be calculated as illustrated in Fig. A.4(d):

$$E_e = P_{\text{lamp}} / (E_{h\nu} A). \quad (\text{A.2})$$

Fig. A.4(d) demonstrates that e.g. at 2.2 eV the irradiance is roughly half of the value at 3.4 eV. This means that in order to get the same amount of photons with energies of 2.2 eV, a two times higher light intensity is required compared to 3.4 eV. While the absolute values of Fig. A.4 are irrelevant for our investigations, the spectral dependences have to be considered. E.g. it is important that due to the cutoff-filter in the range of 3 eV to 3.1 eV (413-400 nm) no reliable measurements are possible, simply due to the largely decreased intensity.

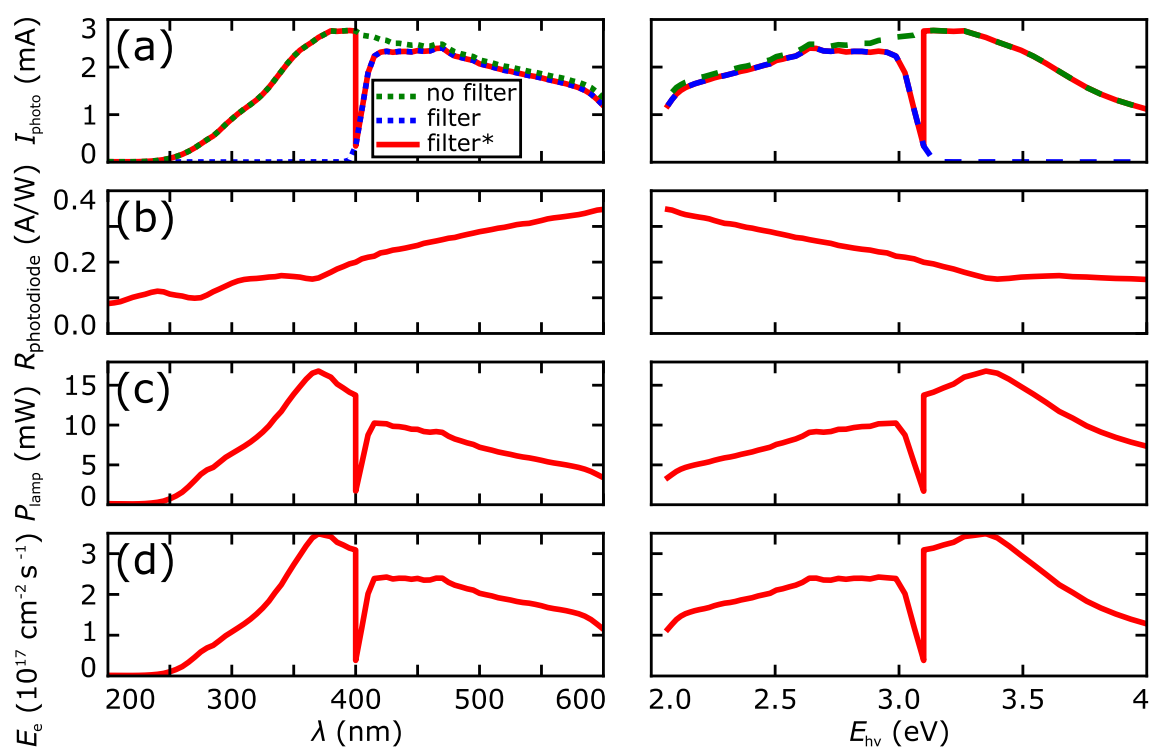


Fig. A.4: (a) Spectral photo current (I_{photo}) measured in photodiode, (b) responsivity of the photo diode ($R_{\text{photodiode}}$) [Tho12], (c) spectral light source power (P_{lamp}) and (d) spectral photon irradiance (E_e). Red solid lines represent measurements in which the cutoff-filter is inserted for $\lambda > 400$ nm.

Bibliography

- [Ale+98] A. Alekseev, S. Bose, P. Rodin, and E. Schöll. “Stability of current filaments in a bistable semiconductor system with global coupling.” In: *Phys. Rev. E* 57 (1998), pp. 2640–2649.
- [Ama+18] H Amano et al. “The 2018 GaN power electronics roadmap.” In: *Journal of Physics D: Applied Physics* 51.16 (2018), p. 163001.
- [Amb+02] O Ambacher et al. “Pyroelectric properties of Al(In)GaN/GaN hetero- and quantum well structures.” In: *Journal of Physics: Condensed Matter* 14.13 (2002), p. 3399.
- [Arm+06] A. Armstrong, C. Poblenz, D. S. Green, U. K. Mishra, J. S. Speck, and S. A. Ringel. “Impact of substrate temperature on the incorporation of carbon-related defects and mechanism for semi-insulating behavior in GaN grown by molecular beam epitaxy.” In: *Applied Physics Letters* 88.8 (2006), p. 082114.
- [Arm06] A. M. Armstrong. “Investigation of deep level defects in GaN:C, GaN:Mg and pseudomorphic AlGaN/GaN films.” PhD thesis. Ohio State University, 2006.
- [Arnen] A. Arneitz. *Analyse des vertikalen Leckstromverhaltens von GaN Hochspannungstransistoren auf Siliziumsubstrat unter Verwendung von dynamischen Charakterisierungsmethoden*. Vienna University of Technology, 2017.
- [AS83] D. E. Aspnes and A. A. Studna. “Dielectric functions and optical parameters of Si, Ge, GaP, GaAs, GaSb, InP, InAs, and InSb from 1.5 to 6.0 eV.” In: *Phys. Rev. B* 27 (1983), pp. 985–1009.
- [AYW05] R. Armitage, Q. Yang, and E. R. Weber. “Analysis of the carbon-related “blue” luminescence in GaN.” In: *Journal of Applied Physics* 97.7 (2005), p. 073524.
- [Bal89] B. J. Baliga. “Power semiconductor device figure of merit for high-frequency applications.” In: *Electron Device Letters, IEEE* 10.10 (1989), pp. 455–457.
- [BI73] A. S. Barker and M. Ilegems. “Infrared Lattice Vibrations and Free-Electron Dispersion in GaN.” In: *Phys. Rev. B* 7 (1973), pp. 743–750.
- [Bin+94] S. Binari, H. Dietrich, G. Kelner, L. Rowland, K. Doverspike, and D. Gaskill. “Electrical characterisation of Ti Schottky barriers on n-type GaN.” In: *Electronics Letters* 30 (1994), 909–911(2).
- [Bis+13] D. Bisi et al. “Deep-Level Characterization in GaN HEMTs-Part I: Advantages and Limitations of Drain Current Transient Measurements.” In: *IEEE Transactions on Electron Devices* 60.10 (2013), pp. 3166–3175.

- [Bis+14a] D. Bisi, A. Stocco, M. Meneghini, F. Rampazzo, A. Cester, G. Meneghesso, and E. Zanoni. “High-voltage double-pulsed measurement system for GaN-based power HEMTs.” In: *2014 IEEE International Reliability Physics Symposium*. 2014, pp. CD.11.1–CD.11.4.
- [Bis+14b] D. Bisi et al. “Kinetics of Buffer-Related RON-Increase in GaN-on-Silicon MIS-HEMTs.” In: *IEEE Electron Device Letters* 35.10 (2014), pp. 1004–1006.
- [Bis+15] D. Bisi et al. “Trapping mechanisms in GaN-based MIS-HEMTs grown on silicon substrate.” In: *physica status solidi (a)* 212.5 (2015), pp. 1122–1129.
- [Bra+16] T. Brazzini et al. “Mechanism of hot electron electroluminescence in GaN-based transistors.” In: *Journal of Physics D: Applied Physics* 49.43 (2016), p. 435101.
- [Cai+05] Y. Cai, Y. Zhou, K. J. Chen, and K. M. Lau. “High-performance enhancement-mode AlGaIn/GaN HEMTs using fluoride-based plasma treatment.” In: *IEEE Electron Device Letters* 26.7 (2005), pp. 435–437.
- [Cha+17] I. Chatterjee, M. J. Uren, S. Karboyan, A. Pooth, P. Moens, A. Banerjee, and M. Kuball. “Lateral Charge Transport in the Carbon-Doped Buffer in AlGaIn/GaN-on-Si HEMTs.” In: *IEEE Transactions on Electron Devices* 64.3 (2017), pp. 977–983.
- [Che+02] C. Q. Chen, J. P. Zhang, M. E. Gaevski, H. M. Wang, W. H. Sun, R. S. Q. Fareed, J. W. Yang, and M. A. Khan. “AlGaIn layers grown on GaN using strain-relief interlayers.” In: *Applied Physics Letters* 81.26 (2002), pp. 4961–4963.
- [Che+17] K. J. Chen, O. Häberlen, A. Lidow, C. I. Tsai, T. Ueda, Y. Uemoto, and Y. Wu. “GaN-on-Si Power Technology: Devices and Applications.” In: *IEEE Transactions on Electron Devices* 64.3 (2017), pp. 779–795.
- [Chi+16] A. Chini, G. Meneghesso, M. Meneghini, F. Fantini, G. Verzellesi, A. Patti, and F. Iucolano. “Experimental and Numerical Analysis of Hole Emission Process From Carbon-Related Traps in GaN Buffer Layers.” In: *IEEE Transactions on Electron Devices* 63.9 (2016), pp. 3473–3478.
- [Chi14] F.-C. Chiu. “A review on conduction mechanisms in dielectric films.” In: *Advances in Materials Science and Engineering* 2014 (2014).
- [Cho+14] W. Choi, H. Ryu, N. Jeon, M. Lee, H.-Y. Cha, and K.-S. Seo. “Improvement of V_{th} instability in normally-off GaN MIS-HEMTs employing PEALD-SiN_x as an interfacial layer.” In: *IEEE Electron Device Lett* 35.1 (2014), pp. 30–32.
- [Chu+11] R. Chu, A. Corrion, M. Chen, R. Li, D. Wong, D. Zehnder, B. Hughes, and K. Boutros. “1200-V Normally Off GaN-on-Si Field-Effect Transistors With Low Dynamic on-Resistance.” In: *IEEE Electron Device Letters* 32.5 (2011), pp. 632–634.
- [Con28] E. U. Condon. “Nuclear Motions Associated with Electron Transitions in Diatomic Molecules.” In: *Phys. Rev.* 32 (1928), pp. 858–872.
- [Cor+11] A. L. Corrion, M. Chen, R. Chu, S. D. Burnham, S. Khalil, D. Zehnder, B. Hughes, and K. Boutros. “Normally-off gate-recessed AlGaIn/GaN-on-Si hybrid MOS-HFET with Al₂O₃ gate dielectric.” In: *69th Device Research Conference*. 2011, pp. 213–214.
- [Cor08] I. T.N. A. Corp. *Saving energy through innovation and technology (white paper)*. 2008.

- [CP58] A. Chynoweth and G. Pearson. “Effect of Dislocations on Breakdown in Silicon p-n Junctions.” In: *Journal of Applied Physics* 29.7 (1958), pp. 1103–1110.
- [Demli] I. I.E.A.T.P. E. Demand. [ONLINE], <http://www.iea.org/weo/>, [Accessed 01.12.2018].
- [Dic+16] J. R. Dickerson et al. “Vertical GaN Power Diodes With a Bilayer Edge Termination.” In: *IEEE Transactions on Electron Devices* 63.1 (2016), pp. 419–425.
- [Feh+11] T. B. Fehlberg, J. S. Milne, G. A. Umana-Membreno, S. Keller, U. K. Mishra, B. D. Nener, and G. Parish. “Transport Studies of AlGa_N/Ga_N Heterostructures of Different Al Mole Fractions With Variable SiN_x Passivation Stress.” In: *IEEE Transactions on Electron Devices* 58.8 (2011), pp. 2589–2596.
- [Fel+01] E. Feltn, B. Beaumont, M. Laügt, P. de Mierry, P. Vennéguès, H. Lahrèche, M. Leroux, and P. Gibart. “Stress control in GaN grown on silicon (111) by metalorganic vapor phase epitaxy.” In: *Applied Physics Letters* 79.20 (2001), pp. 3230–3232.
- [Gam09] A. Gamper. “Das so genannte Selbstplagiat im Lichte des § 103 UG 2002 sowie der guten wissenschaftlichen Praxis.” German. In: *Zeitschrift für Hochschulrecht, Hochschulmanagement und Hochschulpolitik* 8.1 (2009), pp. 2–10.
- [GN02] A. V. Gorbatyuk and F.-J. Niedernostheide. “Spatial current-density instabilities in multilayered semiconductor structures.” In: *Phys. Rev. B* 65 (2002), p. 245318.
- [Hah+12] H. Hahn, A. Alam, M. Heuken, H. Kalisch, and A. Vescan. “Investigation of plasma-oxidized aluminium as a gate dielectric for AlGa_N/Ga_N MISHFETs.” In: *Semiconductor Science and Technology* 27.6 (2012), p. 062001.
- [Hal52] R. N. Hall. “Electron-hole recombination in germanium.” In: *Physical review* 87.2 (1952), p. 387.
- [Hei+02] S. Heikman, S. Keller, S. P. DenBaars, and U. K. Mishra. “Growth of Fe doped semi-insulating GaN by metalorganic chemical vapor deposition.” In: *Applied Physics Letters* 81.3 (2002), pp. 439–441.
- [Hub+16] M. Huber et al. “Characterization of AlN/AlGa_N/Ga_N:C heterostructures grown on Si(111) using atom probe tomography, secondary ion mass spectrometry, and vertical current-voltage measurements.” In: *Journal of Applied Physics* 119.12 (2016), p. 125701.
- [Hug+12] B. Hughes, J. Lazar, S. Hulsey, D. Zehnder, D. Matic, and K. Boutros. “GaN HFET switching characteristics at 350V/20A and synchronous boost converter performance at 1MHz.” In: *2012 Twenty-Seventh Annual IEEE Applied Power Electronics Conference and Exposition (APEC)*. 2012, pp. 2506–2508.
- [Ima+11] T Imada, K Motoyoshi, M Kanamura, and T Kikkawa. “Reliability analysis of enhancement-mode GaN MIS-HEMT with gate-recess structure for power supplies.” In: *Integrated Reliability Workshop Final Report (IRW), 2011 IEEE International*. IEEE. 2011, pp. 38–41.
- [Jam+06] J. Jameson, P. B. Griffin, J. D. Plummer, and Y. Nishi. “Charge Trapping in High-k Gate Stacks Due to the Bilayer Structure Itself.” In: *Electron Devices, IEEE Transactions on* 53.8 (2006), pp. 1858–1867.

- [JBS86] D. Jäger, H. Baumann, and R. Symanczyk. “Experimental observation of spatial structures due to current filament formation in silicon pin diodes.” In: *Physics Letters A* 117.3 (1986), pp. 141–144.
- [Kar+16] S. Karboyan et al. “Dynamic-Ron in Small and Large C-doped AlGa_N/Ga_N-on-Si HEMTs.” In: *CS ManTech Conference* (2016).
- [Kne+16] M. Knetzger, E. Meissner, J. Derluyn, M. Germain, and J. Friedrich. “Correlation of carbon doping variations with the vertical breakdown of Ga_N-on-Si for power electronics.” In: *Microelectronics Reliability* 66 (2016), pp. 16–21.
- [KO89] B. Kerner and V. V. Osipov. “Autosolitons.” In: *Physics-Uspeski* 32.2 (1989), pp. 101–138.
- [Kol+17a] C. Koller, G. Pobegen, C. Ostermaier, and D. Pogany. “Evidence of defect band in carbon-doped Ga_N controlling leakage current and trapping dynamics.” In: *2017 IEEE International Electron Devices Meeting (IEDM)*. 2017, pp. 33.4.1–33.4.4.
- [Kol+17b] C. Koller, G. Pobegen, C. Ostermaier, M. Huber, and D. Pogany. “The interplay of blocking properties with charge and potential redistribution in thin carbon-doped Ga_N on n-doped Ga_N layers.” In: *Applied Physics Letters* 111.3 (2017), p. 032106.
- [Kol+18a] C. Koller, G. Pobegen, C. Ostermaier, and D. Pogany. “Effect of Carbon Doping on Charging/Discharging Dynamics and Leakage Behavior of Carbon-Doped Ga_N.” In: *IEEE Transactions on Electron Devices* 65.12 (2018), pp. 5314–5321.
- [Kol+18b] C. Koller, G. Pobegen, C. Ostermaier, G. Hecke, R. Neumann, M. Holzbauer, G. Strasser, and D. Pogany. “Trap-related breakdown and filamentary conduction in carbon-doped Ga_N.” In: *physica status solidi (b)* (2018, in review process (submitted after minor revisions)).
- [Kri05] M. Krieger. “Transporteigenschaften von Elektronen in Siliziumkarbid bei tiefen Temperaturen und im Kanal von Metall-Oxid-Halbleiter-Transistoren.” PhD thesis. Naturwissenschaftliche Fakultäten der Universität Erlangen-Nürnberg, 2005.
- [Lag14] P. W. Lagger. “Physics and Characterization of the Gate Stack in Gallium Nitride based MIS-HEMTs.” PhD thesis. Vienna University of Technology, Institute of Solid State Electronics, 2014.
- [Lam56] M. A. Lampert. “Simplified Theory of Space-Charge-Limited Currents in an Insulator with Traps.” In: *Phys. Rev.* 103 (1956), pp. 1648–1656.
- [Lan80] P. T. Landsberg. “Stability and dissipation: non-equilibrium phase transition in semiconductors.” In: *European Journal of Physics* 1.1 (1980), p. 31.
- [Li+04] D. S. Li, H. Chen, H. B. Yu, H. Q. Jia, Q. Huang, and J. M. Zhou. “Dependence of leakage current on dislocations in Ga_N-based light-emitting diodes.” In: *Journal of Applied Physics* 96.2 (2004), pp. 1111–1114.
- [LI15] E. W. Lim and R. Ismail. “Conduction Mechanism of Valence Change Resistive Switching Memory: A Survey.” In: *Electronics* 4.3 (2015), pp. 586–613.
- [Lid+14] A. Lidow, J. Strydom, M. De Rooij, and D. Reusch. *GaN transistors for efficient power conversion*. John Wiley & Sons, 2014.

- [LJW10] J. L. Lyons, A. Janotti, and C. G. V. de Walle. “Carbon impurities and the yellow luminescence in GaN.” In: *Applied Physics Letters* 97.15 (2010), p. 152108.
- [LJW14] J. L. Lyons, A. Janotti, and C. G. Van de Walle. “Effects of carbon on the electrical and optical properties of InN, GaN, and AlN.” In: *Phys. Rev. B* 89 (2014), p. 035204.
- [LKV05] M. Levinshtein, J. Kostamovaara, and S. Vainshtein. *Breakdown phenomena in semiconductors and semiconductor devices, In Selected topics in electronics and systems - vol. 36, see p.81*. World Scientific Publishing, 2005.
- [LRS01] M. E. Levinshtein, S. L. Rumyantsev, and M. S. Shur. *Properties of Advanced Semiconductor Materials: GaN, AlN, InN, BN, SiC, SiGe*. John Wiley & Sons, 2001.
- [Mam+09] W Mamane, D Johnsson, P Rodin, S Bychikhin, V Dubec, M Stecher, E Gornik, and D Pogany. “Interaction of traveling current filaments and its relation to a nontrivial thermal breakdown scenario in avalanching bipolar transistor.” In: *Journal of Applied Physics* 105.8 (2009), p. 084501.
- [Mas+17] F. C.-P. Massabuau et al. “Carrier localization in the vicinity of dislocations in In-GaN.” In: *Journal of Applied Physics* 121.1 (2017), p. 013104.
- [MB17] M. Matsubara and E. Bellotti. “A first-principles study of carbon-related energy levels in GaN. II. Complexes formed by carbon and hydrogen, silicon or oxygen.” In: *Journal of Applied Physics* 121.19 (2017), p. 195702.
- [McP10] J. W. McPherson. *Reliability physics and engineering*. Springer, 2010.
- [MD12] N. F. Mott and E. A. Davis. *Electronic processes in non-crystalline materials*. OUP Oxford, 2012.
- [Men+04] G. Meneghesso, G. Verzellesi, R. Pierobon, F. Rampazzo, A. Chini, U. K. Mishra, C. Canali, and E. Zanoni. “Surface-related drain current dispersion effects in AlGaIn-GaN HEMTs.” In: *IEEE Transactions on Electron Devices* 51.10 (2004), pp. 1554–1561.
- [Men+09] M Meneghini, N Trivellin, M Pavesi, M Manfredi, U Zehnder, B Hahn, G Meneghesso, and E Zanoni. “Leakage current and reverse-bias luminescence in InGaIn-based light-emitting diodes.” In: *Applied Physics Letters* 95.17 (2009), p. 173507.
- [Men+14] M. Meneghini et al. “Trapping in GaN-based metal-insulator-semiconductor transistors: Role of high drain bias and hot electrons.” In: *Applied Physics Letters* 104.14 (2014), p. 143505.
- [Men+16] G Meneghesso, M Meneghini, I Rossetto, D Bisi, S Stoffels, M. V. Hove, S Decoutere, and E Zanoni. “Reliability and parasitic issues in GaN-based power HEMTs: a review.” In: *Semiconductor Science and Technology* 31.9 (2016), p. 093004.
- [Men+17] M. Meneghini, O. Hilt, J. Wuerfl, and G. Meneghesso. “Technology and reliability of normally-off GaN HEMTs with p-type gate.” In: *Energies* 10.2 (2017), p. 153.
- [MHR90] K. Mayer, R. Huebener, and U Rau. “Nucleation and growth of current filaments in semiconductors.” In: *Journal of Applied Physics* 67.3 (1990), pp. 1412–1416.
- [MMZ18] G. Meneghesso, M. Meneghini, and E. Zanoni. *Gallium Nitride-enabled High Frequency and High Efficiency Power Conversion*. Springer, 2018.

- [Moe+15a] P. Moens et al. “Impact of buffer leakage on intrinsic reliability of 650V AlGa_N/Ga_N HEMTs.” In: *2015 IEEE International Electron Devices Meeting (IEDM)*. 2015, pp. 35.2.1–35.2.4.
- [Moe+15b] P. Moens et al. “On the impact of carbon-doping on the dynamic Ron and off-state leakage current of 650V Ga_N power devices.” In: *2015 IEEE 27th International Symposium on Power Semiconductor Devices IC’s (ISPSD)*. 2015, pp. 37–40.
- [Moe+16] P. Moens et al. “(Invited) Intrinsic Reliability Assessment of 650V Rated AlGa_N/Ga_N Based Power Devices: An Industry Perspective.” In: *ECS Transactions* 72.4 (2016), pp. 65–76.
- [Mut+97] J. F. Muth, J. H. Lee, I. K. Shmagin, R. M. Kolbas, H. C. Casey, B. P. Keller, U. K. Mishra, and S. P. DenBaars. “Absorption coefficient, energy gap, exciton binding energy, and recombination lifetime of Ga_N obtained from transmission measurements.” In: *Applied Physics Letters* 71.18 (1997), pp. 2572–2574.
- [NC06a] O. P. T. Newport Corporation. *Monochromators and Spectrographs*. 2006.
- [NC06b] O. P. T. Newport Corporation. *Spectral Irradiance*. 2006.
- [NW96] J. Neugebauer and C. G. V. de Walle. “Gallium vacancies and the yellow luminescence in Ga_N.” In: *Applied Physics Letters* 69.4 (1996), pp. 503–505.
- [ON08] T. Oka and T. Nozawa. “AlGa_N/Ga_N Recessed MIS-Gate HFET With High-Threshold-Voltage Normally-Off Operation for Power Electronics Applications.” In: *IEEE Electron Device Letters* 29.7 (2008), pp. 668–670.
- [Pal+06] T. Palacios, C. S. Suh, A. Chakraborty, S. Keller, S. P. DenBaars, and U. K. Mishra. “High-performance E-mode AlGa_N/Ga_N HEMTs.” In: *IEEE Electron Device Letters* 27.6 (2006), pp. 428–430.
- [Pan75] J. Pankove. “Optical properties of Ga_N.” In: *RCA Rev.* 36 (1975), pp. 163–176.
- [Par+00] G. Parish, S. Keller, S. P. Denbaars, and U. K. Mishra. “SIMS investigations into the effect of growth conditions on residual impurity and silicon incorporation in Ga_N and Al_xGa_{1-x}N.” In: *Journal of Electronic Materials* 29.1 (2000), pp. 15–20.
- [Pog+11] D. Pogany, D. Johnsson, S. Bychikhin, K. Esmark, P. Rodin, M. Stecher, E. Gornik, and H. Gossner. “Measuring Holding Voltage Related to Homogeneous Current Flow in Wide ESD Protection Structures Using Multilevel TLP.” In: *Electron Devices, IEEE Transactions on* 58.2 (2011), pp. 411–418.
- [Pol+03] A. Y. Polyakov, N. B. Smirnov, A. V. Govorkov, and S. J. Pearton. “Electrical and optical properties of Fe-doped semi-insulating Ga_N templates.” In: *Applied Physics Letters* 83.16 (2003), pp. 3314–3316.
- [Pur+89] H.-G. Purwins, C. Radehaus, T. Dirksmeyer, R. Dohmen, R. Schmeling, and H. Willebrand. “Application of the activator inhibitor principle to physical systems.” In: *Physics Letters A* 136.9 (1989), pp. 480–484.
- [Rac+18a] B. Rackauskas, M. J. Uren, S. Stoffels, M. Zhao, S. Decoutere, and M. Kuball. “Determination of the Self-Compensation Ratio of Carbon in AlGa_N for HEMTs.” In: *IEEE Transactions on Electron Devices* 65.5 (2018), pp. 1838–1842.

- [Rac+18b] B. Rackauskas, S. Dalcanale, M. J. Uren, T. Kachi, and M. Kuball. “Leakage mechanisms in GaN-on-GaN vertical pn diodes.” In: *Applied Physics Letters* 112.23 (2018), p. 233501.
- [Rei+16] M. Reiche, M. Kittler, H Uebensee, E Pippel, A Haehnel, and S Birner. “Electronic properties of dislocations.” In: *Applied Physics A* 122.4 (2016), pp. 1–7.
- [Res+14] M. A. Reshchikov, D. O. Demchenko, A. Usikov, H. Helava, and Y. Makarov. “Carbon defects as sources of the green and yellow luminescence bands in undoped GaN.” In: *Phys. Rev. B* 90 (2014), p. 235203.
- [Rid63] B. K. Ridley. “Specific Negative Resistance in Solids.” In: *Proceedings of the Physical Society* 82.6 (1963), p. 954.
- [RM05] M. A. Reshchikov and H. Morkoç. “Luminescence properties of defects in GaN.” In: *Journal of Applied Physics* 97.6 (2005), p. 061301.
- [Sai+06] W. Saito, Y. Takada, M. Kuraguchi, K. Tsuda, and I. Omura. “Recessed-gate structure approach toward normally off high-voltage AlGaIn/GaN HEMT for power electronics applications.” In: *IEEE Transactions on Electron Devices* 53.2 (2006), pp. 356–362.
- [San+10] V. Sankin, A. Monakhov, P. Shkrebiy, P. Abramov, N. Sablina, and N. Averkiev. “Peculiarities of impact ionization of Impurity Al in SiC polytypes.” In: *Applied Physics Letters* 97.26 (2010), p. 262118.
- [Sch12] E. Schöll. *Nonequilibrium phase transitions in semiconductors: self-organization induced by generation and recombination processes*. Vol. 35. Springer Science & Business Media, 2012.
- [Sch79] E Schöll. “Formal conditions for non-equilibrium phase transitions in semiconductors.” In: *Proc. R. Soc. Lond. A* 365.1723 (1979), pp. 511–521.
- [Sel+12] S. Selvaraj, A. Watanabe, A. Wakejima, and T. Egawa. “1.4-kV Breakdown Voltage for AlGaIn/GaN High-Electron-Mobility Transistors on Silicon Substrate.” In: *Electron Device Letters, IEEE* 33.10 (2012), pp. 1375–1377.
- [Seo+13] O. Seok, W. Ahn, M.-K. Han, and M.-W. Ha. “High on/off current ratio AlGaIn/GaN MOS-HEMTs employing RF-sputtered HfO₂ gate insulators.” In: *Semiconductor Science and Technology* 28.2 (2013), p. 025001.
- [Sha+11] Q. Shan, D. S. Meyaard, Q. Dai, J. Cho, E. Fred Schubert, J. Kon Son, and C. Sone. “Transport-mechanism analysis of the reverse leakage current in GaInN light-emitting diodes.” In: *Applied Physics Letters* 99.25 (2011), p. 253506.
- [Shi+09] J. Shi, L. F. Eastman, X. Xin, and M. Pophristic. “High performance AlGaIn/GaN power switch with HfO₂ insulation.” In: *Applied Physics Letters* 95.4 (2009), p. 042103.
- [SMG13] M. P. Shaw, V. V. Mitin, and H. L. Grubin. *The physics of instabilities in solid state electron devices*. Plenum Press, New York and London, 2013.
- [Smi78] R. A. Smith. *Semiconductors*. Cambridge Univ. Press, 1978.
- [SN06] S. M. Sze and K. K. Ng. *Physics of Semiconductor Devices*. John Wiley & Sons, 2006.
- [SRJ52] W. Shockley and W. Read Jr. “Statistics of the recombinations of holes and electrons.” In: *Physical review* 87.5 (1952), p. 835.

- [SS01] E. Schöll and E. Scholl. *Nonlinear spatio-temporal dynamics and chaos in semiconductors*. Vol. 10. Cambridge University Press, 2001.
- [SSE09] S. L. Selvaraj, T. Suzue, and T. Egawa. “Breakdown Enhancement of AlGa_N/Ga_N HEMTs on 4-in Silicon by Improving the Ga_N Quality on Thick Buffer Layers.” In: *IEEE Electron Device Letters* 30.6 (2009), pp. 587–589.
- [Sto+15] S. Stoffels et al. “The physical mechanism of dispersion caused by AlGa_N/Ga_N buffers on Si and optimization for low dispersion.” In: *2015 IEEE International Electron Devices Meeting (IEDM)*. 2015, pp. 35.4.1–35.4.4.
- [Str+16] R. Stradiotto, G. Pobegen, C. Ostermaier, and T. Grasser. “Characterization of charge trapping phenomena at III–N/dielectric interfaces.” In: *Solid-State Electronics* 125 (2016), pp. 142–153.
- [Stren] R. Stradiotto. “Characterization of Electrically Active Defects at III-N/Dielectric Interfaces.” PhD thesis. Vienna University of Technology, 2016.
- [Tan+13] K. Tanaka, M. Ishida, T. Ueda, and T. Tanaka. “Effects of Deep Trapping States at High Temperatures on Transient Performance of AlGa_N/Ga_N Heterostructure Field-Effect Transistors.” In: *Japanese Journal of Applied Physics* 52.4S (2013), 04CF07.
- [Tan+15] K. Tanaka et al. “Suppression of current collapse by hole injection from drain in a normally-off Ga_N-based hybrid-drain-embedded gate injection transistor.” In: *Applied Physics Letters* 107.16 (2015), p. 163502.
- [Tan+18] X. Tang, Z. Zhang, J. Wei, B. Li, J. Wang, and K. J. Chen. “Photon emission and current-collapse suppression of AlGa_N/Ga_N field-effect transistors with photonic-ohmic drain at high temperatures.” In: *Applied Physics Express* 11.7 (2018), p. 071003.
- [Tho12] R. D. Thorlabs. *Thorlabs SM1PD2A Photodiode specifications sheet*. 2012.
- [Uem+07] Y. Uemoto et al. “Gate Injection Transistor (GIT): A Normally-Off AlGa_N/Ga_N Power Transistor Using Conductivity Modulation.” In: *IEEE Transactions on Electron Devices* 54.12 (2007), pp. 3393–3399.
- [UMK12] M. J. Uren, J. Moreke, and M. Kuball. “Buffer Design to Minimize Current Collapse in Ga_N/AlGa_N HFETs.” In: *IEEE Transactions on Electron Devices* 59.12 (2012), pp. 3327–3333.
- [Ure+14a] M. J. Uren, M. Cäsar, M. A. Gajda, and M. Kuball. “Buffer transport mechanisms in intentionally carbon doped Ga_N heterojunction field effect transistors.” In: *Applied Physics Letters* 104.26 (2014), p. 263505.
- [Ure+14b] M. J. Uren, M. Silvestri, M. Casar, G. A. M. Hurkx, J. A. Croon, J. Sonsky, and M. Kuball. “Intentionally carbon-doped AlGa_N/Ga_N HEMTs: Necessity for vertical leakage paths.” In: *Electron Device Letters, IEEE* 35.3 (2014), pp. 327–329.
- [Ure+14c] M. Uren, M Silvestri, M Cäsar, J. Pomeroy, G. Hurkx, J. Croon, J Šonský, and M Kuball. “Need for defects in floating-buffer AlGa_N/Ga_N HEMTs.” In: *Proc. CS-MANTECH* (2014), pp. 317–319.

- [Ure+15] M. J. Uren, M. Caesar, S. Karboyan, P. Moens, P. Vanmeerbeek, and M. Kuball. “Electric Field Reduction in C-Doped AlGa_N/Ga_N on Si High Electron Mobility Transistors.” In: *IEEE Electron Device Letters* 36.8 (2015), pp. 826–828.
- [Ure+17] M. Uren, S. Karboyan, I. Chatterjee, A. Pooth, P. Moens, A. Banerjee, and M. Kuball. ““Leaky Dielectric” Model for the Suppression of Dynamic RON in Carbon-Doped AlGa_N/Ga_N HEMTs.” In: *PP* (2017), pp. 1–9.
- [Usa+18a] S. Usami et al. “Correlation between dislocations and leakage current of p-n diodes on a free-standing Ga_N substrate.” In: *Applied Physics Letters* 112.18 (2018), p. 182106.
- [Usa+18b] S. Usami et al. “Effect of dislocations on the growth of p-type Ga_N and on the characteristics of p–n diodes.” In: *physica status solidi (a)* 214.8 (2018), p. 1600837.
- [VCB79] G Vincent, A Chantre, and D Bois. “Electric field effect on the thermal emission of traps in semiconductor junctions.” In: *Journal of Applied Physics* 50.8 (1979), pp. 5484–5487.
- [Ver+14] G. Verzellesi et al. “Influence of Buffer Carbon Doping on Pulse and AC Behavior of Insulated-Gate Field-Plated Power AlGa_N/Ga_N HEMTs.” In: *IEEE Electron Device Letters* 35.4 (2014), pp. 443–445.
- [VK69] A. F. Volkov and S. M. Kogan. “Physical phenomena in semiconductors with negative differential conductivity.” In: *Soviet Physics Uspekhi* 11.6 (1969), p. 881.
- [Wat+03] T. Watanabe, H. H. Funke, R. Torres, M. W. Raynor, J. Vininski, and V. H. Houlding. “Contamination control in gas delivery systems for MOCVD.” In: *Journal of Crystal Growth* 248 (2003), pp. 67–71.
- [Wic+04] A. Wickenden, D. Koleske, R. Henry, M. Twigg, and M. Fatemi. “Resistivity control in unintentionally doped Ga_N films grown by MOCVD.” In: *Journal of Crystal Growth* 260.1 (2004), pp. 54–62.
- [WJ07] C. Wood and D. Jena. *Polarization Effects in Semiconductors: From Ab Initio Theory to Device Applications*. Springer Science & Business Media, 2007.
- [WN04] C. G. Van de Walle and J. Neugebauer. “First-principles calculations for defects and impurities: Applications to III-nitrides.” In: *Journal of Applied Physics* 95.8 (2004), pp. 3851–3879.
- [Wri02] A. F. Wright. “Substitutional and interstitial carbon in wurtzite Ga_N.” In: *Journal of Applied Physics* 92.5 (2002), pp. 2575–2585.
- [Wri61] G. Wright. “Mechanisms of space-charge-limited current in solids.” In: *Solid-State Electronics* 2.2 (1961), pp. 165–189.
- [XWW16] M. Xu, Y. Weng, and H. Wang. “Reduction of leakage current in Ga_N-based high-electron mobility transistor employing carbon-doped Ga_N superlattice buffer layers.” In: *2016 13th China International Forum on Solid State Lighting: International Forum on Wide Bandgap Semiconductors China (SSLChina: IFWS)*. 2016, pp. 62–63.
- [Yac+16] H. Yacoub, D. Fahle, M. Eickelkamp, A. Wille, C. Mauder, M. Heuken, H. Kalisch, and A. Vescan. “Effect of stress voltage on the dynamic buffer response of Ga_N-on-silicon transistors.” In: *Journal of Applied Physics* 119.13 (2016), p. 135704.

- [Yac+17] H. Yacoub, C. Mauder, S. Leone, M. Eickelkamp, D. Fahle, M. Heuken, H. Kalisch, and A. Vescan. “Effect of Different Carbon Doping Techniques on the Dynamic Properties of GaN-on-Si Buffers.” In: *IEEE Transactions on Electron Devices* 64.3 (2017), pp. 991–997.
- [Yac+18] H. Yacoub et al. “Effect of Carbon Doping Level on Static and Dynamic Properties of AlGaN/GaN Heterostructures Grown on Silicon.” In: *IEEE Transactions on Electron Devices* 65.8 (2018), pp. 3192–3198.
- [Yac17] H. Yacoub. “Characterization, Analysis and Modelling of DC and Dynamic Properties of GaN HFETs Grown on Silicon.” PhD thesis. RWTH Aachen University, 2017.
- [Yan+14] S. Yang, C. Zhou, Q. Jiang, J. Lu, B. Huang, and K. J. Chen. “Investigation of buffer traps in AlGaN/GaN-on-Si devices by thermally stimulated current spectroscopy and back-gating measurement.” In: *Applied Physics Letters* 104.1, 013504 (2014).
- [Zha+14] Y. Zhang, M. Sun, D. Piedra, M. Azize, X. Zhang, T. Fujishima, and T. Palacios. “GaN-on-Si vertical Schottky and pn diodes.” In: *IEEE Electron Device Letters* 35.6 (2014), pp. 618–620.
- [Zha+15a] Y. Zhang, H. Y. Wong, M. Sun, S. Joglekar, L. Yu, N. A. Braga, R. V. Mickevicius, and T. Palacios. “Design space and origin of off-state leakage in GaN vertical power diodes.” In: *2015 IEEE International Electron Devices Meeting (IEDM)*. 2015, pp. 35.1.1–35.1.4.
- [Zha+15b] Y. Zhang et al. “Origin and Control of OFF-State Leakage Current in GaN-on-Si Vertical Diodes.” In: *IEEE Transactions on Electron Devices* 62.7 (2015), pp. 2155–2161.
- [Zho+08] Y. Zhou et al. “Formation, etching and electrical characterization of a thermally grown gallium oxide on the Ga-face of a bulk GaN substrate.” In: *Solid-State Electronics* 52.5 (2008), pp. 756–764.
- [Zho+12] C. Zhou, Q. Jiang, S. Huang, and K. J. Chen. “Vertical leakage/breakdown mechanisms in AlGaN/GaN-on-Si devices.” In: *Electron Device Letters, IEEE* 33.8 (2012), pp. 1132–1134.

Own publications

Journal papers

Title	The interplay of blocking properties with charge and potential redistribution in thin carbon-doped GaN on n-doped GaN layers
Authors	C. Koller, G. Pobegen, C. Ostermaier, M. Huber, and D. Pogany
Published in	Applied Physics Letters
Year	2017
Volume	111
Pages	032106
Title	Effect of Carbon-Doping on Charging/Discharging Dynamics and Leakage Behavior of Carbon-Doped GaN
Authors	C. Koller, G. Pobegen, C. Ostermaier, and D. Pogany
Published in	IEEE Transactions on Electron Devices
Year	2018
Volume	65
Issue	12
Pages	5314-5321
Title	Trap-related Breakdown and Filamentary Conduction in Carbon-Doped GaN
Authors	C. Koller, G. Pobegen, C. Ostermaier, G. Hecke, R. Neumann, M. Holzbauer, G. Strasser, and D. Pogany
Published in	physica status solidi (b)
Year	tbd (final version after minor revisions submitted)
Volume	tbd
Number	tbd
Pages	tbd

Conferences

- | | |
|--------------|--|
| Title | Leakage and Voltage Blocking Behavior of Carbon-Doped GaN Buffer Layers |
| Authors | C. Koller, G. Pobegen, C. Ostermaier, M. Huber and D. Pogany |
| Published in | Proceedings of the Workshop on Compound Semiconductor Devices and Integrated Circuits (WOCSDICE) |
| Year | 2017 |
| Pages | 23-24 |
| Location | Las Palmas de Gran Canaria, Spain |
| Presentation | Oral Presentation |
| | |
| Title | Transient capacitance analysis of thin carbon-doped GaN (GaN:C) layers |
| Authors | C. Koller, G. Pobegen, C. Ostermaier, and D. Pogany |
| Published in | Proceedings of the International Conference on Nitride Semiconductors (ICNS) |
| Year | 2017 |
| Location | Strasbourg, France |
| Presentation | Poster |
| | |
| Title | Evidence of defect band in carbon-doped GaN controlling leakage current and trapping dynamics |
| Authors | C. Koller, G. Pobegen, C. Ostermaier, and D. Pogany |
| Published in | Proceedings of the IEEE International Electron Device Meeting (IEDM) |
| Year | 2018 |
| Pages | 33.4.1-33.4.4 |
| Location | San Francisco, United States of America |
| Presentation | Oral Presentation and Paper |
| | |
| Title | Trap-related localized breakdown in carbon-doped GaN |
| Authors | C. Koller, G. Pobegen, C. Ostermaier, and D. Pogany |
| Published in | Proceedings of the International Conference on the Physics of Semiconductors (ICPS) |
| Year | 2018 |
| Location | Montpellier, France |
| Presentation | Oral Presentation (held by D. Pogany) |
| | |
| Title | The Role and Mechanism of Carbon in Insulating GaN Buffers |
| Authors | C. Koller, G. Pobegen, C. Ostermaier, and D. Pogany |
| Published in | Proceedings of the International Workshop on Nitride Semiconductors (IWN) |
| Year | 2018 |
| Location | Kanazawa, Japan |
| Presentation | Invited Oral Presentation |

List of Figures

2.1	Schematic of a HEMT indicating the GaN:C buffer's two main features of interest: 1. vertical leakage current and 2. trapping dynamics.	11
2.2	Theoretical possible specific on-resistance (R_{sp}) vs. breakdown voltage (V_{bd}) for the three semiconductors relevant for power semiconductors: Si, SiC and GaN [Bal89]. Markers further show the performance of real GaN-based HEMT devices [Seo+13; Shi+09; Hah+12].	12
2.3	Formation energy plot for carbon-doped GaN with C_N , C_{Ga} and carbon interstitials C_I . Figure from [LJW14].	15
2.4	Schematic Poole-Frenkel emission from a trap demonstrating how an applied electric field lowers the effective barrier.	16
2.5	Schematic I_{SS} - V characteristic for SCLC as proposed by Lampert [Lam56] for semiconductors with large trap densities. At $V = V_{TFL}$ conduction changes from being limited by Ohmic conduction to being determined by SCLC.	17
2.6	Band diagram demonstrating hopping conduction in a metal-insulator-semiconductor (MIS) structure. Figure from [Chi14].	18
2.7	one-dimensional equivalent circuit representing the HEMT stack according to Uren et al. [Ure+17]. Figure from [Ure+17].	19
2.8	Vertical leakage current vs. (a) reverse and (b) forward bias indicating SCLC according to Zhou et al. [Zho+12]. Figure from [Zho+12].	19
2.9	Vertical breakdown voltages as function of the AlN thickness. Figure from [Yac17].	20
2.10	(a) Leakage current for negative bias on top with variation of the AlN thickness in the inset indicating SCLC, see Eq. (2.8). (b) Leakage current for positive bias for various temperatures indicates Poole-Frenkel conduction, see Eq. (2.7). Figure from [Yac17].	20
2.11	Leakage current as function of estimated voltage drops in GaN:uid (V_1) and in GaN:C (V_2). Figure from [Ure+14a].	21
2.12	Schematic figure of drain current in on-state vs. drain bias, before and after trapping, illustrating the terms current collapse and dynamic $R_{ds,on}$	22
2.13	Schematic substrate ramp measurement illustrating hysteresis curves for no trapping (black), positive charge trapping (blue) and negative charge trapping (red). Arrows indicate the sweep direction, i.e. increasing/decreasing bias.	23
2.14	"On-the-fly" (OTF) measurement on a GaN:C buffer indicating decreasing I_{2DEG} with increasing negative V_{sub} , corresponding to negative charge capture. The inset demonstrates the measurement sequence. Figure from [Yac17].	24

2.15	Schematic HEMT structure and stress conditions for trapping negative charges in the buffer in (a) off-state and (b) backgating condition, figures from [Bis+14b]. (c) Recovery of $R_{ds,on}$ in on-state after the stress-condition due to detrapping from carbon defects, figure from [Bis+15].	25
2.16	Schematic configuration coordinate diagram for an occupied defect ($C(-)$) and an empty defect with an electron in the conduction band ($C(-)+e^-$), E_T represents the trap level. The energy barriers that have to be overcome for (phonon-assisted) electron capture and emission are ΔE_A and $E_A^{ion} + \Delta E_A$, respectively.	25
2.17	Arrhenius plot with time constants derived in recovery after backgating and off-state stresses. c_n represents the trapping rate, which is equivalent to $1/\tau$. Figure from [Men+16].	26
2.18	Typical raw spectra of GaN:C, featuring peaks originating from near band edge emission (NBE), blue luminescence (BL) and yellow luminescence (YL). Indices 'A' to 'F' represent measurements from wafer center to wafer edge, respectively. Figure from [Kne+16].	27
3.1	Schematics of (a) a conventional HEMT stack and (b) an exemplary LUT structure consisting of the electrically inactive base structure and the LUT.	29
3.2	(a) Schematic and simplified equivalent circuit of S_{10b} , (b) C_{SS-V} and (c) I_{SS-V} as well as from data in (c) extracted (d) differential resistance (R_{diff}) for circular contacts with various diameters D	31
3.3	(a) I_{SS-V} and (b) C_{SS-V} characteristics as well as extracted $1/C_{SS-V}$ and $1/C_{Si}^2 - V$ of $S_{Schottky}$, S_{10} and S_{10b} . Measurement data reused from [Kol+17b].	32
3.4	Potential of conduction band minimum in S_{10b} for various V (colored values) in (a) <i>depletion regime</i> and (b) <i>plateau regime</i> . Interface potential φ_i , built-in voltage V_{bi} , depletion width in GaN:Si w_{Si} and potential drop in GaN:C $V_{GaN:C}$ are indicated for $V = \pm 10$ V. Measurement data reused from [Kol+17b].	34
3.5	Accumulated negative charge in GaN:C per area σ_C vs. V in S_{10} and S_{10b} with σ_C extracted from Eq. (3.8) and (3.9) with limiting lines for $y = 0$ (additional bulk charge in <i>plateau regime</i>) and $y = 1$ (only interface charge). Measurement data reused from [Kol+17b].	35
3.6	Band gaps, defect levels and calculated E_F as function of T . (a1) Autocompensation model leads for $N_{acc} = N_{don}$ and $(E_{acc} + E_{don})/2 = 0.7$ eV to T independent $E_F = 0.7$ eV. (a2,a3) However, tiny differences in N_{acc}/N_{don} ratios shift E_F dramatically and make it T -dependent. (b1-b4) In the dominant acceptor model E_{don} is irrelevant but E_F depends slightly on T for large variations in N_{acc}/N_{don} ; E_{acc} are chosen to establish $E_F = 0.7$ eV at $T = 300$ K.	36
3.7	Part of the band diagram calculated by Poisson equation in GaN:C as function of the distance from the GaN:Si interface for $V = 0$ V at 300 K, considering (a) auto-compensation model and (b) dominant acceptor model. The equivalent sheet charge density σ_C is the area between negatively charged acceptors and positive charged donors.	38

3.8	(a) Calculated band diagram using Poisson equation at the GaN:C/metal junction and (b) negatively charged acceptor densities $N_{acc(-)}$, positively charged donor densities ($N_{don(+)}$) and equivalent sheet charge densities indicated by the red areas, whereby $\sigma_{C,Schottky} = \sigma_{m,Schottky}$	39
3.9	(a) Schematic bias step from -9.5 V to various V within <i>depletion regime</i> (i.e. $V \leq 1.5\text{ V}$) and back to -9.5 V . (b) Corresponding measured transient capacitance and (c) calculated transient equivalent sheet charge density in GaN:C (σ_C), using Eq. (3.8). (d) Calculated band diagrams at points in time indicated in (b).	42
3.10	(a) Schematic bias step from 8 V to various V within <i>plateau regime</i> (i.e. $V \geq 1.5\text{ V}$) and back to 8 V . (b) Corresponding measured transient capacitance and (c) calculated transient equivalent sheet charge density in GaN:C (σ_C), using Eq. (3.9) with $y = 1$ (i.e. considering no bulk charge). (d) Calculated band diagrams at points in time indicated in (b).	44
3.11	Normalized $C(t)$ curves for S_{10} for bias steps (a) $0 \rightarrow -9.5\text{ V}$, (b) $-9.5 \rightarrow 0\text{ V}$ and (c) $8 \rightarrow 1.5\text{ V}$ reveal faster processes with increasing T . Quantification of the T dependence for (d) linear T scale and (e) Arrhenius-plot clearly show exponential T dependence of charging/discharging time constants ($\tau \propto e^{aT}$, solid blue line). Arrhenius-dependence ($\tau \propto \exp(E_A/(k_B T))$), dashed green line) with reasonable action energies E_A and hole capture cross section σ_{CC} can clearly be ruled out. Dashed lines in (a) show fits of the data at 150 and 550 K to $\exp(-t/\tau)$	46
3.12	Schematic band diagrams demonstrate the required processes for discharging (left half) and charging (right half) of acceptors in the (a) conventionally considered model with charge transport via valence band and in (b,c) the proposed model for GaN:C with charge transport via defect bands (DBs). In (b) the DB level is located below the carbon acceptor level while in (c) it surrounds the acceptor level. Figures reused from [Kol+17a; Kol+18a].	47
3.13	Evolution of the band diagram in S_{10} after various bias steps (a-d): A) in state “A” SS condition is established for the initial bias; B) “B” shows the quasistatic (QS) condition $30\text{ }\mu\text{s}$ after the bias step; C) in “C” SS is established. Orange arrows indicate negative charge transport. Figure reused from [Kol+18a].	50
3.14	Schematic band diagrams demonstrate how in the <i>plateau regime</i> charge accumulation in carbon acceptors in GaN:C establishes a potential barrier (φ_i) that prevents major charge injection into CB of GaN:C. Schematics in left half show SS cases while (b,d) in the right half illustrate hypothetical quasistatic states (hQS) after increasing the bias from (a,c) respectively and the according negative charge accumulation in blue circles. Green arrows represent negative charge transport. For simplicity, displacement current are not shown in hQS	52
3.15	Fitting of the observed exponential temperature dependence of the transport rate (i.e. r_{DB}), solid black line) by the sum of four contributions (r_{sum} , dashed grey line): r_{VB} , r_{NNH} , $r_{VRH,3D}$, $r_{VRH,1D}$ are the rate contributions due to charge transport in VB, nearest neighbor hopping, variable range hopping in 3D and in 1D, respectively. Simulation equations and parameters are given in Tab. 3.3. Figure reused from [Kol+18a].	55

3.16	Arrhenius plot with literature data from CTS measurements in literature from GaN- and AlGaN-based layers and devices with largely varying growth and doping conditions. Figure from [Bis+13].	57
3.17	E_A in literature related to carbon defects as function of the measurement temperature. Symbols indicate the central temperature, numbers the number of measurement points and bars the temperature ranges of the single studies. Figure reused from [Kol+17a].	57
3.18	(a) Arrhenius plot with discharging time constants after a bias step from $-9.5 \rightarrow 0$ V (blue solid line) and exponential fit (black dashed line). (b) Extracted activation energy E_A considering a classical SRH discharging process (Eq. (3.13)). (c-e) In small T ranges, processes appear Arrhenius-like, only large T ranges as in (a) reveal the non-Arrhenius-like T behavior.	58
3.19	(a) $I_{SS}-V$ of S_{10} for selected temperatures and (b) extracted I_{SS} values at 4 V. Direct comparison of (b) with the trapping rate after various bias steps in (c) reveals the identical T dependence of leakage current and trapping. Figures reused from [Kol+17a].	59
3.20	I_{SS} (black dashed line) as function of \mathcal{E}_C with I_{SS} extracted from $I_{SS}-V$ and \mathcal{E}_C from $C_{SS}-V$. Transient currents after various bias steps (I_C , colored solid lines) are extracted from $C(t)$ analysis and fit well to $I_{SS} - \mathcal{E}_C$. Figure reused from [Kol+17a] and [Kol+18a].	60
3.21	Experimentally observed I_C and I_{SS} from Fig. 3.20 in black represent the current through defect bands, which can be fitted well by a \sinh -function (blue) in the entire \mathcal{E}_C regime and for high \mathcal{E}_C by an exponential function (red).	61
3.22	(a) $C_{SS}-V$ of S_{10} at 300 K and (b) calculated potential at the GaN:Si/GaN:C interface (φ_i) using Eq. (3.21).	62
3.23	(a) Vertical leakage current of a HEMT structure (raw data from [Arnen]) for various T and (b) quantitative comparison of its T dependence with I_{SS} and the charging/discharging rates after various bias steps in S_{10}	64
3.24	(a) $C_{SS}-V$ and (b) $I_{SS}-V$ at 300 K for the four samples $S_{Schottky}$, S_{01} , S_{10} and S_{70} with the latter three being LUT structures with GaN:C layer with different $[C]$ (10^{18} cm^{-3} , 10^{19} cm^{-3} and $7 \times 10^{19} \text{ cm}^{-3}$, respectively). Figures reused from [Kol+18a].	65
3.25	Comparison of normalized $C(t)$ data for (a) S_{01} , (b) S_{10} and (c) S_{70} after various bias steps and for various T reveal the similar T dependence of S_{70} and S_{10} and the very different behavior of S_{01} . Quantification of the T dependence in (d) linear- T - and (e) Arrhenius-plots reveal for S_{70} and S_{10} $\tau \propto e^{aT}$ (solid lines) in contrast to $\tau \propto \exp(E_A/(k_B T))$ with $E_A = 0.8 \text{ eV}$ for S_{01} [Kol+18a]. Figures reused from [Kol+18a].	66
3.26	(a) Normalized $C(t)$ after bias steps $-9.5 \rightarrow 0$ V and $0 \rightarrow -9.5$ V representing discharging and charging processes, respectively. (b) Quantification in Arrhenius-plot shows Arrhenius-like T dependence with identical time constants for both processes. Figures reused from [Kol+18a].	67

- 3.27 Schematic band diagrams for bias steps with (a) $\Delta V > 0$ and (b) $\Delta V < 0$ within *depletion regime* at different points in time: (A) initial SS condition before bias step, (B) directly ($\approx 30 \mu\text{s}$) after bias step in quasistatic state, before charge redistribution occurs in GaN:C and (C) in SS. Orange arrows indicate the hole transport through GaN:C. 68
- 3.28 Estimated band diagrams after bias step with $\Delta V > 0$ in (a) quasistatic state and (b) SS, considering an effective acceptor concentration $N_{\text{acc}}^* = 5 \times 10^{17} \text{ cm}^{-3}$. The finite carbon concentration leads to non-negligible space charge regions with finite widths next to top metal (w_{T1}) and w_{C} next to the GaN:Si/GaN:C interface. Orange arrows illustrate the acceptor discharging process, leading to SS. Figures reused from [Kol+18a]. 69
- 3.29 Normalized $C(t)$ after bias step $-9.5 \rightarrow 0 \text{ V}$ reveal multiple capacitance rises/drops, all with same activation energies E_{A} but different prefactor. 70
- 3.30 (a) Band diagram, (b) occupation factor and (c) net space charge density density for cases when E_{F} is above E_{acc} , at E_{acc} and below E_{acc} , establishing respectively negative, zero and positive net space charge. N_{acc} is considered $2 \times N_{\text{don}}$ 71
- 3.31 $I_{\text{SS}}-V$ characteristics for S_{10} in (a) voltage and (b) current controlled mode. Red and blue lines represent respective up- and down-sweeps. For comparison, in (b) voltage-controlled measurements from (a) are illustrated with light grey lines. Figures are reused from [Kol+18b]. 73
- 3.32 (a) Voltage-controlled up- and down-sweep $I_{\text{SS}}-V$ characteristics for S_{10} in linear scale. (b) $I_{\text{SS}}-V$ characteristics for different d_{LUT} (i.e. S_{10}/S_{10b}). Figure (b) reused from [Kol+18b]. 73
- 3.33 (a) Schematic EMMI (and electro- and photoluminescence spectroscopy) setup. (b) Ratio of detected photons by CCD to emitted photons in GaN (i.e. responsivity R_{EMMI}) as function of the photon energy, the grey area under R_{EMMI} represents the measureable part of the signal. R_{EMMI} is determined by the transmissivity of the contact metals (T_{metal}), the optics (T_{optics}) and the responsivity of the CCD (R_{CCD}). (c) Transmissivity of GaN for light with energies above GaN band gap (T_{GaN}) as a function of the distance from the surface (x). 75
- 3.34 Optical image of the top electrode, superimposed with the EMMI signal for $V = 14 \text{ V}$ with $I_{\text{SS}} = 10 \mu\text{A}$. Yellow lines indicate the position of the contacting needle forming a black spot, the light grey area represents the top contact and blue circles the superimposed EMMI signal. 75
- 3.35 EMMI images of parts of the used fragment with the left part unbiased, showing the contacted device and the right part when bias is applied via the needle on the left side. The EMMI spot at the spalled edge shows enhanced current flow centimeters away from the contact. 76
- 3.36 (a) EMMI image in off-state at $T = 475 \text{ K}$ with an integration time $t_{\text{int}} = 600 \text{ s}$. The location of the electrode is indicated by a black dotted line at its perimeter. (b-f) EMMI images in on-state at room temperature with $t_{\text{int}} = 1 \text{ s}$ and different V as labeled in the figures. For better visibility (b-f) show only $10 \mu\text{m} \times 10 \mu\text{m}$ excerpts of the contact area, in outer regions no significant EMMI signal is found. Figures reused from [Kol+18b]. 77

3.37	Frames of an EMMI video at six chosen moments in time for $V = 10\text{ V}$ with $I_{\text{SS}} = 3\text{ }\mu\text{A}$ demonstrate current filament splitting, moving and merging. For better visibility only $22\text{ }\mu\text{m} \times 15\text{ }\mu\text{m}$ excerpts, including the only apparent EMMI spots, are shown. "CF1" in (c) marks a pinned filament. Figures reused from [Kol+18b].	77
3.38	An EMMI image recorded at $V = 14\text{ V}$ and $I_{\text{SS}} = 10\text{ }\mu\text{A}$ demonstrates the existence of multiple current filaments. Figure reused from [Kol+18b].	78
3.39	Schematic setup for electroluminescence and photoluminescence spectroscopy (EL and PL).	79
3.40	Normalized spectra ($I_{\text{PL}}, I_{\text{EL}}$) and corrected spectra ($I_{\text{PL}}/R_{\text{EMMI}}^*, I_{\text{EL}}/R_{\text{EMMI}}$) for EL and PL, respectively. R_{EMMI} considers the wavelength-dependent responsivity of the optical setup, whereby it has to be considered that as for PL no metal contact is required, so that $R_{\text{EMMI}}^* = R_{\text{EMMI}}/T_{\text{metal}}$. The "ringing" signal in EL is assumed to result from interference due to reflections at bottom (and top) interfaces of the GaN stack.	79
3.41	Schematic configuration coordinate diagram comparing the capture and emission energies for thermal (E_{A}) and optical ($E_{\text{opt}}, E_{\text{spec}}$) transitions between negatively charged and neutral acceptor charge states ($\text{C}_{\text{N}}(-), \text{C}_{\text{N}}(0)$). E_{opt} and E_{spec} are shifted compared to E_{th} by the Franck-Condon shifts $d_{\text{FC},1}$ and $d_{\text{FC},2}$, respectively.	81
3.42	Schematic band diagram of S_{10} for $V = 10\text{ V}$ showing that the energy of the emitted light (E_{spec}) might differ from classically expected values in Fig. 3.41.	82
3.43	(a) Transient $I(t)$ measurements after bias steps from 0 to various V and (b) several consecutive measurements for steps to $V = 9.5\text{ V}$, indicating statistical distribution of time-to-filamentation (t_{fil}). Stress times in (b) are 100s with 10s recovery time between measurements, numbers indicate the sweep number. Figure (b) reused from [Kol+18b].	83
3.44	(a) 100 consecutive bias steps from 0 to 9.5 V with stress times of 100s and recovery times of 10s, scales for I are logarithmic. (b) Cumulative distribution function (CDF) for devices in on-state vs. t_{fil}	83
3.45	(a) $I_{\text{SS}}-V$ characteristics (up- and down-sweeps) of 180 consecutive measurements on a single device with a ramp rate of 1.5 V s^{-1} at 300 K. (b) Evolution of $V_{\text{fil,up}}$ and $V_{\text{fil,down}}$ with number of up-/down-cycles (n).	84
3.46	(a) $I_{\text{SS}}-V$ characteristics (up- and down-sweeps) of 100 devices on the same wafer on sample S_{10} with a ramp rate of 1.5 V s^{-1} at 300 K. (b,c) Dependence of V_{fil} on the distance of the measured wafer from the wafer center (z).	85
3.47	(a) $I_{\text{SS}}-V$ for various T with a fixed ramp rate of 0.3 V s^{-1} and (b) V_{fil} vs. T , revealing a mainly linear relation.	86
3.48	(a) $I_{\text{SS}}-V$ characterization at 340 K with a ramp rate of 0.3 V s^{-1} in dark condition ("dark") and with the device being illuminated with monochromatic light with varying photon energies ($E_{\text{h}\nu}$). (b) Analysis of V_{fil} as function of $E_{\text{h}\nu}$ reveals significant decrease of V_{fil} above roughly 3.2 eV.	86

- 3.49 (a) Band diagram in off-state, the blue arrow indicates negative charge injection from CB of GaN:Si to DBs in GaN:C. (b) Schematic energy - wave vector (k) diagram with equation describing impurity impact ionization with $C_N(-)$ and $C_N(0)$ as respective occupied and unoccupied carbon acceptors. (c,d) Band diagrams demonstrate impurity impact ionization at the filamentation onset and in on-state, respectively. An injected electron from GaN:Si can impact an electron in a carbon acceptor and eventually excite it to the conduction band, leaving a neutrally charged acceptor. (d) This results in decreased σ_C and consequently a decrease of φ_i by $\Delta\varphi_i$. The thick red arrow in (d) indicates the resulting massive electron injection, the two red dots represent the two electrons from (c). Figure reused from [Kol+18b]. 87
- 3.50 The schematic S-shape $I_{SS}-V$ characteristic demonstrates the decrease of $V_{fil,up}$ with stress time from curves marked with "1" to the one marked with "3". For curve "2" the moment of filamentation is shown. When the decreasing $V_{fil,up}$ becomes smaller than the applied bias V , transition from off- to on-state occurs with the abrupt current jump marked with the dashed arrow. Figure reused from [Kol+18b]. 89
- 3.51 (a) Schematic model of the LUT with current flow lines represented by yellow arrows. The LUT can be represented with GaN:C as active non-linear layer and GaN:Si as passive Ohmic layer. (b,c,d) show respective I , E_{CB} and σ_C distributions in GaN:C with x as lateral coordinate. (e) Simplified equivalent circuit with the active GaN:C layer represented by current sources in CFs (I_{act}), the passive GaN:Si layer represented by R_{pas} and the base structure represented by R_{com} . Two black arrows demonstrate the parallel components of R_{pas} due to lateral current flow in GaN:Si. Figure reused from [Kol+18b]. 90
- 3.52 (a,b) $I_{SS}-V$ characteristics without illumination ("dark") and illuminated with various $E_{h\nu}$. (c) Quantitative analysis of the spectral dependence of I_{SS} at $V = -10$ V. 92
- 3.53 (a) $I_{SS}-V$ characteristics in dark condition and under illumination with $E_{h\nu} = 3.54$ eV ($\lambda = 350$ nm) and various P_{amp} (i.e. various E_e). (b) I_{SS} vs. P_{amp} at various V as indicated in (a). 93
- 3.54 (a) $C_{SS}-V$ and (b) $1/C_{Si}^2 - V$ for $S_{10,Au}$ at 343 K reveal a horizontal shift by 12.4 V to lower V for characterization under illumination with $E_{h\nu} = 3.54$ eV ($\lambda = 360$ nm). 93
- 3.55 (a) Calculated band diagrams for $S_{10,Au}$ at 343 K in (a1) dark and (a2) illuminated condition, derived from data in Fig. 3.54. (b1-b4) illustrate schematically the main generation and recombination processes indicated in (a2). Orange wavy arrows represent photons. 93
- 3.56 Potential distributions calculated from data in Fig. 3.54(a) under (a) dark and (b) illuminated condition. Comments in (b) indicate bias regions with maximum, positive and negative charge in GaN:C (σ_C), quantified in Fig. 3.58. 95
- 3.57 (a) Interface potential (φ_i) and (b) electric field in GaN:C (\mathcal{E}_C) as function of V under dark and illuminated condition. Calculations base on data in Fig. 3.54(a). 96
- 3.58 (a) Bias-dependent equivalent sheet charge in GaN:C (σ_C) and (b) schematic band diagrams indicating the charge states in the different bias ranges in (a). Calculations base on data in Fig. 3.54(a). 96

3.59	(a) Simulated current flow through defect bands in GaN:C ($I_{DB,sim}$) based on extracted \mathcal{E}_C from Fig. 3.54(a) and $I_{DB}(\mathcal{E}_C)$ -relations shown in Fig. 3.20. (b) Measured I_{SS} - V characteristics.	97
3.60	(a) C_{SS} - V and (b) $1/C_{Si}^2 - V$ for $S_{10,Au}$ reveal T independence under dark and a horizontal shift to lower V with decreasing T under illuminated condition with $E_{h\nu} = 3.54 \text{ eV}$ ($\lambda = 360 \text{ nm}$).	97
3.61	(a) Interface potential (φ_i), (b) electric field in GaN:C (\mathcal{E}_C), (c) depletion width in GaN:Si (w_{Si}) and equivalent sheet charge density in GaN:C (σ_C) as function of V under dark and illuminated condition for various T , whereby in dark condition the parameters are approximately T independent. Calculations base on data in Fig. 3.60(a).	98
3.62	(a) Simulated current flow through defect bands in GaN:C ($I_{DB,sim}$) based on extracted \mathcal{E}_C from Fig. 3.60(a) and $I_{DB}(\mathcal{E}_C)$ -relations shown in Fig. 3.20 with T dependence extracted from Fig. 3.19. (b) Measured I_{SS} - V characteristics.	98
3.63	(a,b) σ_C - V in dark and illuminated condition for $S_{10,Au}$ at 343 K, derived from data in Fig. 3.54. (a) Change of σ_C after bias steps from -9 V to various V_{rec} , indicated with different colors, the corresponding color map is used in $C(t)$ in (c) and (e). (b,d,f) are analogous to (a,c,e) but show bias steps from 9 V to various V_{rec} , i.e. the vice versa process. *Data from dotted green lines could not be derived from SS measurements due to artifacts from high conductance, instead data is gained from high-frequency $C(t)$ measurements using lock-in technique.	99
3.64	Acceptor discharging (negative charge emission) time constants τ as a function of V_{rec} after (a) $V_{str} = -9 \text{ V}$ and (b) $V_{str} = 9 \text{ V}$ in dark and lighted condition, derived from data in Fig. 3.63. τ in lighted condition for $V_{rec} = -9 \text{ V}$ are too small to be measured, see Fig. 3.63(e).	100
3.65	τ - V_{rec} with (a) logarithmic and (b) linear ordinate in dark (black) and lighted condition (colored) with various V_{str} ; derived from data in Fig. 3.63.	100
3.66	(a) $C(t)$ after bias steps $9 \rightarrow 2 \text{ V}$ in dark and lighted condition for various T . (b) Quantitative analysis of trapping time constants τ for $V_{str} = 9 \text{ V}$ as a function of V_{rec} for various T . (c,d) τ for various V_{str} vs. V_{rec} at $T = 408 \text{ K}$ demonstrates that τ under light cannot exceed τ in dark.	101
4.1	Schematic set of LUT structures discussed within this chapter.	104
4.2	Simplified model of a hypothetical GaN:C layer with (a) no electric field \mathcal{E}_C and (b) with a hypothetical \mathcal{E}_C , which causes charge flow, indicated by the green arrow. . .	104
4.3	Schematic band diagrams and equivalent circuit on top and space charge density (ρ) distribution on bottom for a hypothetical GaN:C layer between two ideal "barrier-free" contacts for (a) $V = 0$ and (b) $V \neq 0$	105

4.4	Schematic band diagrams and equivalent circuit on top and charge distribution on bottom for a hypothetical structure consisting of a GaN:C layer and an "ideal" dielectric (with same permittivity as GaN:C) between two ideal "barrier-free" contacts. After $V = 0$ in (a) a negative bias is applied on the left contact. (b) As charge transport is many orders of magnitude faster in the metal than in GaN:C, there is a quasistatic state (QS), in which charges already accumulated in the metal but no charge transport through GaN:C occurred yet. (c) After longer recovery time also charge transport through GaN:C occurred, resulting in SS. (d,e) are analogous to (b,c) but for positive bias on the left contact. Arrows indicate apparent (transient) negative charge transport, whereby solid lines represent "real" charge transport (i.e. "conduction current") while dashed lines represent displacement current I_d ; C_1 is the capacitance of ideal dielectric.	106
4.5	Schematic band diagrams and equivalent circuit on top and charge distribution on bottom for a hypothetical structure consisting of a GaN:C layer sandwiched between ideal dielectrics and ideal "barrier-free" contacts. After (a) $V = 0$ a bias is applied, leading to (b) QS condition and finally (c) SS condition (for definition see caption Fig. 4.4). Arrows indicate apparent (transient) negative charge transport, whereby solid lines represent "conduction current" while dashed lines represent displacement current I_d ; C_1 is the capacitance of ideal dielectric.	107
4.6	Schematic band diagrams on top and charge distribution on bottom for S_{10} . (a) SS condition for the quiescent bias $V = 0$. (b) Increasing the bias from the quiescent to a more positive value results in "ultrafast" electron injection from GaN:Si to GaN:C acceptors, establishing SS. Increasing the bias from the quiescent to a more negative value results first in (c) QS condition, in which charges already redistributed in GaN:Si but not in GaN:C and finally in (d) SS condition, in which charges also redistributed in GaN:C. For better readability, values of w_C and N_{Si} are multiplied by a factor of 3. Arrows indicate apparent (transient) negative charge transport, whereby solid lines represent "conduction current" while dashed lines represent displacement current I_d	108
4.7	(a) $I_{SS}-V$ and (b) $C_{SS}-V$ characteristics as well as extracted $1/C_{Si}^2 - V$ for $S_{Schottky}$, S_{10} and $S_{10,uid}$ at room temperature. The dashed line in (a) additionally shows $S_{10,uid}$ under elevated T	110
4.8	Calculated band diagram on top and charge distribution on bottom for $S_{10,uid}$ at $V = 0$. For better readability N_{uid} and N_{Si} are magnified by a factor of 20 and w_{C+} and w_C by a factor of 5. Calculations base on data shown in Fig. 4.7.	111
4.9	Calculated band diagrams for $S_{10,uid}$ at 300 K for several bias conditions. Calculations base on data shown in Fig. 4.7.	112
4.10	Transient capacitance for $S_{10,uid}$ during bias step from 0 to +/- 9.5 V and back with description of occurring processes in every time range. For points in time marked with green letters 'A'-'C' band diagrams and potential distributions are calculated and shown in Fig. 4.11-4.15.	113

4.11	(a) Schematic band diagrams and (b) charge distributions in every layer of $S_{10,uid}$ after a bias step from 0 to -9.5 V. Arrows represent (transient) current flow, whereby their thickness scales with the current; for simplicity displacement currents are not shown. 'A' represents a quasistatic state before charge redistribution occurred in GaN:C while 'B' represents SS. Estimations base on data from Fig. 4.10.	114
4.12	Equivalent circuit of sample $S_{10,uid}$ in QS with "conduction currents" indicated by solid green arrows and displacement currents indicated by dashed red lines.	115
4.13	(a) Schematic band diagrams, (b) charge distributions and transient "conduction currents" (represented by arrows) in every layer of $S_{10,uid}$ after a bias step from -9.5 to 0 V. 'A' represents a quasistatic state before charge redistribution occurred in GaN:C, 'B' a quasistatic state in which charge redistribution in GaN:C finished but no charge exchange with electrodes occurred yet. Finally, in 'C' the structure is in SS, details on the evolution in time are provided in Fig. 4.10. Estimations base on data from Fig. 4.10.	117
4.14	(a) Schematic band diagrams, (b) charge distributions and "conduction currents" (represented by arrows) in every layer of $S_{10,uid}$ after a bias step from 0 to 9.5 V. 'A' represents a quasistatic state before charge redistribution occurred in GaN:C while 'B' represents SS, see also Fig. 4.10. Estimations base on data from Fig. 4.10.	118
4.15	(a) Schematic band diagrams, (b) charge distributions and transient "conduction currents" (represented by arrows) in every layer of $S_{10,uid}$ after a bias step from 9.5 to 0 V. 'A' represents a quasistatic state before charge redistribution occurred in GaN:C, 'B' a quasistatic state in which charge redistribution in GaN:C finished but no charge exchange with electrodes occurred yet. Finally, in 'C' the structure is in SS, details on the evolution in time are provided in Fig. 4.10. Estimations base on data from Fig. 4.10.	119
4.16	Normalized transient capacitances for $S_{10,uid}$ after bias steps (a) from 0 to -9.5 V and (b) back to 0 at various T . (c,d) Time constants τ as function of T , (d) representing an Arrhenius-plot. Grey lines represent fits to Arrhenius law with $E_A = 0.7$ eV and black lines show τ according to the defect band model, derived from S_{10} (i.e. $\tau \propto e^{-aT}$) with $a = 0.03$ K $^{-1}$).	120
4.17	Comparison of (a) $C_{SS}-V$ and (b) $I_{SS}-V$ for $S_{Schottky}$, S_{10} and S_{Al} at room temperature. 122	
4.18	(a) $I_{SS}-V$ for S_{Al} at various T and (b) I_{SS} at 4 V compared for S_{Al} ($I_{SAI}@4V$) and S_{10} ($I_{S10}@4V$) as well as I_{SS} at 800 V for a HEMT structure ($I_{HEMT}@800V$) and trapping rate in S_{10} ($r_{S10}(-9.5 \rightarrow 0V)$). Remarkably, all currents as well as the trapping rate follow same T dependence, even with same constant a	122
4.19	(a-d) Schematic band diagrams (top) and charge distributions (bottom) for various hypothetical structures demonstrate the effect of polarization in (Al)GaN which leads for sufficiently thick AlGaN layers as in (d) to the formation of a 2DEG. (e) Values for spontaneous and piezoelectric polarization (polarization charge σ_{pol} and polarization field \mathcal{E}_{pol}) in (Al)GaN [WJ07; Lag14].	123
4.20	Theoretical calculation of band diagrams (left) and charge distributions (right) for S_{Al} considering the dominant acceptor model (see Section 3.2.2), a polarization sheet charge (σ_{pol}) of 1.4×10^{13} C cm $^{-2}$ and for varying effective acceptor concentration (N_{acc}^*) as indicated in (a-c).	124

4.21	Calculated band diagrams for S_{Al} for various bias conditions, based on $C_{SS}-V$ data depicted in Fig. 4.17(a).	127
4.22	Transient capacitance analysis at 390 K after various bias steps in (a) <i>depletion regime</i> and (b) <i>plateau regime</i> with indicated carbon acceptor charging/discharging processes.	128
4.23	Theoretically calculated band diagrams (left) and charge distributions (right) for an AlGa _N :C/GaN:C interface with AlGa _N :C on top, considering same effective acceptor concentrations (N_{acc}^* ; varying for (a-c)) in GaN:C and AlGa _N :C.	129
4.24	Theoretically calculated band diagrams (left) and charge distributions (right) for an AlGa _N :C/GaN:C interface with GaN:C on top, considering same donor concentrations (N_{don} ; varying values in (a-c)) in AlGa _N :C and GaN:C.	130
4.25	Comparison of (a) $I_{SS}-V$ and (b) $C_{SS}-V$ for samples S_{10} , S_{Al} and S_{SL} . (c) Calculated total depletion width w based on data from (b).	131
4.26	Speculative schematic SS band diagrams for reverse biased S_{SL} structures based on $C_{SS}-V$ and $I_{SS}-V$ characteristics shown in Fig. 4.25(a,b).	132
4.27	Speculative schematic SS band diagrams for forward biased S_{SL} structures based on $C_{SS}-V$ and $I_{SS}-V$ characteristics shown in Fig. 4.25(a,b).	133
A.1	Spectra of various discharge lamps, whereby the upper one (“6258 300 W Xe OZON FREE”) is used. Figure from [NC06b].	140
A.2	Inner workings of the monochromator with gratings as wavelength-filtering part. Figure from [NC06a].	140
A.3	Spectral transmittance of the light guide, whereby the one labelled “UV-VIS” has been used. Figure from Newport datasheet.	142
A.4	(a) Spectral photo current (I_{photo}) measured in photodiode, (b) responsivity of the photo diode ($R_{photodiode}$) [Tho12], (c) spectral light source power (P_{lamp}) and (d) spectral photon irradiance (E_e). Red solid lines represent measurements in which the cutoff-filter is inserted for $\lambda > 400$ nm.	143

List of Tables

3.1	Stacks of all investigated samples (LUT structures) and designated names.	30
3.2	All dynamic processes can be attributed to one of four representative bias steps. . .	45
3.3	Expressions for charge transport rates in Fig. 3.15 with simulation parameters. Table reused from [Kol+18a].	56
3.4	Summary of the T dependence of SS leakage currents I_{SS} and charging/discharging time constants τ after various bias steps as indicated in the index of τ for S_{01} , S_{10} and S_{70} with their different carbon concentrations $[C]$ [Kol+18a].	66

Acronyms

$C(t)$	transient capacitance measurements, measured using lock-in technique with a frequency of 785 kHz.
C_{Ga}	point defect in which a C atom substitutes a Ga atom in the crystal.
C_{I}	point defect in which a C atom occupies an interstitial site in the crystal.
C_{N}	point defect in which a C atom substitutes an N atom in the crystal.
S_{01}	for sample definition see Tab. 2.1.
$S_{10,\text{Au}}$	for sample definition see Tab. 2.1.
$S_{10,\text{uid}}$	for sample definition see Tab. 2.1.
$S_{10\text{b}}$	for sample definition see Tab. 2.1.
S_{70}	for sample definition see Tab. 2.1.
S_{Al}	for sample definition see Tab. 2.1.
S_{SL}	for sample definition see Tab. 2.1.
S_{Schottky}	for sample definition see Tab. 2.1.
S_{10}	for sample definition see Tab. 2.1.
<i>Ohmic regime</i>	bias regime, in which the Ohmic current is filamented in the LUT and limited by R_{BS} .
<i>ac</i>	alternating current.
<i>dc</i>	direct current.
<i>depletion regime</i>	bias regime, in which reverse bias increasingly depletes the GaN:Si layer of a LUT structure; analogous to MOS capacitor in depletion.
<i>plateau regime</i>	bias regime, in which C_{SS} and φ_{i} in LUT structures are roughly bias-independent.
2DEG	two-dimensional electron gas.
2DHG	two-dimensional hole gas.
ACM	auto-compensation model.
AG	Aktiengesellschaft (german, incorporated company).
Al	aluminum.
AlGa _x N	Al _x Ga _{1-x} N with $x=[\text{Al}]/([\text{Al}]+[\text{Ga}])$; if not explicitly stated different, $x = 0.3$ is considered.
AlGa _x N:C	C-doped AlGa _x N.
AlN	aluminum nitride.
APT	atom probe tomography.

Au	gold.
C	carbon.
CB	conduction band.
CBM	conduction band minimum.
CC	current collapse.
CCD	charge-coupled device.
CF	current filament.
CTS	current transient spectroscopy.
DAM	dominant acceptor model.
DB	defect band.
DOS	density of states.
e^-	electron.
e.g.	exemplī grātiā (latin, read as <i>for example</i>).
EL	electroluminescence spectroscopy.
EMMI	emission microscopy.
Eq.	Equation.
Fe	iron.
Fig.	Figure.
Ga	gallium.
GaN	gallium nitride.
GaN:C	C-doped GaN.
GaN:Si	Si-doped GaN.
GaN:uid	unintentionally doped GaN.
h^+	hole.
HEMT	high-electron-mobility transistor.
i.e.	id est (latin, read as <i>that is to say</i>).
IGBT	insulated-gate bipolar transistor.
InGaN	$In_xGa_{1-x}N$ with $x=[In]/([In]+[Ga])$, [In] being the In concentration.
KAI GmbH	Kompetenzzentrum für Automobil- und Industrieelektronik GmbH (german, competence center for automotive and industrial electronics limited liability company).
LED	light-emitting diode.
LUT	”layer under test”, i.e. layers above the base structure that can be electrically characterized separately from the base structure.
MOCVD	metalorganic chemical vapor phase epitaxy.
MOS	metal-oxide-semiconductor structure.
MOSFET	metal-oxide-semiconductor field-effect transistor.
N	nitrogen.
NDR	negative differential resistance.
Ni	nickel.

PL	photoluminescence spectroscopy.
QS	quasistatic state.
SCLC	space-charge-limited conduction.
Si	silicon.
SiC	silicon carbide.
SRH	Shockley-Read-Hall.
SS	steady state.
Tab.	Table.
TCAD	technology computer aided design.
Ti	titan.
VB	valence band.
VBM	valence band maximum.
VRH	variable range hopping.
vs.	versus.

Symbol list

Symbol	Description	Unit
A	top contact area	cm^2
$C_{\text{GaN:C}}$	capacitance per area of GaN:C layer	F cm^{-2}
C_{SS}	SS capacitance per area, measured with a standard commercially available impedance analyzer with a frequency of 10 kHz	F cm^{-2}
C_{Si}	capacitance per area of GaN:Si layer	F cm^{-2}
C	capacitance per area	F cm^{-2}
$E_{\text{A}}^{\text{ion}}$	defect ionization energy, i.e. energy difference between defect energy and related band edge	eV
E_{A}	thermal activation energy	eV
E_{CB}	energy level of conduction band minimum	eV
E_{DB}	defect band energy level	eV
E_{F}	Fermi level energy	eV
E_{VB}	energy level of valence band maximum	eV
E_{acc}	carbon acceptor energy level	eV
E_{bg}	bandgap	eV
E_{don}	donor energy level	eV
E_{e}	photon irradiance	$\text{s}^{-1} \text{m}^{-2}$
$E_{\text{h}\nu}$	photon energy	eV
E_{opt}	optical excitation energy, i.e. required energy for a photon to ionize a carbon acceptor	eV
E_{spec}	photon energy emitted from electron capture	eV
E_{th}	thermal energy barrier	eV
I_0	T and \mathcal{E}_{C} independent pre-factor in defect band current density expression	A cm^{-2}
$I_{2\text{DEG}}$	current density in 2DEG	A mm^{-1}
I_{C}	transient charging/discharging current density, i.e. flow of charges through GaN:C captured by or emitted from carbon acceptors	A cm^{-2}
$I_{\text{DB,sim}}$	simulated current density through defect bands, calculated from empiric found relation for I_{DB}	A cm^{-2}
I_{DB}	current density through defect bands	A cm^{-2}
I_{HEMT}	SS vertical leakage current density through a HEMT-like test structure	A cm^{-2}
I_{Ohm}	Ohmic current density	A cm^{-2}
I_{PF}	Poole-Frenkel current density	A cm^{-2}

Symbol	Description	Unit
I_{SS}	SS current density, measured by a standard commercially available parameter analyzer	$A\text{ cm}^{-2}$
I_{Si}	injection current density from GaN:Si to GaN:C	$A\text{ cm}^{-2}$
I_{Ti}	current density in the top Ti electrode	$A\text{ cm}^{-2}$
I_{bot}	current density in the bottom electrode	$A\text{ cm}^{-2}$
I_d	displacement current density	$A\text{ cm}^{-2}$
I_h	difference of hole and electron capture rates in GaN:C (times q) due to illumination per area and time interval	$A\text{ cm}^{-2}$
I_{photo}	photo current density	$A\text{ cm}^{-2}$
I_{uid}	current density through GaN:uid	$A\text{ cm}^{-2}$
I	current density	$A\text{ cm}^{-2}$
L_{gd}	gate-drain length	μm
N_{CB}	effective DOS in CB	cm^{-3}
N_{Si}	Si donor doping concentration in GaN:Si	cm^{-3}
N_{VB}	effective DOS in VB	cm^{-3}
$N_{acc,crit}^*$	critical N_{acc}^* below which a 2DEG forms at GaN/AlGaIn interfaces at 0 V	cm^{-3}
N_{acc}^*	"effective" acceptor concentration in GaN:C, i.e. $N_{acc}^* = N_{acc} - N_{don}$	cm^{-3}
N_{acc}	carbon acceptor concentration	cm^{-3}
N_{crit}	critical carbon concentration for formation of defect bands	cm^{-3}
N_{don}	carbon donor concentration	cm^{-3}
N_{uid}	effective impurity donor concentration in GaN:uid	cm^{-3}
P_{lamp}	output power of light source	W
R_{BS}	resistance of the base structure	Ω
R_{CCD}	responsivity of used CCD	%
R_{EMMI}	responsivity of entire EMMI setup	%
R_{LUT}	resistance of LUT	Ωcm^2
R_{diff}	differential resistance	Ωcm^2
$R_{ds,on}$	on-resistance in HEMT	Ωcm^2
$R_{photodiode}$	photodiode responsivity	$A\text{ W}^{-1}$
T_{metal}	transmissivity through metal contact	%
T_{optics}	transmissivity of optics	%
T	temperature	K
V_C	voltage drop in the space charge region of an (Al)GaN:C layer next to its interface to GaN:Si	V
$V_{GaN:C}$	voltage drop in GaN:C layer	V
$V_{GaN:uid}$	voltage drop in GaN:uid layer	V
V_{Si}	voltage drop in GaN:Si layer	V
V_{TFL}	trap-filled limit voltage in SCLC	V
V_{bd}	breakdown voltage	V
$V_{bi,lighted}$	V_{bi} under illumination	V

Symbol	Description	Unit
V_{bi}	built-in voltage, i.e. root of extrapolated $1/C_{Si}^2 - V$ in <i>depletion regime</i>	V
$V_{fil,down}$	V_{fil} during down-sweep	V
$V_{fil,up}$	V_{fil} during up-sweep	V
V_{fil}	filamentation bias i.e. transition bias between <i>plateau</i> and <i>Ohmic regime</i>	V
V_{rec}	bias during recovery pulse	V
V_{str}	bias during stress pulse	V
V_{sub}	applied bias at Si substrate	V
V_{th}	threshold voltage for formation of a 2DEG at AlGa _N /Ga _N interface	V
V	applied bias at top electrode	V
Z_{BS}	impedance of the base structure	Ωcm^2
Z_{LUT}	impedance of LUT	Ωcm^2
$\Delta E_{A,DB}$	energy difference between E_{acc} and E_{DB}	eV
$\Delta\sigma_C$	change of charge per area in (Al)Ga _N :C after a bias step	C cm^{-2}
$\Delta\sigma_{pol}$	apparent σ_{pol} at Ga _N /AlGa _N or AlGa _N /Ga _N interfaces due to different polarization in both materials	C cm^{-2}
$\tau_{cap,VB}^h$	time constant for capture of holes in carbon acceptors from VB	s
$\tau_{em,VB}^h$	time constant for emission of holes from carbon acceptors to VB	s
$\tau_{Schottky}$	time constant for emission of holes from top electrode to Ga _N :C VB	s
τ_{cap}	capture time constant	s
τ_{charge}	charging time constant, i.e. time constant for negative charge accumulation in (Al)Ga _N :C	s
$\tau_{disch.}$	discharging time constant, i.e. time constant for negative charge dissipation in Ga _N :C	s
τ_{em}	emission time constant	s
$\tau_{trans,VB}$	transport time constant in Ga _N :C VB	s
λ	wavelength	nm
\mathcal{E}_C	electric field in Ga _N :C layer	kV cm^{-1}
\mathcal{E}_{pol}	polarization field in (Al)Ga _N	kV cm^{-1}
\mathcal{E}	electric field	kV cm^{-1}
μ	charge mobility	$\text{cm}^2 \text{V}^{-1} \text{s}^{-1}$
ν_{th}	thermal velocity	m s^{-1}
ρ_{BS}	resistivity of the base structure	Ωcm
ρ	space charge density	C cm^{-3}
σ_{2DEG}	2DEG sheet charge density	C cm^{-2}
σ_{CC}	capture cross section	cm^2
σ_C	charge per area in (Al)Ga _N :C	C cm^{-2}
σ_{Si}	charge per area in depleted Ga _N :Si	C cm^{-2}
σ_{pol}	polarization sheet charge density	C cm^{-2}
τ	time constant	s
[C]	carbon concentration	%

Symbol	Description	Unit
ε_0	vacuum permittivity $\varepsilon_0 = 8.854 \times 10^{-14} \text{ F cm}^{-1}$ [SN06]	F cm^{-1}
ε_r	relative permittivity of GaN $\varepsilon_r \approx 9.5$ [LRS01,BI73]	
ε	permittivity of GaN $\varepsilon = \varepsilon_r \times \varepsilon_0 = 8.4115 \times 10^{-13} \text{ F cm}^{-1}$	F cm^{-1}
$\varphi_{\text{S,CB}}$	electrostatic potential difference of metal and CBM in GaN	V
φ_i	electrostatic potential of CBM at GaN:Si/GaN:C interface	V
φ	electrostatic potential, defined as potential of the CBM	V
c	speed of light $c = 299\,792\,000 \text{ m s}^{-1}$ [SN06]	m s^{-1}
$d_{\text{FC},1}$	Franck-Condon shift for photon capture	eV
$d_{\text{FC},2}$	Franck-Condon shift for photon emission	eV
d_{LUT}	thickness of semiconductor layers in LUT structures above GaN:Si	nm
d_{slit}	monochromator output slit width	m
$g_{\text{e-h}^+}$	electron-hole pair generation rate	s^{-1}
h	Planck constant $h = 6.626 \times 10^{-34} \text{ J s}$ [SN06]	J s
k_B	Boltzmann constant $k_B = 8.6174 \times 10^{-5} \text{ eV K}^{-1}$ [SN06]	eV K^{-1}
m_0	rest mass of an electron $m_0 = 9.110 \times 10^{-31} \text{ kg}$ [SN06]	kg
m_e	effective electron mass $m_e = 0.2 \times m_0$ [LRS01]	kg
m_h	effective hole mass $m_h = 0.8 \times m_0$ [Pan75]	kg
n_0	positive integer in Bragg's law	%
n	free electron density in CB	cm^{-3}
p	free hole density in VB	cm^{-3}
q	elementary charge $q = 1.602 \times 10^{-19} \text{ C}$ [SN06]	C
r_{DB}	trapping rate in GaN:C, determined by I_{DB}	s^{-1}
$r_{\text{e-h}^+}$	band-to-band recombination rate	s^{-1}
t_{fil}	time until filamentation	s
t_{int}	integration time	s
t	time	s
w_{C^+}	space charge region width in GaN:C next to its top interface (if no metal)	nm
w_{C}	space charge region width in GaN:C next to its bottom interface	nm
w_{Si}	depletion width in GaN:Si	nm
w_{Ti}	space charge region width in GaN:C next to its interface to Ti	nm
w	depletion width	nm
[Al]	aluminum concentration	%
[Ga]	gallium concentration	%

Christian Koller

Curriculum Vitae

Marksgasse 5/10
9500 Villach, Austria
☎ (+43) 664 3803008
✉ christian.kohlsen@gmail.com



Personal Information

Nationality **Austrian.**
Date of Birth **January 11th, 1989.**
Place of Birth **Zwettl, Austria.**

Education

- 2015-present **Doctoral program technical sciences**, Vienna University of Technology, Faculty of Electrical Engineering and Information Technology, Institute of Solid State Electronics, Vienna, Austria.
- Doctoral Thesis *The Role of Carbon in Creating Insulating Behavior in GaN-on-Si Buffers: A Physical Model*, awarded with the PhD Innovation Award 2018 from Infineon Technologies Austria AG
- 2013-2015 **Master program technical physics**, degree with distinction, Vienna University of Technology, Faculty of Physics, Vienna, Austria.
- Master Thesis *Investigation of Surface Oxidation of III-N Materials by AES*
- 2013-2014 Participation in "TUtheTOP", the High Potential Program of Vienna University of Technology
- 08/2012-02/2013 **International student exchange program**, University of Texas at Austin, College of Natural Sciences, Department of Physics, Austin, Texas, United States of America.
- 2009-2013 **Bachelor program technical physics**, degree with distinction, Vienna University of Technology, Faculty of Physics, Vienna, Austria.
- 2003-2008 **Technical college building engineering**, degree with distinction, HTL Krems, Krems, Austria.

Experiences

- 05/2018-present **Junior researcher**, Kompetenzzentrum für Automobil und Industrieelektronik, Villach, Austria.
- 02/2015-present **Industrial PhD thesis**, Kompetenzzentrum für Automobil und Industrieelektronik, Villach, Austria.
- 02/2014-10/2014 **Industrial master thesis**, Infineon Technologies Austria AG, Villach, Austria.

- 08/2013-09/2013 **Internship**, *Flughafen Wien AG*, Schwechat, Austria.
08/2011-10/2011
08/2010-10/2010
08/2009-10/2009 **Internship**, *Leyrer + Graf BaugmbH*, Gmünd, Austria.
09/2008-10/2008
08/2007-09/2007
08/2006-09/2006
08/2005-09/2005
10/2008-07/2008 **Civilian service**, *Austrian red cross*, Gmünd, Austria.
08/2008-09/2008 **Internship**, *A. Porr AG*, Vienna, Austria.
08/2004-09/2004 **Internship**, *Oppolzer BaugmbH*, Gmünd, Austria.

Computer skills

- Basic C, FORTRAN, LUA
Advanced PYTHON, MATHEMATICA, ORIGIN, L^AT_EX, INKSCAPE, AUTOCAD, ARCHICAD

Languages

- German Mothertongue
English C2, *Common European Framework of Reference for Languages, self-assessment*

Interests and Miscellaneous

- Driving license Car, Austrian category B
Hobbies mountaneering, climbing, skitouring, beach volleyball